Theses & Dissertations   Graduate Studies

Spring 5-7-2016

Block Copolymer Based Magnetic Nanoclusters for Cancer-Theranostics: Synthesis, Characterization and In Vitro Evaluation

Hemant M. Vishwasrao
University of Nebraska Medical Center

BLOCK COPOLYMER BASED MAGNETIC NANOCLUSTERS FOR CANCER-THERANOSTICS: SYNTHESIS, CHARACTERIZATION AND *IN VITRO* EVALUATION

By

Hemant Motiram Vishwasrao

A DISSERTATION

Presented to the Faculty of

The University of Nebraska Graduate College

in Partial Fulfillment of the Requirements

For the Degree of Doctor of Philosophy

Pharmaceutical Sciences Graduate Program

Under the Supervision of Professor Alexander V. Kabanov

University of Nebraska Medical Center

Omaha, Nebraska

January, 2016

Supervisory Committee

Alexander V. Kabanov, Ph.D., Dr.Sci   Tatiana Bronich, Ph.D.

Dong Wang, Ph.D.   Michael Boska, Ph.D.

ACKNOWLEDGEMENTS

"Life's battles don't always go to the stronger or the faster man. But sooner or later, the man who win's, is the man who thinks he can."

- Vince Lombardi

So far, I have lived my life believing that "I CAN". My decision to undertake this behemoth (for me it was) task of doing a Ph.D. was solely based on this self-belief that "Yes I can". But it took concerted efforts, support and guidance of many; my teachers, friends and family to come this far and succeed. It is indeed a great pleasure and a moment of immense satisfaction for me to express my gratitude and indebtedness towards my advisor Dr. Alexander 'Sasha' Kabanov, for accepting me as his mentee and providing me with all the backing and trust required for the successful completion of my doctoral dissertation. It has been an honor to be a student of a stalwart in the field of drug delivery and nanomedicine, who inspires one and all by his work ethics, competitive spirit and immense patience. I fall short of words to express my deepest gratitude for Sasha for his moral support and words of encouragement whenever he sensed I was low on confidence. As I move ahead in life, I will have an opportunity to work under the guidance of many 'bosses'. But I will never find a kind hearted, magnanimous and honest chief like Sasha.

I would like to thank my Ph.D. advisory committee members Dr. Tatiana (Tanya) Bronich, Dr. Michael Boska and Dr. Dong Wang for their continued support, understanding and guidance in my research work. In spite of me being off-campus at UNC-Chapel Hill, they were always only a phone call away whenever I needed their valuable suggestions. I am especially thankful to Dr. Boska for helping me understand the concepts of MRI and associated contrast systems. There has not been a week when I have not missed Tanya ever since we moved to UNC-Chapel Hill. Her timely advises and dedication towards us

students in general will always be cherished. Dr. Wang has always been there to answer my questions and help me think in the right direction. Then be it regarding science or about managing and dealing with life's issues, he could be approached at any time and I was always sure that I would find my path after talking to him. I am very fortunate in having Dr. Marina Sokolsky as my project supervisor. She has been my constant source of encouragement throughout these years in the lab. When the going got tough, she was always there to find solutions and when nothing worked, gave a patient ear as I vented my frustration. I would like to make a special mention of our collaborators at Virginia Tech. Had it not been for the extensive training and support offered by Dr. Judy Riffle, Dr. Nikorn Pothayee and Dr. Richey Davis, I would not have been able to stand on my own in this field of magnetic nanoparticles and flash nanoprecipitation. Hence a big thanks to both, especially to Dr. Davis, who fabricated the MIVM mixer for our lab and spent his valuable time discussing my work over Skype on numerous occasions.

I want to thank all my colleagues and friends from the old CDDN group at UNMC and the new lab members at the new lab in UNC-Chapel Hill, especially Dr. Swapnil Desale, Dr. Jinjin Zhang, Dr. Devika Manickam, Christine Allmon, Jubina Bregu, Dr. Elena Batrakova, Matt Haney, Youngee Seo, Xiaomeng Wan, Duhyong Hwang, Dongfen Yuan, Yuhang Jiang, Yuling Zhang, Philise Williams, Dr. Daria Alakhova, and Nazar Filonov. I will fail in my duty as a friend if I do not say a special thank you to my dear friend and 'partner in crime' Dr. Alyssa Master. Ever since she joined the lab, she has constantly helped me with my experiments, at times keeping her work aside. I am highly indebted to her for helping me with my manuscript writing. I cannot thank her enough.

Finally, I would like to thank my family members for their love, patience and constant support throughout this extended school life. I thank my father for his unconditional support and belief in me and his critiques, which helped me 'stay in the game'. Many thanks to my

brother Jayesh and my sister-in-law Manisha for giving me the confidence to keep moving ahead without worrying about anything back home in India. I would especially like to mention the two women in my life; my mother, Vrishali for believing in me and being the main pillar of strength to my family and my better half, or should I say my better three-quarters - my wife Dr. Sheetal. Her arrival in my life showed me what lady luck means. I am indebted to her more than anyone else for supporting me through my Ph.D. She has sacrificed her career as a dentist to see me get my doctorate. As I complete my Ph.D., I have no doubt that she will be the happiest person in the world and so will be my in-laws who have been equally patient and eagerly awaiting to see us flourish in our respective professions. I cannot forget the three gems in my life, my niece Paree, nephew Neel, and my little Simba- my son Shaan for giving all of us a reason to smile and for adding to the strength of my bond with my family back home in India. Their smiles constantly remind me of the existence of the supreme almighty who has sent them to make our lives more meaningful.

Last but not the least, I express my heart-felt gratitude to the entire Molecular Pharmaceutics Division and Eshelman School of Pharmacy at University of North Carolina at Chapel Hill for accommodating and making us UNMC students feel at home. They accepted us as their own and constantly encouraged us to participate in all their events. The valuable experience I gained, the friends I made and the innumerable professional bonds I forged here is something I will cherish for a long time to come.

Thank you.

Hemant Vishwasrao

BLOCK COPOLYMER BASED MAGNETIC NANOCLUSTERS FOR CANCER-THERANOSTICS: SYNTHESIS, CHARACTERIZATION AND *IN VITRO* EVALUATION

Hemant Motiram Vishwasrao, Ph.D.

University of Nebraska Medical Center, 2016

Advisor: Alexander V. Kabanov, Ph.D., Dr.Sci.

"There is plenty of room at the bottom". In this visionary lecture in 1959 Prof. Richard Feynman spoke of the interesting ramifications of working with matter at the atomic scale. Since then, scientists have worked relentlessly towards realizing his vision. The influence of nanobiotechnology on material science and polymer chemistry has given rise to a new field called 'theranostics', combining drug delivery and diagnostics within the same nanostructures, thereby enabling simultaneous diagnosis, targeted drug delivery and continued therapy monitoring. Iron oxide nanoparticles (MNPs) are one such class of MRI contrast agents that can be converted into theranostic nanomedicines for cancer therapy. However, development of a stable theranostic contrast system comprising of MNPs is complex and requires a careful balance between the therapeutic diagnostic components.

We explored the potential of biodegradable hydrophilic block ionomers such as anionic poly (glutamic acid-*b*-ethylene glycol) and cationic poly (l-lysine-*b*-ethylene glycol) in formulating stable magnetic nanoclusters (MNCs). These MNCs were extensively characterized for their composition, colloidal stability and factors influencing their MRI capability. Extensive *in vitro* studies revealed that the anionic cisplatin-loaded MNCs showed minimal non-specific uptake, a highly preferred feature for targeted cancer therapy. Luteinizing hormone releasing hormone receptor (LHRHr) targeting significantly enhanced the uptake of these formulations in LHRHr-positive ovarian cancer cells. LHRHr

targeting also helped improve the theranostic efficacy in cisplatin resistant ovarian cancer cells. One the other hand, cationic MNCs were used to demonstrate the potential of MNCs to function as stimuli-responsive theranostic systems capable of releasing the payload in the acidic milieu breast and ovarian cancer cells. These cationic MNCs also exhibited significantly enhanced T2-weighted MRI contrasts at much lower concentrations than the anionic counterparts.

Finally, we successfully evaluated the feasibility of kinetically controlled flash nanoprecipitation technique using multi-inlet vortex mixer (MIVM) to formulate well-defined MNCs from non-ionic amphiphilic Pluronic tri-block copolymers. In comparison to self-assembly techniques, flash nanoprecipitation resulted in significant reduction in polydispersity. It was observed that the hydrophobic block-length of the copolymer dictates the extent of encapsulation hydrophobic therapeutic agents along with the MNPs. exhibited the potential to function as both T_1 and T_2 contrast agents.

In summary, looking at the bigger picture, the work presented here emphasizes on the importance of product development in establishing a critical balance between the therapeutic and imaging functionalities when designing an efficient targeted theranostic nanosystems.

TABLE OF CONTENTS

CHAPTER ONE

INTRODUCTION

CHAPTER 2

LHRHR-TARGETED MAGNETIC NANOCLUSTERS STABILIZED BY BIS-PHOSPHONATE-MODIFIED POLY (GLUTAMIC ACID)-B-POLY (ETHYLENE GLYCOL) FOR OVARIAN CANCER THERANOSTICS

CHAPTER 3

CATIONIC MAGNETIC NANOCLUSTERS STABILIZED BY POLY (L-LYSINE)-B-POLY (ETHYLENE GLYCOL) FOR CANCER THERANOSTICS

CHAPTER 4

NON-IONIC MAGNETIC NANOCLUSTERS FOR DUAL-PURPOSE MRI IMAGING

CHAPTER 5

SUMMARY

LIST OF FIGURES

LIST OF SCHEMES

LIST OF TABLES

LIST OF ABBREVIATIONS

MNP Magnetic nanoparticles

QDs Quantum Dots

GFP Green fluorescence protein

PLE Poly (Glutamic acid)

PEG Polyethylene glycol

SQUID Superconducting quantum interference device

FRET Förster resonance energy transfer

PEI Poly (ethyleneimine)

PLK Poly(l-lysine)

M.W. Molecular weight

PVA Poly vinyl alcohol

MRI Magnetic resonance imaging

$t_{1/2}$ Half-life (biological or radioactive)

TAT trans-activator of transcription

HIV Human immunodeficiency virus

FCS fluorescence correlation spectroscopy

DNA Deoxyribonucleic acid

FFS fluorescence fluctuation spectroscopy

KDa Kilo Daltons

FTIR Fourier transform infrared

IgG   Immunoglobulin G

HER   Human epidermal growth factor receptor

pDNA   Plasmid DNA

FePt   Iron-Platinum

Gd   Gadolinium

PET   Positron Emission Tomography

SPECT   Single Photon Emission Computed Tomography

mAb   monoclonal antibody

DOX   Doxorubicin

PTX   Paclitaxel

MNC   Magnetite nanoclusters

PAMAM   poly (amidoamine)

DSPE   1,2-distearoyl-*sn*-glycero-3-phosphoethanolamine-N-[amino(polyethylene

       glycol)

PDT   Photodynamic therapy

PLA   Poly (lactic acid)

PAT   Photo acoustic tomography

fMRI   Functional Magnetic Resonance Imaging

PFC   Perfluorocarbons

PCL   poly(ε-caprolactone)

PNB   Plasmonic nanobubbles

CNT   Carbon nanotubes

MWCNT   Multi-walled Carbon nanotubes

SWCNT   Single-wall Carbon nanotubes

AuNP   Gold nanoparticles

MIVM   Multi inlet vortex mixer

PTT   Photo thermal therapy

EGFR   Epidermal growth factor receptor

CT   Computed Tomography

USPION   Ultra-small superparamagnetic iron oxide nanoparticles

BBB   Blood-brain barrier

TBI   Traumatic brain injury

FDA   Food and drug administration

HSP   Heat-shock protein

BSA   Bovine serum albumin

LDL   Low density lipoproteins

VEGF   Vascular endothelial growth factor

MFH   Magnetic fluid hyperthermia

SAR   specific absorption rate

ms   milliseconds

NSCLC   Non-small cell lung cancer

RGD   Arginylglycylaspartic acid

PNIPAM   poly-n-(isopropyl acrylamide

5-FU   5-Fluorouracil

PBS   Phosphate buffered saline

ABS   Acetate buffered saline

MRA   Magnetic resonance angiography

WT   wild-type

LHRH   Luteinizing hormone releasing hormone

LHRHr   Luteinizing hormone releasing hormone receptor

Fe(acac)$_3$ Iron (III) acetylacetonate

BA   Benzyl alcohol

ALN   Alendronate

RT   Room temperature

DI   De-ionized

DMSO   Dimethoxy sulfoxide

TGA   Thermogravimetric analysis

ICPMS   Inductively coupled plasma mass spectrometry

T_1 Longitudinal relaxation time

T_2 Transverse relaxation time

R_1 Longitudinal relaxation rate

R_2 Transverse relaxation rate

r_1 Longitudinal relaxivity

r_2 Transverse relaxivity

LOI   Loss on ignition

MWCO   Molecular weight cut-off

TE   Echo time

TR   Repetition time

FA   Flip-angle

M_s Magnetization saturation

DLS   Dynamic light scattering

ppm   parts per million

ppb   parts per billion

CisR   Cisplatin resistant

SPDP   N-Succinimidyl 3-[2-pyridyldithio]-propionate

DMF   n,n-dimethylformamide

EMCH   3, 3´-N-[ε-Maleimidocaproic acid] hydrazide

DTT   Dithiothreitol

HZN   Hydrazone

D_{eff} Effective diameter/ Z-average diameter as recorded on zetasizer

CIJ   Confined Impingement Jet

HPLC   High performance liquid chromatography

%TLC   Theoretical loading capacity expressed in percent

R_e Reynolds number

%LC Loading capacity

%CE Efficiency of conjugation reaction

%EE Encapsulation efficiency

cac critical aggregation concentration

CMC Critical Micelle Concentration

TEM Transmission electron microscopy

LIST OF CONTRIBUTORS

a) CHAPTER 2: SCHEME 2.1 was illustrated by Dr. Daria Alakhova

b) Dr. Marina Sokolsky provided assistance with TEM images while at the UNMC. Ms. Victoria Madden provided assistance and required training for TEM imaging at MSLUNC-Chapel Hill while Dr. Amar Kumbhar assisted with the TEM images at UNC CHANL.

c) Nazar Filonov, ex-director of UNC-NCore, assisted in the ICPMS analysis.

d) Dr. Mike Boska and Ms. Mellissa Mellon at UNMC radiology provided assistance with the relaxivity measurements and data interpretation. At UNC-Chapel Hill, Ms Amber Abernethy Leinwand and Xiaopeng Zong of UNC-BRIC provided assistance with phantom imaging and relaxivity measurements in 3T and 7T human scanner. Joseph Merrill provided with relaxivity measurements and animal imaging on 9.4T small animal MRI scanner.

e) Dr. Alyssa Master provided the training while assisting in all the confocal microscopy experiments described in this dissertation and helped in preparing the manuscripts for publication.

f) Youngee Seo provided assistance with magnetic susceptibility measurements on the magnetic nanoparticles at North Carolina State University.

g) Hemant Vishwasrao made major contributions in all the chapters under the supervision of Dr. Marina Sokolsky. The work was designed under the guidance of Dr. Alexander Kabanov and Dr. Marina Sokolsky. Hemant Vishwasrao has written the published papers based on these studies under the guidance of Dr. Marina Sokolsky and Dr. Alexander Kabanov.

CHAPTER ONE

INTRODUCTION

1.1. THERANOSTIC SYSTEMS FOR SIMULTANEOUS DETECTION AND DRUG DELIVERY: AN OVERVIEW

For many decades' clinicians and researchers have desired to develop non-invasive strategies for diagnosis, therapy and monitoring of numerous pathological conditions in humans. The advent of nanotechnology and the extensive research into its medical applications has spawned a new era in the field of pharmaceutics and drug delivery. The development of novel nano-vehicles such as liposomes, nanogels, micelles etc. for delivery of therapeutic payloads to specific target organs has significantly improved the treatment of diseases such as cancer. Their successes in significantly reducing undesired side effects in healthy tissues has directed the research towards developing systems capable of concomitant detection and localized treatment while allowing for therapy monitoring [1-3]. Such single-entity nano-platforms capable of simultaneously targeting, detecting and treating diseased tissue for a prolonged period of time are much desired in clinical settings and thus, the field of 'theranostics' has emerged. The term "theranostics" has been coined by the combination of the terms 'therapy' and 'diagnostics' to describe this promising new field of research that focuses on the creation of a single therapeutic carrier system with integrated diagnostic agents for combined capabilities [4, 5].

The theranostic approach promises therapeutic specificity due to the molecular characters of the disease and also promises a broader choice of contrast agents to objectively monitor therapeutic response. The current focus of theranostic formulations is development of systems with stealth properties that enable prolonged circulation times

and sustained release of the drug while simultaneously providing noninvasive *in vivo* imaging capability [6,7]. It would be highly beneficial from the pharmacokinetic standpoint if the circulation time and organ accumulation of the various nanomedicines could be studied in real time. Such systems can also help in formulation characterization by studying the *in vivo* drug release patterns. Targeted theranostic nano-systems go a step further in terms of tissue-specificity due to their ability to accumulate preferentially at the desired site of action. As exciting as the potential applications of theranostic nanosystems are, the formulation process of such multi-component systems is complex and requires meticulous control. The following section briefly describes the different fabrication approaches used for different theranostic systems.

1.2. DESIGN COMPONENTS OF A THERANOSTIC NANO-FORMULATION

CONTRAST AGENTS
- MNPs
- Radionuclides
- Porphyrins
- Quantum Dots
- Gold nanoparticles
- Micro/ nanobubbles

THERAPEUTIC AGENTS
- Small molecules
- Proteins/ Nucleic acids

NANOCARRIER BUILDING BLOCKS
- Block copolymers
- Lipids
- PVA/ Low M.W. PEG
- Targeting Ligands

Liposomes/ Polymersomes

Matrix nanoparticles

Dendrimers

Micelles /Clusters
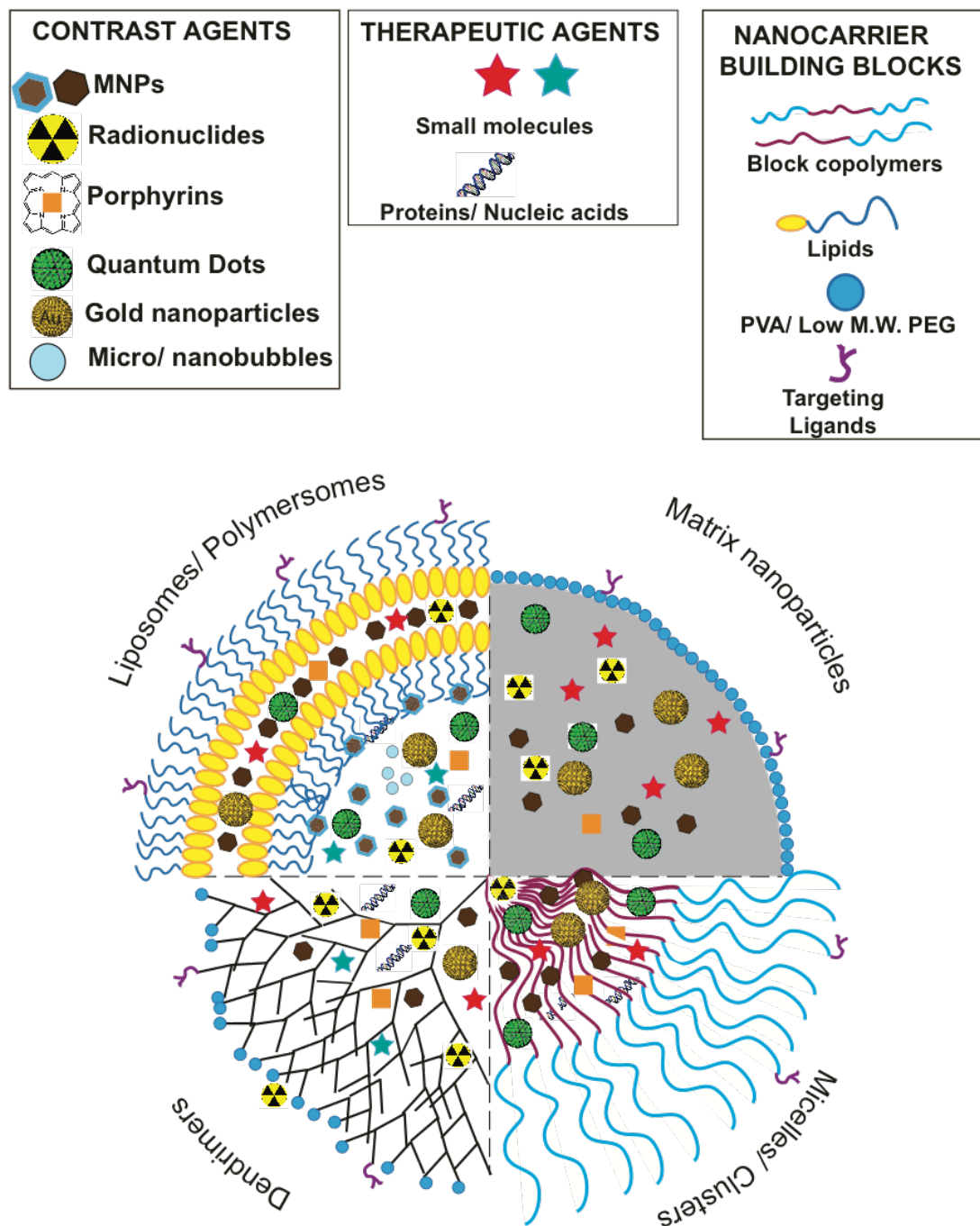
Figure 1.1. Components of a theranostic nanosystem

A typical targeted theranostic nano-particulate system is composed of the following components (Figure 1): -

a) Therapeutic agent, which can include small molecules, protein and peptide therapeutics or nucleic acids

b) Diagnostic/contrast or some other type of imaging agent

c) Nano-vehicle

d) Targeting moiety

1.2.1. DESIGN CRITERIA AFFECTING THE CHOICE OF THE THERANOSTIC COMPONENTS

Several factors have to be considered in the design of a theranostic nanosystem. These include: -

1. Physico-chemical properties of the therapeutic and contrast agents: Physico-chemical properties such as the solubilities of the drug and contrast agents affect the choice of nano-vehicle, which can carry both the components simultaneously. For example, the combination of a water-soluble therapeutic agent such as gemcitabine and a hydrophobic contrast agent such as magnetic nanoparticles demands a multi-component nano-vehicle comprising of both hydrophilic and hydrophobic compartments. Multilamellar vesicles such as liposomes and polymersomes serve as superior delivery vehicles in such cases.

2. Pathological condition and target tissue: The disease and physiology of the target tissue dictate the choice of contrast agent in terms of circulation time and tissue perfusion. For example, positive contrast gadolinium-based imaging compounds are the agents of choice for magnetic resonance imaging (MRI) which is known to provide superior contrast in soft tissues and is generally preferred in nasopharyngeal and other soft-tissue

carcinomas including brain tumors [8, 9]. In comparison, blood pool agents, which are a special class of MR angiography contrast agents, require significantly longer vascular circulation times which is achieved through the use of higher molecular weight compounds [10, 11]. The high molecular weight prevents leakage into interstitial spaces and diffusion in the vascular epithelium. This also enables higher relaxivities and a better signal-to-noise ratio (SNR) leading to superior images [12]. Thus, blood pool agents are usually larger molecules such as albumin[13] or high molecular weight polymers conjugated to the MR contrast agents [14,15].

3. Biocompatibility and biodegradability: Biocompatibility and preferably biodegradability are an absolute requirement when designing theranostic nanosystems[16]. These factors have proven to be substantial roadblocks in regulatory approval and commercial acceptance of nanoformulations. Numerous contrast agents such as Gd suffer from low circulation half-lives ($t_{1/2}$) which then necessitates higher doses of this nephrotoxic compound[17-20]. Hence, several successful attempts were made to enhance the $t_{1/2}$ and simultaneously increase the biocompatibility of such contrast agents by conjugating them to materials capable of masking the toxicity[21-23]. Liposomes have been studied extensively and rendered safe as nanovehicles for delivery of various payloads including various contrast agents[24, 25]. Other biodegradable materials such as poly(amino acids) serve well as biodegradable building blocks for various nanovehicles such as polymeric micelles[26-28] and nanogels[29, 30]. Pluronic®, also generically known as poloxamers, are another class of biocompatible tri-block copolymers which are used extensively in the design of nanoparticulate drug delivery vehicles[31-33]. Pluronic® have been used to formulate magnetic nanoparticle-based theranostic systems for sustained delivery of anti-cancer agents such as doxorubicin[34-36]. These examples show the variety and importance of nanomaterial choice in the design of theranostic nano-systems.

1.3 CLASSIFICATION OF THERANOSTIC NANOSYSTEMS

The different theranostic systems are classified below based upon the imaging modality for which they were designed.

1.3.1 OPTICAL THERANOSTIC SYSTEMS

These nanoformulations constitute the simplest of all the classes of theranostic systems that can be developed for simultaneous drug delivery and imaging. The relative small molecular size of the various flurophores opens numerous avenues for encapsulation.

1.3.1.1. Organic fluorescent dyes

The use of fluorescent probes as ligands on several nanosystems is probably the simplest and earliest class of theranostic nanosystems developed by researchers. Even today, fluorophore-based formulations are predominantly used in research for *in vivo* animal studies and histological analysis of excised tissue. Fluorescent dyes are used extensively in understanding the trafficking of nanoformulations and subsequent endocytotic paths followed by the nanoparticles into the cells and various cellular organelles. For this purpose, several nanovehicles such as micelles, liposomes, dendrimers or simple ionic polyplexes have be developed and studied in great detail for their theranostic capabilities. For instance, Kleemann et al. investigated the intracellular trafficking of polyplexes comprised of poly(ethyleneimine) (PEI)-plasmid peGFP-N1 targeted to the lungs by the TAT peptide domain of HIV-1 [37]. The targeting and transfection efficiency of the targeted polyplexes was determined by measuring the fluorescence of the green fluorescence protein (GFP) in the plasmid. In a similar study, the intracellular trafficking of PEI-DNA polyplexes was studied by confocal laser scanning microscopy. PEI and DNA were labeled with Oregon Green 488 and rhodamine respectively and the co-

localized yellow signal was monitored to determine intracellular fate of the polyplexes. This method was used to observe that the polyplexes were intact when entering the nucleus. Recently, more sophisticated imaging techniques such as fluorescence resonance energy transfer (FRET)[38] and fluorescence correlation spectroscopy (FCS)[39] have been employed to overcome the drawbacks of traditional confocal microscopy such as inherently low spatial resolution. These advances have enabled more precise information regarding the dissociation of DNA complexes within the cells thereby improving the theranostic efficacy of the formulations. For instance, Lucas et al. utilized fluorescence fluctuation spectroscopy (FFS) to study the trafficking and intracellular fate of DNA polyplexes labeled with Cy5 and rhodamine. FFS enabled the researchers to distinguish between the intact and dissociated complexes. It was also observed that the fate of the polyplex was dependent on the molecular weight of the cationic polymer. The poly(L-lysine)-oligonucleotide complexes made from 30 KDa poly(L-lysine) dissociated upon entry into the nucleus while the polyplexes comprised of poly (2-dimethylaminoethyl methacrylate) (pDMAEMA), a 1700 KDa polymer, dissociated in the cytoplasm itself[40]. Self-fluorescing small molecule therapeutics such as doxorubicin provide a dual functionality and added advantage in enabling extensive characterization of the encapsulating nanosystems in that the *in vivo* accumulation and release of the formulation can be monitored continuously while also providing therapeutic effect[25].

However, theranostic nanosystems based on fluorescent dyes, show numerous limitations such as photo-bleaching, self-quenching, rapid decay of signal and non-uniform labeling of the nanoformulations. Furthermore, certain fluorophores such as Cy5 have also been shown to inhibit the ability of the backbone polymer to bind to the nucleic acids[41]. These limitations have been addressed by other imaging agents called quantum dots (QDs), which will be discussed next.

1.3.1.2. Quantum Dots

Quantum dots (QDs) are a novel class of inorganic fluorophores, which are gaining widespread recognition as a result of their exceptional photophysical properties. They are defined as particles with a crystal size on the order of the size of the exciton Bohr radius[42]. QDs are typically 2-7nm in size and made from semiconductor materials such as Cadmium-Selenium composites (CdSe). After excitation by visible light, energy is emitted in the form of a photon with a characteristic frequency and wavelength, which is dependent upon the QD material and structure. QDs have unique advantages over current fluorophores including having broad absorption spectra and narrow emission spectra with wavelengths ranging from ultraviolet (UV) to infrared (IR). This enables excitation of multiple different colored QDs using a single wavelength. QDs are also easily tunable in that altering the particle size, composition and surface stabilizing coatings can easily control the emission spectra of QDs. Another highly desirable feature of QDs is their photo stability. While conventional organic fluorophores are prone to photo-bleaching after only a few minutes, QDs are extremely stable and can undergo many recurring excitation/emission cycles while retaining high brightness [43, 44]. Comparative studies have shown QDs to be significantly more photostable than Alexa-Fluor dyes,[45] which are regarded as some of the most stable organic dyes available [46].

Bare QD nanocrystals are prone to emission irregularities such as fluorescence blinking and photochemical degradation which leads to the need for surface stabilization. Zinc sulfide (ZnS) capping of the QDs is a widely used process and has been found to improve stability and fluorescence. However, for biomedical applications, QDs require coating which can render them soluble in physiological fluids, impart stealth properties, biocompatibility and enhance *in vivo* stability and circulation times. These surface modifications influence the physico-chemical properties and the toxicity of QDs [47]. These

stabilizing moieties allow for further functionalization of QDs with targeting ligands. To this end, Wu et al.[45] used two different QDs conjugated with immunoglobulin G (IgG) and streptavidin to label the breast cancer marker human epidermal growth factor receptor 2 (HER2). QDs have also been successfully co-delivered with therapeutic molecules leading to the development of QD-based theranostic systems. One such example involves development of D-alpha-tocopheryl polyethylene glycol 1000 succinate mono-ester (TPGS) coated multi-functional (theranostic) liposomes, which contained both docetaxel and quantum dots (QDs) for cancer imaging and therapy [6]. These liposomes were further conjugated with folic acid to target the folate receptor overexpressed in a large percentage of breast cancers. The inclusion of QDs enabled the researchers to qualitatively track the internalization of the liposomes at the target site and also monitor the therapy for an extended period of time. Functionalized QDs have also been employed as intracellular tracers to monitor plasmid DNA (pDNA) delivery [48].

Multimodal contrast agents based on the combination of QDs and MNPs are an exciting class of bioimaging nanosystems. With two functionalities integrated in a single nanoparticle, a sensitive contrast agent for two very powerful and highly complementary imaging techniques (fluorescence imaging and MRI) is obtained. Such magnetic QDs can be obtained by four different approaches. In the first, QDs are overgrown as a uniform layer on the MNP surface followed by stabilization of the entire particle. Gao et al. reported the synthesis of FePt cores with a diameter of 3 nm, surrounded by a 3–5 nm CdSe (QD) shell through this method [48]. The second approach involves doping of ions of the magnetic material into the QDs to impart magnetic properties to them. Paramagnetic ions that have energy states within the QD bandgap introduce 'trap' states that determine the wavelength and lifetime of the doped QD luminescence. In a study by Santra et al.,[49] the use of CdS:Mn/ZnS QDs for bimodal imaging was demonstrated prominently for the first time.

The third method simply involves co-encapsulation of QDs and MNPs in single nanoparticulate structures such as PLGA matrix nanoparticles or mesoporous silica. This method was used by Kim et al. to obtain uniform mesoporous silica spheres embedded with monodisperse magnetic and semiconductor nanocrystals[50]. Finally, paramagnetic substances such as gadolinium can be chelated into the coordination shells of the QDs. Mulder et al.,[51] used a lipidic micelle surrounding a QD to incorporate Gd-DTPA complexes. Surface coating of this type of multi-modal imaging agents is critical from the point of increasing colloidal stability and enhancing solubility as well as reducing degradation of the QDs and increasing the biological half-life of the MRI contrast agent.

Thus, QDs have significantly superior optical properties than organic fluorophores, which makes them a better alternative to the organic fluorescent dyes. However, the toxicity of QDs is still a concern and most of the research currently is directed towards reducing the toxicity through the use of different coating techniques that will have minimal impact on the optical properties.

1.3.2 RADIO-THERANOSTIC SYSTEMS

Radiopharmaceuticals are an important class of therapeutic compounds, which have been in clinical use for more than 20 years. Also known as radiotracers, these molecules are routinely used in clinical practice either as diagnostics or for treatment of certain pathological conditions such as cancer, myocardial infarction and several inflammatory conditions [52, 53]. Current diagnostic techniques in nuclear medicine include non-invasive Positron Emission Tomography (PET) and Single Photon Emission Computed Tomography (SPECT). These techniques utilize positron and gamma ray emitting radionuclides respectively for generation of a signal. There is great utility of these radionuclides in early detection strategies, first-line therapy and then also prognostic follow-up. The ability of a single system to perform all these functions simultaneously is a

very desirable feature and constitutes the main rationale behind development of theranostic radiopharmaceuticals. To this end, significant amount of data is available on the efficacy of theranostic radionuclides in targeting various molecular targets expressed in different types of cancers.

Numerous physico-chemical factors are considered when formulating such radio-theranostic agents comprising of separate imaging and therapeutic modalities. First and foremost, it is very essential to compare and match the pharmacokinetic properties of the compounds. Maximum tolerated doses for critical normal tissues are necessary to know so that the maximal possible dose can be given to the tumor cells. One of the critical parameters to be considered in designing radio-theranostics is the residence time of the molecules. Given the rapid radioactive decay that these radionuclides undergo, it is of paramount importance to ensure the time accumulation of formulations in sufficient concentrations in the target tissue. Radiopharmaceuticals with short radioactive $t_{1/2}$ ranging from as low as several minutes to about two months have been approved for radiotherapy in several conditions such as cancer. These include β-particle emitting radionuclide molecules such as Iodine-131 (^{131}I; $t_{1/2}$ 193 h), Strontium-89 chloride (^{89}Sr; $t_{1/2}$ 50 days), Yttrium-90 (^{90}Y; $t_{1/2}$ 64 h) and Lutetium-177 (^{177}Lu; $t_{1/2}$ 161 h) and α-emitters such as Astatine-221 (^{211}At; $t_{1/2\ 7.2h}$), Bismuth-212 (^{212}Bi; $t_{1/2}$ 1h), Bismuth-212 (^{213}Bi, $t_{1/2}$ 45min), Actinium-225 (^{225}Ac; $t_{1/2}$ 10 days), and Thorium-227 (^{227}Th; $t_{1/2}$ 19 days) to name a few [54]. On the other hand, radionuclides for imaging purposes include ^{99m}Tc, ^{111}In, and ^{123}I for SPECT or ^{18}F, ^{64}Cu, ^{68}Ga, ^{7}6Br, ^{86}Y, ^{89}Zr, ^{110}In, and ^{124}I for PET. Several of these radionuclides have been formulated into peptide or monoclonal antibody (mAb) targeted cancer therapeutics. For instance, targeted radionuclide therapy using radiolabeled somatostatin analog peptides (^{17}7Lu-Octreotate) for treatment of neuroendocrine tumors

and radiolabeled anti-CD20 antibodies (^{90}Y-Zevalin) for treatment of chemotherapy-resistant lymphomas have been used clinically for a long time [55].

While research on targeted radionuclides conjugated with synthetic peptides and mAbs has been at the forefront of product development efforts in cancer radio-theranostics, significant amount of work is currently underway towards development of radio-theranostic nano-vehicles loaded with or conjugated with different radionuclides. Li et al.[56] designed and constructed a multifunctional theranostic liposomal drug delivery system, which integrated multimodality magnetic resonance (MR), near infrared (NIR) fluorescent and nuclear imaging of liposomal drug delivery. The payloads comprised of a lipidized NIR fluorescent tracer, IRDye-DSPE and Doxorubicin post-loaded into the multifunctional liposomes. The multifunctional doxorubicin-liposomes were further stably radiolabeled with ^{99m}Tc or ^{64}Cu for SPECT or PET respectively. This multifunctional drug carrying liposome system exhibited superior imaging capability in squamous cell carcinoma of head and neck (SCCHN) tumor xenografts in nude rats following intratumoral injection. NIR fluorescent, SPECT and PET images clearly showed either the high intratumoral retention or distribution of the multifunctional liposomes. Similarly, unimolecular micelles were formed by dendritic amphiphilic block copolymers poly (amidoamine)–poly (l-lactide)-*b*-poly (ethylene glycol) (PAMAM–PLA-*b*-PEG–TRC105) and conjugated with anti-CD105 monoclonal antibody (TRC105).[57] 1,4,7-triazacyclononane-N, N', N-triacetic acid (NOTA, a macrocyclic chelator for ^{64}Cu) was conjugated as the radiotracer while Doxorubicin was loaded into the hydrophobic PAMAM-PLA core. The ^{64}Cu-label enabled continuous monitoring of the biodistribution as well the therapeutic efficacy of the chemotherapeutic agent. Simultaneous radiotherapy and photodynamic therapy (PDT) has also attempted by Sugiyama et al.[58] The tumor response

to this combination therapy was continuously monitored by use of 3′-Deoxy-3′-^{18}F-Fluorothymidine radionuclide.

Despite the plethora of research efforts, radio-theranostics are still in a nascent stage of development due to numerous shortcomings that need to be addressed. Most important is the rapid decay of the radionuclides *in vivo*, which requires rapid uptake of the formulations in the target tissue. This necessitates very careful product development strategies and choice of radioisotopes, which can compliment each other in terms of their biological $t_{1/2}$. The physical stability, leakage of the payloads and stray exposure of the healthy tissue are issues that plague the development of these theranostic agents even today, although encapsulation within vesicular nanosystems such as liposomes shows a potential solution to this problem. In all, radio-theranostic nano-systems have a considerable distance to cover before they find clinical acceptance though current research shows promise for the future of this class of theranostic agents.

1.3.3 PHOTO-ACOUSTIC AND PLASMONIC RESONANCE THERANOSTIC AGENTS

1.3.3.1. Porphyrins

Porphyrins exist abundantly in nature. In humans, the porphyrins in blood (i.e. hemoglobin and myoglobin) serve not only as carriers of oxygen, but also as the bright red contrast agent that clearly demarcates injury sites. They have proven valuable as whole body imaging modalities have emerged, with endogenous hemoglobin porphyrins being used for new approaches such as functional magnetic resonance imaging (fMRI) and photo acoustic tomography (PAT). Functional MRI has been used effectively in detailed three-dimensional volumetric mapping of brain activity. The presence of the hemoglobin in abundance enables indirect measurement of intracranial metabolic activity and blood changes caused by neural activity [59, 60]. Hemoglobin, in the form of oxy-

hemoglobin, shuttles molecular oxygen to and from the cells for cellular respiration. The iron chelated in the center of this hemoglobin can change its valency between Fe^{2+} and Fe^{3+} to help enable precise oxygen delivery. The differences between oxy and deoxyhemoglobin can be detected by fMRI because it has been shown that when diamagnetic oxyhemoglobin releases its oxygen, the de-oxyhemoglobin becomes paramagnetic, which influences the transverse relaxation rates of water proton spins in the immediate vicinity of vessels, resulting in the blood oxygenation level dependent contrast [61-63].

With the capability for both NIR fluorescence imaging and phototherapy, porphyrins were the first exogenous molecules that were used with inherent multimodal theranostic properties[64]. Porphyrins have been used as tumor-specific diagnostic fluorescence imaging agents since the early 1920's, [65, 66] as positron emission agents since 1951, [67] and as magnetic resonance (MR) contrast agents since 1987. In addition, exogenous porphyrins such as Photofrin® remain in clinical use for photodynamic therapy applications. However, these exogenous porphyrins suffer from the drug delivery issues seen with other hydrophobic pharmaceuticals. Researchers have attempted to address these issues using polymeric nano-vehicles, which serve well for stabilization and stability enhancement of porphyrins. For example, Hsu et al.[68] fabricated a robust polymersome nano-vesicle comprising of a 4-armed porphyrin conjugated to poly lactic acid (PLA). The so-called 'porphysomes' combined the cytotoxicity of PDT with ultra-sound based imaging capability thereby serving as an ideal theranostic system for cancer therapy. In another study, a porphyrin−phospholipid conjugate with quenched fluorescence was developed to serve as both the Raman dye and a stabilizing, biocompatible surface coating agent on gold nanoparticles [69]. Here the porphyrin molecule was chelated with a central Mn^{2+} to quench the fluorescent properties of the porphyrin while enhanced MR capability. This

AuNP-porphyrin conjugate served as a novel surface enhanced Raman scattering (SERS) probe capable of being used for cellular imaging. Porphyrins have also been encapsulated into stable polymeric micelles systems. For example, micelles made of poly- (ethylene glycol)-*co*-poly (D, L-lactic acid) (PEG-PLA) yielded 85% loading of tetrakis (meso-hydroxyphenyl) porphyrin (mTHPP) while micelles made from poly(ethylene glycol)-*co*-poly(caprolactone) (PEG-PCL) yielded approximately 70% encapsulation efficiency of silicon pthalocyanine 4 (Pc 4), a porphyrin derivative [70, 71].

Thus to summarize, endogenous porphyrins enable optical and magnetic detection serving as an effective natural theranostic agent. Exogenous porphyrins have also been developed successfully into stable theranostic nanosystems, with new agents facilitating multimodal imaging and therapy for numerous pathological conditions.

1.3.3.2. Micro/ nanobubbles

Microbubbles and nanobubbles are spherical cavities less than 10µm in size that are filled with different perfluorocarbon (PFC) gases such as octofluoropropane (C_3F_8), decafluorobutane (C_4F_{10}) or sulfur hexafluoride (SF_6). Microbubbles are formed by ultra-sonication resulting in the encapsulation of the sterile PF gases into amphiphilic polymeric micelle solutions to form nanoemulsion foams at low temperatures. Advanced techniques such as microfluidics have also been employed to produce these microbubbles.[72, 73] The encapsulated microbubbles undergo oscillations in an acoustic field depending upon the field strength. These oscillations result in the generation of strong acoustic signals that produce a contrast in comparison to the surrounding medium. The microbubble signal and the resulting contrast are dependent on a number of factors such as the bubble size, the density and viscosity of the entrapped gas, the density of the surrounding medium, and the applied field power and frequency [74]. These unique contrast agents have revolutionized the field of ultrasound imaging. Microbubbles have been used extensively

in imaging blood-flow related conditions such as arterial inflammation, angiogenesis, restenosis and even cerebrovascular conditions such as stroke [75, 76]. Recently, researchers have attempted to go a step further and add a co-therapeutic dimension to these imaging systems, resulting in the development of theranostic micro/nanobubbles systems. Gao et al.[77] successfully incorporated doxorubicin into the polymeric shell of perfluoropentane microbubbles prepared from PLA-PEG and poly(ε-caprolactone)-PEG (PCL-PEG). The non-targeted microbubbles were shown to accumulate passively in tumor tissues and coalesce at physiological temperature to form microbubbles. Under an ultrasound field these microbubbles oscillate and collapse to release the encapsulate drug while simultaneously enabling visualization of the tumor tissue.

Microbubbles have also been studied as potential carriers of oxygen to the hypoxic area of tumors.[78] This strategy is seen as a means to reduce the hypoxia-induced resistance to radiotherapy and photodynamic therapy. Another unique approach, as demonstrated by Lukianova-Hleb et al.[79] involved the formation of transient plasmonic photothermal vapor nanobubbles from gold nanoparticles. When activated by a laser pulse, an intracellular AuNP acted as a heat source and generated a transient plasmonic nanobubbles (PNBs) in the surrounding medium. PNBs of nanometer-scale size and nanosecond-scale duration act as diagnostic probes by scattering light from the probe laser. Larger micron-scale PNBs provide a localized therapeutic action through a mechanical, non-thermal impact due to their rapid expansion and collapse, thus disrupting the cell membrane. Ultrasound imaging of the disruptive PNBs can guide their therapeutic action. Thus, the PNBs may combine diagnostics, therapy, and therapy guidance. This group of researchers went a step further and demonstrated the theranostic ability of these PNBs generated by AuNPs within the liposomes to disrupt liposomal membranes thereby enabling optically guided delivery and release of the therapeutic payloads [80]. Another

potential application is to use microbubble disruption to accelerate thrombolysis.[81] The same mechanism that promoted clot lysis in the former case has been applied to permeabilize and disrupt the blood–brain barrier, which could be useful for enhancing delivery of therapeutic agents to brain tissue while continuously monitoring the therapy by ultrasound.[82]

Although a relatively new field in ultrasound imaging itself, micro and nanobubble research has rapidly expanded beyond mere ultrasound imaging. The astounding success of the initial attempts at developing theranostic micro/nanobubbles are very successful and have paved way for the next step in development of targeted theranostic microbubble systems. The ability to generate plasmonic nanobubbles within nanovehicles is the first step towards directing the bubbles in the desired tissue site. The main limitation of the PNB technology is that it shows less potential in deeper tissues where laser penetration is difficult and hence generation of transient PNBs is a perceived challenge. Nonetheless, this technology shows tremendous promise as a potential theranostic nano-system.

1.3.3.3. Carbon nanotubes (CNTs)

Over the last decade, carbon nanotubes (CNTs) have attracted the attention of many scientists across the globe. These hollow cylindrical nanosized tubes are composed entirely of carbon and can be either single walled (SWCNTs) or multi-walled (MWCNTs). The uniqueness of the nanotube arises from its structure and the inherent subtleness in the structure, which is the helical arrangement of the carbon atoms in hexagonal arrays on their surface honeycomb lattices. The helicity (local symmetry), along with the diameter introduces significant changes in the electronic density of states, and hence provides a unique electronic character for the nanotubes. These novel tunable electronic properties create a range of fascinating applications, including those in the biomedical field. Numerous studies have shown their ability to carry large payloads, either therapeutic[83-86]

or contrast agents[87] alone or a combination of both agents[88, 89]. There are a few studies that have attempted to 'think outside the box' and exploit the optical properties of CNTs. For example, Zarda et al.[90] explored the optical imaging capabilities of SWCNTs in tumors planted in murine models. The successfully showed that intravenously administered SWCNTs conjugated with cyclic Arg-Gly-Asp (RGD) peptides showed eight times greater photoacoustic signal in the tumor than mice injected with non-targeted nanotubes. While a very enticing proposition, it remains to be explored whether drug loading can affect these photoacoustic properties.

What is even more fascinating about the use of CNTs is that surface modification does not affect their photoacoustic ability while still rendering them non-toxic and biocompatible; a drawback that significantly retarded the pace of research into the biomedical applications of CNTs in the initial years of this century. But the current efforts in the direction of exploring the diagnostic capabilities of CNTs will definitely usher in a new era in CNT biomedical research.

1.3.3.4. Gold nanoparticles

In the last decade, gold nanoparticles (AuNPs) have risen as one of the most extensively utilized nanosystems for the imaging, diagnosis, monitoring and treatment of various diseases, predominantly cancer. AuNPs have been successfully applied in a broad range of biomedical fields such as analytical chemistry, biological sensing and immunoassays, optical bioimaging, photothermolysis of cancer cells and targeted delivery of drugs, peptides, DNA, and antigens.[91] The unique optical properties of AuNPs are related to localized plasmonic excitations in metal nanostructures interacting with light which cause enhanced optical phenomena such as absorption, Mie scattering, Raman scattering, and various nonlinear effects.[92] AuNPs have been used as non-fluorescent probes owing to their photostability, small toxicity, high light scattering efficiency, and

ability to serve as carriers for different molecular cargos.[93] AuNPs have also been used in designing theranostic nanosystems capable of simultaneous imaging and therapy either in the form of photothermal therapy or by co-encapsulating with several conventional therapeutic agents. Photothermal therapy involves the use of light and a photosensitizer to generate heat for therapeutic purposes. In contrast to conventional photodynamic therapy, PTT does not require the presence of oxygen, which may be of importance when a tumor is large enough to have a hypoxic center. Moon et al.[94] reported development of a new theranostic system comprising of hollow AuNPs filled with a low melting point (36-40°C) phase-changing material (PCM) carrying the therapeutic agent. This system had capabilities to both enhance the contrast of photoacoustic (PA) imaging and control the release of a chemical or biological effectors by high-intensity focused ultrasound. Exposure to the ultrasound caused heating of the AuNPs, which melted the PCM. So long as the light was incident on the AuNPs, the molten PCM leached out of the hollow vehicles thereby allowing for controlled release of the payload. In another study Heo et al.[95] developed targeted AuNPs conjugated with anti-cancer agent paclitaxel. The biotin-conjugated formulations were rapidly internalized preferentially in the cancer cells and were easily detected as bright areas when observed in dark field microscopy. Similar study performed by El Sayed et al.[96] reported the diagnostic efficacy of EGFR-targeted AuNPs in oral cancer cells. In addition to their photoacoustic properties, AuNPs have also been reported to be useful in computed tomography aided imaging studies.[97]

Thus, numerous nanoparticulate systems have been studied for potential theranostic applications combining photo acoustic imaging with various forms of therapeutic approaches for the diagnosis and treatment of several condition, the primary focus being cancer.

1.3.4. MRI CONTRAST AGENTS

Magnetic resonance imaging (MRI) has become an essential tool for diagnosis and evaluation of a broad variety of diseases. This technique was first developed in early 1973, thanks to the pioneering work of Paul Lauterbur.[98] Briefly, MRI relies on the imaging of water molecule protons found in abundance in the tissues in the body. Due to its spin and charge, protons have a minute magnetic field and hence, when placed in a magnetic field, the protons align themselves either parallel or anti-parallel to the field. Upon application of radiofrequency energy of a specific strength (Larmor frequency) the protons originally aligned with the field absorb the energy and reverse their direction. Upon removal of the field they eventually release this energy and relax back into their original alignment. The rates at which this relaxation occurs are known as T_1 and T_2 relaxation times. These times vary with the tissue properties. The relaxation produces a magnetic resonance signal. Depending on the imaging technique, magnetic pulse sequence, intensity of the signal and the type of relaxation, a specific region of interest (ROI) in the final image is represented as a bright or dark spot.[99]

It is particularly helpful in diagnosis of intracranial anomalies.[100-102] One important way to improve the contrast in MRI is to introduce contrast agents, which are a unique class of pharmaceuticals that augment the image contrast between normal and diseased tissue. They can indicate the status of organ function or blood flow by increasing the relaxation rates of water protons in the tissue in which the agent accumulates.

1.3.4.1. Basic Principals of MRI

Magnetic resonance imaging (MRI) is an imaging technique based on the nuclear magnetic resonance phenomenon. Due to its ability to provide images of various soft tissues in the body non-invasively, it has continued to be one of the widely used diagnostic

techniques for imaging of various organs for nearly last 25 years. In contrast to other techniques such as computed tomography (CT) and x-rays MRI provides a stronger tissue contrast and minimum energy deposition in the tissues. The development of various contrast agents for MRI has further added to the benefits of this technique. Before delving the field of biomedical applications of MRI contrast agents, this section will provide the necessary background for understanding the fundamentals of MRI.

In conventional MR imaging, the main source of signal that generates an image is the nucleus of the hydrogen atom (^{1}H) consisting of a single proton and half-integral value of this integral spin angular momentum (I = ½), which is abundant in the living tissue in the form of water and fat.[103, 104] The ^{1}H nucleus has one of the largest magnetic moments of all nuclei, resulting in a significant MR signal. The quantum mechanical properties of the ^{1}H nucleus impart a high magnetic moment to it.[105] Such nuclei with net magnetic dipole moments have odd number of protons and neutrons.[106] When exposed to an external magnetic field (B), these protons are aligned parallel and antiparallel to magnetic field. This is essentially a quantized system comprising of two energy levels wherein the protons with antiparallel spins are at the higher energy level than those with parallel spins. These protons constantly move or 'precess' around the external magnetic field. The speed at which they precess is known as precession frequency. Precession frequency is governed by the external magnetic field strength (B).[107] The stronger the B value, the higher is the precession rate and frequency of the protons. The precession frequency is calculated by the 'Larmor equation'[108]

$$\omega_0 = \gamma \cdot B_0 \qquad \qquad \text{…Eqn. 1.1}$$

where:-

ω_0 is the precession frequency, γ is the gyromagnetic ratio and B_0 is the magnetic field strength in Tesla (T).

The ω_0 value for ^1H protons is approximately 42MHz at B of 1T.[104, 105] The opposing magnetic forces arising from the protons precessing in the opposing directions cancel each other. Only the magnetizations along the direction of the magnetic field do not cancel. All magnetic moment vectors add up resulting in net magnetization along the direction of, or longitudinal to, the applied external magnetic field. This is known as **longitudinal magnetization (M_0)**.[109, 110] Thus, if a patient is placed in an external magnetic field of a MRI scanner, (s)he has a net M_0 which cannot be measured. The inability to measure the static magnetic moment is due to it being in the same direction as that of the external magnetic field (B) and very small in comparison. However, it is possible to 'flip' the net longitudinal magnetization at a right angle to the direction of the external field by using a radiofrequency [111] pulse at the 'Larmor' frequency. This external pulse provides the energy necessary to disturb the equilibrium arrangement of the spins parallel and antiparallel to B and transiently point the net magnetization towards a plane transverse to the external magnetic field thereby producing a signal, which is recorded by a receiver coil The instant this 90° RF pulse is turned off, the newly established transverse magnetization gradually decays by dissipating the stored energy to the surrounding (lattice). This dissipation of energy results in re-alignment of the magnetization in the longitudinal direction to re-establish the original equilibrium. This process is known as T_1 relaxation.[104, 112] Once back to the equilibrium state the protons are ready again for a new RF pulse. However, if the TR is less (TR < 5.T_1), the previous relaxation is not complete and hence the subsequent RF pulse generates lower signal. This is the source of T_1-based contrast since the tissue with a shorter T_1 will undergo a more complete recovery, thereby producing a brighter signal.

Relaxation is a time-dependent process characterized by relaxation time, which is a rate constant for this phenomenon. There are two distinct relaxation processes occurring

simultaneously namely longitudinal relaxation, also known as spin-lattice relaxation, denoted as T_1 and transverse relaxation or spin-spin relaxation, denoted as T_2. T2 relaxation occurs due to a complete loss of signal following the RF pulse. It is a phenomenon dominated by entropy rather than energy transfer. While both T_1 and T_2 measure the natural energy transfer by an excited proton, they differ in the final disposition of the energy.

a. Relaxation

Measurement of magnetic resonance (MR) can be analyzed in terms of energy transfer. The process by which the protons release energy absorbed from the applied RF pulse is known as relaxation.[104] Relaxation is the fundamental property of MR and affords the principal mechanism for image contrast or MRI.

i. Longitudinal (T_1) relaxation

T_1 relaxation time is the time required for the disturbed M_0 (M) to return to 63% of its original M_0. T_1 relaxation provides the mechanism by which the protons give up their gained energy to return to their original orientation and magnetization (M_0). This return of magnetization typically follows an exponential growth process. T_1 relaxation times in the tissues are relatively slow with the values ranging from few milliseconds to several seconds.[113, 114] In practice pulsed RF energy is applied to the protons repeatedly with a delay time (TR) between the pulses, which allows for T_1 relaxation to occur. As the protons return to their original orientations, a difference is established between protons in the parallel and anti-parallel spins. This allows for the energy absorption to recur after the next RF pulse. These repetitions cause more dissipation of energy and hence generation of a larger signal following repeated pulses. TR is generally insufficient for complete T_1 relaxation to occur. Application of a second RF pulse before complete relaxation causes M to flip again in the transverse plane, albeit with a smaller magnitude than the previous.

After a few repetitions M returns to its original magnitude prior to the RF pulse, thus achieving a steady state value, which depends five parameters namely[106, 110, 113]

1. The external magnetic field B. The larger the field, larger is M

2. Proton density per unit volume of the tissue

3. The amount of energy absorbed by the protons (flip angle)

4. The repetition time or rate of RF pulse application

5. T_1 relaxation time

The repetition time (TR) is a critical parameter since it controls the efficiency of energy transfer. If TR is significantly smaller than T1 relaxation time, the spin will not relax completely and hence the next pulse will produce a proportionately smaller magnetization signal which will undergo relaxation at a faster rate, thereby producing a brighter signal. In practice, each tissue saturates differently due to different T_1 relaxation times, which affects its maximum potential signal.

As discussed previously, spin-lattice relaxation measures the rate of energy transfer from an excited proton to the surroundings. Such a transfer also relies on the presence of either a vibrational or rotational molecular motion of the lattice in the vicinity of the excited protons. The intrinsic frequency of such a motion (ω_L) matches ω_0. The closer these two frequencies are, the sooner do the protons return to their equilibration state.[105] Thus the presence of several protein structures and metal ions in the tissue greatly influences the ω_L. Iron (Fe) and Manganese (Mn) have significant magnetic moments that can potentially affect the local environment. T_1 decreases with decreasing B. However, a larger B does not necessarily mean a greater signal since longer T_1 times are prone to saturation.[113]

ii. Transverse (T$_2$) relaxation

T_2 relaxation or spin-spin relaxation time is the time required for the transverse component of M to decay to 37% of its initial value, the loss of signal occurring due to irreversible processes. As described previously, when a RF pulse is applied, the precessing protons absorb this energy and hence the longitudinal magnetization (M_0) is disturbed and rotates in the transverse plae.[103, 105, 106, 113]

When in the transverse plane, all protons precess with the same Larmor frequency ω_O. Thus a proton having a similar molecular milieu and precessing with the same frequency can absorb the energy being dissipated by its neighboring proton. This transfer of energy from between two excited protons of the same kind in a similar environment is called spin-spin relaxation. The absorbed energy is retained as spin relaxation without being transferred to the surroundings as in T_1 relaxation. Several inter and intra-molecular interactions such a vibrations and rotations cause transient fluctuations, which lead to gradual loss of the transverse magnetization. T_2 is the time when this transverse magnetization is at 37% of this original value immediately after the RF pulse. If the TR is faster than the relaxation time, the corresponding M will rotate continuously and while doing so gradually decrease in magnitude until it disappears as the proton populations at the higher and lower energy levels will equalize leading to zero net magnetization. As a result, no signal is produced; a condition known as saturation or magnetization saturation (M_s).[115, 116] There is a limited amount of energy that the protons can absorb before reaching saturation. If more time relapses, this transverse coherence completely disappears and T_1 relaxation occurs. One important difference between T_1 and T_2 relaxation is the influence of B. T_1 is sensitive to B while T_2 is relatively insensitive to B.

1.3.4.2. Contrast agents

MRI revolutionized the field of medical diagnostics. It has perhaps been the most powerful method for the non-invasive investigation of human anatomy, physiology and

pathophysiology. Compared to other imaging techniques, such as computed tomography (CT), MRI does not involve radiation or radionuclides and provides significant amount of intrinsic contrast between different tissues, making it widely used in neurological, musculoskeletal, cardiovascular, and oncological imaging. This contrast is based upon different signal intensities between the adjacent tissues. This contrast is obtained primarily due to the differences in the T_1/ T_2 relaxation times of the different tissues accentuated by the chosen parameters such as TR and TE.

In spite of this intrinsic contrast between the tissues, distinction between diseased and normal tissue can still be challenging as the pathological organ may have similar T_1/ T_2 times as that of the adjacent normal tissue. In other situations, the region of interest may contain significant amounts of normal tissue, making the contrast low. In either case, a promising approach is to increase the signal difference between normal and pathologic tissue, which can be achieved successfully by administering a suitable contrast agent.

Contrast agents for MRI are indirect contrast agents. Unlike those used in CT (direct agents), most MRI contrast agents are indirect agents and not visualized directly in the image. Instead, they affect the relaxation times of the numerous water protons in the nearby tissue. The concentrations at which these agents are used are also very low, thereby explaining the low occurrence of side effects to MRI agents. MRI contrast agents can be categorized into three groups with most of them falling into one of two categories: T_1-agents and T_2-agents. T_1-agents generally increase the longitudinal (spin-lattice) relaxation rates ($1/T_1$) of water protons in tissue more than the transverse (spin-spin) relaxation rates ($1/T_2$). With most conventional pulse sequences, this dominant T_1-lowering effect gives rise to increases in signal intensity predominant on T_1 weighted images; thus, these are positive contrast agents that produce a brighter contrast. On the other hand, T_2-agents largely increase the $1/T_2$ of tissue rather selectively, leading to

decreases in signal intensity; predominant on T_2 weighted images, and thus these represent negative contrast agents, which produce a dark contrast. However, non-proton agents, such as certain perfluorocarbons, by virtue of the absence of hydrogen, do not affect relaxation rates (or the signal) in MRI but produce low signal intensity at completely different resonance frequencies (19F) than those of the conventional Gd or iron oxide-based contrast agents. These represent a third class of MRI contrast agents. Whether the contrast agent functions as a T_1-agent or T_2-agent depends on a function of the imaging sequence used, the field strength, the correlation time and how the contrast agent is compartmentalized in the tissue. The ability of the agent to reduce the T_1- and T_2-relaxation times are respectively described by the r_1 and r_2 relaxivity values of the agent. The following section describes in brief, the mechanisms of contrast enhancement in the presence of T_1 or T_2 relaxation agents.

a. T_1 contrast agents

Almost all T_1 relaxation agents currently in clinical use are gadolinium-based intravenous agents. Gadolinium (Gd) in a rare earth metal with a large magnetic moment.[117, 118] The primary mechanism of contrast generation for T_1 contrast agents is by functioning as a relaxation sink for water protons.[119] As described previous in this section, following a RF excitation pulse, T_1 relaxation depends upon the decay of the absorbed energy from the proton to the 'lattice'. For the energy transfer to occur efficiently, these protons should be in the coordination sphere, i.e. in the innermost layer of atoms surrounding the metal ion.[110, 120] Gd-based contrast agents are formulated as Gd chelates to reduce the toxicity of Gd as a free metal ion.[121, 122] These chelate molecules are relatively larger with multiple bonds to the central Gd metal ion,[123] which limits free space in the inner coordination sphere.[110, 113] This limits the fats and other large molecules from gaining sufficient proximity to central metal ion for efficient energy transfer. However, the

water present in these tissues can penetrate into the coordination space, dissipate its energy and subsequently exchange with the bulk tissue water, thus allowing for additional water molecules to enter the coordination sphere.[110] This process occurs very rapidly and hence the water in the bulk tissue is relaxed and available for the subsequent pulse. As a result, the tissue water near the contrast agent has a larger net value of M than water in the neighboring tissue, thus contributing to a greater and brighter signal in a T_1-weighted image. The rapid exchange process ensures that a single Gd-complex can affect numerous water molecules. This reduces the dose of Gd-based T_1 contrast agents.

In addition to gadolinium (Gd^{3+}), the other most common paramagnetic species in nature are metal ions with unpaired electrons, such as manganese (Mn^{2+}, Mn^{3+}), iron (Fe^{2+}, Fe^{3+}), lanthanide (La^{3+}) and dysprosium (Dy^{3+}) which have been used in MRI contrast agents.[124-126] The gadolinium ion Gd^{3+} is the most widely used paramagnetic ion for MRI contrast agents because it has a high magnetic moment and a symmetric electronic ground state. However, paramagnetic metals cannot be used as contrast agents in the ionic form due to their undesirable bio-distribution, very short biological half-lives and relatively high toxicities. To address this issue of short circulation times and severe systemic toxicities, Gd chelates with various stabilizing ligands have been designed. Acyclic and macrocyclic polyaminocarboxylates, such as diethylenetriaminepentaacetic acid (DTPA), 1,4,7,10-tetraazacyclododecane-N,N^{I},N^{II},N^{III}-tetraacetic acids (DOTA), and their derivatives, have been the main ligand used to stabilize Gd. The Gd (III) chelates such as Gd-DTPA (Magnevist, Schering AG, Germany), Gd-DTPA-BMA (diethylenetriaminepentaacetic acid-(bismethylamide); Omniscan_, Amersham-Nycomed, Norway), Gd-DO3A-HP (1,4,7,10- tetraazacyclododecane-1-(2-hydroxypropyl)-4,7,10-triacetic acid; ProHance_, Bracco Imaging, Italy), and Gd-DTOA (Dotarem_, Guerbet SA, France) are currently in clinical use. Gd-chelates have been

further modified to target specific tissues in the body. For instance, the first generation MRI contrast agents, such as Gd-DTPA were modified to form neutral molecules, which thus exhibit much lower osmolality, longer circulation times and higher safety.[127, 128] Some suitable residues have been incorporated into either the acetic side arms or the diethylenetriamine backbone of Gd-DTPA and Gd-DOTA to obtain tissue or organ-specific contrast agents. Thus, Gd-based contrast agents specifically targeted to the liver, tumor and blood pool have been developed, which can localize in these target sites thereby producing greater signal in the MR images.[129] Gd-based positive contrast agents are in greater demand and are preferred contrast agents in clinics due to their bright contrast that enabled clear demarcation and non-invasive visualization of the disease tissue.

Apart from Gd-chelates, Mn-based compounds and ultra-small superparamagnetic iron oxide nanoparticles (USPIOs; 3-5nm) have also been used to generate positive contrast. Manganese dipyridoxyl-diphosphate (mangafodipir, Mn-DPDP, Teslascan_, Nycomed Amersham Imaging, Princeton, NJ) is a contrast agent developed for imaging of the hepatobiliary system.[130] USPIOs, on the other hand, have been incorporated into numerous nanoformulations such as liposomes,[131, 132] micelles,[133, 134] polymersomes,[135] dendrimers[136] to name a few, in order to impart hydrophilicity, enhance stability and most importantly increase circulation times. Long circulation times are specifically required since these contrast agents are extensively used blood pool agents.[15, 129]

b. T_2 contrast agents

T_2 or negative contrast agents mainly include superparamagnetic magnetite (Fe_3O_4), maghemite (Υ-Fe_2O_3) (collectively referred to as MNPs hereafter) or their composites with other ferromagnetic metals such as cobalt (Co), nickel (Ni) and manganese (Mn).[137, 138] Paramagnetic substances such as Gd-based complexes have no net magnetization in absence of a magnetic field.[110] However, ferromagnetic macromolecular structures such

as iron oxide have very high magnetic susceptibility, which can persist even on removal of the external magnetic field.[139] Magnetic susceptibility is the degree of magnetization of a metal in response to an external magnetic field. This persistence of magnetization (remnant magnetization) is dependent on the physical properties of the iron oxide such as particle size.[140] These MNPs lose their magnetization upon removal of magnetic field and hence are known as superparamagnetic nanoparticles.[141] Likewise, when an external magnetic field is applied, due to their high magnetic susceptibility, these nanoparticles exhibit a very strong net magnetization resulting in distortion of the local magnetic field in their vicinity.[142] The microscopic field inhomogeneity causes the nearby water protons to dephase more rapidly than the surrounding tissue, thereby leading to significant decrease in signal intensity as a result of the shortening of the T_2 and T_2^* relaxation times.

Biocompatible MNPs such as magnetite have been widely used for *in vivo* biomedical applications including MRI contrast enhancement, tissue specific release of therapeutic agents, hyperthermia, and magnetic field-assisted radionuclide therapy. Their slower renal clearance and higher transverse (T_2) relaxation values compared to the Gd-based contrast agents make them more attractive for imaging purposes.[143] Biomedical applications require that the SPIONs be stable in water, in physiological conditions and not be recognized by the body's phagocytic mechanisms. Various factors such as core size, surface charge, surface ligands and chemistry, affect the colloidal stability of the MNPs. To control the surface properties, MNPs are commonly coated with a biocompatible polymer, a step that significantly controls the size of the resulting MNP clusters while preventing formation of large aggregates. In addition, polymer coating can also allow binding of drugs and targeting ligands onto the MNP surface. Some MNPs with core sizes of 3–6 nm and dextran coating (with 20–150 nm hydrodynamic sizes) such as Feridex (discontinued in USA), Endorem, Combidex and Sinerem are approved for MRI in

patients.[144] Recently, Zhao et al. [145] synthesized octopod-shaped MNPs with extremely high T_2 relaxivity (six-fold higher) values compared to the spherical counterparts of similar chemical composition. These MNPs have significantly higher values than all the commercial MNPs currently available. In addition, drug loaded MNPs have also been surface-modified with various targeting ligands and can be guided to the desired target area using an external magnetic field while simultaneously tracking the biodistribution of the particles.[146]

Composites of iron oxide nanoparticles are obtaining by replacing a mole fraction of the Fe moiety by other metals, which exhibit significantly higher (T_2) relaxation values. Magnetite composites with Co having T_2 relaxivity values almost 4-fold higher than pure MNPs have been reported.[147] Similar observations have been made with Ni-based MNP composites.[148] However these composites have, so far, suffered from significant toxicity and biocompatibility issues. Although surface-modification has helped reduce the toxicity considerably, when compared with pristine MNP formulations these composite cores are inherently toxic and degradation of the cores has been shown to contribute significantly to formulation toxicity. Thus, given the extensive research in the field of magnetic nanoparticles, iron oxide based MNP formulations continue to show tremendous promise in development as theranostic nanosystems. The fact that these MNPs are already available for clinical use in European nations and still continues to be used on a proprietary basis in US further adds to the optimism.

1.4. THERAPEUTIC AREAS WITH POTENTIAL BENEFITS FROM 'NANO-THERANOSTICS'

Therapeutic and technological advances in medicine have enabled prompt diagnosis and improved precision in therapy for many pathological conditions. However, there is a tremendous scope and an increasing need for improvement in management of certain diseases.

1.4.1. NON-MALIGNANT NEUROLOGICAL DISORDERS

Nanovehicles capable of carrying multiple payloads present distinct advantages in targeting the hard-to-reach areas of the brain. Nanoparticles can be surface-functionalized to readily transmigrate across the blood-brain barrier (BBB), which otherwise posed a near-impermeable barrier to the delivery of therapeutics to the brain.[149] The ability to tailor nano-formulations as per the requirements of specific pathological conditions is a highly desired feature. To this end, liposomes serve as the ideal nano-delivery vehicles capable of carry multiple payloads simultaneously for brain targeting and bioimaging with imaging agents such as Gd/ MNP-based MRI agents or quantum dots.[150, 151] One such example of brain disorders where nanomedicine and theranostics show tremendous promise is traumatic brain injury (TBI). Affecting almost 2 million patients annually in the US alone, there are no FDA approved treatments for TBI. Numerous clinical trials focusing on conventional single drug therapy have failed.[152] Technological advances in proteomics have enabled the identification of therapeutic pathway-specific biomarkers of TBI. Although indirect and involving multiple steps, biomarker driven methods of detection and diagnosis have paved the way for timely and personalized treatment of such patients. Stroke or cerebral ischemia is another dreaded cerebrovascular condition with very limited treatment alternatives. The use of theranostics capable of timely treatment and

subsequent maintenance therapy along with continuous therapy monitoring is considered to be a very valuable approach to stroke management. To this end, Agulla et al. have designed stealth immunoliposomes targeted towards HSP72 protein in the peri-infarct region with dual imaging capabilities (fluorescence and MRI). Loaded with citicoline, these dual modal theranostic immunoliposomes showed a 30% decrease in lesion volume when compared to non-encapsulated drugs. Encapsulation of Gd-DTPA-BSA enabled a continuous monitoring of the targeting efficiency of the formulation, tissue accumulation and progression of therapy over a period of 7 days.[153]

During the last decade, there has been an unprecedented increase in the number of cases of neurodegenerative conditions such as Alzheimer's disease (AD) and Parkinson's disease. The primary hurdle in the management of these conditions is early diagnosis. CdSe-ZnS quantum dots (QD) conjugated to dihydrolipoic acid have be demonstrated to successfully detect the amyloid plaques, block their growth and thus reduce the fibrillation process along with detection.[154] Skaat et al.[155] used fluorescent maghemite nanoparticles coated with LPFFD peptide for simultaneous detection, treatment and therapy monitoring. These theranostic MNPs inhibited the associated fibrillation, which could be monitored by MRI. In addition, numerous biomarkers such as the new 79-amino acid Alzheimer's associated protein ALZAS67 have been identified[156], which can aid in early detection of amyloid plaques, thereby enabling preventive measures against further development of the condition.

Commercial blood pool agent Endorem® has been used as a marker for long-term noninvasive MR tracking of transplanted bone marrow and embryonic stem cells in rat brain and spinal cord.[157] In this study, the migration of mesenchymal stem cells labeled with Endorem could be tracked successfully to the injured site for a prolonged period of time. While these are only a few representative examples of the relentless efforts currently

being made towards the development of theranostic systems for brain, they do highlight the advantages of theranostic nanosystems in several pathological conditions of the brain.

1.4.2. CARDIOVASCULAR DISEASE

Cardiovascular disease is the leading cause of morbidity and mortality all over the world. Several theranostic nanosystems have been studied for several cardiovascular conditions with interesting and encouraging findings. Numerous studies have successfully demonstrated the potential of several theranostic nanosystems in detection and treatment of atherosclerosis. Certain molecules such as $\alpha_v\beta_3$-integrin are overexpressed on the endothelial cells in the atherosclerotic plaques. These molecules serve as direct targets for long-circulating targeted nanoparticles. Functionalization of nanoparticles to target macrophages or oxidized low-density lipoproteins (LDL) within the plaques. The ability to target these processes allows for simultaneous targeting of therapeutic agents as well as contrast agents. The applicability of theranostic nanosystems was evaluated as follows:

a. Nanoparticulate contrast agents co-delivered with conventional therapeutics to evaluate the efficacy of the therapy: USPIO's, popularly used as blood pool agents, have been shown to have significantly high uptake in macrophages in atherosclerotic plaques both pre-clinically [158, 159] and clinically[160]. Morris et al. exploited this finding to demonstrate the potential of USPIO-enhanced MRI in monitoring the therapeutic efficacy of p38 kinase inhibitor in mouse model of atherosclerosis. MR images showed reduction in contrast in the aortic area of animals treated with p38 indicating reduced accumulation of macrophages in the atherosclerotic plaques in the treatment group.[161] This approach was used successfully for the first time in humans to non-invasively evaluate the efficacy of treatment of atorvastatin in carotid plaques. [162, 163] Theranostic nanosystems can also be used in monitoring the treatment of peripheral artery disease. $\alpha_v\beta_3$-integrin-targeted perfluorocarbon nanoparticles were used to monitor the effect of dietary L-arginine in

decreasing the symptoms of peripheral artery disease by increasing arteriogenesis. [164] [19]F MRI using perfluorocarbons has been used effectively for the detection of inflammation due the efficient uptake of these emulsified contrast agents into monocytes and macrophages, which in turn infiltrate the affected tissue. [165] Targeting of the nanoparticles to the ischemic tissue enhanced the signal and contrast two-folds in comparison to the nontargeted nanoparticles thereby significantly improving the ability for non-invasive monitoring of therapy progression and success wherein oral dietary L-arginine resulted in significant development of collateral blood vessels in the affect tissue.

b. Nanoparticulate therapeutics co-delivered with free contrast agents to evaluate efficacy of nanotherapy: Stenotic arteries formed due to progression of atherosclerosis are often dilated by balloon dilation followed by placement of a metallic stent. However, restenosis in such arteries often leads to other complications such as myocardial damage and impeded peripheral circulation. Drug eluting stents, which are often used for such conditions, can add to the complications by interfering with the healing of the endothelial membrane. [166-168] $\alpha_v\beta_3$-targeted rapamycin loaded[169] nanoparticles co-encapsulating 20% (v/v) perfluorooctylbromide and 30 mol% Gadolinium diethylene-triamine-pentaacetic acid-bisoleate as the paramagnetic components successfully reduced the extent of stenosis in the related arteries. This improvement was tracked by MR angiograms over a period of two weeks. Perfluorocarbon-containing nanoparticles conjugated with Phe [D]-Pro-Arg-chloromethylketone (PPACK), a molecule with high affinity for thrombin, were studied in the treatment of thrombosis in a mouse model of thrombosis. The site-specific accumulation of the 160nm nanoparticles was observed by ^{19}F MRI imaging.[170] In another approach, paclitaxel (PTX)-loaded MNPs were employed to replenish the drug-depleted stents. While MNPs were used exclusively to aid in targeting and accumulation in the desired region, fluorescent probes were conjugated on the nanosystems to evaluate the

therapeutics efficacy as observed by delayed cell proliferation.[171] This approach has also been used to demonstrate improved perfusion of the affected tissue in peripheral artery disease. Gold nanoparticles carrying vascular endothelial growth factor (VEGF) were targeted to the ischemic tissue in order to promote angiogenesis and increase perfusion in a murine hind limb ischemia model. The therapeutic effects of the targeted gold nanoparticles were visualized by laser Doppler perfusion imaging. The targeted nanoparticles helped increase the circulation half-life of VEGF while reducing the undesired side effects. Similarly, adenosine-loaded liposomes administered intravenously significantly reduced myocardial infarction in murine model.[172] Fluorescent ligands decorated on the liposome surface were used to track the accumulation of the nanoformulations at the affected site. This formulation was specifically beneficial from the point of significant reduction in the unwanted side effects of free adenosine when administered intravenously.

c. Co-encapsulated therapeutic and contrast agents for simultaneous diagnosis and treatment and subsequent monitoring of therapy: Co-encapsulated theranostic nano-systems provide significant advantages in terms of spatio-temporal delivery of both the essential components without measurable loss. This approach helps improve the treatment and overall management of previously mentioned conditions such as restenosis. Successful attempts have been made to inhibit the smooth muscle proliferation in the stented blood vessels. Perfluorocarbon nanoemulsions loaded with anti-proliferation drugs doxorubicin (DOX) as well as PTX were targeted to tissue factor on the smooth muscle cells in the restenotic artery walls. In this *in vitro* study, the uptake of the particles was detected by T_1-weighted MRI imaging while ^{19}F MRI helped further enhance the contrast and distinguish the tissue from the nanoparticles. The pattern of DOX fluorescence was monitored to observe and study the pattern of drug release over time.[173]

PFCs encapsulated within nanoformulations have shown significant improvement in site-specific signal enhancement in all cardiovascular conditions associated with inflammation. The very first study to demonstrate the advantages of co-encapsulation in treatment of atherosclerosis used perfluorocarbons along with anti-angiogenic drug fumagillin.[174] PFCs were encapsulated in nano-emulsions stabilized by a surfactant co-mixture of lecithin, polyethylene glycol (PEG)$_{2000}$- phosphatidylethanolamine, phosphatidylethanolamine and gadolinium diethylene-triamine-pentaacetic acid-bis-oleate. Fumagillin partitioned into the surfactant layer surrounding the paramagnetic perfluorocarbon molecule. The therapeutic response of the drug could be monitored over an extended period of time. Theranostic nanosystems have also been studied using multiple modes of visualization of a single contrast agent. Such an approach helps to separate the tracking of the nanosystems from evaluating the therapeutic efficacy. Labotto et al.[175] developed Gd-containing liposomes co-loaded with anti-inflammatory glycoprotein PLP. The liposomes produced significant T_1-weighted contrast by dynamic contrast enhanced MRI (DCE-MRI), which was used to monitor the delivery and accumulation of the formulations in the atherosclerotic plaques while ^{18}F-fluoro-deoxy-glucose (^{18}F-FDG) was injected separately to study the therapeutic efficacy of the liposomal formulation by PET/CT. In another study, a multi-modal nano-theranostic agent comprising of dextran-coated MNPs and near-infrared fluorophore AF750 with phototoxic capacity was prepared. These nanoparticles were readily internalized by murine macrophages as observed in the *in vitro* experiments. The *in vivo* studies revealed preferential accumulation of the nanoparticles in macrophage-rich inflamed atherosclerotic lesions as visualized by intravital fluorescence microscopy. When irradiated by 650nm light, AF750 was activated resulting in phototoxicity in the atherosclerotic area, causing significant reduction in inflammation and lesion stabilization. Such a theranostic system provided for simultaneous imaging and therapeutic response by a single multi-purpose NIR fluorophore.[176]

While many of the above-mentioned theranostic nanosystems are still in the experimental stages and thus need further characterization, quality control and toxicological evaluation, there is no doubt that compared to conventional formulations and contrast techniques, such theranostic nanosystems have proven to be superior in terms of therapeutic efficacy as well as continuous monitoring of therapy in several cardiovascular conditions, predominantly atherosclerosis and stroke.

1.4.3. CANCER

Cancer is steadily growing into a global public health problem and is feared to take over cardiovascular diseases and obesity as the disease with the highest mortality and morbidity rates. Cancer statistics of 2014 estimated over 1.6 million new cases and over 500 thousand deaths in the United States itself.[177] These numbers justify the federal emphasis on research aimed at prevention, early diagnosis and therapy of cancer. Given the diverse nature of the disease, every new case is unique in terms of the diagnosis, the molecular markers expressed and the response to therapy. These complexities have spurred concerted efforts in the direction of personalized therapy wherein each patient's biomarker profiling is recommended to design and optimize the therapeutic strategy. Nanomedicine, via its extensively target-centric approach, has opened new avenues, which can enable early diagnosis and highly personalized anti-cancer therapy. The ability to functionalize nanoparticles to target different types of diagnostic and therapeutic payloads exclusively to the malignancy helps reduce the dose, enhance accumulation of the therapeutic and also significantly reduce the incidence of unwanted side effects that plague conventional cancer treatments. The need to detect the malignancy in early stages, treat it and simultaneously monitor the progression of therapy noninvasively is a highly desired feature in cancer chemotherapy. This has given rise to what is termed as

'cancer theranostics', i.e. simultaneous therapy and non-invasive diagnostic monitoring of the disease.

The development of a theranostic nanosystem for cancer is guided by numerous factors. The location and stage of the disease is a primary factor which dictates the type of contrast agent to be selected. With that in mind, several potential theranostic anti-cancer nanoformulations have been reported so far. Radio-theranostic nanosystems (discussed in section 1.3.2.) are the most versatile since the diagnostic component is not quenched in deeper tissues and can be consistently monitored. Radiopharmaceuticals can be used for the treatment of the deepest tissues in the human body such as for treatment and imaging of bone metastasis.[178] Recently, nanobodies radiolabeled with [99]mTc were generated against the paratope of M-protein expressed in multiple myeloma cells as a tool to image multiple myeloma progression using SPECT/microCT. Targeted radionuclide therapy using a ^{177}Lu-labeled anti-5T2 MM nanobody led to an inhibition of disease progression.[54] Optical theranostic nanosystems have also been shown to be successful. Zhang et al.[179] developed a multifunctional nanocomposite by loading copper sulfide (CuS) into Cy5.5-conjugated hyaluronic acid nanoparticles (HANP), obtaining an

activatable Cy5.5_HANP/CuS (HANPC) nanocomposite. Cus quenched the Cy5.5 fluorescent signal inside the intact particles. Upon complete degradation by hyaluronidase present in the tumor stroma, strong fluorescence signals delineated the tumor. Thus, CuS with strong NIR absorbance appears to be an excellent contrast agent for photoacoustic (PA) imaging and an effective PTT agent.

Ultrasound mediated imaging is another technique with potential for applications in different types of cancer, given the ability of ultrasound to penetrate deep in the body tissues.[180] Carson et al. demonstrated the use of targeted ultrasound microbubbles in squamous cell carcinoma for detection and burst-initiated siRNA release and therapy.[181]

Liposomes have been used extensively in ultrasound-assisted anti-cancer therapy. Microbubbles conjugated with paclitaxel (PTX)-loaded liposomes were targeted towards breast cancer.[182] Other optical theranostic nanosystems such as porphyrins have also been successfully shown to inhibit tumors. Shi et al.[183] successfully investigated the potential of a 64Cu-containing nanosystem comprising of porphyrin-peptide-folate nanoprobe for simultaneous PDT and PET imaging. However, it must be noted here that PDT application are limited to superficial cancers such as those of the head and neck since activation of the porphyrin in deeper tissues is difficult. Similar argument can be made for theranostics with AuNPs for photothermal therapy combined with photoacoustic imaging. Lastly, MRI contrast agents are another extremely versatile choice across all types of cancers. The advances in MRI technology enable whole body scans with excellent contrast between malignant and healthy tissues, including those in the brain. In the next section we exclusively discuss these applications of magnetic (iron oxide) nanoformulations.

1.5. APPLICATIONS OF MAGNETIC NANOPARTICLES (MNPS) IN CANCER THERANOSTICS

The biocompatibility and biodegradability of magnetic nanoparticles, particularly of those made from magnetite, coupled with its MRI capability makes them ideal candidates for numerous biomedical applications. The ease of stabilization and case-specific functionalization (personalization) of these MNPs finds use in cancer diagnosis, therapeutics and therapy monitoring. Here we review the different applications of MNPs and their nanoformulations in overall management of cancer.

1.5.1. MAGNETIC FLUID HYPERTHERMIA (MFH) AND IMAGING

When MNPs are exposed to an alternating current (AC) magnetic field, the resulting eddy current, hysteresis, and energy losses due to Neél and Brownian relaxation mechanism experienced by the MNPs result in localized heating in the associated tissue around the nanoscale source.[184] It is known that cells, when exposed to elevated temperature of about 42-45 °C for sufficient time period initiate apoptotic processes leading to cell death.[185] The capacity to combine MRI capability and therapy in the form of hyperthermia as well as the possibility of functionalizing particles specific to a patient's biomarkers has directed research in this direction to further advance the use of magnetic nanoparticles in cancer treatment. Classical hyperthermia is known to induce a reversible damage to cells and tissues and has been known to work very effectively as an adjunct treatment to conventional radiotherapy or chemotherapy. Maier Hauff et al. studied the efficacy of intratumorally administered MNPs and radiotherapy on patients with recurrent gliobloastoma multiforme.[186] It was observed that pre-treatment with field –induced hyperthermia followed by radiotherapy led to longer overall survival following diagnosis of the first tumor recurrence. The efficacy of the treatment regimen was monitored by regular

MRI and CT scans. Another study conducted in prostate cancer patients evaluated the ability of transperinially administered MNPs in monitoring the therapeutic responses of repeated magnetic fluid hyperthermia (MFH) by CT.[187] Simultaneous MFH and MRI imaging faces challenges related to the properties of MNPs.[188] For successful MFH is it essential that MNPs be localized in the target tissue in high enough concentration. However, this interferes with ability of MR scanners to produce clear images. At high enough concentration MRI images are not without any artifacts and hence CT is the preferred technique in such cases. This has prompted the development of composite MNPs wherein Fe is doped with high metals such as Co, Mn or Ni in order to increase the specific absorption rate (SAR) of the resulting MNPs. Such an approach is driven on the hypothesis that composite MNPs, due to their high SAR will be able to generate sufficient localized heating at significantly lower concentrations, which can aid in obtaining better images by MRI itself. Nonetheless, the application of MNPs in simultaneous hyperthermia and targeted chemotherapy has been successfully tested in human trials as well[189-191] which has renewed the interest in applying MNPs for dual therapy in cancer.

1.5.2. SIMULTANEOUS CHEMOTHERAPY AND MRI

Over the last decade, the availability of a broad range of polymeric and other biodegradable and biocompatible has led to an explosion in the research in the direction of development of magnetic nanoparticle-based theranostic systems capable of carrying a therapeutic payload and simultaneously enabling MR imaging. The ease of functionalization of these nano-systems has made it possible to target them to patient-specific biomarkers. Extensive research in cancer genetics has shown that cancers show significant heterogeneity and hence the concept of 'one size fits all' cannot work at least here.[192, 193] This has brought about a paradigm shift in the process of oncological drug development. The focus is now on designing targeted or personalized therapies as per

the genetic constitution of the disease in every patient. A classic example is breast cancer wherein different cases present with different biomarkers or, still worst, none at all.[194] The human epidermal growth factor receptor overexpressed in several cases of cancers has many subtypes namely HER1/EGFR, HER2, HER3 and HER4.[195] Accordingly, the therapeutic strategies differ. For instance, Tarceva® (erlotinib) is the preferred line of therapy to target HER1 in patients with non-small cell lung cancer (NSCLC). HER2, overexpressed in breast and ovarian cancer is targeted using mAb Herceptin® (trastazumab).

Theranostic nanomedicine shows tremendous potential in not only targeting, but also controlling the release of the payload and monitoring the therapeutic response. Schleich et al.[196] compared the different *in vivo* targeting strategies of PLGA nanoparticles co-loaded with PTX and MNPs. They concluded that dual targeting (i.e. active targeting of $\alpha_v\beta_3$ integrin via RGD grafting along with magnetic targeting) resulted in maximum accumulation of nanoparticles which in turn enhanced therapeutic and MRI contrast efficacy. Thermoresponsive anti-cancer nanosystems have also been developed to control the release of the therapeutic payload via the hyperthermic potential of MNPs. Purushotham et al.[197] developed core-shell magnetite (Fe_3O_4)–poly-n-(isopropyl acrylamide (pNIPAM) composite MNPs loaded with DOX. In an alternating magnetic field, the MNPs generated heat leading to localized temperature rise. Above the lower critical solution temperature of PNIPAM, the nanostructure released DOX thus acting as an on/off switch to control drug release. Clares et al.[198] reported the development of magnetoliposomes loaded with 5-fluorouracil (5-FU) for the colon cancer. These non-targeted formulations showed thermo-responsive release of 5-FU in response to local hyperthermia in AC field.

Physiological stimuli-responsive MNP-based theranostic systems have also been designed to control the drug release form the nanocarriers. Luo et al.[199] exploited the presence of intra-cellular redox conditions to trigger drug release from MNP-cyclodextrin nanoformulations loaded with camptothecin. Li et al.[200] went a step further by developing folate-targeted magnetic bovine serum albumin microcapsules loaded with coumarin-6. The microcapsules exhibited redox-responsive enhancement in drug release. The pH difference between healthy tissues and tumor microenvironment has also been utilize pH responsive theranostic nanosystems. Sahoo et al.[201] designed DOX-loaded theranostic MNPs comprising of pNIPAM. These systems showed preferentially release of DOX conjugated via a pH labile linker only under physiological temperature. Another interesting attempt was made by Gan et al., who developed 'MNP-gated' mesophorous silica nanoparticles. In this system, MNPs capped the pores on the drug loaded silica nanoparticles via pH labile linkers. At acidic pH the MNPs opened the pores thereby causing controlled release of the payload.

Several successful attempts have been made to employ low frequency non-heating AC magnetic field to release the drug from the theranostic MNPs. In one such example, polymersomes were loaded with USPIOs and DOX were tested for field-responsive in vitro drug release and cytotoxicity in HeLa cells.[135] They observed that when exposed to 15mT fields at 750 KHz, the formulation exhibited 18% increase in cytotoxicity. It was postulated that in response to Neel relaxation mechanisms, the MNPs dissipated heat, which was sufficient enough to cause poration in the polymersomal membrane and thus release the therapeutic agents. In the last of their series of four publications demonstrating the application of various stimuli for drug release from 'gated mesoporous silica nanoparticles', Thomas et al.[202] demonstrated that in presence of external AC magnetic field having a frequency of 500kHz and 37.4 KA/m field strength, Zn-doped MNPs

generated local heat, which caused the cucurbit(6)uril nanovalves on the pores to open and release DOX. Controlling the duration of the applied AC field pulse could control the drug release. These gated systems could also serve as theranostic systems for MRI imaging.

1.6. CONCLUSION

Theranostics is emerging as a new field that combines the modalities of therapy and diagnostic imaging. Nanotechnology holds the key to the fructification of this vision. The ability to 'pack' therapeutic and diagnostic modalities in a single carrier helps overcome unwanted differences in biodistribution, selectivity thereby ensuring the simultaneous presence of both the components in the desired site. The eventual aim of the field of theranostics is to gain the ability to image and monitor the diseased organ, drug delivery kinetics, and therapeutic efficacy, eventually being able to tune the therapy and dosing as per the needs of the patient. Clinicians are increasingly advocating such personalization of therapy. In fact, numerous cancer treatment centers across the US, have started studying the genetic make-up of the patients in order to design a treatment strategy on a case-by-case basis. However, given the short response time available once diagnosed with fatal diseases such as cancer, it is an uphill task to formulate a personalized formulation with required precision. Hence the onus is now on researchers in the field of Pharmaceutics and drug delivery to device techniques for addressing this need. As exemplified in this overview, tremendous efforts are underway in the direction of development of theranostic nanoformulations for numerous pathological conditions. In terms of imaging modalities, there are various options available, from simple fluorescence based systems to complex ultra-sound based photoacoustic agents, each with its advantages and disadvantages. However, in case of MNP-based theranostic nanosystems, thanks to the relentless efforts for the last two-three decades, the advantages outweigh the limitations. The ability to tune almost every character of MNPs, from their magnetic properties to addition of various targeting moieties makes them a favorable choice, especially for cancer management. One factor that still plagues this class of theranostic systems is their systemic stability and associated toxicity.

We aim to design highly stable and completely biodegradable MNP-based theranostic nanoclusters capable of targeted drug delivery and MR imaging. Given that the primary requirement in a theranostic system is to strike a right balance between the amounts of therapeutic and contrast agents carried by the nanocarrier, development of such a nanosystems is a very complicated process. Through the next chapters we demonstrate the challenges faced and the strategies employed to meet these challenges in development of theranostic magnetic nanoclusters for cancer theranostics.

1.7. REFERENCES

1. Davis, M. E.; Shin, D. M., Nanoparticle therapeutics: an emerging treatment modality for cancer. *Nat. Rev. Drug Discovery* **2008,** 7, 771-782.

2. Heath, J. R.; Davis, M. E., Nanotechnology and cancer. *Annu. Rev. Med.* **2008,** 59, 251.

3. Ferrari, M., Cancer nanotechnology: opportunities and challenges. *Nature Reviews Cancer* **2005,** 5, 161-171.

4. Lammers, T.; Aime, S.; Hennink, W. E.; Storm, G.; Kiessling, F., Theranostic nanomedicine. *Acc. Chem. Res.* **2011,** 44, 1029-1038.

5. Chen, X.; Wong, S. T., Cancer Theranostics: An Introduction.

6. Muthu, M. S.; Kulkarni, S. A.; Raju, A.; Feng, S.-S., Theranostic liposomes of TPGS coating for targeted co-delivery of docetaxel and quantum dots. *Biomaterials* **2012,** 33, 3494-3501.

7. Muthu, M. S.; Feng, S.-S., Theranostic liposomes for cancer diagnosis and treatment: current development and pre-clinical success. *Expert Opin. Drug Delivery* **2013,** 10, 151-155.

8. Ng, S.; Chang, T.; Ko, S.; Yen, P.; Wan, Y.; Tang, L.; Tsai, M., Nasopharyngeal carcinoma: MRI and CT assessment. *Neuroradiology* **1997,** 39, 741-746.

9. Aisen, A. M.; Martel, W.; Braunstein, E. M.; McMillin, K. I.; Phillips, W. A.; Kling, T., MRI and CT evaluation of primary bone and soft-tissue tumors. *Am. J. Roentgenol.* **1986,** 146, 749-756.

10. Kroft, L. J.; de Roos, A., Blood pool contrast agents for cardiovascular MR imaging. *J. Magn. Reson. Imaging* **1999,** 10, 395-403.

11. Bogdanov, A. A.; Weissleder, R.; Brady, T. J., Long-circulating blood pool imaging agents. *Adv. Drug Del. Rev.* **1995,** 16, 335-348.

12. Hofman, M.; Henson, R. E.; Kovacs, S. J.; Fischer, S. E.; Lauffer, R. B.; Adzamli, K.; De Becker, J.; Wickline, S. A.; Lorenz, C. H., Blood pool agent strongly improves 3D magnetic resonance coronary angiography using an inversion pre-pulse. *Magn. Reson. Med.* **1999,** 41, 360-367.

13. Lauffer, R. B.; Parmelee, D. J.; Dunham, S. U.; Ouellet, H. S.; Dolan, R. P.; Witte, S.; McMurry, T. J.; Walovitch, R. C., MS-325: albumin-targeted contrast agent for MR angiography. *Radiology* **1998,** 207, 529-538.

14. Adam, G.; Neuerburg, J.; Spüntrup, E.; Mühler, A.; Günther, R. W., Gd-DTPA-cascade-polymer: Potential blood pool contrast agent for MR imaging. *J. Magn. Reson. Imaging* **1994,** 4, 462-466.

15. Anzai, Y.; Prince, M. R.; Chenevert, T. L.; Maki, J. H.; London, F. L. M.; McLachlan, S. J., MR angiography with an ultrasmall superparamagnetic iron oxide blood pool agent. *J. Magn. Reson. Imaging* **1997,** 7, 209-214.

16. Kaur, I. P.; Singh, M.; Yadav, M.; Sandhu, S. K.; Deol, P. K.; Sharma, G. In *Potential of Nanomaterials as Movers and Packers for Drug Molecules*, Solid State Phenomena, 2015; Trans Tech Publ: 2015; pp 159-178.

17. Margerum, L. D.; Campion, B. K.; Koo, M.; Shargill, N.; Lai, J.-J.; Marumoto, A.; Sontum, P. C., Gadolinium (III) DO3A macrocycles and polyethylene glycol coupled to dendrimers Effect of molecular weight on physical and biological properties of macromolecular magnetic resonance imaging contrast agents. *J. Alloys Compd.* **1997,** 249, 185-190.

18. Liang, X.; Li, Y.; Li, X.; Jing, L.; Deng, Z.; Yue, X.; Li, C.; Dai, Z., PEGylated Polypyrrole Nanoparticles Conjugating Gadolinium Chelates for Dual-Modal MRI/Photoacoustic Imaging Guided Photothermal Therapy of Cancer. *Adv. Funct. Mater.* **2015,** 25, 1451-1462.

19. Perazella, M. A., Gadolinium-contrast toxicity in patients with kidney disease: nephrotoxicity and nephrogenic systemic fibrosis. *Current drug safety* **2008,** 3, 67-75.

20. Perazella, M. A., Current status of gadolinium toxicity in patients with kidney disease. *Clin. J. Am. Soc. Nephrol.* **2009,** 4, 461-469.

21. Spinosa, D. J.; Fritz Angle, J.; Hartwell, G. D.; Hagspiel, K. D.; Leung, D. A.; Matsumoto, A. H., Gadolinium-based contrast agents in angiography and interventional radiology. *Radiol. Clin. North Am.* **2002,** 40, 693-710.

22. Townsend, R. R.; Cohen, D. L.; Katholi, R.; Swan, S. K.; Davies, B. E.; Bensel, K.; Lambrecht, L.; Parker, J., Safety of intravenous gadolinium (Gd-BOPTA) infusion in patients with renal insufficiency. *Am. J. Kidney Dis.* **2000,** 36, 1207-1212.

23. Ersoy, H.; Rybicki, F. J., Biochemical safety profiles of gadolinium-based extracellular contrast agents and nephrogenic systemic fibrosis. *J. Magn. Reson. Imaging* **2007,** 26, 1190-1197.

24. Torchilin, V. P., Recent advances with liposomes as pharmaceutical carriers. *Nat. Rev. Drug Discovery* **2005,** 4, 145-160.

25. Janib, S. M.; Moses, A. S.; MacKay, J. A., Imaging and drug delivery using theranostic nanoparticles. *Adv. Drug Del. Rev.* **2010,** 62, 1052-1063.

26. Cabral, H.; Kataoka, K., Progress of drug-loaded polymeric micelles into clinical studies. *J. Controlled Release* **2014,** 190, 465-476.

27. Kwon, G. S.; Kataoka, K., Block copolymer micelles as long-circulating drug vehicles. *Adv. Drug Del. Rev.* **2012,** 64, 237-245.

28. Liao, Z.-X.; Peng, S.-F.; Chiu, Y.-L.; Hsiao, C.-W.; Liu, H.-Y.; Lim, W.-H.; Lu, H.-M.; Sung, H.-W., Enhancement of efficiency of chitosan-based complexes for gene transfection with poly (γ-glutamic acid) by augmenting their cellular uptake and intracellular unpackage. *J. Controlled Release* **2014,** 193, 304-315.

29. Desale, S. S.; Raja, S. M.; Kim, J. O.; Mohapatra, B.; Soni, K. S.; Luan, H.; Williams, S. H.; Bielecki, T. A.; Feng, D.; Storck, M., Polypeptide-based nanogels co-encapsulating a synergistic combination of doxorubicin with 17-AAG show potent anti-tumor activity in ErbB2-driven breast cancer models. *J. Controlled Release* **2015,** 208, 59-66.

30. Desale, S. S.; Cohen, S. M.; Zhao, Y.; Kabanov, A. V.; Bronich, T. K., Biodegradable hybrid polymer micelles for combination drug therapy in ovarian cancer. *J. Controlled Release* **2013,** 171, 339-348.

31. Xiong, X.; Tam, K.; Gan, L., Polymeric nanostructures for drug delivery applications based on Pluronic copolymer systems. *J. Nanosci. Nanotechnol.* **2006,** 6, 2638-2650.

32. Shachaf, Y.; Gonen-Wadmany, M.; Seliktar, D., The biocompatibility of Pluronic® F127 fibrinogen-based hydrogels. *Biomaterials* **2010,** 31, 2836-2847.

33. Ricci, E.; Lunardi, L.; Nanclares, D.; Marchetti, J., Sustained release of lidocaine from Poloxamer 407 gels. *Int. J. Pharm.* **2005,** 288, 235-244.

34. Qin, J.; Laurent, S.; Jo, Y. S.; Roch, A.; Mikhaylova, M.; Bhujwalla, Z. M.; Muller, R. N.; Mohammed, M., A high-performance magnetic resonance imaging T2 contrast agent. *Adv. Mater.* **2007,** 19, 1874-1878.

35. Liu, Z.; Ding, J.; Xue, J., A new family of biocompatible and stable magnetic nanoparticles: silica cross-linked pluronic F127 micelles loaded with iron oxides. *New J. Chem.* **2009,** 33, 88-92.

36. Jain, T. K.; Richey, J.; Strand, M.; Leslie-Pelecky, D. L.; Flask, C. A.; Labhasetwar, V., Magnetic nanoparticles with dual functional properties: drug delivery and magnetic resonance imaging. *Biomaterials* **2008,** 29, 4012-4021.

37. Kleemann, E.; Neu, M.; Jekel, N.; Fink, L.; Schmehl, T.; Gessler, T.; Seeger, W.; Kissel, T., Nano-carriers for DNA delivery to the lung based upon a TAT-derived peptide covalently coupled to PEG–PEI. *J. Controlled Release* **2005,** 109, 299-316.

38. Heim, R.; Tsien, R. Y., Engineering green fluorescent protein for improved brightness, longer wavelengths and fluorescence resonance energy transfer. *Curr. Biol.* **1996,** 6, 178-182.

39. Schwille, P.; Korlach, J.; Webb, W. W., Fluorescence correlation spectroscopy with single-molecule sensitivity on cell and model membranes. *Cytometry* **1999,** 36, 176-182.

40. Lucas, B.; Remaut, K.; Sanders, N.; Braeckmans, K.; De Smedt, S.; Demeester, J., Studying the intracellular dissociation of polymer-oligonucleotide complexes by dual color fluorescence fluctuation spectroscopy and confocal imaging. *Biochemistry* **2005,** 44, 9905-9912.

41. Remaut, K.; Lucas, B.; Raemdonck, K.; Braeckmans, K.; Demeester, J.; De Smedt, S., Can we better understand the intracellular behavior of DNA nanoparticles by fluorescence correlation spectroscopy? *J. Controlled Release* **2007,** 121, 49-63.

42. Buhro, W. E.; Colvin, V. L., Semiconductor nanocrystals: shape matters. *Nat. Mater.* **2003,** 2, 138-139.

43. Resch-Genger, U.; Grabolle, M.; Cavaliere-Jaricot, S.; Nitschke, R.; Nann, T., Quantum dots versus organic dyes as fluorescent labels. *Nat. Methods* **2008,** 5, 763-775.

44. Leutwyler, W. K.; Bürgi, S. L.; Burgl, H., Semiconductor clusters, nanocrystals, and quantum dots. *Science* **1996,** 271, 933-937.

45. Wu, X.; Liu, H.; Liu, J.; Haley, K. N.; Treadway, J. A.; Larson, J. P.; Ge, N.; Peale, F.; Bruchez, M. P., Immunofluorescent labeling of cancer marker Her2 and other cellular targets with semiconductor quantum dots. *Nat. Biotechnol.* **2003,** 21, 41-46.

46. Panchuk-Voloshina, N.; Haugland, R. P.; Bishop-Stewart, J.; Bhalgat, M. K.; Millard, P. J.; Mao, F.; Leung, W.-Y.; Haugland, R. P., Alexa dyes, a series of new fluorescent dyes that yield exceptionally bright, photostable conjugates. *J. Histochem. Cytochem.* **1999,** 47, 1179-1188.

47. Hoshino, A.; Fujioka, K.; Oku, T.; Suga, M.; Sasaki, Y. F.; Ohta, T.; Yasuhara, M.; Suzuki, K.; Yamamoto, K., Physicochemical properties and cellular toxicity of nanocrystal quantum dots depend on their surface modification. *Nano Lett.* **2004,** 4, 2163-2169.

48. Srinivasan, C.; Lee, J.; Papadimitrakopoulos, F.; Silbart, L. K.; Zhao, M.; Burgess, D. J., Labeling and intracellular tracking of functionally active plasmid DNA with semiconductor quantum dots. *Mol. Ther.* **2006,** 14, 192-201.

49. Santra, S.; Yang, H.; Holloway, P. H.; Stanley, J. T.; Mericle, R. A., Synthesis of water-dispersible fluorescent, radio-opaque, and paramagnetic CdS: Mn/ZnS quantum dots: a multifunctional probe for bioimaging. *J. Am. Chem. Soc.* **2005,** 127, 1656-1657.

50. Kim, J.; Lee, J. E.; Lee, J.; Yu, J. H.; Kim, B. C.; An, K.; Hwang, Y.; Shin, C.-H.; Park, J.-G.; Kim, J.; Hyeon, T., Magnetic Fluorescent Delivery Vehicle Using Uniform Mesoporous Silica Spheres Embedded with Monodisperse Magnetic and Semiconductor Nanocrystals. *J. Am. Chem. Soc.* **2006,** 128, 688-689.

51. Mulder, W. J.; Koole, R.; Brandwijk, R. J.; Storm, G.; Chin, P. T.; Strijkers, G. J.; de Mello Donegá, C.; Nicolay, K.; Griffioen, A. W., Quantum dots with a paramagnetic coating as a bimodal molecular imaging probe. *Nano Lett.* **2006,** 6, 1-6.

52. Anderson, C. J.; Welch, M. J., Radiometal-labeled agents (non-technetium) for diagnostic imaging. *Chem. Rev.* **1999,** 99, 2219-2234.

53. Jurisson, S. S.; Lydon, J. D., Potential technetium small molecule radiopharmaceuticals. *Chem. Rev.* **1999,** 99, 2205-2218.

54. D'Huyvetter, M.; Xavier, C.; Caveliers, V.; Lahoutte, T.; Muyldermans, S.; Devoogdt, N., Radiolabeled nanobodies as theranostic tools in targeted radionuclide therapy of cancer. *Expert Opin. Drug Delivery* **2014,** 11, 1939-1954.

55. Sharkey, R. M.; Goldenberg, D. M., Cancer radioimmunotherapy. *Immunotherapy* **2011,** 3, 349-370.

56. Li, S.; Goins, B.; Zhang, L.; Bao, A., Novel multifunctional theranostic liposome drug delivery system: construction, characterization, and multimodality MR, near-infrared fluorescent, and nuclear imaging. *Bioconj. Chem.* **2012,** 23, 1322-1332.

57. Guo, J.; Hong, H.; Chen, G.; Shi, S.; Zheng, Q.; Zhang, Y.; Theuer, C. P.; Barnhart, T. E.; Cai, W.; Gong, S., Image-guided and tumor-targeted drug delivery with radiolabeled unimolecular micelles. *Biomaterials* **2013,** 34, 8323-8332.

58. Sugiyama, M.; Sakahara, H.; Sato, K.; Harada, N.; Fukumoto, D.; Kakiuchi, T.; Hirano, T.; Kohno, E.; Tsukada, H., Evaluation of 3′-deoxy-3′-18F-fluorothymidine for monitoring tumor response to radiotherapy and photodynamic therapy in mice. *J. Nucl. Med.* **2004,** 45, 1754-1758.

59. Shonat, R. D.; Wachman, E. S.; Niu, W.-h.; Koretsky, A. P.; Farkas, D. L., Near-simultaneous hemoglobin saturation and oxygen tension maps in mouse brain using an AOTF microscope. *Biophys. J.* **1997,** 73, 1223.

60. Olivo, M.; Wilson, B. C., Mapping ALA-induced PPIX fluorescence in normal brain and brain tumour using confocal fluorescence microscopy. *Int. J. Oncol.* **2004,** 25, 37-45.

61. Blamire, A. M.; Ogawa, S.; Ugurbil, K.; Rothman, D.; McCarthy, G.; Ellermann, J. M.; Hyder, F.; Rattner, Z.; Shulman, R. G., Dynamic mapping of the human visual cortex by high-speed magnetic resonance imaging. *Proc. Natl. Acad. Sci. U. S. A.* **1992,** 89, 11069-11073.

62. Gillis, P.; Petö, S.; Moiny, F.; Mispelter, J.; Cuenod, C. A., Proton transverse nuclear magnetic relaxation in oxidized blood: a numerical approach. *Magn. Reson. Med.* **1995,** 33, 93-100.

63. Millen, S. J.; Haughton, V.; Yetkin, Z., Functional magnetic resonance imaging of the central auditory pathway following speech and pure-tone stimuli. *The Laryngoscope* **1995,** 105, 1305-1310.

64. Zhang, Y.; Lovell, J. F., Porphyrins as Theranostic Agents from Prehistoric to Modern Times. *Theranostics* **2012,** 2, 905-915.

65. Policard, A., Etude sur les aspects offerts par des tumeurs experimentales examinees a la lumiere de Wood. *CR Soc Biol* **1924,** 91, 1423-1424.

66. Ackroyd, R.; Kelty, C.; Brown, N.; Reed, M., The history of photodetection and photodynamic therapy¶. *Photochem. Photobiol.* **2001,** 74, 656-669.

67. Wrenn, F. R.; Good, M. L.; Handler, P., The use of positron-emitting radioisotopes for the localization of brain tumors. *Science* **1951,** 113, 525-527.

68. Hsu, C.-Y.; Nieh, M.-P.; Lai, P.-S., Facile self-assembly of porphyrin-embedded polymeric vesicles for theranostic applications. *Chem. Commun.* **2012,** 48, 9343-9345.

69. Tam, N. C.; McVeigh, P. Z.; MacDonald, T. D.; Farhadi, A.; Wilson, B. C.; Zheng, G., Porphyrin–lipid stabilized gold nanoparticles for surface enhanced raman scattering based imaging. *Bioconj. Chem.* **2012,** 23, 1726-1730.

70. Cohen, E. M.; Ding, H.; Kessinger, C. W.; Khemtong, C.; Gao, J.; Sumer, B. D., Polymeric micelle nanoparticles for photodynamic treatment of head and neck cancer cells. *Otolaryngology-Head and Neck Surgery* **2010,** 143, 109-115.

71. Master, A. M.; Rodriguez, M. E.; Kenney, M. E.; Oleinick, N. L.; Sen Gupta, A., Delivery of the photosensitizer Pc 4 in PEG-PCL micelles for in vitro PDT studies. *J. Pharm. Sci.* **2010,** 99, 2386-2398.

72. Wan, J.; Bick, A.; Sullivan, M.; Stone, H. A., Controllable Microfluidic Production of Microbubbles in Water-in-Oil Emulsions and the Formation of Porous Microparticles. *Adv. Mater.* **2008,** 20, 3314-3318.

73. Ahmed, D.; Mao, X.; Juluri, B. K.; Huang, T. J., A fast microfluidic mixer based on acoustically driven sidewall-trapped microbubbles. *Microfluid. Nanofluid.* **2009,** 7, 727-731.

74. de Jong, N.; Hoff, L.; Skotland, T.; Bom, N., Absorption and scatter of encapsulated gas filled microspheres: theoretical considerations and some measurements. *Ultrasonics* **1992,** 30, 95-103.

75. Culp, W. C.; Porter, T. R.; Lowery, J.; Xie, F.; Roberson, P. K.; Marky, L., Intracranial clot lysis with intravenous microbubbles and transcranial ultrasound in swine. *Stroke* **2004,** 35, 2407-2411.

76. Perren, F.; Loulidi, J.; Poglia, D.; Landis, T.; Sztajzel, R., Microbubble potentiated transcranial duplex ultrasound enhances IV thrombolysis in acute stroke. *J. Thromb. Thrombolysis* **2008,** 25, 219-223.

77. Gao, Z.; Kennedy, A. M.; Christensen, D. A.; Rapoport, N. Y., Drug-loaded nano/microbubbles for combining ultrasonography and targeted chemotherapy. *Ultrasonics* **2008,** 48, 260-270.

78. Kwan, J. J.; Kaya, M.; Borden, M. A.; Dayton, P. A., Theranostic Oxygen Delivery Using Ultrasound and Microbubbles. *Theranostics* **2012,** 2, 1174-1184.

79. Lukianova-Hleb, E.; Hanna, E.; Hafner, J.; Lapotko, D., Tunable plasmonic nanobubbles for cell theranostics. *Nanotechnology* **2010,** 21, 085102.

80. Anderson, L. J.; Hansen, E.; Lukianova-Hleb, E. Y.; Hafner, J. H.; Lapotko, D. O., Optically guided controlled release from liposomes with tunable plasmonic nanobubbles. *J. Controlled Release* **2010,** 144, 151-158.

81. Tachibana, K.; Tachibana, S., Albumin microbubble echo-contrast material as an enhancer for ultrasound accelerated thrombolysis. *Circulation* **1995,** 92, 1148-1150.

82. Hynynen, K.; McDannold, N.; Vykhodtseva, N.; Jolesz, F., Non-invasive opening of BBB by focused ultrasound. In *Brain Edema XII*, Springer: 2003; pp 555-558.

83. Lay, C. L.; Liu, H. Q.; Tan, H. R.; Liu, Y., Delivery of paclitaxel by physically loading onto poly (ethylene glycol)(PEG)-graftcarbon nanotubes for potent cancer therapeutics. *Nanotechnology* **2010,** 21, 065101.

84. Dhar, S.; Gu, F. X.; Langer, R.; Farokhzad, O. C.; Lippard, S. J., Targeted delivery of cisplatin to prostate cancer cells by aptamer functionalized Pt (IV) prodrug-PLGA–PEG nanoparticles. *Proc. Natl. Acad. Sci. U. S. A.* **2008,** 105, 17356-17361.

85. Karchemski, F.; Zucker, D.; Barenholz, Y.; Regev, O., Carbon nanotubes-liposomes conjugate as a platform for drug delivery into cells. *J. Controlled Release* **2012,** 160, 339-345.

86. Feazell, R. P.; Nakayama-Ratchford, N.; Dai, H.; Lippard, S. J., Soluble single-walled carbon nanotubes as longboat delivery systems for platinum (IV) anticancer drug design. *J. Am. Chem. Soc.* **2007,** 129, 8438-8439.

87. Keren, S.; Zavaleta, C.; Cheng, Z.; de La Zerda, A.; Gheysens, O.; Gambhir, S., Noninvasive molecular imaging of small living subjects using Raman spectroscopy. *Proc. Natl. Acad. Sci. U. S. A.* **2008,** 105, 5844-5849.

88. Liu, Z.; Tabakman, S.; Welsher, K.; Dai, H., Carbon nanotubes in biology and medicine: in vitro and in vivo detection, imaging and drug delivery. *Nano Res.* **2009,** 2, 85-120.

89. Guo, Y.; Shi, D.; Cho, H.; Dong, Z.; Kulkarni, A.; Pauletti, G. M.; Wang, W.; Lian, J.; Liu, W.; Ren, L., In vivo Imaging and Drug Storage by Quantum-Dot-Conjugated Carbon Nanotubes. *Adv. Funct. Mater.* **2008,** 18, 2489-2497.

90. De La Zerda, A.; Zavaleta, C.; Keren, S.; Vaithilingam, S.; Bodapati, S.; Liu, Z.; Levi, J.; Smith, B. R.; Ma, T.-J.; Oralkan, O., Carbon nanotubes as photoacoustic molecular imaging agents in living mice. *Nat. Nanotechnol.* **2008,** 3, 557-562.

91. Sperling, R. A.; Gil, P. R.; Zhang, F.; Zanella, M.; Parak, W. J., Biological applications of gold nanoparticles. *Chem. Soc. Rev.* **2008,** 37, 1896-1908.

92. Daniel, M.-C.; Astruc, D., Gold nanoparticles: assembly, supramolecular chemistry, quantum-size-related properties, and applications toward biology, catalysis, and nanotechnology. *Chem. Rev.* **2004,** 104, 293-346.

93. Huang, X.; Jain, P. K.; El-Sayed, I. H.; El-Sayed, M. A., Gold nanoparticles: interesting optical properties and recent applications in cancer diagnostics and therapy. *Future Medicine* **2007**, 681-693.

94. Moon, G. D.; Choi, S.-W.; Cai, X.; Li, W.; Cho, E. C.; Jeong, U.; Wang, L. V.; Xia, Y., A New Theranostic System Based on Gold Nanocages and Phase-Change Materials with Unique Features for Photoacoustic Imaging and Controlled Release. *J. Am. Chem. Soc.* **2011,** 133, 4762-4765.

95. Heo, D. N.; Yang, D. H.; Moon, H.-J.; Lee, J. B.; Bae, M. S.; Lee, S. C.; Lee, W. J.; Sun, I.-C.; Kwon, I. K., Gold nanoparticles surface-functionalized with paclitaxel drug and biotin receptor as theranostic agents for cancer therapy. *Biomaterials* **2012,** 33, 856-866.

96. El-Sayed, I. H.; Huang, X.; El-Sayed, M. A., Surface plasmon resonance scattering and absorption of anti-EGFR antibody conjugated gold nanoparticles in cancer diagnostics: applications in oral cancer. *Nano Lett.* **2005,** 5, 829-834.

97. Curry, T.; Kopelman, R.; Shilo, M.; Popovtzer, R., Multifunctional theranostic gold nanoparticles for targeted CT imaging and photothermal therapy. *Contrast Media Mol. Imaging* **2014,** 9, 53-61.

98. Hilger, I.; Kaiser, W. A., Iron oxide-based nanostructures for MRI and magnetic hyperthermia. *Nanomedicine* **2012,** 7, 1443-1459.

99. Ogawa, S.; Lee, T.-M.; Kay, A. R.; Tank, D. W., Brain magnetic resonance imaging with contrast dependent on blood oxygenation. *Proc. Natl. Acad. Sci. U. S. A.* **1990,** 87, 9868-9872.

100. Law, M., Magnetic Resonance Imaging in Brain Tumors: Update. *Top. Magn. Reson. Imaging* **2015,** 24, 125.

101.   Shenton, M.; Hamoda, H.; Schneiderman, J.; Bouix, S.; Pasternak, O.; Rathi, Y.; Vu, M.-A.; Purohit, M.; Helmer, K.; Koerte, I., A review of magnetic resonance imaging and diffusion tensor imaging findings in mild traumatic brain injury. *Brain imaging and behavior* **2012,** 6, 137-192.

102.   Tang, J.; Sheng, Y.; Hu, H.; Shen, Y., Macromolecular MRI contrast agents: Structures, properties and applications. *Prog. Polym. Sci.* **2013,** 38, 462-502.

103.   Gerothanassis, I. P.; Troganis, A.; Exarchou, V.; Barbarossou, K., Nuclear magnetic resonance (NMR) spectroscopy: basic principles and phenomena, and their applications to chemistry, biology and medicine. *Chem. Educ. Res. Pract.* **2002,** 3, 229-252.

104.   Chavhan, G. B., *MRI made easy*. JP Medical Ltd: 2013;

105.   Nayak, S. M., MRI: Basic Principles and Applications. *Radiology* **1996,** 200, 142-142.

106.   Pykett, I. L.; Newhouse, J. H.; Buonanno, F. S.; Brady, T. J.; Goldman, M. R.; Kistler, J. P.; Pohost, G. M., Principles of nuclear magnetic resonance imaging. *Radiology* **1982,** 143, 157-168.

107.   Sisan, D. R.; Mujica, N.; Tillotson, W. A.; Huang, Y.-M.; Dorland, W.; Hassam, A. B.; Antonsen, T. M.; Lathrop, D. P., Experimental observation and characterization of the magnetorotational instability. *Phys. Rev. Lett.* **2004,** 93, 114502.

108.   Bitar, R.; Leung, G.; Perng, R.; Tadros, S.; Moody, A. R.; Sarrazin, J.; McGregor, C.; Christakis, M.; Symons, S.; Nelson, A., MR pulse sequences: What every radiologist wants to know but is afraid to ask 1. *Radiographics* **2006,** 26, 513-537.

109. Henkelman, R. M.; Huang, X.; Xiang, Q. S.; Stanisz, G.; Swanson, S. D.; Bronskill, M. J., Quantitative interpretation of magnetization transfer. *Magn. Reson. Med.* **1993,** 29, 759-766.

110. Brown, M. A.; Semelka, R. C., *MRI: basic principles and applications*. John Wiley & Sons: 2011;

111. Sosnovik, D. E.; Nahrendorf, M.; Weissleder, R., Molecular Magnetic Resonance Imaging in Cardiovascular Medicine. *Circulation* **2007,** 115, 2076-2086.

112. Arora, J., *AC-susceptibility studies of magnetic relaxation mechanisms in superparamagnetic nanoparticles*. ProQuest: 2007;

113. Slichter, C. P., *Principles of magnetic resonance*. Springer Science & Business Media: 2013; Vol. 1

114. Bloembergen, N., *Nuclear magnetic relaxation*. Springer: 1961;

115. Han, D.; Wang, J.; Luo, H., Crystallite size effect on saturation magnetization of fine ferrimagnetic particles. *J. Magn. Magn. Mater.* **1994,** 136, 176-182.

116. Bacri, J.-C.; Perzynski, R.; Salin, D.; Cabuil, V.; Massart, R., Magnetic colloidal properties of ionic ferrofluids. *J. Magn. Magn. Mater.* **1986,** 62, 36-46.

117. Bucher, J., Magnetism of free transition metal and rare earth clusters. In *Physics and Chemistry of Finite Systems: From Clusters to Crystals*, Springer: 1992; pp 721-732.

118. Koehler, W. C., Magnetic Properties of Rare-Earth Metals and Alloys. *J. Appl. Phys.* **1965,** 36, 1078-1087.

119. Botta, M., Second coordination sphere water molecules and relaxivity of gadolinium (III) complexes: implications for MRI contrast agents. *Eur. J. Inorg. Chem.* **2000,** 2000, 399-407.

120.   Caravan, P., Strategies for increasing the sensitivity of gadolinium based MRI contrast agents. *Chem. Soc. Rev.* **2006,** 35, 512-523.

121.   Bousquet, J.-C.; Saini, S.; Stark, D.; Hahn, P.; Nigam, M.; Wittenberg, J.; Ferrucci Jr, J., Gd-DOTA: characterization of a new paramagnetic complex. *Radiology* **1988,** 166, 693-698.

122.   Morcos, S., Extracellular gadolinium contrast agents: differences in stability. *Eur. J. Radiol.* **2008,** 66, 175-179.

123.   Aime, S.; Barge, A.; Cabella, C.; Crich, S. G.; Gianolio, E., Targeting cells with MR imaging probes based on paramagnetic Gd (III) chelates. *Curr. Pharm. Biotechnol.* **2004,** 5, 509-518.

124.   Elhabiri, M.; Abada, S.; Sy, M.; Nonat, A.; Choquet, P.; Esteban-Gómez, D.; Cassino, C.; Platas-Iglesias, C.; Botta, M.; Charbonnière, L. J., Importance of Outer-Sphere and Aggregation Phenomena in the Relaxation Properties of Phosphonated Gadolinium Complexes with Potential Applications as MRI Contrast Agents. *Chemistry-A European Journal* **2015,** 21, 6535-6546.

125.   Debroye, E.; Parac-Vogt, T. N., Towards polymetallic lanthanide complexes as dual contrast agents for magnetic resonance and optical imaging. *Chem. Soc. Rev.* **2014,** 43, 8178-8192.

126.   Chauvin, T.; Torres, S.; Rosseto, R.; Kotek, J.; Badet, B.; Durand, P.; Tóth, É., Lanthanide (III) Complexes That Contain a Self-Immolative Arm: Potential Enzyme Responsive Contrast Agents for Magnetic Resonance Imaging. *Chemistry-A European Journal* **2012,** 18, 1408-1418.

127. Tei, L.; Barge, A.; Galli, M.; Pinalli, R.; Lattuada, L.; Gianolio, E.; Aime, S., Polyhydroxylated GdDTPA-derivatives as high relaxivity magnetic resonance imaging contrast agents. *RSC Advances* **2015,** 5, 74734-74743.

128. Mi, P.; Cabral, H.; Kokuryo, D.; Rafi, M.; Terada, Y.; Aoki, I.; Saga, T.; Takehiko, I.; Nishiyama, N.; Kataoka, K., Gd-DTPA-loaded polymer–metal complex micelles with high relaxivity for MR cancer imaging. *Biomaterials* **2013,** 34, 492-500.

129. Weinmann, H.-J.; Ebert, W.; Misselwitz, B.; Schmitt-Willich, H., Tissue-specific MR contrast agents. *Eur. J. Radiol.* **2003,** 46, 33-44.

130. Gupta, R. T., Evaluation of the biliary tree and gallbladder with hepatocellular MR contrast agents. *Curr. Probl. Diagn. Radiol.* **2013,** 42, 67-76.

131. Skouras, A.; Mourtas, S.; Markoutsa, E.; De Goltstein, M.-C.; Wallon, C.; Catoen, S.; Antimisiaris, S. G., Magnetoliposomes with high USPIO entrapping efficiency, stability and magnetic properties. *Nanomed. Nanotechnol. Biol. Med.* **2011,** 7, 572-579.

132. Frascione, D.; Diwoky, C.; Almer, G.; Opriessnig, P.; Vonach, C.; Gradauer, K.; Leitinger, G.; Mangge, H.; Stollberger, R.; Prassl, R., Ultrasmall superparamagnetic iron oxide (USPIO)-based liposomes as magnetic resonance imaging probes. *Int. J. Nanomed.* **2012,** 7, 2349.

133. Agut, W.; Taton, D.; Brûlet, A.; Sandre, O.; Lecommandoux, S., Depletion induced vesicle-to-micelle transition from self-assembled rod–coil diblock copolymers with spherical magnetic nanoparticles. *Soft Matter* **2011,** 7, 9744-9750.

134. Shann, S. Y.; Lau, C. M.; Thomas, S. N.; Jerome, W. G.; Maron, D. J.; Dickerson, J. H.; Hubbell, J. A.; Giorgio, T. D., Size-and charge-dependent non-specific uptake of PEGylated nanoparticles by macrophages. *Int. J. Nanomed.* **2012,** 7, 799.

135. Oliveira, H.; Pérez-Andrés, E.; Thevenot, J.; Sandre, O.; Berra, E.; Lecommandoux, S., Magnetic field triggered drug release from polymersomes for cancer therapeutics. *J. Controlled Release* **2013,** 169, 165-170.

136. McCann, T. E.; Kosaka, N.; Turkbey, B.; Mitsunaga, M.; Choyke, P. L.; Kobayashi, H., Molecular imaging of tumor invasion and metastases: the role of MRI. *NMR Biomed.* **2011,** 24, 561-568.

137. Yoon, T. J.; Lee, H.; Shao, H.; Hilderbrand, S. A.; Weissleder, R., Multicore assemblies potentiate magnetic properties of biomagnetic nanoparticles. *Adv. Mater.* **2011,** 23, 4793-4797.

138. Kim, D.-H.; Zeng, H.; Ng, T. C.; Brazel, C. S., T 1 and T 2 relaxivities of succimer-coated MFe 2 3+ O 4 (M= Mn 2+, Fe 2+ and Co 2+) inverse spinel ferrites for potential use as phase-contrast agents in medical MRI. *J. Magn. Magn. Mater.* **2009,** 321, 3899-3904.

139. Sun, C.; Lee, J. S.; Zhang, M., Magnetic nanoparticles in MR imaging and drug delivery. *Adv. Drug Del. Rev.* **2008,** 60, 1252-1265.

140. Saini, S.; Frankel, R.; Stark, D.; Ferrucci Jr, J., Magnetism: a primer and review. *Am. J. Roentgenol.* **1988,** 150, 735-743.

141. Mikhaylova, M.; Kim, D. K.; Bobrysheva, N.; Osmolowsky, M.; Semenov, V.; Tsakalakos, T.; Muhammed, M., Superparamagnetism of magnetite nanoparticles: dependence on surface modification. *Langmuir* **2004,** 20, 2472-2477.

142. Na, H. B.; Song, I. C.; Hyeon, T., Inorganic nanoparticles for MRI contrast agents. *Adv. Mater.* **2009,** 21, 2133-2148.

143.   Mahmoudi, M.; Sant, S.; Wang, B.; Laurent, S.; Sen, T., Superparamagnetic iron oxide nanoparticles (SPIONs): Development, surface modification and applications in chemotherapy. *Adv. Drug Del. Rev.* **2011,** 63, 24-46.

144.   Talelli, M.; Rijcken, C. J. F.; Lammers, T.; Seevinck, P. R.; Storm, G.; van Nostrum, C. F.; Hennink, W. E., Superparamagnetic Iron Oxide Nanoparticles Encapsulated in Biodegradable Thermosensitive Polymeric Micelles: Toward a Targeted Nanomedicine Suitable for Image-Guided Drug Delivery. *Langmuir* **2009,** 25, 2060-2067.

145.   Zhao, Z.; Zhou, Z.; Bao, J.; Wang, Z.; Hu, J.; Chi, X.; Ni, K.; Wang, R.; Chen, X.; Chen, Z., Octapod iron oxide nanoparticles as high-performance T2 contrast agents for magnetic resonance imaging. *Nat. Commun.* **2013,** 4.

146.   Shubayev, V. I.; Pisanic Ii, T. R.; Jin, S., Magnetic nanoparticles for theragnostics. *Adv. Drug Del. Rev.* **2009,** 61, 467-477.

147.   Urbanova, V.; Magro, M.; Gedanken, A.; Baratella, D.; Vianello, F.; Zboril, R., Nanocrystalline Iron Oxides, Composites, and Related Materials as a Platform for Electrochemical, Magnetic, and Chemical Biosensors. *Chem. Mater.* **2014,** 26, 6653-6673.

148.   Tserotas, P.; Lazaridis, T.; Statharas, E., Controlled Synthesis of Composite Iron Oxide Nanoparticles. *Key Eng. Mater.* **2014,** 605, 689-692.

149.   Bhaskar, S.; Tian, F.; Stoeger, T.; Kreyling, W.; de la Fuente, J. M.; Grazú, V.; Borm, P.; Estrada, G.; Ntziachristos, V.; Razansky, D., Multifunctional Nanocarriers for diagnostics, drug delivery and targeted treatment across blood-brain barrier: perspectives on tracking and neuroimaging. *Part. Fibre Toxicol.* **2010,** 7, 3.

150. Wen, C.-J.; Zhang, L.-W.; Al-Suwayeh, S. A.; Yen, T.-C.; Fang, J.-Y., Theranostic liposomes loaded with quantum dots and apomorphine for brain targeting and bioimaging. *Int. J. Nanomed.* **2012,** 7, 1599.

151. Chertok, B.; Moffat, B. A.; David, A. E.; Yu, F.; Bergemann, C.; Ross, B. D.; Yang, V. C., Iron oxide nanoparticles as a drug delivery vehicle for MRI monitored magnetic targeting of brain tumors. *Biomaterials* **2008,** 29, 487-496.

152. Zhang, Z.; Larner, S. F.; Kobeissy, F.; Hayes, R. L.; Wang, K. K., Systems biology and theranostic approach to drug discovery and development to treat traumatic brain injury. In *Systems Biology in Drug Discovery and Development*, Springer: 2010; pp 317-329.

153. Agulla, J.; Brea, D.; Campos, F.; Sobrino, T.; Argibay, B.; Al-Soufi, W.; Blanco, M.; Castillo, J.; Ramos-Cabrer, P., In vivo theranostics at the peri-infarct region in cerebral ischemia. *Theranostics* **2014,** 4, 90.

154. Thakur, G.; Micic, M.; Yang, Y.; Li, W.; Movia, D.; Giordani, S.; Zhang, H.; Leblanc, R. M., Conjugated Quantum Dots Inhibit the Amyloid β (1–42) Fibrillation Process. *International Journal of Alzheimer's Disease* **2011,** 2011.

155. Skaat, H.; Shafir, G.; Margel, S., Acceleration and inhibition of amyloid-β fibril formation by peptide-conjugated fluorescent-maghemite nanoparticles. *J. Nanopart. Res.* **2011,** 13, 3521-3534.

156. Jellinger, K. A.; Janetzky, B.; Attems, J.; Kienzl, E., Biomarkers for early diagnosis of Alzheimer disease:'ALZheimer ASsociated gene'–a new blood biomarker? *J. Cell. Mol. Med.* **2008,** 12, 1094-1117.

157. Jendelová, P.; Herynek, V.; Urdzikova, L.; Glogarová, K.; Kroupová, J.; Andersson, B.; Bryja, V.; Burian, M.; Hájek, M.; Syková, E., Magnetic resonance tracking of

transplanted bone marrow and embryonic stem cells labeled by iron oxide nanoparticles in rat brain and spinal cord. *J. Neurosci. Res.* **2004,** 76, 232-243.

158.   Ruehm, S. G.; Corot, C.; Vogt, P.; Kolb, S.; Debatin, J. F., Magnetic resonance imaging of atherosclerotic plaque with ultrasmall superparamagnetic particles of iron oxide in hyperlipidemic rabbits. *Circulation* **2001,** 103, 415-422.

159.   Trivedi, R. A.; Mallawarachi, C.; Jean-Marie, U.; Graves, M. J.; Horsley, J.; Goddard, M. J.; Brown, A.; Wang, L.; Kirkpatrick, P. J.; Brown, J., Identifying inflamed carotid plaques using in vivo USPIO-enhanced MR imaging to label plaque macrophages. *Atertio. Thromb. Vasc. Biol.* **2006,** 26, 1601-1606.

160.   Kooi, M. E.; Cappendijk, V.; Cleutjens, K.; Kessels, A.; Kitslaar, P.; Borgers, M.; Frederik, P.; Daemen, M.; Van Engelshoven, J., Accumulation of ultrasmall superparamagnetic particles of iron oxide in human atherosclerotic plaques can be detected by in vivo magnetic resonance imaging. *Circulation* **2003,** 107, 2453-2458.

161.   Morris, J. B.; Olzinski, A. R.; Bernard, R. E.; Aravindhan, K.; Mirabile, R. C.; Boyce, R.; Willette, R. N.; Jucker, B. M., p38 MAPK Inhibition Reduces Aortic Ultrasmall Superparamagnetic Iron Oxide Uptake in a Mouse Model of Atherosclerosis MRI Assessment. *Atertio. Thromb. Vasc. Biol.* **2008,** 28, 265-271.

162.   Tang, T. Y.; Howarth, S. P.; Miller, S. R.; Graves, M. J.; Patterson, A. J.; Jean-Marie, U.; Li, Z. Y.; Walsh, S. R.; Brown, A. P.; Kirkpatrick, P. J., The ATHEROMA (Atorvastatin Therapy: Effects on Reduction of Macrophage Activity) Study: evaluation using ultrasmall superparamagnetic iron oxide-enhanced magnetic resonance imaging in carotid disease. *J. Am. Coll. Cardiol.* **2009,** 53, 2039-2050.

163.   Yokoi, H.; Nobuyoshi, M.; Mitsudo, K.; Kawaguchi, A.; Yamamoto, A., Three-year follow-up results of angiographic intervention trial using an HMG-CoA reductase inhibitor

to evaluate retardation of obstructive multiple atheroma (ATHEROMA) study. *Circ. J.* **2005,** 69, 875-883.

164.   Winter, P. M.; Caruthers, S. D.; Allen, J. S.; Cai, K.; Williams, T. A.; Lanza, G. M.; Wickline, S. A., Molecular imaging of angiogenic therapy in peripheral vascular disease with αvβ3-integrin-targeted nanoparticles. *Magn. Reson. Med.* **2010,** 64, 369-376.

165.   Jacoby, C.; Temme, S.; Mayenfels, F.; Benoit, N.; Krafft, M. P.; Schubert, R.; Schrader, J.; Flögel, U., Probing different perfluorocarbons for in vivo inflammation imaging by 19F MRI: image reconstruction, biological half-lives and sensitivity. *NMR Biomed.* **2014,** 27, 261-271.

166.   Ong, A. T.; McFadden, E. P.; Regar, E.; de Jaegere, P. P.; van Domburg, R. T.; Serruys, P. W., Late angiographic stent thrombosis (LAST) events with drug-eluting stents. *J. Am. Coll. Cardiol.* **2005,** 45, 2088-2092.

167.   Cook, S.; Wenaweser, P.; Togni, M.; Billinger, M.; Morger, C.; Seiler, C.; Vogel, R.; Hess, O.; Meier, B.; Windecker, S., Incomplete stent apposition and very late stent thrombosis after drug-eluting stent implantation. *Circulation* **2007,** 115, 2426-2434.

168.   Joner, M.; Finn, A. V.; Farb, A.; Mont, E. K.; Kolodgie, F. D.; Ladich, E.; Kutys, R.; Skorija, K.; Gold, H. K.; Virmani, R., Pathology of drug-eluting stents in humans: delayed healing and late thrombotic risk. *J. Am. Coll. Cardiol.* **2006,** 48, 193-202.

169.   Cyrus, T.; Zhang, H.; Allen, J. S.; Williams, T. A.; Hu, G.; Caruthers, S. D.; Wickline, S. A.; Lanza, G. M., Intramural delivery of rapamycin with αvβ3-targeted paramagnetic nanoparticles inhibits stenosis after balloon injury. *Atertio. Thromb. Vasc. Biol.* **2008,** 28, 820-826.

170. Myerson, J.; He, L.; Lanza, G.; Tollefsen, D.; Wickline, S., Thrombin-inhibiting perfluorocarbon nanoparticles provide a novel strategy for the treatment and magnetic resonance imaging of acute thrombosis. *J. Thromb. Haemost.* **2011,** 9, 1292-1300.

171. Chorny, M.; Fishbein, I.; Yellen, B. B.; Alferiev, I. S.; Bakay, M.; Ganta, S.; Adamo, R.; Amiji, M.; Friedman, G.; Levy, R. J., Targeting stents with local delivery of paclitaxel-loaded magnetic nanoparticles using uniform fields. *Proc. Natl. Acad. Sci. U. S. A.* **2010,** 107, 8346-8351.

172. Takahama, H.; Minamino, T.; Asanuma, H.; Fujita, M.; Asai, T.; Wakeno, M.; Sasaki, H.; Kikuchi, H.; Hashimoto, K.; Oku, N., Prolonged targeting of ischemic/reperfused myocardium by liposomal adenosine augments cardioprotection in rats. *J. Am. Coll. Cardiol.* **2009,** 53, 709-717.

173. Lanza, G. M.; Yu, X.; Winter, P. M.; Abendschein, D. R.; Karukstis, K. K.; Scott, M. J.; Chinen, L. K.; Fuhrhop, R. W.; Scherrer, D. E.; Wickline, S. A., Targeted antiproliferative drug delivery to vascular smooth muscle cells with a magnetic resonance imaging nanoparticle contrast agent implications for rational therapy of restenosis. *Circulation* **2002,** 106, 2842-2847.

174. Winter, P. M.; Neubauer, A. M.; Caruthers, S. D.; Harris, T. D.; Robertson, J. D.; Williams, T. A.; Schmieder, A. H.; Hu, G.; Allen, J. S.; Lacy, E. K.; Zhang, H.; Wickline, S. A.; Lanza, G. M., Endothelial αvβ3 Integrin–Targeted Fumagillin Nanoparticles Inhibit Angiogenesis in Atherosclerosis. *Atertio. Thromb. Vasc. Biol.* **2006,** 26, 2103-2109.

175. Lobatto, M. E.; Fayad, Z. A.; Silvera, S.; Vucic, E.; Calcagno, C.; Mani, V.; Dickson, S. D.; Nicolay, K.; Banciu, M.; Schiffelers, R. M.; Metselaar, J. M.; van Bloois, L.; Wu, H.-S.; Fallon, J. T.; Rudd, J. H.; Fuster, V.; Fisher, E. A.; Storm, G.; Mulder, W. J. M.,

Multimodal clinical imaging to longitudinally assess a nanomedical anti-inflammatory treatment in experimental atherosclerosis. *Mol. Pharm.* **2010,** 7, 2020-2029.

176.   McCarthy, J. R.; Korngold, E.; Weissleder, R.; Jaffer, F. A., A Light-activated Theranostic Nanoagent for Targeted Macrophage Ablation in Inflammatory Atherosclerosis. *Small (Weinheim an der Bergstrasse, Germany)* **2010,** 6, 2041-2049.

177.   Siegel, R.; Ma, J.; Zou, Z.; Jemal, A., Cancer statistics, 2014. *CA Cancer J. Clin.* **2014,** 64, 9-29.

178.   Shirley, M.; McCormack, P. L., Radium-223 dichloride: a review of its use in patients with castration-resistant prostate cancer with symptomatic bone metastases. *Drugs* **2014,** 74, 579-586.

179.   Zhang, L.; Gao, S.; Zhang, F.; Yang, K.; Ma, Q.; Zhu, L., Activatable hyaluronic Acid nanoparticle as a theranostic agent for optical/photoacoustic image-guided photothermal therapy. *ACS Nano* **2014,** 8, 12250-12258.

180.   Ibsen, S.; Schutt, C. E.; Esener, S., Microbubble-mediated ultrasound therapy: a review of its potential in cancer treatment. *Drug Des. Devel. Ther.* **2013,** 7, 375.

181.   Carson, A. R.; McTiernan, C. F.; Lavery, L.; Grata, M.; Leng, X.; Wang, J.; Chen, X.; Villanueva, F. S., Ultrasound-targeted microbubble destruction to deliver siRNA cancer therapy. *Cancer Res.* **2012,** 72, 6191-6199.

182.   Yan, F.; Li, L.; Deng, Z.; Jin, Q.; Chen, J.; Yang, W.; Yeh, C.-K.; Wu, J.; Shandas, R.; Liu, X., Paclitaxel-liposome–microbubble complexes as ultrasound-triggered therapeutic drug delivery carriers. *J. Controlled Release* **2013,** 166, 246-255.

183.   Shi, J.; Liu, T. W.; Chen, J.; Green, D.; Jaffray, D.; Wilson, B. C.; Wang, F.; Zheng, G., Transforming a targeted porphyrin theranostic agent into a PET imaging probe for cancer. *Theranostics* **2011,** 1, 363.

184.   Jordan, A.; Scholz, R.; Wust, P.; Fähling, H.; Felix, R., Magnetic fluid hyperthermia (MFH): Cancer treatment with AC magnetic field induced excitation of biocompatible superparamagnetic nanoparticles. *J. Magn. Magn. Mater.* **1999,** 201, 413-419.

185.   Prasad, N.; Rathinasamy, K.; Panda, D.; Bahadur, D., Mechanism of cell death induced by magnetic hyperthermia with nanoparticles of γ-Mn x Fe 2–x O 3 synthesized by a single step process. *J. Mater. Chem.* **2007,** 17, 5042-5051.

186.   Maier-Hauff, K.; Ulrich, F.; Nestler, D.; Niehoff, H.; Wust, P.; Thiesen, B.; Orawa, H.; Budach, V.; Jordan, A., Efficacy and safety of intratumoral thermotherapy using magnetic iron-oxide nanoparticles combined with external beam radiotherapy on patients with recurrent glioblastoma multiforme. *J. Neurooncol.* **2011,** 103, 317-324.

187.   Johannsen, M.; Gneveckow, U.; Thiesen, B.; Taymoorian, K.; Cho, C. H.; Waldöfner, N.; Scholz, R.; Jordan, A.; Loening, S. A.; Wust, P., Thermotherapy of Prostate Cancer Using Magnetic Nanoparticles: Feasibility, Imaging, and Three-Dimensional Temperature Distribution. *Eur. Urol.* **2007,** 52, 1653-1662.

188.   Jordan, A.; Wust, P.; Fähling, H.; John, W.; Hinz, A.; Felix, R., Inductive heating of ferrimagnetic particles and magnetic fluids: physical evaluation of their potential for hyperthermia. *Int. J. Hyperthermia* **2009,** 25, 499-511.

189.   Alexiou, C.; Arnold, W.; Klein, R. J.; Parak, F. G.; Hulin, P.; Bergemann, C.; Erhardt, W.; Wagenpfeil, S.; Luebbe, A. S., Locoregional cancer treatment with magnetic drug targeting. *Cancer Res.* **2000,** 60, 6641-6648.

190.   Gupta, A. K.; Gupta, M., Synthesis and surface engineering of iron oxide nanoparticles for biomedical applications. *Biomaterials* **2005,** 26, 3995-4021.

191.   Yan, S.; Zhang, D.; Gu, N.; Zheng, J.; Ding, A.; Wang, Z.; Xing, B.; Ma, M.; Zhang, Y., Therapeutic effect of Fe2O3 nanoparticles combined with magnetic fluid hyperthermia

on cultured liver cancer cells and xenograft liver cancers. *J. Nanosci. Nanotechnol.* **2005,** 5, 1185-1192.

192.   Verma, M., Personalized medicine and cancer. *Journal of personalized medicine* **2012,** 2, 1-14.

193.   Chin, L.; Andersen, J. N.; Futreal, P. A., Cancer genomics: from discovery science to personalized medicine. *Nat. Med.* **2011,** 17, 297-303.

194.   Nguyen, P. L.; Taghian, A. G.; Katz, M. S.; Niemierko, A.; Raad, R. F. A.; Boon, W. L.; Bellon, J. R.; Wong, J. S.; Smith, B. L.; Harris, J. R., Breast cancer subtype approximated by estrogen receptor, progesterone receptor, and HER-2 is associated with local and distant recurrence after breast-conserving therapy. *J. Clin. Oncol.* **2008,** 26, 2373-2378.

195.   Mass, R. D., The HER receptor family: a rich target for therapeutic development. *International Journal of Radiation Oncology*Biology*Physics* **2004,** 58, 932-940.

196.   Schleich, N.; Po, C.; Jacobs, D.; Ucakar, B.; Gallez, B.; Danhier, F.; Préat, V., Comparison of active, passive and magnetic targeting to tumors of multifunctional paclitaxel/SPIO-loaded nanoparticles for tumor imaging and therapy. *J. Controlled Release* **2014,** 194, 82-91.

197.   Purushotham, S.; Ramanujan, R., Thermoresponsive magnetic composite nanomaterials for multimodal cancer therapy. *Acta Biomater.* **2010,** 6, 502-510.

198.   Clares, B.; Biedma-Ortiz, R. A.; Sáez-Fernández, E.; Prados, J. C.; Melguizo, C.; Cabeza, L.; Ortiz, R.; Arias, J. L., Nano-engineering of 5-fluorouracil-loaded magnetoliposomes for combined hyperthermia and chemotherapy against colon cancer. *Eur. J. Pharm. Biopharm.* **2013,** 85, 329-338.

199.   Luo, Z.; Cai, K.; Hu, Y.; Li, J.; Ding, X.; Zhang, B.; Xu, D.; Yang, W.; Liu, P., Redox-Responsive Molecular Nanoreservoirs for Controlled Intracellular Anticancer Drug Delivery Based on Magnetic Nanoparticles. *Adv. Mater.* **2012,** 24, 431-435.

200.   Li, Z.; Liu, S.; Wang, S.; Qiang, L.; Yang, T.; Wang, H.; Möhwald, H.; Cui, X., Synthesis of folic acid functionalized redox-responsive magnetic proteinous microcapsules for targeted drug delivery. *J. Colloid Interface Sci.* **2015,** 450, 325-331.

201.   Sahoo, B.; Devi, K. S. P.; Banerjee, R.; Maiti, T. K.; Pramanik, P.; Dhara, D., Thermal and pH responsive polymer-tethered multifunctional magnetic nanoparticles for targeted delivery of anticancer drug. *ACS applied materials & interfaces* **2013,** 5, 3884-3893.

202.   Thomas, C. R.; Ferris, D. P.; Lee, J.-H.; Choi, E.; Cho, M. H.; Kim, E. S.; Stoddart, J. F.; Shin, J.-S.; Cheon, J.; Zink, J. I., Noninvasive remote-controlled release of drug molecules in vitro using magnetic actuation of mechanized nanoparticles. *J. Am. Chem. Soc.* **2010,** 132, 10623-10625.

CHAPTER 2

LHRHR-TARGETED MAGNETIC NANOCLUSTERS STABILIZED BY BIS-PHOSPHONATE-MODIFIED POLY (GLUTAMIC ACID)-B-POLY (ETHYLENE GLYCOL) FOR OVARIAN CANCER THERANOSTICS

2.1. INTRODUCTION

Recent advances in nanomedicine have shown the capability to realize the long-desired spatio-temporal delivery of drugs, genes and imaging agents. Enhancement in material sciences has enabled the design of nano-carriers capable of releasing their payload in response to specific biological stimuli such as pH[1-3], temperature[4-6], redox potential[7-9] etc. Over the last two decades, superparamagnetic iron oxide nanoparticles (MNPs) have been studied comprehensively and used in a wide variety of fields ranging from high capacity data storage and water purification[10] to numerous biomedical applications such as protein and antibody detection[11-13], protein[14] bacteria[15] and toxin[16] separation and most importantly as magnetic resonance imaging (MRI) contrast agents[15]. The ability of MNPs to interact with protons of water molecule and shorten their transverse (T_2) relaxation times produces dark T_2-weighted negative contrasts in the accumulating tissues. The MRI capacity of MNPs had been applied clinically for diagnosis of several diseases. MNP formulations have been designed and used clinically as blood pool agents in magnetic resonance angiography (MRA)[17, 18] for imaging of the aortoiliac region and coronary arteries.[19]

The first-generation commercial MNP-based MRI contrast agents such as Feridex® showed a higher propensity for aggregation *in vivo* and rapid systemic clearance.[20, 21].Rapid clearance necessitates an increased dose to achieve the desired contrast, which in turn induces toxicity. All these factors seem to have led to the withdrawal of Feridex®[22] in the United States. To be clinically relevant, negative contrast agents depend on higher transverse (T_2) relaxivity. Transverse relaxivity is governed by several factors such as MNP core size, chemical nature, oxidation state, applied magnetic field, site-specific uptake and proximity of the metal ions to the water. A formulation that enables deeper penetration of the water molecules towards the magnetic core allows for faster relaxation of the protons and a higher T_2-relaxivity. Clusters of magnetic nanoparticles experience a greater force than single, well separated MNPs in a magnetic field gradient.[23] Several successful attempts have been made to functionalize MNPs with therapeutic agents for specific disease. Such 'theranostic' systems, as they are termed, present a desirable improvement in cancer chemotherapy due to their ability to target the tumor and simultaneously allow noninvasive visualization and treatment[24] [25]. Development of a MNP-based theranostic nanosystem is an intricate task as it requires correct balance of the diagnostic and therapeutic components. For example, biodegradable polymersomes loaded with MNPs and doxorubicin exhibited magnetic field-responsive drug release along with excellent MRI contrast.[26].Similarly MNP clusters stabilized by Pluronic® F127 and loaded with doxorubicin have been shown to exhibit a sustained drug release *in vivo* while simultaneously enabling MR imaging of the target tumor tissue.[27] However, formulation-related issues such as colloidal stability and toxicity still hinder the clinical development of such MNP-based 'theranostic' systems.

Selection of an appropriate polymer for coating is critical to ensure colloidal stability, long circulation times of the MNCs and to allow effective drug loading. The need for

biocompatibility and biodegradability of the polymer further limits the choices. Block ionomers comprising of biodegradable charged poly (amino acid) chains can serve as ideal stabilizing agents for formation of MNCs. Each year there are about 22,000 new cases and over 14,000 deaths annually due to ovarian cancer in the US.[28] In spite of the dose limiting nephrotoxicity and other severe side effects,[29] cisplatin still remains the first line of treatment for ovarian cancer. To address the severe toxicity, several successful attempts have been made at loading cisplatin into nanoparticles and targeting it exclusively to the malignancy via several targeting ligands. For instance, previously, cisplatin was incorporated within folate-receptor targeted nanogels to successfully treat folate-receptor-positive ovarian cancer xenografts in mice.[30] The membrane receptor for Luteinizing hormone releasing hormone (LHRHr) is overexpressed in more than 70% human ovarian cancers[31-33]. Luteinizing hormone releasing hormone peptide (LHRH), a synthetic analogue of the nautral hormone has been used to successfully target chemotherapeutic agents to LHRHr overexpressed on the tumor tissue.[34, 35] LHRH-targeted nanogels conjugated with cisplatin were used to enhance the *in vivo* cytotoxic efficacy in treatment of LHRHr-positive ovarian cancer xenografts in mice.[36] In a separate study MNPs were conjugated directly with LHRH-peptide in order to improve the uptake in LHRH overexpressing breast cancer cells.[37]

Herein we report a simple process for formulation of theranostic MNCs for anti-cancer therapy and simultaneous MR imaging. The MNCs were prepared by stabilization with anionic bisphosphonate-modified poly (glutamic acid)-*b*-(ethylene glycol) (PLE-*b*-PEG) by an entirely hydrophilic route. The MNCs were loaded with cisplatin though electrostatic interactions and LHRH was conjugated to the MNCs surface as targeting moiety. Stable cisplatin-MNC conjugates (PtMNCs) exhibited selective uptake, cytotoxic efficacy comparable to free cisplatin and significantly higher T_2 relaxivity than Feridex® in LHRHr

overexpressing A2780-wild type (A2780-WT) and cisplatin-resistant (A2780-CisR) ovarian cancer cells. The LHRHr targeted MNCs is an effective T_2 contrast agent for simultaneous chemotherapeutic efficacy in LHRHr-positive tumors.

2.2. EXPERIMENTAL SECTION

2.2.1. MATERIALS

Chemicals: Poly (glutamic acid)-b-poly (ethylene glycol) block copolymers with different poly (glutamic acid) [38] block lengths namely PLE_{10}-*b*-PEG_{113}, PLE_{50}-b-PEG_{113}, PLE_{100}-b-PEG_{113} and poly (aspartic acid)$_{100}$-b-PEG_{113} (PLD_{100}-b-PEG_{113}) and the respective homopolymers were purchased from Alamanda Polymers (Huntsville, AL). Here and below the numbers in subscripts after the copolymer blocks define the number of the repeating units (r.u.) in the respective block. The free end of PEG contained methoxy groups. Alendronate sodium trihydrate was purchased from Ultratech (Navi Mumbai, India). 1-Ethyl-3-(3-dimethylaminopropyl)-carbodiimide (EDC), N-hydroxysuccinimide (NHS), iron (III) acetylacetonate ($Fe(acac)_3$), benzyl alcohol (anhydrous), nitric acid (TraceSELECT), hydrochloric acid (TraceSELECT), ICP grade standards for Fe, Pt and P (Fluka) and 3-(4,5-dimethylthiazol -2-yl)-2,5-diphenyl tetrazolium bromide (MTT) were purchased from Sigma-Aldrich (St. Louis, MO). Acetone (histology grade), n,n-dimethylformamide (DMF), cisplatin, Pyridine, DMSO and all other anhydrous HPLC grade organic solvents were purchased from Thermo Fisher Scientific (Waltham, MA). N-hydroxysulfosuccinimide (S-NHS) was purchased from Covachem (Loves Park, IL). D-Lys-6-LHRH (Glp−His−Trp−Ser−Tyr−DLys−Leu−Arg−Pro−Gly) peptide was purchased from American Peptide Company (Sunnyvale, CA). Alexa Fluor®-647, Lysotracker Green and Hoechst 33342 were purchased from Life Technologies (Carlsbad, CA).

Cell lines: A2780 wild-type human ovarian cancer cells were purchased from American Type culture collection (ATCC, Manassas, VA). Cisplatin-resistant A2780 human ovarian cancer cells were derived from the wild-type cells by repeated exposure to sub therapeutic concentrations of cisplatin over a prolonged period.

2.2.2. METHODS

2.2.2.1. One-pot Synthesis of Magnetite Nanoparticles

Magnetite nanoparticles (MNPs) were synthesized by thermal decomposition of iron (III) acetylacetonate (Fe (acac)$_3$) in benzyl alcohol with minor modifications to the method developed by Pinna et.al.[39] Briefly, 6.2 µmoles of Fe (acac)$_3$ was charged to a three-necked flask containing 45mL anhydrous benzyl alcohol. The reaction mixture was heated at 110°C for 1h to ensure complete evaporation of water. The size of the MNPs was tuned by subsequently varying the heating rates of the reaction. Four different heating profiles were employed as described below and depicted in Figure 1.

Profile A: The reaction mixture was heated gradually at 0.4°C/min to 205°C. Once at reflux the temperature was kept constant for 40h.

Profile B: The mixture was heated to 150°C at 4°C/min and kept isothermal at 150°C for 2h following which the temperature was raised to reflux at 4°C/min and heated for 40h at reflux.

Profile C: The reaction mixture was heated to 180°C at 4°C/min and kept isothermal at 180°C for 2h after which the temperature was raised to reflux at 4°C/min and heated for 40h at reflux.

Profile D: The reaction mixture was heated quickly at 5°C/min to reflux and heated at reflux for 40h.

All the reactions were conducted under inert atmosphere. After cooling, the nanoparticles were precipitated and washed in acetone. The final product was collected by magnetic separation, dried under vacuum and stored for further use under vacuum in a sealed vial filled with argon. The benzyl alcohol content in the final product was estimated by thermogravimetry (TGA; TGA Q50, TA Instruments, DE). Briefly, 20 mg sample was heated at 5°C/min to 1000°C. Benzyl alcohol content was obtained by subtracting the weight of the residue from the initial weight of the sample. The saturation magnetization (M; emu/g) of the smallest and the largest particles obtained was determined by SQUID-VSM (Quantum Design Co.) at 300 K.

2.2.2.2. Alendronate Conjugation to PLE$_{50}$-*b*-PEG$_{113}$

Prior to ALN conjugation, PLE$_{50}$-*b*-PEG$_{113}$ sodium salt was de-protected by dissolving in de-ionized water and acidified by slow addition of 0.1N HCl to restore the carboxylic acid functionality. The precipitate was dialyzed overnight against de-ionized water and lyophilized to obtain the de-protected polymer. For the conjugation reaction, 5µmoles of the de-protected polymer was dissolved in 3mL DMSO. In a separate vial, 0.16 mmoles EDC and 0.8 mmoles NHS were dissolved in 0.5mL DMSO and added to the polymer solution. The reaction mixture was stirred for 4h at RT. 0.44 mmoles ALN.Na was dissolved in 4mL de-ionized water followed by adjustment of the pH to 9.5 by addition of NaOH. The EDC-NHS-activated PLE$_{50}$-*b*-PEG$_{113}$ in DMSO was added dropwise to the aqueous solution of ALN and the reaction was stirred for 48h. The unconjugated ALN as well as the reaction by-products were removed by centrifugal filtration through 3000 MWCO PES centrifugal membrane filters (Sartorius, NY) and the resultant ALN-conjugated PLE$_{50}$-*b*-PEG$_{113}$ was lyophilized. The ALN conjugation was confirmed qualitatively by ^{31}P-NMR. The degree of conjugation (D$_{conj}$) was quantified from ^{1}H-NMR of the final ALN-conjugated polymer by comparing the integrals of the multiplet of the

conjugated ALN at 3.0 – 3.22 ppm with the broad singlet of the H-atom on the chiral carbon of PLE block at 4.0 – 4.34 ppm (Figure 2.5) and by inductively coupled plasma mass spectrometry (ICP-MS).[40] Briefly, a standard curve was prepared from commercial standard solution of phosphorus (Fluka) in the 50 – 500 ppb concentration range. The lyophilized polymer was dispersed in 1 ml of DI water at a concentration of 1mg/mL. 50 µL concentrated HCl (TraceSELECT) was added to it and the mixture was incubated at 70°C for 12h. The sample was allowed to cool to room temperature (RT) after which the volume was adjusted to 2mL with DI water. The final solution was filtered through 0.2µm nylon syringe filter and analyzed by ICP-MS to quantify the bisphosphonate end groups in the polymer using argon and oxygen carrier gases.

2.2.2.3. Preparation of Polymer-Stabilized MNCs

a. **30-40nm MNCs**: Briefly, the polymer was dissolved in 10 mL alkaline water (pH 9-9.5) and added to a 10 mL MNP dispersion in alkaline water (pH 12) in a 2:1 (w/w) ratio.

b. **65-85nm MNCs:** Larger sized MNCs were obtained by dissolving the polymer and MNCs in 5mL of respective solvents.

The mixture was then stirred for 12-15h followed by extensive dialysis for 72h, with six water changes. To obtain the final product, the dialyzed mixture was further purified by filtration through 0.45 and 0.22 µm Whatman Anotop syringe filters, lyophilized to dryness and stored under vacuum in a sealed vial filled with argon for further studies.

2.2.2.4. Preparation of Cisplatin-Loaded MNCs

Cisplatin was loaded by electrostatic interactions onto the free carboxyl groups of the PLE block of the MNCs. Briefly, prior to loading the number of moles of carboxyl groups available were quantified by potentiometric titration. The MNCs were dispersed in deionized water at 5-10mg/mL. The pH of the colloidal dispersion was adjusted to 9.5 with

NaOH. Cisplatin (equivalent to 50 or 75 mol% of the available carboxyl groups in the formulation) was dissolved in n,n-dimethylformamide (DMF) and added under stirring to the colloidal MNCs. The solution was stirred for 48h in the dark. The unconjugated cisplatin was separated by centrifugal filtration (2000-MWCO, Sartorius, location USA) and the final product was lyophilized and stored in vacuum at -20°C for further use.

2.2.2.5 Preparation of LHRH-conjugated MNCs

DLys6-LHRH was conjugated to the free carboxylic groups on MNCs by EDC/sulfo-NHS coupling reaction via the D-lysine group on the peptide. Briefly, 10mg lyophilized MNC or PtMNC formulations were dispersed in MES buffer (pH 6; 0.05M) at a concentration of 20 µg/mL. EDC/sulfo NHS (3 equiv/6 equiv) at RT was used to activate 5 mol% of the total available carboxylic groups (concentration of carboxylic groups was calculated by potentiometric titrations) for 2h. The excess of the unreacted chemicals was neutralized by 2-mercaptoethanol (20mM). (D-Lys6)-LHRH was dissolved in PBS (20mM, pH 7.4) at a concentration of 10mg/mL. 0.4mL of this solution was mixed with the activated MNC and PtMNC formulations. pH of the mixture was adjusted to 7.4 and the solutions were stirred for 7h at RT. The dispersions were purified by centrifugal filtration (3000 MWCO; 3 washes) to remove the unreacted peptide and other reactants. The final formulations were lyophilized and stored under vacuum at -20°C for further use.

2.2.2.6. Physiochemical Characterization of MNCS

a. Dynamic light scattering (DLS)**.** The z-average hydrodynamic diameter (D_{eff}), polydispersity index (PDI) and **ζ**-potential was determined by DLS using a Malvern Zetasizer (Malvern Instruments, MA, and USA). The concentration of the dispersed phase was 1 mg/mL

b. MNC composition. The composition of the unloaded MNCs was determined by

thermogravimetric analysis (TGA). Briefly, 5-10mg of the lyophilized unloaded-formulation was placed on the tared TGA pan. The formulation was dried in the furnace at 110°C in order to remove the moisture followed by steady heating at 5°C/min to 1000°C. The obtained thermogram was analyzed using the Universal Analysis software (TA Instruments, DE) to deduce the total loss of the organic components [41] and amount of MNPs per mg of MNCs. The content of benzyl alcohol coating was determined by loss of organic components upon thermal decomposition of MNPs by TGA. The LOI of MNCs was corrected by subtracting the content of benzyl alcohol in the MNPs to obtain the content of polymer in the MNCs.

c. Relaxation measurements: A Bruker Biospec MRI and spectroscopy (MS) system (7T/21 cm, Bruker, Karlshure, Germany) was used to determine the longitudinal (r_1) and transverse (r_2) relaxivities of the different MNC formulations. The sequence used for T_2 mapping was a CPMG phase cycled single slice multiecho sequence. One 1 mm thick coronal image was acquired with an acquisition matrix of 256 x 128, 40 mm field of view, 32 echoes at 10 ms first echo time and 10 ms echo spacing, repetition time of 3000 ms, one average, for a total acquisition time of 6.4 min. The stabilized colloidal particle dispersions were diluted to 0, 0.018, 0.045, 0.09, 0.18, 0.27 and 0.36 mM Fe with distilled water and 20mM PBS. T_1 and T_2 relaxation times were measured and converted to their corresponding relaxation rates (R_1 and R_2; 1/T; s^{-1}). The r_1 (longitudinal relaxivity) and r_2 (transverse relaxivity) values ($s^{-1}.mM^{-1}$) were obtained as the slope of the plots of R_1 or R_2 versus the corresponding Fe concentrations.

2.2.2.7. Determination of Drug Release from Cisplatin-Loaded MNCS

The drug release of the anionic formulations was studied in pH 7.4 phosphate buffered saline (PBS; 20mM) and pH 5.5 sodium acetate buffered saline (50mM). Briefly, formulation equivalent to 25μg of cisplatin was placed in Float-a-lyzer© dialysis membrane

tubes (3.5 – 5KDa MWCO; 1ml capacity; Spectrum Labs, USA). The volume in the tube membrane was adjusted to 1mL and the assembly was placed in a 24ml dissolution medium and stirred at approximately 125 rpm for five days. At specific time points during the study, 0.5ml aliquots were removed from the dissolution medium outside the dialysis membrane and replaced with same volume of fresh buffer. The cumulative release of cisplatin was quantified by ICP-MS and plotted against time.

2.2.2.8. Cellular Uptake of MNCS

a. Quantitative determination by ICPMS: A2780-WT and A2780-CisR cells (10^6 cells/ well) were treated with a 2ml colloidal dispersion of the different formulations (equivalent to Fe concentration of 5µg/ml) and incubated for 24h. At various time points during the incubation period the medium was removed from the wells and the cells were washed three times with ice-cold PBS and acid saline (pH 3). The cells were harvested and the viability was determined by trypan blue assay and centrifuged to form a pellet. The supernatant was removed completely and 0.5ml of a100ppb solution of Iridium in 2% HNO_3 was added to the pellets. The cells were then lysed mechanically by probe-sonication. 50µl concentrated nitric acid (TraCERT; Fluka) was added to the lysate, which was then digested overnight at 70°C. The digested samples were then appropriately diluted to 5ml with 2% HNO_3. The cell debris was separated by ultra-centrifugation at 10000rpm for 30 mins. The supernatant was further filtered through 0.2um syringe filters and analyzed by Nexion 300-D ICP-MS equipped with collision cell and auto sampler (Perkin Elmer, USA). The intensities of the ^{57}Fe and ^{195}Pt isotopes were considered for quantification of the uptake. The final Fe or Pt content was normalized to the total protein content of the cells (as determined by standard BCA assay) and uptake was expressed as µg per mg of total cellular protein.

b. Confocal microscopy: Simultaneously, live-cell confocal microscopy was performed

to study the cellular localization pattern of the different fluorescent-labeled MNCs. A2780-WT and A2780-CisR cells were incubated with Alexa Fluor®-647 labeled MNCs for 1, 3 and 24h followed by visualization under a LSM 710 (Zeiss, CA) confocal microscope equipped with a live-cell imaging stage.

2.2.2.9. *In Vitro* Cytotoxicity of PtMNCs

The cytotoxic potential of the cisplatin-conjugated PtMNCs was estimated *in vitro* in A2780-WT and A2780-CisR human ovarian carcinoma cell lines. Briefly, the cells were cultured in complete RPMI 1640 medium in conditions mentioned previously. Twenty four hours after seeding about 3000 cells per well in 96-well plates, the cells were treated with either free drug cisplatin, blank MNCs or PtMNCs (+/- LHRH) at different concentrations. The cells were then incubated for 24 and 72h. At the end of each time point the culture medium was replaced with complete RPMI and the cells were further incubated for 12h. Finally, the cell viability was estimated by standard MTT assay. Briefly, 0.02mL of a 5mg/mL solution of MTT in PBS was added to each well and the plates were incubated for 4h. The plates were then centrifuged and the supernatant was removed. The resulting formazan crystals were dissolved in DMSO and the color intensity was measured at 560nm using Spectramax M3 plate reader. The cell viability was determined by comparing the different treatment groups with the control (untreated) wells.

2.2.2.10. *In Vitro* Determination of MR Potential

Approximately 10 million A2780-WT and A2780-CisR cells were incubated with LHRH-conjugated and unconjugated particles at Fe concentrations of 0.045, 0.09 and 0.18 mM for a period of 24h. Following incubation, the cells were collected and cell viability was determined by trypan blue assay. 9 million viable cells were re-dispersed in 0.5mL PBS and mixed carefully with equal volume of hot 4% w/v agar solution. The samples were cooled at 4°C for to allow the formation of a solid matrix. As a control 9 million un-treated

cells were used. Phantom gels were scanned in Siemens Magnetom TIM Trio 3T human MR scanner. Images of the phantom gels were obtained by using a multigradient echo pulse sequence at a 1.64ms/3000ms TE/ TR and 40° flip angle for T_1 and 112.5ms/ 3000ms TE/TR for T_2. The cellular phantoms were compared with phantoms of similar concentrations of formulations without any cells.

2.2.3. STATISTICAL ANALYSIS

Statistical analysis was performed using IBM SPSS 23 statistical software. Experimental designs with two groups were analyzed by student's t-tests. Designs with more than two groups were analyzed by appropriate ANOVA test followed by Bonferroni post-hoc test for multiple comparisons using IBM SPSS 23.

2.3. RESULTS

2.3.1. SYNTHESIS AND CHARACTERIZATION OF MAGNETITE NANOPARTICLES (MNPS)
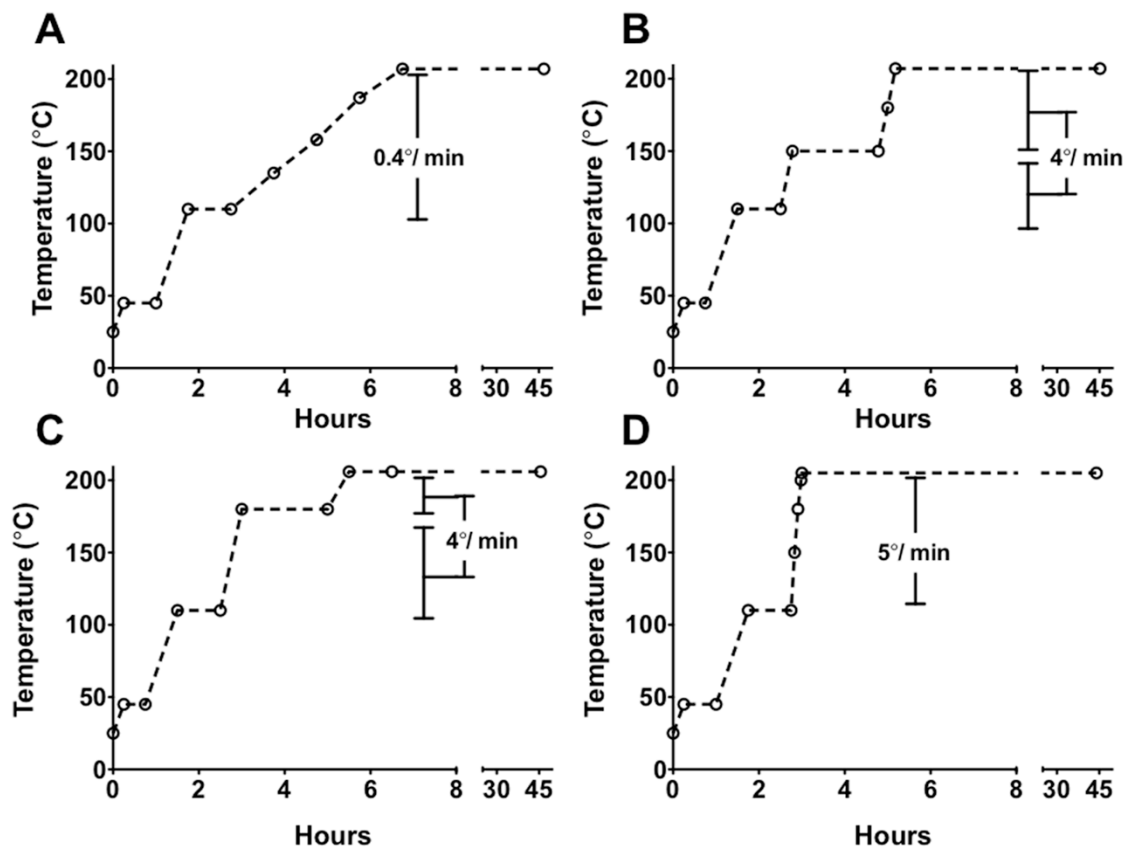
Figure 2.1. Various heating regimes during the synthesis of MNPs by thermal decomposition of $Fe(acac)_3$

At the onset of this work we concluded that it was important to control and fine-tune the sizes of the MNPs as these sizes could affect the properties of the resulting MNCs. In the modified one-pot solvent-controlled synthesis of magnetite nanocrystals[39, 42] benzyl alcohol acts as a solvent and reducing agent as well as a ligand or a mild surfactant. In this process the colloidal metal oxide nanocrystal nuclei of MNPs grow by consuming the

surrounding Fe(acac)$_3$ precursor while Ostwald's ripening or oriented attachment mechanisms are not observed.[43, 44]
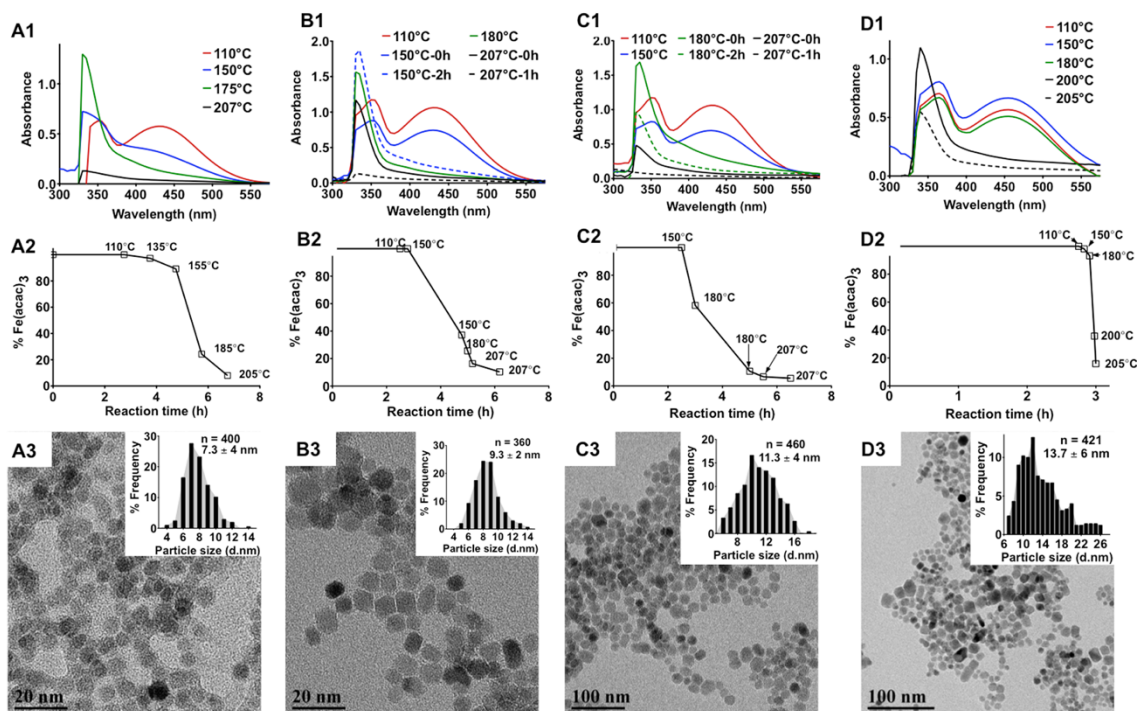
Figure 2.2. Effect of the heating patterns on the diameter of magnetite nanoparticles (MNPs). **A1-D1**: UV-absorption spectra of the reaction mixtures under different heating patterns as depicted in **Figure 2.1**. Aliquots of the reaction mixture were collected at specific time intervals, precipitated in acetone, centrifuged to separate any formed MNPs and absorbance spectrum of the supernatant was measured to determine the nucleation and growth phases during the synthesis of MNPs. The solid lines correspond to measurement taken at the start of the incubation periods where the reaction mixture was kept isothermal for two hours. The dashed lines are spectra taken 2 h after incubation of the system at a given temperature except for D1 where the spectra were taken at the start of reflux. **A2-D2**: Amount of unreacted Fe(acac)$_3$ in the reaction mixture at the corresponding temperatures during the ramp phase of the heating process as measured by ICPMS. **A3-D3**: TEM images of the MNPs synthesized by different heating patterns. Particle size distributions are shown in the respective insets. Diameters of the MNPs were calculated from the TEM images using Image J software**.**

Notably, the thermal decomposition of Fe(acac)$_3$ in benzyl alcohol allows good control over the nucleation and growth stages of the colloidal nanocrystals of magnetite and yields MNPs with a narrow size distribution as compared to the widely used co-precipitation technique.[39] The rate of decomposition of Fe(acac)$_3$ and therefore the onset, rate and extent of the nucleation phase in nanocrystallization of magnetite from the organometallic precursor were controlled by changing the heating rate and temperature of the reaction

mixture. To determine the rate of decomposition of the precursor during the MNPs nucleation and growth phases, 5-μL aliquots of the reaction mixture were collected, diluted with HPLC-grade acetone, centrifuged and the supernatant was analyzed by UV spectroscopy in the 250-600 nm wavelength range. The broad peaks at 355 and 435 nm correspond to the precursor while the sharp peak at 330 nm corresponds to the colloidal nuclei in the reaction mixture.[45] The Fe content in the supernatant was also quantified by ICP-MS. Several heating regimes were evaluated as depicted in **Figure 2.1.**

1). **Slow heating:** As the temperature was raised slowly at 0.4°C/min (**Figure 2.1A**) the nucleation stage was initiated very early (at ~150°C), as indicated by the attenuation of the precursor peaks intensities at 355 and 435 nm and elevation of the colloidal nuclei peak intensity at 330 nm (**Figure 2.2A1**). Approximately 75% of the precursor was converted into colloidal nuclei at around 160-180°C (**Figure 2.2A2**). As the temperature approached reflux (205°C), the remaining precursor in the reaction mixture was entirely consumed for the growth of the nuclei as shown by a complete loss of the absorbance (**Figure 1A1**). The mean size of the resultant MNPs was 7 ± 4 nm (**Figure 2.2A3**).

2). **Step-wise heating at 150°C:** In this regime the reaction mixture was heated to 150°C at 4°C/min and then the temperature was kept constant at 150°C for 2 hours to prolong the nucleation stage compared to the regime 1) by slowing down the precursor decomposition (**Figure 2.1B**). Under those conditions approximately 70 wt% of the precursor was consumed during the nucleation stage (**Figures 2.2B1 and B2**) resulting in nearly monodisperse MNPs with a mean diameter of 9 ± 2 nm (**Figure 2.2B3**).

3). **Step-wise heating at 180°C:** In this regime the reaction mixture was heated at 4°C/min to 180°C and then the temperature was kept constant for 2 hours at 180°C (**Figure 2.1C**). As a result, the nucleation phase was shortened compared to regimes 1 and 2. Under these conditions, at 180°C and above, a large excess of the precursor was involved in the

particles growth on the existing nuclei as demonstrated by the attenuation of the peak intensity at 330 nm (**Figure 2.2C1**). After 2 hours at 180°C, a significant amount of nuclei had undergone growth and precipitated as discrete MNPs (**Figure 2.2C2**). Larger MNPs with a mean diameter of 11 ± 4 nm and a broader size distribution were obtained using this regime (**Figure 2.2C3**).

4). **Rapid heating:** In the final regime the temperature was increased rapidly at a rate of 5°C/min until the reaction mixture refluxed (205°C) and this was followed by 40 hours of annealing (**Figure 2.1D**). Rapid heating of the mixture resulted in an overlap of the nucleation and growth phases leading to availability of large excesses of the precursor to promote rapid growth of the formed nuclei (**Figures 2.2D1 and D2**). This regime resulted in particles with a mean diameter of 14 ± 7nm (**Figure 2.2D3**),
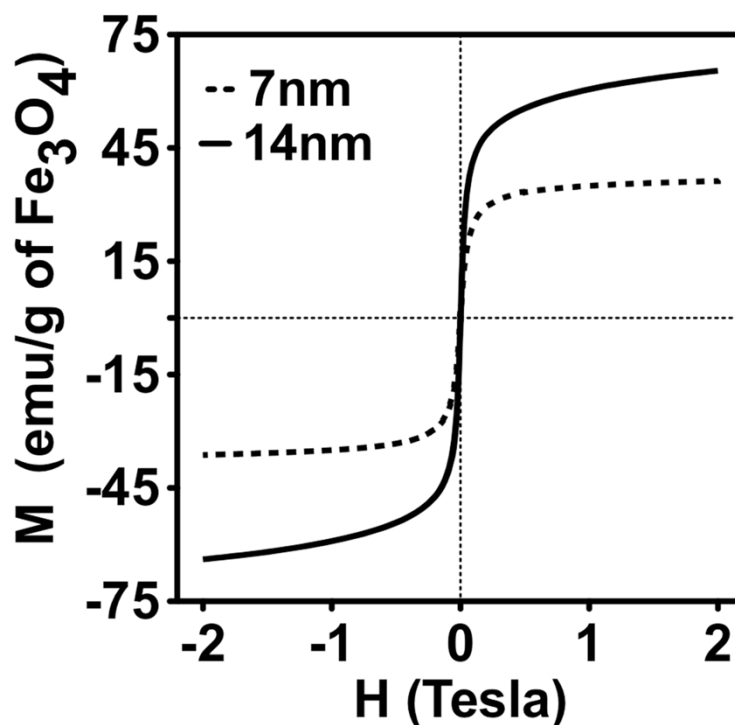
Figure 2.3. Magnetization saturation of MNPs with two different core sizes synthesized by thermal decomposition of Fe (acac)$_3$

The rapid increase in temperature and prolonged high temperature annealing is known to provide a higher degree of control over the crystal size.[46] Specifically, high temperature annealing was shown to enhance the saturation magnetization (M_S) of the superparamagnetic single domain MNPs synthesized by thermal decomposition.[47, 48]

The magnetic properties of the 7 nm and 14 nm diameter MNPs were studied by measuring the saturation magnetization (Ms) at 300K (**Figure 2.3**). The magnetization curves did not show any hysteresis which is consistent with the superparamagnetic properties of the MNPs.[49] As the particle size increased from 7 nm to 14 nm their M_S nearly doubled from 36.2 emu/g to 65.5 emu/g while their superparamagnetic behavior was preserved. Larger MNPs, due to their lower surface-volume ratio, have smaller numbers of atoms at the surface thereby leading to decreased surface effects such as spin-spin canting and spin-glass-like behavior.[50] As a result, the number of atoms contributing to the magnetic moment of the MNPs increases leading to higher MS values.[51] Increase in M_S also leads to an increased T_2 relaxation capability of the MNPs.[49, 52] Therefore, from the theranostic perspective, the 14-nm MNPs were expected to have higher T_2 relaxivity and darker negative contrast.

2.3.2. PREPARATION AND CHARACTERIZATION OF POLYMER-STABILIZED MNCS

MNCs stabilized by PLE-*b*-PEG block copolymers were formed via electrostatic binding of pendant carboxylate groups of the PLE blocks and the MNP surface (**Scheme 2.1**). In this study the length of the PEG block of the PLE-*b*-PEG was kept constant, while the PLE block length was varied. The hydrodynamic diameters of the resulting clusters (**Figure 2.4**) varied in the range of 40 to 70 nm depending on the length of the PLE block (**Table 2.1**). All MNCs were negatively charged as was evident from their ζ-potential values. In this study we also prepared MNCs stabilized by PLE$_{100}$ homopolymer as well as PLD$_{100}$-*b*-PEG$_{113}$ block copolymer and PLD$_{100}$ homopolymer. All these clusters in de-

ionized water had relatively small particle size (under 100 nm), and negative ζ-potential

(**Table 2.2**).

Scheme 2.1. Formulation process for preparation of MNP nanoclusters stabilized by PLE-PEG or ALN-modified PLE-PEG
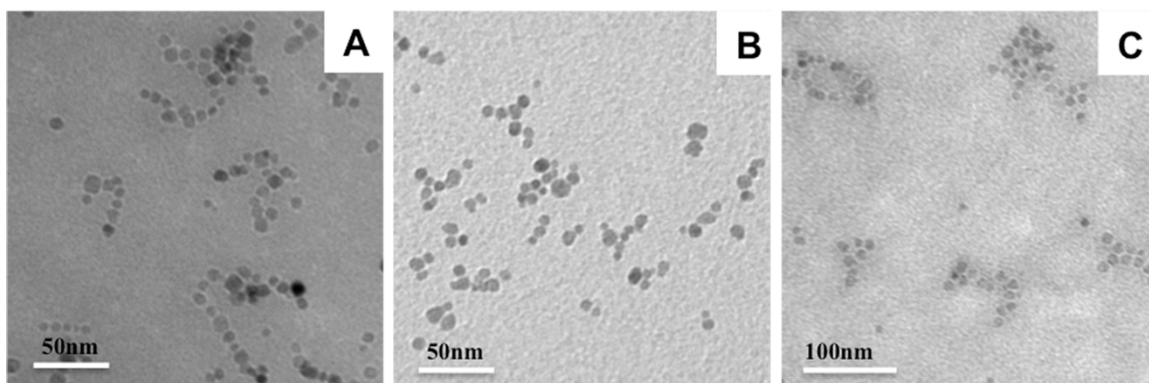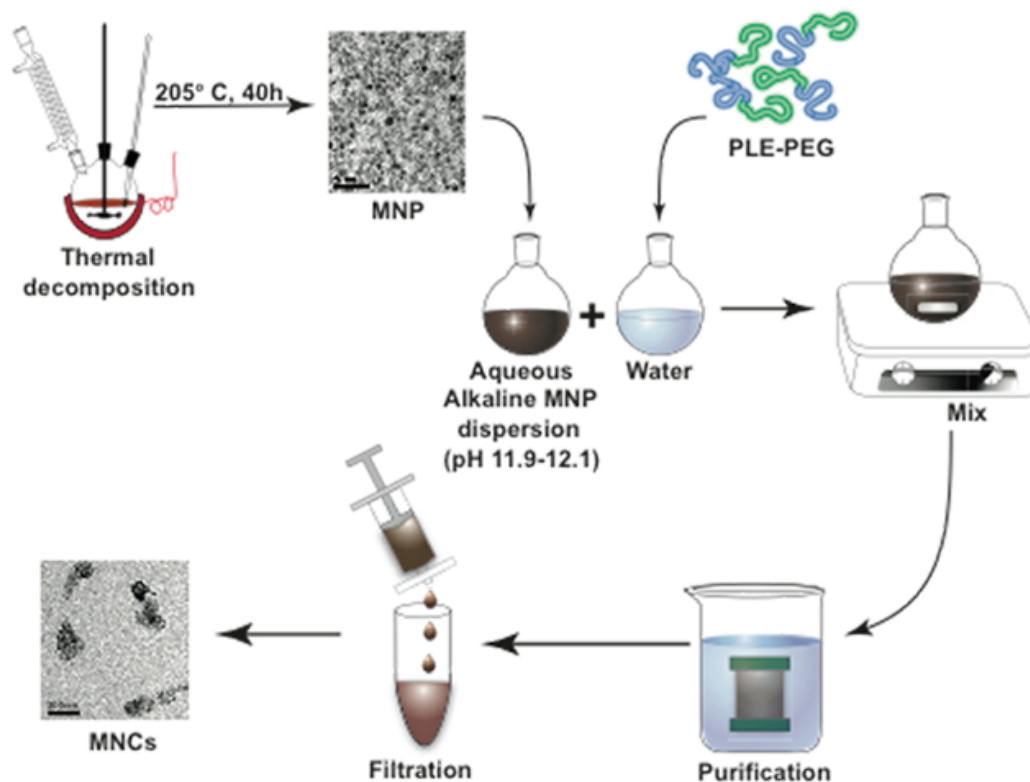
Figure 2.4. TEM images of (**A**) E_{10}-MNC, (**B**) E_{50}-MNC and (**C**) E_{100}-MNC formulations

Table 2.1: Physicochemical characteristics of MNCs stabilized by anionic PLE-*b*-PEG block copolymers having different PLE block lengths

Formulation [(a)]	Abbreviated designation	Composition (wt%) [(b)]		MNP	DLS characteristics [(c)]		
		Organic content			D_{eff} (nm)	PDI	ζ-potential (mV)
		Polymer	BA [(d)]				
PLE$_{10}$-*b*-PEG$_{113}$/MNP	E$_{10}$-MNC	19	6.7	74.3	51.4 ± 11.3	0.334 ± 0.01	-20
PLE$_{50}$-*b*-PEG$_{113}$/MNP	E$_{50}$-MNC	65.7	4.6	29.7	45.2 ± 4.3	0.171 ± 0.01	-26
PLE$_{100}$-*b*-PEG$_{113}$/MNP	E$_{100}$-MNC	56.2	5.5	38.3	68.8 ± 7.8	0.222 ± 0.04	-36

[(a)] The size of the MNPs in all formulations was 6 nm as quantified by Image J software from TEM images

[(b)] The composition of the MNCs was determined by TGA. 5-8 mg MNCs was heated to 110°C at 5°C/min. The temperature was maintained at 110°C for 10 min. and then elevated to 1000°C at 5°C/min. The polymer content was determined by subtracting the benzyl alcohol ligand content on the MNP from the overall organic fraction content.

[(c)] DLS characteristics were measured in de-ionized water at 0.5 mg/ml MNCs at 25°C.

[(d)] BA, benzyl alcohol.

Table 2.2: Physicochemical characterization of MNCs stabilized by homopolymers PLD, PLE, and PLD$_{100}$-b-PEG$_{113}$.

Formulation [a]	Abbreviation	DLS Characteristics [b]		
		D_{eff} (nm)	PDI	ζ-potential (mV)
PLE$_{100}$/MNP	hE$_{100}$-MNC	27.3 ± 4.8	0.171 ± 0.03	-34.6
PLD$_{100}$-*b*-PEG$_{113}$/MNP	D$_{100}$-MNC	94.8 ± 4.2	0.189 ± 0.01	-24.7
PLD$_{100}$/MNP	hD$_{100}$-MNC	67.2 ± 3.4	0.168 ± 0.03	-47.2

[(a), (b)] as described in footnotes under Table 2.1
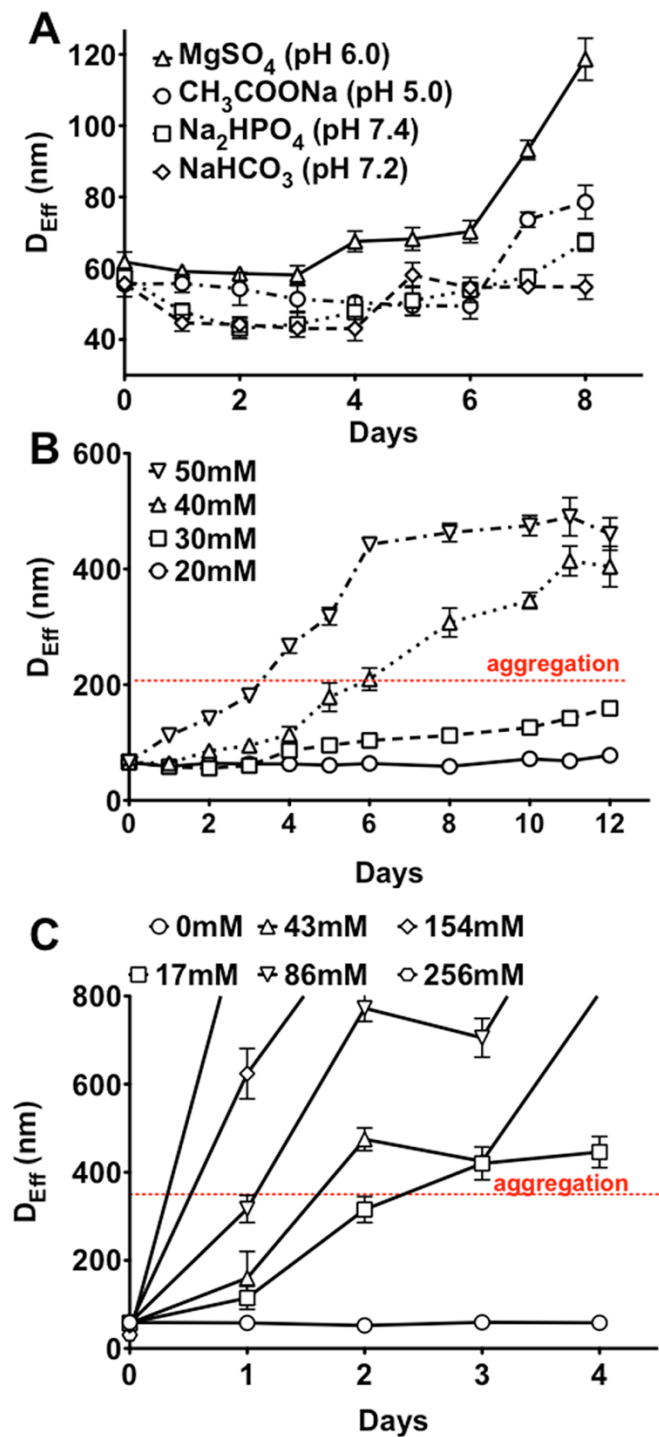
Figure 2.5. Colloidal stability of $E_{100}MNC$ as a function of (**A**) pH and salt composition (20 mM each), (**B**) concentrations of phosphate buffer, pH 7.4 and (**C**) NaCl concentration in 10 mM phosphate buffer, pH 7.4 All samples were prepared at a concentration of 0.5 mg/mL. Data are mean ± SD (n = 3)

Pegylated polymers are preferable in our work because they impart stealth properties and enhance systemic circulation of nanofomulations.[53, 54] PLE-*b*-PEG was chosen because of more facile lysosomal biodegradation of PLE compared to PLD and the respective block copolymer.[55, 56] PLD$_{100}$-*b*-PEG$_{113}$ and the corresponding homopolymer based MNCs were anticipated to undergo degradation at a slower rate and hence were not developed further.

For the PLE-*b*-PEG stabilized MNCs, altering the PLE block length affected the polydispersity and composition of the clusters. Interestingly, the greatest MNPs content in the clusters, as determined by TGA, was observed in E$_{10}$-MNC formed using copolymers with the shortest PLE chain (10 r.u.). As the ionic block length increased, the MNP content decreased to ~30-40 wt % in E$_{50}$-MNCs and in E$_{100}$-MNC compared to ~74 % in E$_{10}$-MNC. The presence of the PEG block also appears to have sterically hindered increased coordination of MNPs with the PLE block in E$_{100}$MNCs, which may have controlled the size of the resulting MNCs. Irrespective of the length of the PLE block in the copolymer used for cluster formation, the MNCs showed considerable sensitivity to the environmental pH, as well as the concentration and/or composition of the elementary salts in the solution. For example, E$_{100}$-MNC appeared to be less stable in magnesium sulfate, pH 6.0 than in sodium acetate, pH 5.0, sodium bicarbonate, pH 7.2 or disodium phosphate, pH 7.4 solutions (**Figure 2.5A**). This is possibly explained by the coordination of the divalent magnesium cation with the PLE block[57] resulting in detachment of this block from the MNPs surface. In the phosphate buffer (pH 7.4) the E$_{100}$-MNC stability strongly depended on the concentration of the disodium phosphate (**Figure 2.5B**) or NaCl (**Figure 2.5C**). This was attributed to a relatively weak attachment of the pendant carboxylate groups of the PLE to the MNP surface that can be substituted by the phosphate ions or disrupted by increasing the ionic strength.

2.3.3. ALN CONJUGATION ON PLE$_{50}$-*b*-PEG$_{113}$ POLYMER

Scheme 2.2. Schematic representation of ALN conjugation on PLE$_{50}$-b-PEG$_{113}$ polymer
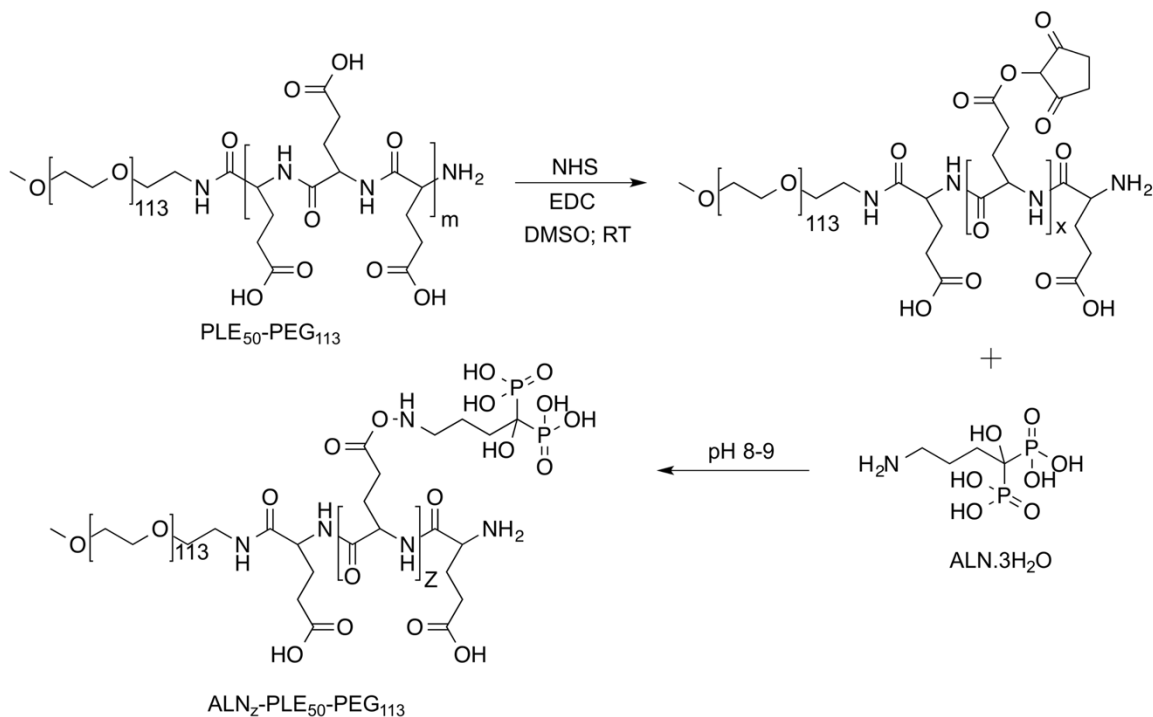
Introducing anchor groups such as dopamine[58-60] or bisphosphonate-containing compounds that form very strong coordination complexes with the MNPs[42, 61] can enhance binding of the block copolymer to the MNP surface and increase stability of the resulting MNCs under physiological conditions. Towards this goal we conjugated ALN to the PLE chain of PLE$_{50}$-*b*-PEG$_{113}$ by EDC/NHS chemistry in DMSO-water system (**Scheme 2.2**). The product of the reaction was confirmed by ^{1}H-NMR (**Figure 2.6**) and ^{31}P-NMR (**Figure 2.7**). The number of ALN groups linked to the PLE chain, termed here "degree of conjugation" (D$_{conj}$), was quantified by ICP-MS as well as NMR (**Table 2.3).**
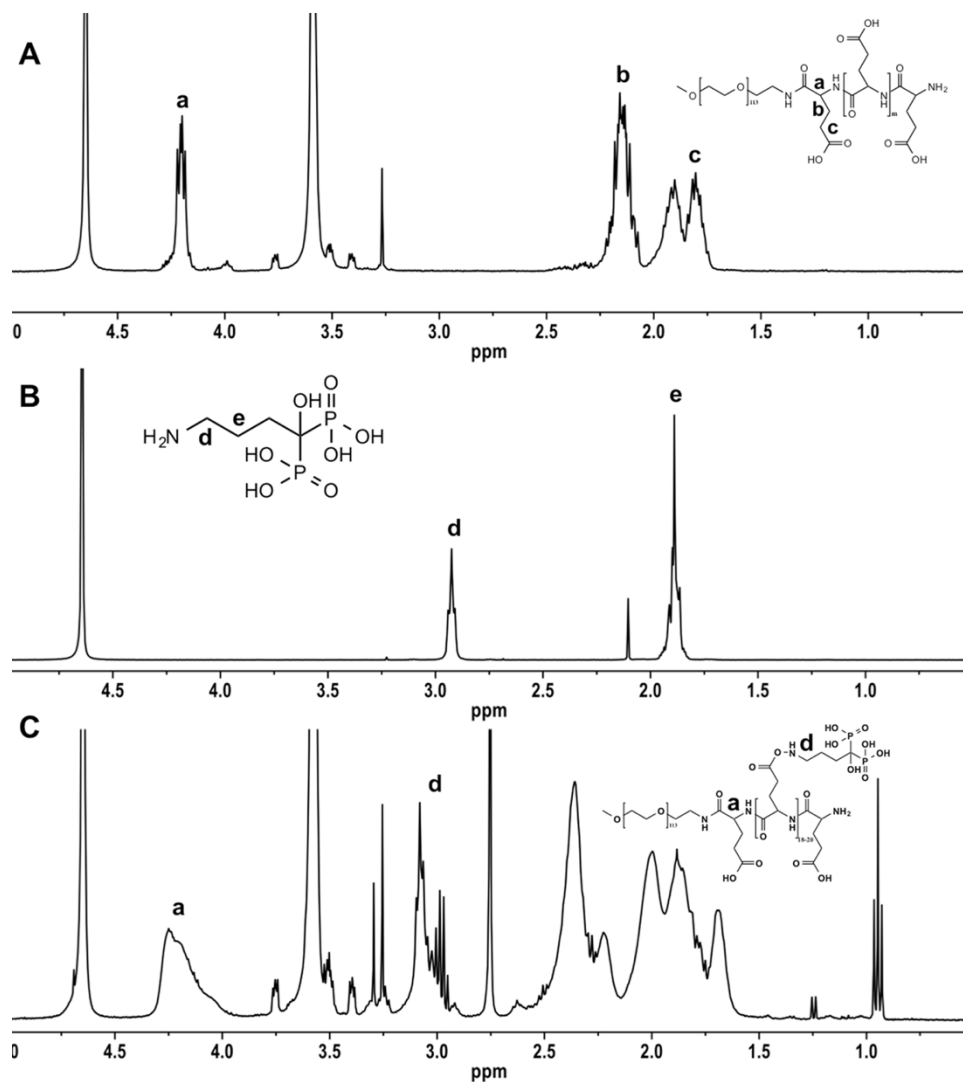
Figure 2.6. ^{1}H-NMR in D$_2$O of (**A**) PLE$_{50}$-*b*-PEG$_{113}$, (**B**) ALN and (**C**) ALN-modified PLE$_{50}$-*b*-PEG$_{113}$. Peak assignments are as follows: (**A**) δ ppm= 1.85 (2H, m, -CH$_2$-; c), 2.2 (2H, m, CH$_2$; b), 4.2 (H, t, -CH-; a); (**B**) δ ppm= 1.88 (2H, m, -CH$_2$-; e), 2.9 (2H, t, -CH$_2$; d); (**C**) δ ppm= 2.9 - 3.1 (2H, m, -CH$_2$-; d), 4.28 (H, d, -CH-; a).

Table 2.3. Quantitation of ALN conjugation by ^{1}H-NMR

Formulation	ALN units per chain (D$_{conj}$)
A$_6$-MNC	5.8
A$_{12}$-MNC	10.7
A$_{19}$-MNC-1	19.3
A$_{19}$-MNC-2	18.5
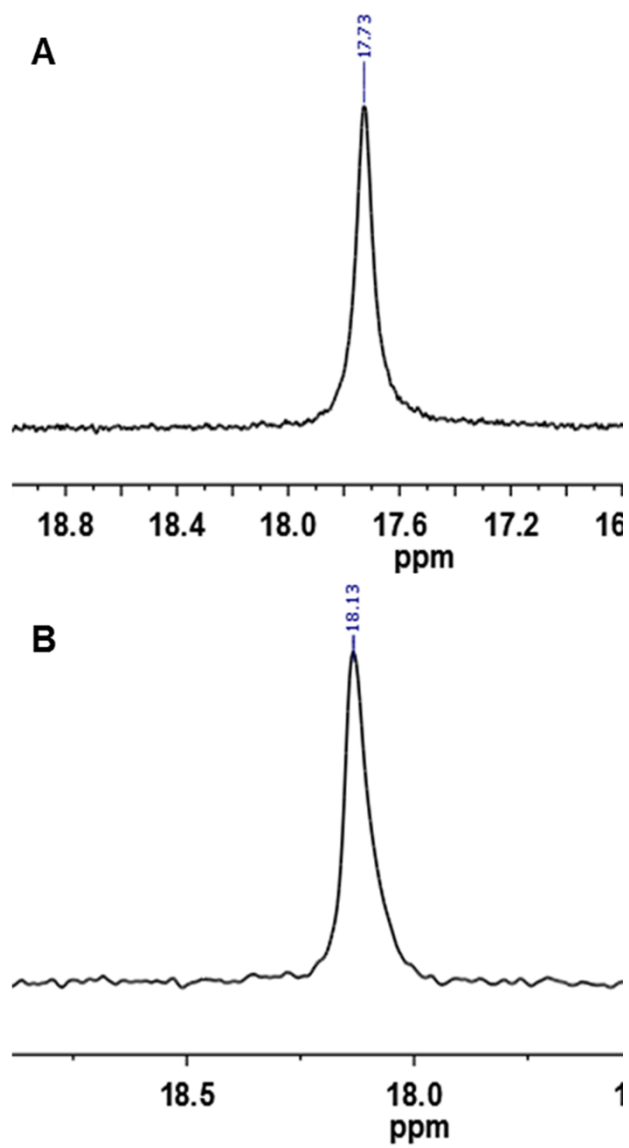
Figure 2.7. ^{31}P-NMR in D$_2$O of (**A**) unconjugated ALN (δ ppm: 17.73) and (**B**) ALN-modified PLE$_{50}$-PEG$_{113}$ (δ ppm: 18.13$_)$

Table 2.4. Physicochemical characteristics of MNCs stabilized by ALN-conjugated PLE_{50}-b-PEG_{113} copolymers.

Formulation	Abbreviated designation	ALN groups per PLE chain [a]	COOH groups (µmole per mg MNC)[b]	MNP diameter (nm) [c]	Composition (wt %) [d]			DLS Characteristics [d]				
					Organic content		MNP	DI water			PBS pH7.4	
					Polymer	BA		D_{eff} (nm)	PDI	ζ-potential (mV)	D_{eff} (nm)	PDI
ALN_6-PLE_{50}-b-PEG_{113}/MNP	A_6-MNC	6*	8.5	9	76	2.5	21.5	33.4 ± 6	0.21 ± 0.05	-24.6	39.6 ± 11	0.31 ± 0.05
ALN_{12}-PLE_{50}-b-PEG_{113}/MNP	A_{12}-MNC	12	11.5	9	67.3	3.1	29.6	35.4 ± 8.4	0.25 ± 0.07	-33.1	34.6 ± 9	0.25 ± 0.06
ALN_{19}-PLE_{50}-b-PEG_{113}/MNP-1	A_{19}-MNC-1	19	16.5	9	53.7	5.8	40.7	69.5 ± 5.4	0.22 ± 0.06	-29.7	67.4 ± 10	0.24 ± 0.03
ALN_{19}-PLE_{50}-b-PEG_{113}/MNP-2	A_{19}-MNC-2	19	26.7	12	68.4	4.8	26.8	78 ± 7.2	0.20 ± 0.01	-20.4	79.8 ± 7	0.22 ± 0.04

[a] Number of ALN molecules per polymer chain was quantified by ICP-MS except for A_6-MNC (*) wherein the number of ALN units per polymer chain were estimated from ^{1}H-NMR.

[b] Carboxylic acid (COOH) groups concentration was determined by potentiometric acid-base titration on formulation diluted to 0.1 mg/mL in DI water.

[c] The average MNP sizes were estimated from TEM images by measuring a minimum of 400 core particle sizes with Image J software.

[d] The composition and DLS characteristics of the MNCs were determined as explained in **Table 1**, except for the last two columns where the DLS measurements were done in PBS, pH 7.4.

The cluster size was altered by increasing the concentration of the polymer and MNP solution by two-folds. The number of ALN groups also strongly influenced the size of the resulting MNCs (**Table 2.5**). The A_6-MNC and A_{12}-MNC formed using copolymers with D_{conj} equal to 6 and 12 respectively were relatively small (~33 – 35 nm). As D_{conj} increased to 19 in A_{19}-MNC-1 the particle size increased nearly two fold. Interestingly, TEM images suggest that A_{19}-MNC-1 particles appear to be more elongated and display greater proportion of chain-like structures compared to A_{12}-MNC (**Figure 2.8**). Using the copolymer with D_{conj} = 19 and MNPs with different particle diameter (9 and 12 nm) we also produced two types of clusters, A_{19}-MNC-1 and A_{19}-MNC-2.
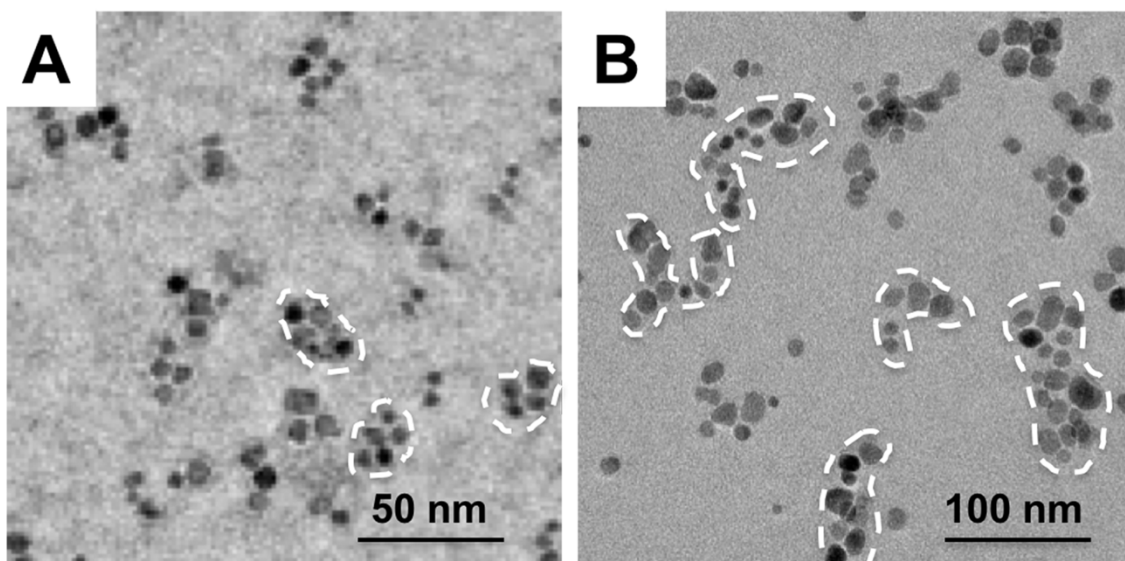
Figure 2.8. TEM images of (**A**) A_{12}-MNC and (**B**) A_{19}-MNC-1 formulations

Despite the difference in their MNPs sizes the resulting clusters had practically the same overall particle size. Similar to above described non-stabilized clusters, the MNCs obtained using the ALN copolymers were negatively charged as was evident from the high absolute values of their negative ζ-potential (**Table 2.5**). Perhaps, the greatest difference between these clusters was in their stability in physiological ionic strength conditions. Thus all ALN-stabilized clusters had nearly same particle size in PBS, pH 7.4 as in the DI water.

When compared with each other the A_6-MNC and A_{12}-MNC having smaller number of ALN groups per copolymer were relatively less stable upon storage and aggregated over time in contrast, A_{19}-MNC-1 was stable in both DI water and PBS at RT and 37°C displaying little if any change in particles size upon incubation for at least 30 days (**Figure 2.9**).
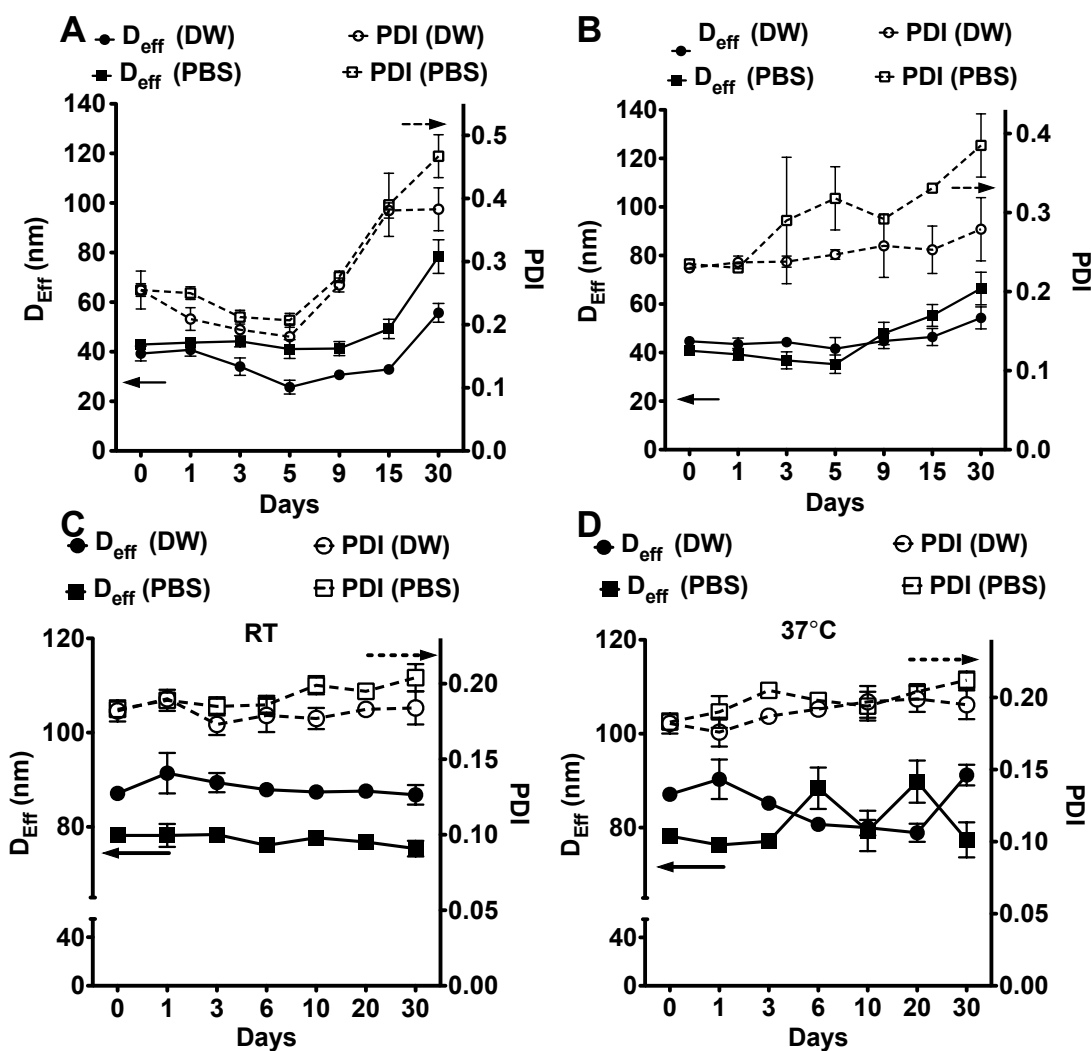
Figure 2.9. Colloidal stability of (**A**) A_6-MNC and (**B**). A_{12}-MNC formulations in DI water (DW) and 20mM pH 7.4 PBS at RT and A_{19}-MNC formulation in DW and PBS at (**C**). RT and (**D**). 37°C

Table 2.5. Physicochemical characteristics of cisplatin-loaded MNCs.

MNC used to prepare cisplatin-containing formulation [a]	Abbreviated designation	DLS Characteristics [b]					LE (%) [c]	LC (%) [d]
		DI Water			PBS pH 7.4			
		D_{eff} (nm)	PDI	ζ-potential (mV)	Deff (nm)	PDI		
A_6E_{50}-PEG$_{113}$/MNP	Pt-A$_6$-MNC	38.6 ± 8.2	0.261 ± 0.03	-28.3	36.4 ± 11.4	0.348 ± 0.06	24	3.8
$A_{12}E_{50}$-PEG$_{113}$/MNP	Pt-A$_{12}$-MNC	41.7 ± 11.3	0.243 ± 0.03	-36.1	43.3 ± 8.2	0.267 ± 0.03	32.7	5.2
$A_{19}E_{50}$-PEG$_{113}$/MNP	Pt-A$_{19}$-MNC -1	69.3 ± 9.3	0.255 ± 0.02	-35.4	70.2 ± 7	0.203 ± 0.04	37.3	8.4
$A_{19}E_{50}$-PEG$_{113}$/MNP	Pt-A$_{19}$-MNC -2	86 ± 5.1	0.218 ± 0.02	-43.4	83.8 ± 7.2	0.211 ± 0.01	40	17.6

(a) The loading procedure is described in Materials and Methods.

(b) DLS characteristics were measured in DI water or PBS, pH 7.4 at 0.5 mg/mL MNCs at 25°C.

(c) The loading efficiency (LE) was determined by ICP-MS as the percent of the drug incorporated in MNCs vs. the drug added during loading.

(d) The loading capacity (LC) was determined as the weight percent of cisplatin per the dispersed phase. Briefly, the drug-loaded MNCs were lyophilized and the amount of cisplatin per mg of the formulation was determined by ICP-MS.

2.3.4. LOADING OF CISPLATIN IN MNCS

Cisplatin was loaded into the MNCs via the formation of a coordination complex of drug molecules with the carboxylate groups of PLE chains at pH 9.5. The technique employed for the drug loading was similar to that previously described by us for the loading of the cross-linked anionic nanogels.[30, 62] In addition, the bisphosphonate groups introduced on the polymer chain are also likely to have a higher binding affinity towards cisplatin than the carboxylates.[63] We targeted 70 mol% of the total carboxylate groups available in MNCs, assuming that each mole of cisplatin reacts with two moles of the carboxylate groups. Four different types of ALN-stabilized MNCs described in the previous section were used in these experiments. The characteristics of the resulting cisplatin-loaded MNCs are presented in **Table 2.6**. In all cases from 24 to 40 % of the drug used for the loading was actually incorporated in the MNCs. Both, the loading efficiency (LE) and loading capacity (LC) appeared to increase as the number of ALN moieties elevated in the following order A_6-MNC < A_{12}-MNC < A_{19}-MNC-1. As mentioned earlier, increase in the bisphosphonate groups (two bisphosphonates introduced per each carboxylate group attached) is also very likely to contribute to this trend in LE and LC due to higher affinity for cisplatin. However, in A_{19}-MNC-2, as the size of the MNP grains increased, there was nearly two-fold increase in the LC compared to A_{19}-MNC-1. Although these two unloaded clusters had similar particle size, the greater phosphonate and carboxylate groups content in A_{19}-MNC-2 compared to A_{19}-MNC-1 probably explained the difference in the LC between them (**Table 2.6**). Notably, the particle size of all clusters in DI water noticeably did not change upon loading (**Tables 2.5 and 2.6**). However, and quite interestingly in all cases the ζ-potentials of the loaded clusters appeared to become more negative after loading, which might seem counterintuitive as the ionic groups are partially consumed by cisplatin coordination. However, we believe that this effect may be explained by the

thickening of the effective Stern layer that, as previously discussed[30] in the nanogel-like particles, can span throughout the entire particle volume. Coordination of the drug is likely to displace the counter ions from the interior of the MNCs to the more "hydrodynamically mobile" surface and periphery layers, resulting in an effective increase in the density of the uncompensated negative charge and absolute ζ-potential value of the particles.
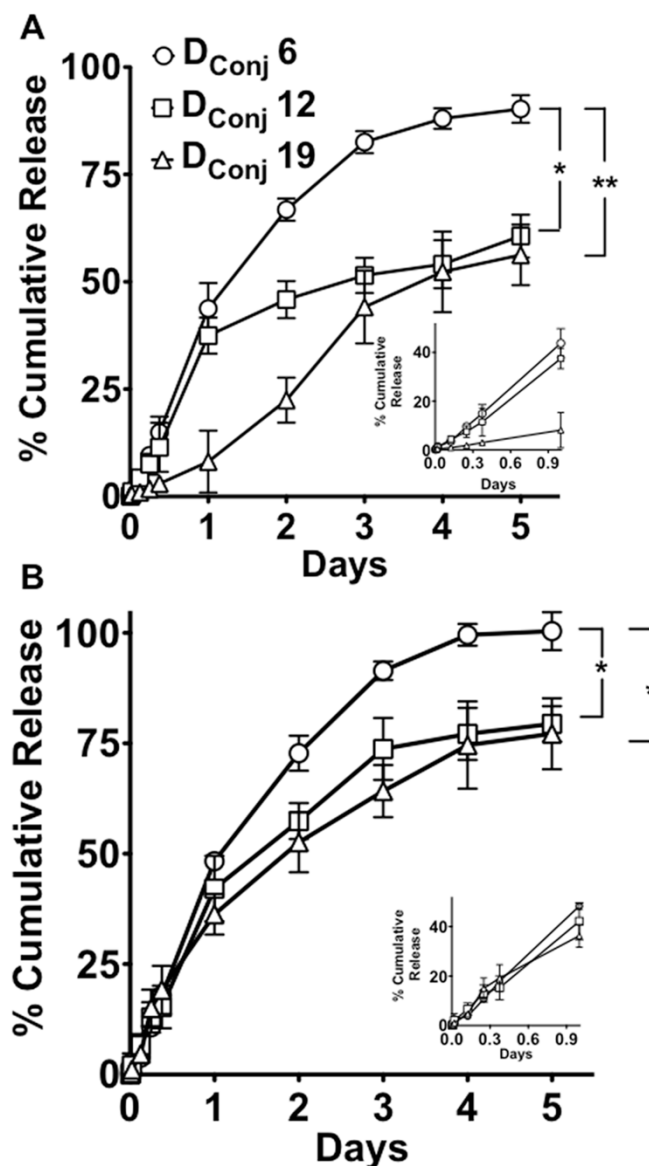
Figure 2.10. Release of cisplatin from Pt-A$_6$-MNC, Pt-A$_{12}$-MNC and Pt-A$_{19}$-MNC-1 at (**A**) pH 7.4 and (**B**) pH 5.5. Data are mean ± SD (n = 3); Statistical analysis performed by ANOVA using SPSS statistical software, * p <0.05; ** p< 0.01. The graphs in the insets of both the plots show the release patterns in the first 24h

2.3.5. RELEASE OF CISPLATIN FROM MNCS

Cisplatin release was studied at 37°C at pH 7.4 (PBS; 0.14M NaCl) and pH 5.5 acetate buffered saline (ABS; 0.14M NaCl), that mimic conditions in extracellular media and endosomal compartments, respectively. As shown in **Figure 2.10.,** both pH and D_{conj} of the MNCs affected the drug release. In all cases the fastest release kinetics was observed in Pt-A_6-MNC having the smallest number of ALN anchor groups in the copolymer and lowest LC. As the D_{conj} increased, the release rate decreased, lowest being in in Pt-A_{19}-MNC-1. For all systems the release was faster at pH 5.5 than pH 7.4 although this difference was the smallest in Pt-A_6-MNC and the greatest in Pt-A_{19}-MNC.
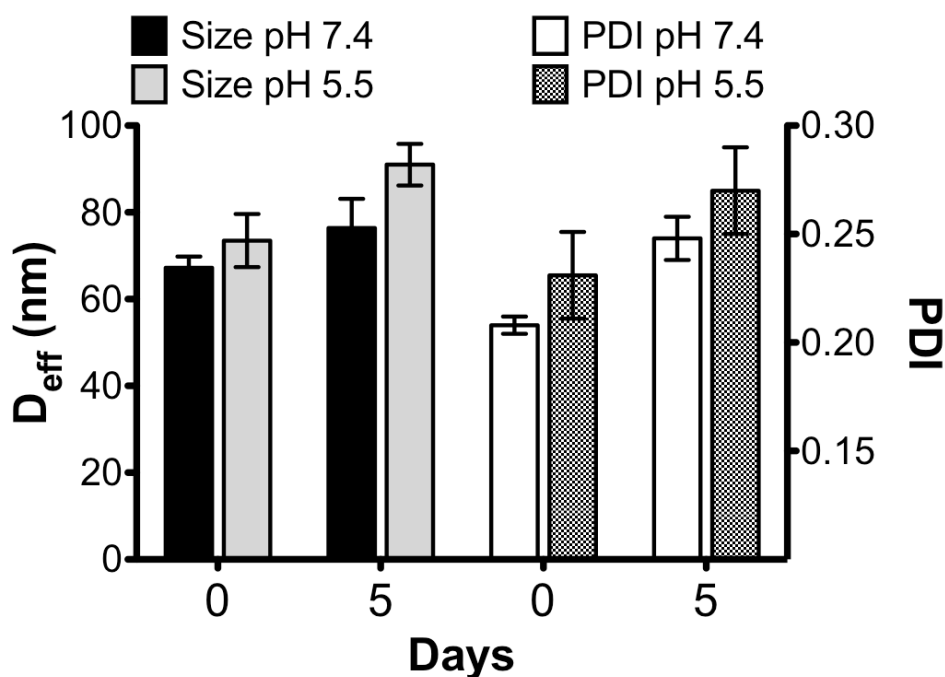
Figure 2.11. Colloidal stability of cisplatin loaded Pt-A_{19}-MNC formulation before and after cisplatin release from the formulation. The particle size (D_{eff}) of the samples used for release kinetics study (**Figure 2.10**) was determined by DLS before and at the end of the release study

The pKa of the protons on the phosphonate groups of ALN may also play an important role in the drug release. The third pKa of alendronic acid is 6.4.[64] Hence, at pH 5.5, the respective phosphonate groups of ALN can become protonated and if these groups participate in binding cisplatin this could also cause increase in the drug release rate.

Interestingly, Pt-A$_{19}$-MNC-1 at pH 7.4 displayed a complex release kinetics with very slow release of the drug during the first two days followed its by acceleration thereafter. The slow phase could be possibly attributed to the initial compact morphology of the cluster, which becomes looser as the drug loading decreases, thereby facilitating drug diffusion out of the particle. Notably, the slow release phase was not seen at pH 5.5 with the drug release being overall much faster and monotonic. It is noteworthy that the formulations did not aggregate of lose colloidal stability over the entire period of the study in either buffer systems (**Figure 2.11**).

2.3.6. RELAXOMETRY MEASUREMENTS OF MNC FORMULATIONS
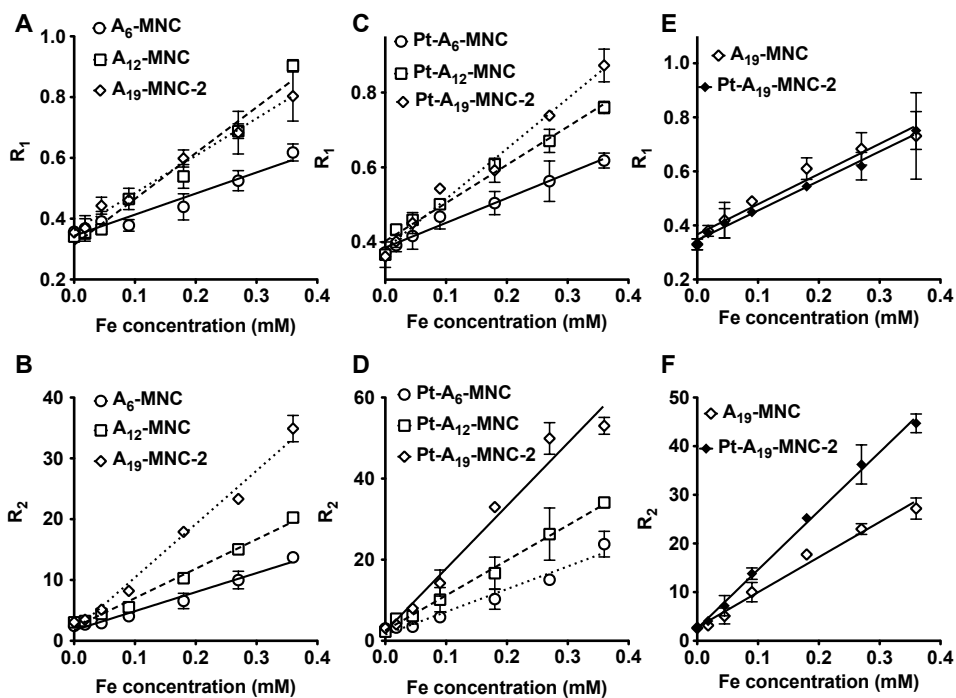
Figure 2.12. r_1 (longitudinal) and r_2 (transverse) relaxivity measurement of different unloaded (**A, B**) and cisplatin loaded (**C, D**) MNCs in PBS. Formulations with maximum relaxivity values were further dispersed in 4% agar and relaxivities were measured in the resulting phantom gels (**E, F**). Relaxivity is the linear slopes of the plots of relaxation time (R1/ R2) vs. Fe concentration (mM) and expressed as $S^{-1}.mM^{-1}$ (See Table 2.7)

The use of contrast agents for MRI depends on their ability to shorten the relaxation times of the surrounding protons.[65, 66] Positive contrast agents reduce T_1 relaxation times to give a brighter signal while negative contrast agents reduce T_2 resulting in a darker signal. The reciprocals of the relaxation times are called the relaxation rates, R_1 and R_2, with the effectiveness of contrast agents expressed as relaxivities, r_1 and r_2, which are determined from the slope of the relaxation rate curves expressed as a function of total Fe concentration (mM) (**Figure 2.12**). In all cases the r_1 relaxivity values of MNCs in PBS pH 7.4 values were relatively low and did not change or decrease upon drug loading (**Table 2.6**).

Table 2.6. Longitudinal (r_1) and transverse (r_2) relaxivity of the different MNC formulations

Formulation	$r_1(s^{-1}.mM^{-1})$ [a]	$r_2(s^{-1}.mM^{-1})$ [a]
A_6-MNC	0.694 ± 0.07	31.3 ± 2
Pt-A_6-MNC	0.66 ± 0.04	56 ± 4.7
A_{12}-MNC	1.91 ± 0.11	48.3 ± 2.2
Pt-A_{12}-MNC	1.02 ± 0.06	86.5 ± 2.8
A_{19}-MNC-1	1.23 ± 0.05	87.8 ± 4.4
Pt-A_{19}-MNC-1	1.02 ± 0.16	154.8 ± 11.5
A_{19}-MNC-1 [b]	1.12 ± 0.1	72.2 ± 4.02
Pt-A_{19}-MNC-1 [b]	0.9 ± 0.04	120.8 ± 3
A_{19}-MNC -2	1.34 ± 0.08	81.4 ± 3.3
Pt-A_{19}-MNC -2	1.18 ± 0.07	140.3 ± 12

[a] Data are mean ± SD (n = 3)

[b] Relaxivity measurements of phantom gels in 2% v/v agar. All other measurements were conducted in PBS pH 7.4.

In contrast the r_2 values of MNCs increased progressively as the D_{conj} value increased A_6-MNC < A_{12}-MNC < A_{19}-MNC-1 (**Table 2.7**). Notably for each empty and drug loaded MNCs the r_2 value appeared to be higher as the particle size was larger. But quite unexpectedly for all MNCs the r_2 value increased considerably, ~1.6 to 1.8 times after the drug loading although the particle size (**Tables 2.5 and 2.6)** did not change that

significantly. For example, Pt-A_{19}-MNC-1 had r_2 values of 154.8 s^{-1}.mM^{-1} vs 87.8 s^{-1}.mM^{-1}

for the unloaded A_{19}-MNC-1. The T_1 and T_2 relaxivities of A_{19}-MNC-1 and Pt-A_{19}-MNC-1

were further measured in buffered (PBS pH 7.4) 2% w/w agar gel. Phantom agar gel is

commonly used as reference material to mimic biological tissues due to similarities of its

T_1 and T_2 values to those of biological tissues.[67] In the gel the r_1 and r_2 values of both the

loaded and unloaded MNCs showed only a minor decline compared to these values in

PBS dispersion suggesting good potential for negative contrast in biological tissues.
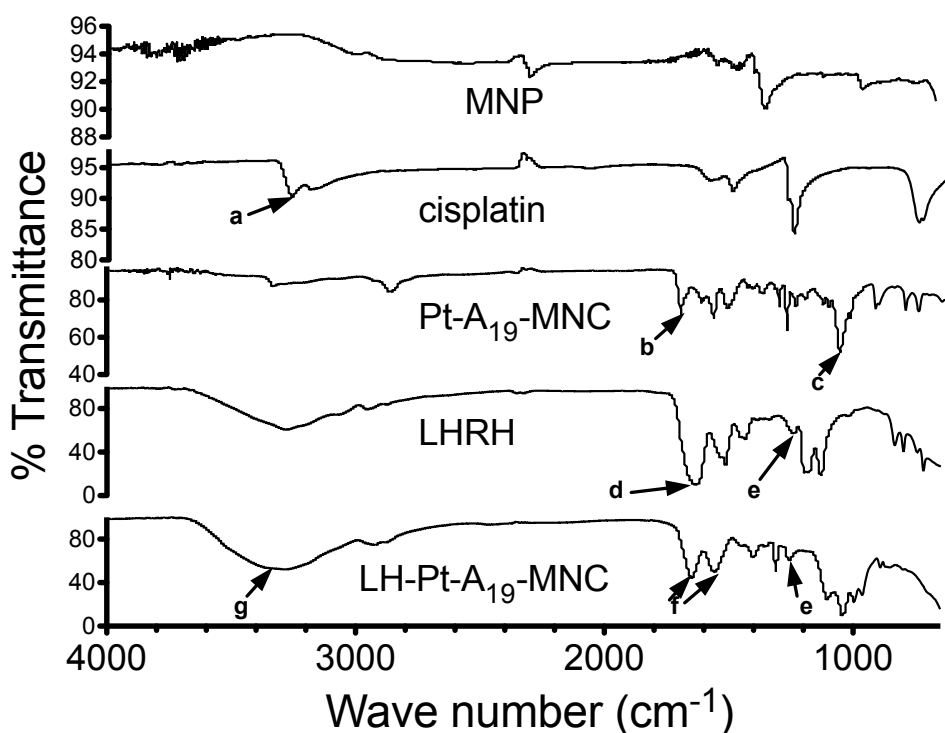
Figure 2.13. FTIR spectrum of LHRH-conjugated LH-Pt-A_{19}-MNC formulation showing **a.** N-H stretch of the primary amine of cisplatin at 3280 cm^{-1} **b.** carbonyl stretch of carboxylic acid on the polymer at 1730 cm^{-1} **c.** C-O stretch of PEG at 1110 cm^{-1} **d.** N-H bend of primary amines 1650 cm^{-1} **e.** C-N stretch of aliphatic amines at 1260 cm^{-1} **f.** formation of secondary amide bonds following conjugation of LHRH on the PtMNC at 1660, 1580 cm^{-1} and **g.** N-H stretch of secondary amide bonds at 3400 cm^{-}

2.3.7. SYNTHESIS OF LHRH-TARGETED MNCS

Unloaded A_{19}-MNC-1 and Pt-A_{19}-MNC-1 (41 wt% MNP and 8.4 wt% cisplatin) were used in this work as representative MNCs for LHRH conjugation. Similar to our previous publication on cisplatin containing nanogels[36] (D-Lys6)-LHRH was conjugated through its lysine primary amino group to the free carboxyl groups of the A_{19}-MNC-1 and Pt-A_{19}-MNC-1 using EDC/S-NHS coupling chemistry.

The conjugation was confirmed by an HPLC assay[68] by measuring the amount of the free (D-Lys6)-LHRH in the filtrate after purification of the modified clusters by centrifugal filtration (3000 MWCO). Only 13.3% and 28.7% of the total reagent added in the reaction mixtures was present in the filtrates of A_{19}-MNC-1 and Pt-A_{19}-MNC-1 samples, respectively. The apparent greater yield of conjugation of the peptide to A_{19}-MNC-1 compared to Pt-A_{19}-MNC-1 was explained by availability of a greater number of free carboxylate groups prior to loading of the drug. The FTIR spectra (**Figure 2.13**) of the LHRH-conjugated Pt-A_{19}-MNC-1 (LH-Pt-A_{19}-MNC-1) suggested formation of a secondary amide bond between the primary amino group of the (D-Lys6)-LHRH and the carboxylic acid groups of the PLE.

2.3.8. UPTAKE OF LHRH-TARGETED CISPLATIN-LOADED MNCs IN OVARIAN CANCER CELLS

The cell uptake of the unloaded LHRHr-targeted (LH-A_{19}-MNC-1) and untargeted (A_{19}-MNC-1) MNCs was studied by confocal microscopy in LHRHr overexpressing A2780-WT and A2780-CisR human ovarian cancer cells. A2780 human ovarian cancer cells are known for LHRHr over-expression. Numerous studies have characterized LHRHr expression by Western Blot analysis.[34-36] As seen in **Figure 2.14**, untargeted MNCs showed very low cellular uptake even after 24 hours in both wild type and cisplatin-

resistant cells. The internalized MNCs were localized in the lysosomal compartments of the cells visualized by the bright yellow punctate regions in the overlay images. Conjugation of LHRH significantly enhanced the LH-A$_{19}$-MNC-1 cellular uptake. In the A2780-WT cells the LH-A$_{19}$-MNC-1 were seen localized along the cell membrane (red) and within the lysosomes (yellow punctate regions) as early as at 1-hour post incubation.

Although the uptake of LH-A$_{19}$-MNC-1 in A2780-CisR cells was slower, a significant red fluorescence of the labeled clusters was observed in the cells at as early as 3 hours. Interestingly, literature reports suggest that certain cisplatin-resistant cancer cells (e.g. ovarian epidermal carcinoma) exhibit significant reduction in non-receptor mediated fluid-phase endocytosis compared to their wild-type counterparts while the receptor-mediated endocytosis remains unaffected.[69] The observed increased uptake of LH-A$_{19}$-MNC-1 in A2780-CisR cells specifically, is in line with these reports and strongly suggests that receptor-mediated targeted therapy is an effective strategy for achieving a faster onset and selective enhancement of cellular uptake in drug resistant tumors as it circumvents the defective mechanisms of uptake in drug resistant cancers.
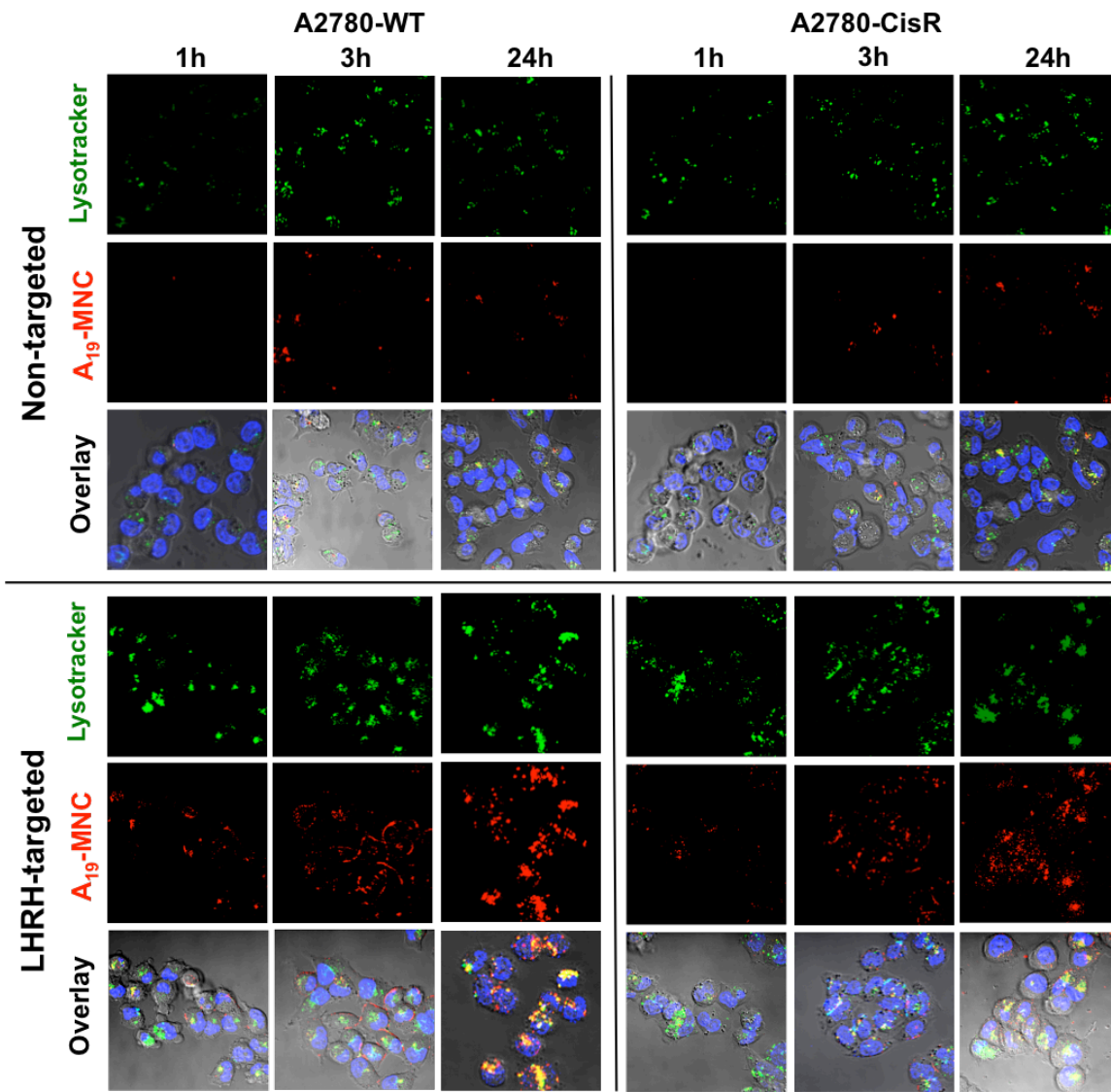
Figure 2.14. Confocal microscopy of the wild-type A2780-WT and cisplatin resistant A2780-CisR human ovarian cancer cells at different time points during their incubation with non-targeted A_{19}-MNC-1 and LHRH-conjugated A_{19}-MNC-1. Live cells were exposed to the said Alexa-Fluor 647 labeled (RED) MNCs and stained with the lysotracker green (GREEN) and Hoechst nuclear stain (BLUE) for 30 min. The colocalization of the labeled MNCs in lysosomes is seen in the overlay (YELLOW punctate regions). (Magnification 63X).
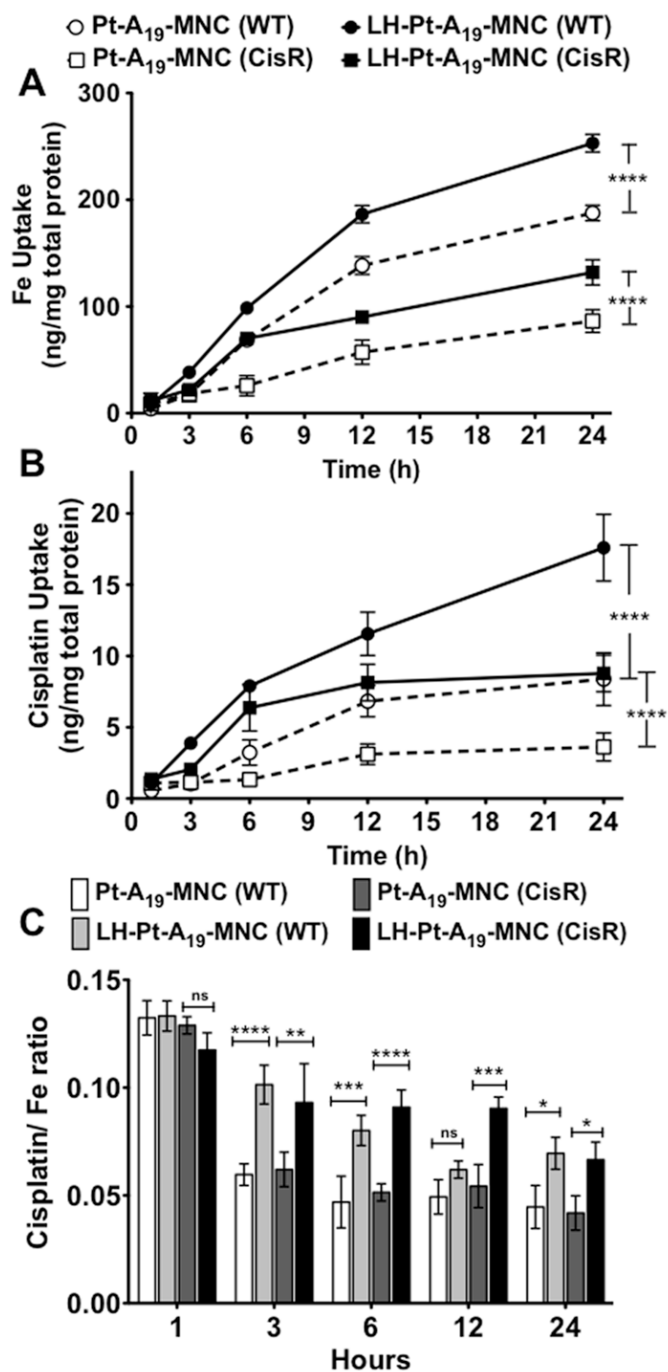
Figure 2.15. Uptake of LHRH-targeted and untargeted cisplatin-loaded MNCs in A2780-WT and A2780-CisR cells as quantified by ICP-MS and presented as (**A**) Fe levels, (**B**) Pt (cisplatin) levels and (**C**) cisplatin / Fe ratio over time. Data are mean ± SD. Statistical analysis done by ANOVA using SPSS software. Statistical significance denoted as: * $p < 0.05$, ** $p < 0.01$, *** $p < 0.001$, **** $p < 0.0001$ (n = 3).

The uptake was further quantified by ICP-MS. In this case the cells were incubated with Pt-A$_{19}$-MNC-1 and LH-Pt-A$_{19}$-MNC-1 for up to 24 hours and the Fe and Pt content in the cells was normalized per mg of cellular protein and plotted over time (**Figure 2.15**). Similar to the trend observed in the confocal images, LHRH conjugation resulted in an almost 2-fold increase in intracellular Fe concentration in the A2780-WT cells (**Figure 2.15A**). In the A2780-CisR cells there was also a significant increase in the uptake of targeted LH-Pt-A$_{19}$-MNC-1 compared to untargeted Pt-A$_{19}$-MNC-1 although, as expected the overall uptake was slower than that in the WT cells. A similar pattern was observed for the intracellular Pt content also (**Figure 2.15B**). It is important to note that LHRH targeting significantly improved the rate of uptake of the cisplatin-loaded MNCs during the first few hours, thereby decreasing the effect of the release of free cisplatin in the culture medium. This was apparent in the analysis of the ratios of the cisplatin/Fe cell levels (**Figure 2.15C**). In the case of the non-targeted Pt-A$_{19}$-MNC formulation the cisplatin/Fe ratio in both cell lines decreased significantly after 3 hours over time indicating that a significant amount of drug was released into the media during the incubation time. For the targeted LH-Pt-A$_{19}$-MNC-1 formulation this ratio although steadily decreased over time but remained much higher than that for Pt-A$_{19}$-MNC-1. This was consistent with more rapid internalization of the drug-loaded particles prior to a considerable release of the drug into the media.
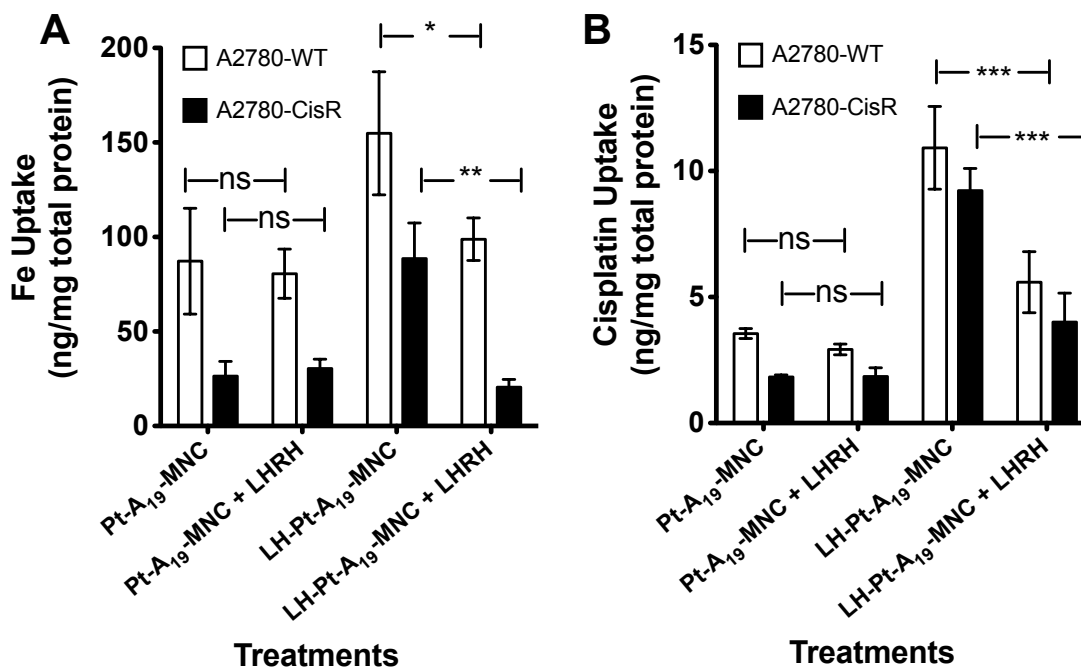
Figure 2.16. Inhibition of intracellular uptake of (**A**) Fe and (**B**) Cisplatin (Pt) in A2780-WT and A2780-CisR cells pre-incubated with D-Lys-6-LHRH peptide for 1h followed by 6h incubation with targeted and non-targeted PtMNC formulations. Statistical significance: * $p < 0.05$, ** $p < 0.01$, *** $p < 0.001$ (n=3).

Finally, pre-incubating both cell lines with 100 nM free D-Lys-6-LHRH peptide for 1 h before adding the MNCs greatly diminished the uptake of LH-Pt-A_{19}-MNC-1 and had little if any effect on Pt-A_{19}-MNC-1 (**Figure 2.16**). This suggests that the free peptide competitively inhibited the uptake of LHRH-targeted LH-Pt-A_{19}-MNC-1 and reinforces the receptor-mediated mechanism of its internalization in cancer cells.
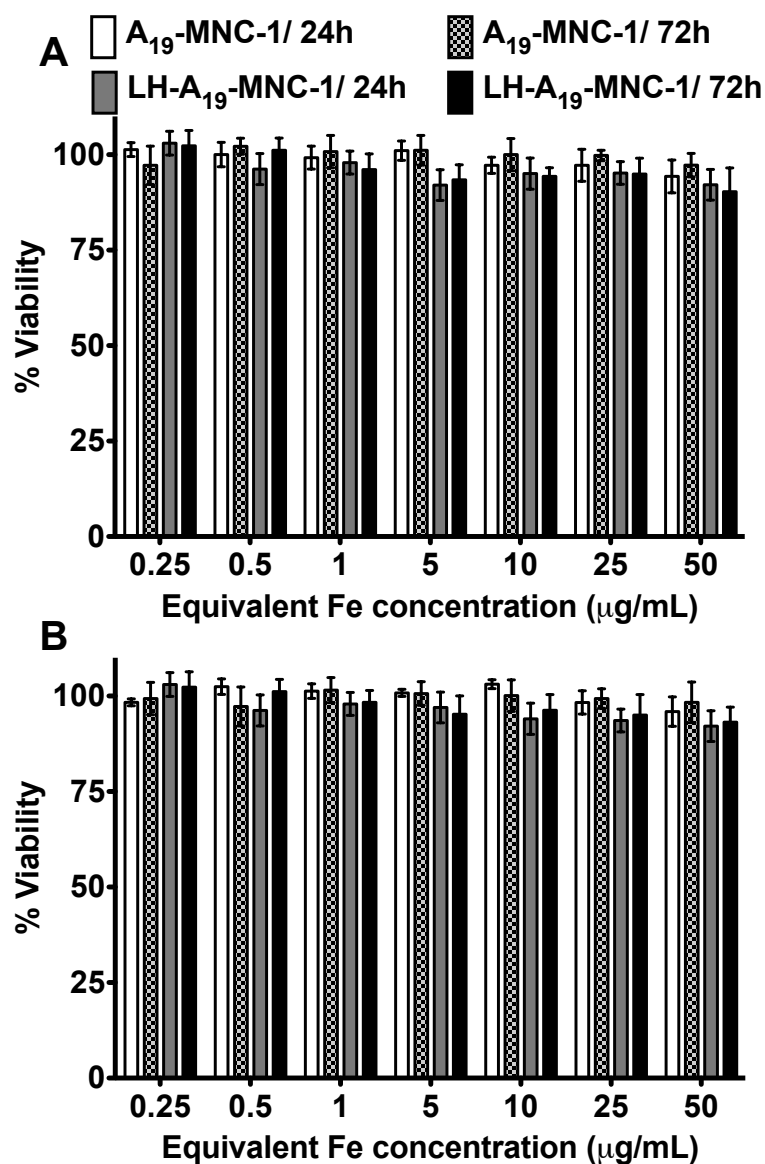
Figure 2.17. Formulation toxicity of unloaded non-targeted A_{19}-MNC-1 and targeted LH-A_{19}-MNC-1 formulations in (**A**) A2780-WT and (**B**) A2780-CisR cells. Cells were seeded in 96-well plates at a density of $3\cdot10^3$ cells/well and incubated at 37°C in 5% CO_2. After 24 h, they were treated with various concentrations of the said formulations and further incubated for 24h or 72h. At the end of each treatment period cell viability was measured by MTT assay. Mean ± SD (n = 12).

2.3.9. ANTI-CANCER OF LHRHr-TARGETED CISPLATIN-LOADED MNCS IN OVARIAN CANCER CELLS
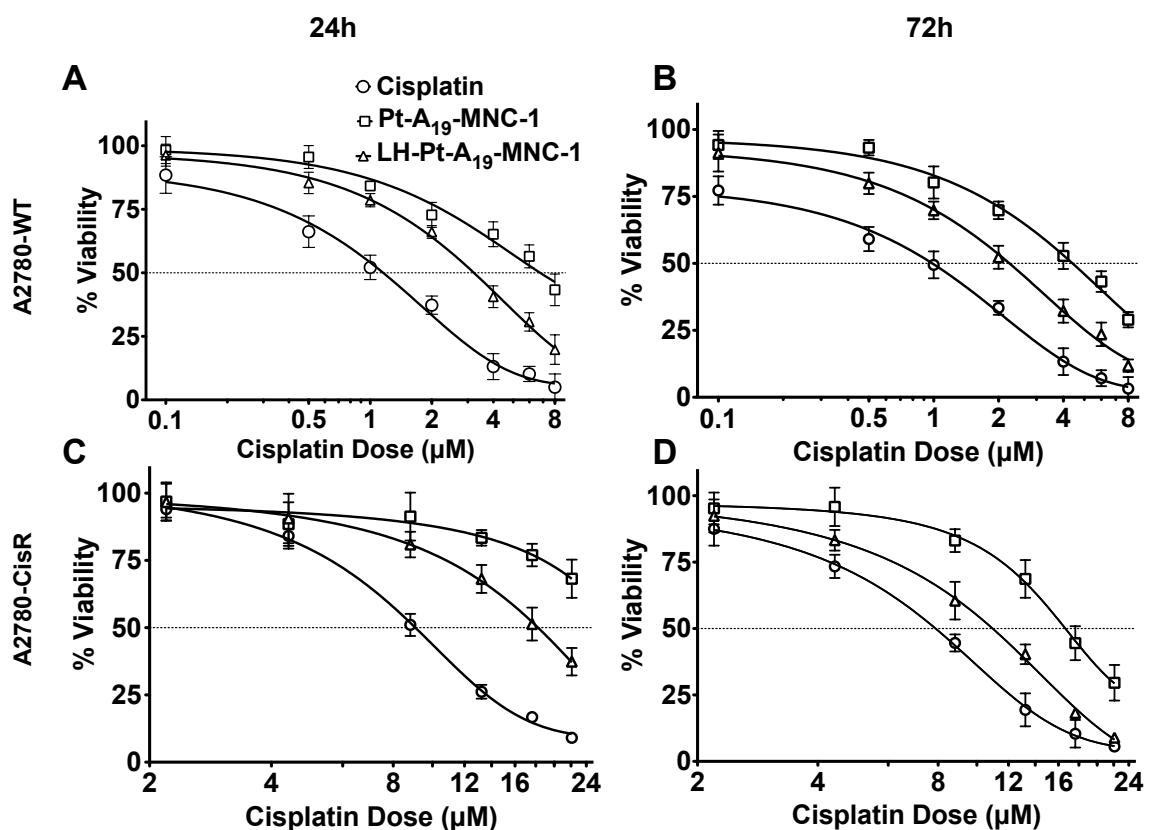
Figure 2.18. Cytotoxic efficacy of cisplatin and LHRH-targeted and untargeted cisplatin-loaded MNCs in (**A, B**) A2780-WT and (**C, D**) A2780-CisR cells exposed for drugs for (**A, C**) 24 h and (**B, D**) 72 h. Data are mean ± SD (n = 6).

Prior to evaluating the anticancer activity of drug formulations the toxicity of unloaded MNCs was determined in A2780-WT and A278-CisR cells. The cells were incubated with various concentrations of A_{19}-MNC-1 and LH-A_{19}-MNC-1 for 24 h and 72 hours and cell viability was measured by a MTT assay. The unloaded formulations did not show toxicity in a broad range of concentrations (**Figure 2.17**) and they were further used to assess the anticancer activity of the drug loaded MNCs.

The anticancer activity of LHRH-targeted and untargeted cisplatin-loaded MNCs was determined in A2780-WT and A278-CisR cells after 24 and 72-hour treatments. The two time points were used initially to exclude possible effects of the release of the drug into

the extracellular media from the untargeted and targeted MNCs. However, the observed trends in cytotoxicity were essentially the same for both exposure times. As expected, the untargeted Pt-A_{19}-MNC-1 was several folds less active compared to the free cisplatin in both A2780-WT and A2780-CisR cells (**Figure 2.18 and Table 2.8**). LH-Pt-A_{19}-MNC-1 was more active compared to untargeted Pt-A_{19}-MNC-1 in both cell lines. Although LH-Pt-A_{19}-MNC-1 was still less active than the free drug in the resistant cells, its IC_{50} was close to that of cisplatin (10.9 μM vs 7.9 μM; 72 h). This trend in activity of MNC formulations is consistent with the slow and low cellular uptake of the untargeted MNCs and somewhat faster uptake of the LHRH targeted particles. Since, as discussed above, during the cell exposure time the free drug may release from nanoparticles into the extracellular media and contribute to cytotoxicity, the "actual" difference in the activity of the targeted and untargeted MNCs could be even greater than revealed herein.

Table 2.7. IC_{50} values of different treatment groups in A2780-WT and cisplatin resistant A2780-CisR ovarian cancer cell lines.

Exposure time[a]	Treatment	IC_{50} values (μM)	
		A2780-WT	A2780-CisR (μM)
24 h	Cisplatin	1.1	9.1
	Pt-A_{19}-MNC-1	6.8	28.6
	LH-Pt-A_{19}-MNC-1	3.2	18.3
72 h	Cisplatin	0.9	7.9
	Pt-A_{19}-MNC-1	4.4	16.7
	LH-Pt-A_{19}-MNC-1	2.3	10.9

2.3.10. IN-VITRO EVALUATION OF THE MRI POTENTIAL OF MNCS
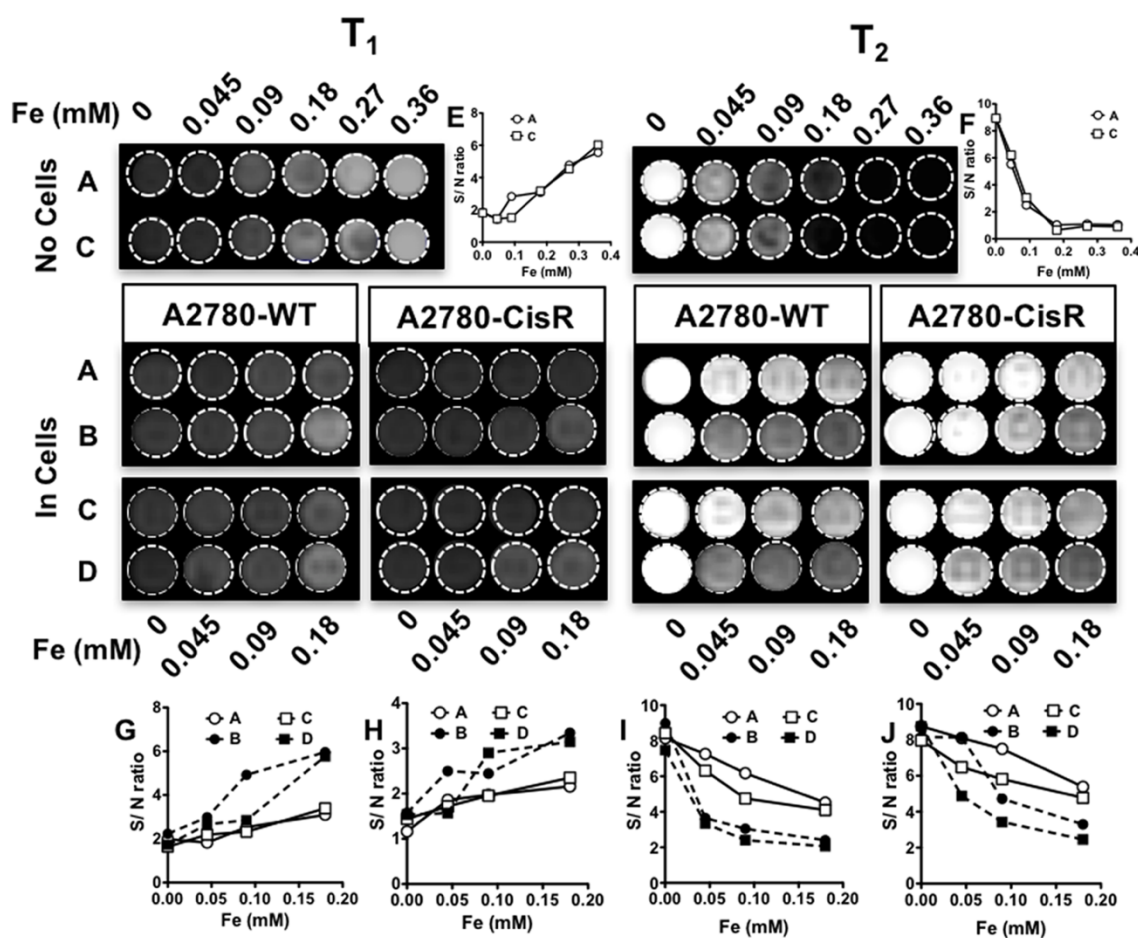
Figure 2.19: *In vitro* evaluation of MRI potential of different formulations T_1 and T_2 images of phantom gels of A2780-WT and A2780-CisR cells incubated with different concentrations of (**A**) A_{19}-MNC-1, (**B**) LH-A_{19}-MNC-1 (**C**) Pt-A_{19}-MNC-1 and (**D**) LH-Pt-A_{19}-MNC-1. The image contrasts are compared with those obtained from serial dilutions of A_{19}-MNC-1 and Pt-A_{19}-MNC-1 in the absence of cells (top). The signal-to-noise (S/N) ratios for the different sets of contrasts were plotted against the corresponding Fe concentrations to quantitatively compare the contrasts obtained by the four different formulations A-D. The comparisons of S/ N ratios of T_1 and T_2-weighted contrasts of formulations A and C in phantoms with no cells are represented in **Figures E and F** respectively. **Figures G and I** represent the S/N ratios of T_1 and T_2-weighted contrasts in phantoms of A2870-WT cells while **Figures H and J** represent the same of A2780-CisR cells incubated with different concentrations of formulations A-D.

The effect of LHRHr targeting on the MRI capability of the formulations was studied in both cell lines. Following 24 hours of incubation with different unloaded and cisplatin loaded MNCs A_{19}-MNC-1, LH-A_{19}-MNC-1, Pt-A_{19}-MNC-1 and LH-Pt-A_{19}-MNC-1 at various Fe concentrations, the cells were washed with 1X PBS, harvested and. $9 \cdot 10^6$ live cells per group were molded into agar and scanned in the Seimens 3T human MR scanner to obtain T_1 and T_2-weighted contrast images (**Figure 2.19**). MNPs are predominantly used as negative (T_2) contrast agents. The negative contrast was indeed more prominent and showed a dose-dependent increase. LHRH conjugation promoted cellular uptake of LH-Pt-A_{19}-MNC-1 and resulted in greater T_2 contrast and this was more profound in the A2780-WT cells that took up more material than A2780-CisR. In line with the relaxivity values, the presence of cisplatin resulted in greater contrasts irrespective of the presence of LHRH. This was more obvious in the case of A2780-CisR cells than in A2780-WT cells due to overexposure in the latter. Overall, when compared to the contrast obtained with the phantom gels the targeted MNCs provided significant T_2 contrast even after internalization within the cells.

2.4. DISCUSSION

Thus, to summarize, we have developed the new superparamagnetic nanoformulations for drug delivery and MRI and demonstrated 1) their use as carriers for a chemotherapeutic drug, cisplatin, 2) their targeted receptor mediated delivery into drug resistant and sensitive ovarian cancer cells and 3) and their potential use as MR contrast agents for future theranostic applications. Structurally, these systems are distant relatives of previously described nanogels or polymeric micelles with cross-linked polyion cores and PEG shells that have been synthesized using the anionic block copolymers, including PLE-*b*-PEG.[30, 36, 70, 71] However, instead of chemical crosslinks the polyion chains of the block copolymers are physically cross-linked through ionic interactions with the magnetite MNPs that bind these chains to each other.

To synthesize the MNPs we employed a well-established method of thermal decomposition of Fe(acac)$_3$, which is a simple one-pot technique allowing to access relatively uniform MNPs having good magnetization properties. In this method the solvent serves as a mild surfactant as well as a reducing agent.[39] The sizes of the MNPs are governed by the rate of heating while magnetic properties depend on the annealing temperature and duration of the reaction.[72, 73] High boiling point solvents such as benzyl ether (298°C) are known to allow for shortening of the duration of synthesis but require additional surfactants and reducing agents.[74] We show herein that in spite of a relatively lower reflux temperature in benzyl alcohol, the nucleation and growth phases could be effectively controlled in this solvent by altering the rate of reaction thereby enabling control over the core size.

Formation of nanoclusters by unmodified block copolymers was governed by the PLE block length. There exists a complex interplay of the electrostatic interaction between the carboxylate groups and magnetite surface and the steric hindrance due to the presence

of the bulkier PEG block during the cluster formation step. The increase in the number of anchoring groups has been shown to reduce aggregation due to incomplete surface coating of the MNPs and form more stable clusters of MNPs. [75] The shortest block copolymer PLE_{10}-PEG_{113} resulted in interactions of single polymer chain with different MNPs resulting in higher degree of catenation as well as more MNPs per cluster. The steric hindrance due to the PEG block eventually curbed the cluster formation process. However, the so formed E10-MNC nanoclusters had incomplete surface coverage and hence were also the least stable. Colloidal stabilities of the MNPs of defined size obtained by this method in aqueous dispersion were obtained by using biodegradable ALN-modified PLE-*b*-PEG block copolymer.[70] Hydrogels of carboxylated polymers are known to exhibit significant swelling behavior at physiological pH due to the presence of charged carboxylate groups.[76-78] In the case of crosslinked nanogels formed by anionic block copolymers such as PLE-*b*-PEG, swelling results in significant increase in the particle size that is varied by changing the crosslinking degree. Moreover, crosslinking can significantly enhance the colloidal stability of nanogels and define the rate of the release of the encapsulated payload.[70, 79]

In this work we have demonstrated that MNCs, can be successfully stabilized by introducing sufficient amount of ALN bis-phosphonate groups onto the PLE block that tightly anchor the copolymer to the MNP surface. Cisplatin loading in the MNCs was successfully achieved by coordinating the drug with a fraction of the remaining carboxylic and phosphonate groups of the PLE chains. The presence of MNPs did not hinder the loading as was evident from the relatively high LC values. The drug loaded MNCs exhibited sustained drug release profiles that were altered by changing the number of bis-phosphonate "cross-links" between the polymer and the MNPs. The utilization of a few carboxylate groups for cisplatin loading did not hamper the colloidal stability of the

formulations. The samples were intact and did not undergo any aggregation throughout the study period. In addition, we postulate that cisplatin loading can, in fact, further increase the stability and integrity of the formulation by simultaneously crosslinking the polymer chains within the cluster.

Recently, Pothayee et al.[80] developed theranostic MNCs by adsorbing the polyacrylate block of an amino functional poly(ethylene glycol-*b*-acrylate) (H_2N-PEG-*b*-PAA) copolymer onto magnetite MNP and loaded these MNCs with a cationic antibacterial drug, gentamycin through electrostatic interactions. Despite some similarities that can be found with this prior work there were major differences with our nanoformulations. First, in contrast to H_2N-PEG-*b*-PAA the PLE-*b*-PEG used here has a biodegradable PLE block, which is essential for the use of this nanoformulation for systemic drug delivery. Second, H_2N-PEG-*b*-PAA chains were covalently cross-linked via non-degradable PEG diacrylate oligomer to form the nanoclusters. In this work we introduced controlled levels of bisphosphonate groups onto the PLE block via ALN addition. The bisphosphonates form stronger links to both the magnetite and the Pt from cisplatin than having only carboxylates present. These interactions allow for facile non-covalent self-assembly of MNCs. Such clusters based on ALN-modified PLE have stable colloidal sizes in physiological pH and ionic strength. Selection of an appropriate polymer coating is critical to ensure colloidal stability, high drug loading capacity, biocompatibility and biodegradability and long circulation time of the MNP-based nanoformulations. Block copolymers comprising biodegradable charged polyaminoacid chains can serve as ideal stabilizing agents for formation of MNCs. In our case, the resulting MNCs contained an excess of carboxyl and bisphosphonate groups that were used to load an anticancer drug, cisplatin. Since the loading proceeded through coordination of the drug with the ionic groups, it increased as

the amount of these groups was increased and achieved a maximum of 17.6%, which is an excellent LC value for a nanoformulation used in cancer therapy.

A key element in our nanoformulation design is the decoration of MNCs with a targeting moiety to increase accumulation of the MNCs and their payload in ovarian cancer cells. Ovarian cancer represents a major health problem accounting for about 22,000 new cases and over 14,000 deaths annually in the US alone.[28] In spite of the dose limiting nephrotoxicity and other severe side effects,[29] cisplatin still remains the first line of treatment for ovarian cancer. To address the toxicity and delivery issues of cisplatin the drug has previously been loaded into various polymeric nanocarriers.[71] Attempts of targeted delivery of cisplatin have also been reported. For example, cisplatin has been incorporated within the folate-decorated crosslinked PEG-*b*-polymethacrylate (PEG-*b*-PMA) nanogels to treat the folate receptor positive ovarian cancer tumor in mice.[30] Here we targeted LHRHr that is overexpressed in more than 70% of human ovarian cancers as well as several other cancers.[31, 32, 81] These receptors are not present in most visceral organs, which could help reducing the off-target delivery of the nanoformulations to normal tissues and decrease side effects. The LHRH peptide, a synthetic analogue of the natural hormone has successfully been used to improve delivery of chemotherapeutic agents to LHRHr overexpressing tumors.[74] We also previously used this approach with LHRH-decorated PEG-b-PMA nanogels loaded with cisplatin to target LHRHr-positive ovarian cancer in mice.[36] In a separate study MNPs were conjugated directly with LHRH-peptide in order to improve the uptake of such MNPs in LHRH overexpressing breast cancer cells.[37]

As expected, decoration of the MNCs with LHRH resulted in the increased uptake of both MNPs and the drug presumably due to the LHRHr-mediated endocytosis of the targeted nanoformulation.[82-84] This translated to increased cytotoxic effects of the targeted

nanoformulated drug in both cisplatin-sensitive and resistant cancer cells. Notably, cisplatin loaded in untargeted nanoformulations was also active albeit much less than the free drug. The differences between the free and nanoformulated drug were minimal in the drug resistant cell line. Interestingly, our targeted nanoformulations were somewhat more active in A2780 cells in comparison to previously reported LHRH-decorated PEG-b-PMA nanogels loaded with cisplatin (24 h $IC_{50} \approx 30$ µM).[36] We attribute the enhanced efficacy of our new nanofomulation to the biodegradability of PLE-b-PEG in the lysosomal compartments, which can enhance the drug release.[71] As MNCs accumulate in endosomal-lysosomal organelles, the drug release is triggered by acidic pH in these organelles. Hydrolysis of the neutral cisplatin molecule inside the cells results in aquation of the molecule involving displacement of the chlorine ligand with water. LHRH targeting further increases influx of the drug-loaded MNCs in the targeted cancer cells where the paucity of chloride ions facilitates drug activation. The activated cationic mono- and di-aqua complexes of cisplatin are thereby released and trapped within the target cells where they intercalate with the N7 atoms of the purines in the DNA base pairs, which prevents DNA repair and DNA replication and leads to cell death.[71, 85, 86] By incorporating cisplatin in the targeted MNCs one can protect the drug from premature aquation in the blood that is responsible for undesired side effects and more selectively affect tumor cells.

Interestingly we also show here that targeting can improve the MRI imaging of cancer cells, which is consistent with increased uptake of LHRH-decorated MNCs in these cells. This result reinforces the importance of tissue specific targeting in designing successful theranostic nanosystems, which can enable diagnosis as well continuous monitoring of therapy. The MNP-based MR contrast agents have been in commercial clinical use in several countries for almost a decade.[87, 88] To be clinically relevant, negative contrast agents should have higher transverse (T_2) relaxivities. Transverse relaxivity is governed

by several factors such as MNP core size, chemical nature, oxidation state, applied magnetic field, site-specific uptake and proximity of the metal ions to the water.[89-92] A formulation that enables deeper penetration of the water molecules towards the magnetic core allows for faster relaxation of the protons and a higher T_2-relaxivity.[82] Clusters of magnetic nanoparticles experience a greater force and magnetic moment than single, well separated MNPs in a magnetic field gradient resulting in an increase in saturation magnetization.[23] Clustering of several MNP cores into compact agglomerates has been shown to be beneficial especially in the case of T_2 relaxivity.[93, 94] It was previously reported that aggregates comprising few closely held MNPs measured with long pulse-echo times, can result in greatly improved T_2-relaxivity.[95, 96] Berret et al.[97] have shown that ionic block copolymers having an opposite charge to that of the MNPs can be successfully used to formulate stable MNCs wherein the aggregation number of the MNPs can be controlled by altering the copolymer block length. The MNCs discussed herein exhibited a similar trend, where T_2 relaxivity was governed by the cluster size and MNP loading in the clusters. In contrast the T_1 relaxivity was only marginally affected either by cluster formation or increased uptake since the primary factor governing T_1-weighted positive contrast is the MNP core size. Only ultra-small superparamagnetic iron oxide nanoparticles (less than 5-6 nm in size, are known to exhibit positive contrast enhancement as well.[98] Hence, the 9 nm MNP cores were expected to produce only marginal changes in T_1 images.

Unexpectedly, we discovered that cisplatin loading in the MNCs considerably increased the T_2 relaxivities for all of our nanoformulations. It is well known that platinum (Pt) has paramagnetic properties and incorporation of Pt in MNPs results in significant enhancement in relaxivities of FePt alloys.[99] Although our MNPs are comprised of magnetite only, we speculate that cisplatin molecules introduced in close proximity to

magnetite MNPs can play a similar role. Each mole of cisplatin can interact with two moles of carboxylate and bisphosphonate groups on the polymer chains. This can cause additional intra or inter cluster crosslinking, thereby leading to further immobilization and stabilization of the MNCs and an increase in T_2 relaxivity. Several metal-cluster compounds, made of different metals such as Pt and Ni closely held together via coordination complexes by organic ligands containing carbonyl anchor groups, have been shown to exhibit significant increase in magnetic susceptibility of the resulting clusters. [100] The magnetic moments of these 'metal-carbonyl' clusters increased with increase in metallic composition of the clusters with larger clusters. Pt in particular contributed to a small but significant increase in the net susceptibility of these clusters. The cisplatin-loaded MNCs formulated in this paper closely mimic such metal-carbonyl clusters and the loaded Pt (~8wt%) can contribute significantly to the net susceptibility and hence relaxivity of the superparamagnetic MNCs. Lastly, incorporation of cisplatin can also enhance water penetration in close proximity of the MNPs by diminishing the hydrophobicity around the core, which can also further enhance the T_2 contrast capability of the cisplatin-loaded MNC formulation. This effect, nonetheless, deserves further study and could play positive role in theranostic applications using cisplatin loaded MNCs.

2.4. CONCLUSION

We have produced stable MNCs by reacting magnetite MNPs with the biodegradable PLE50-PEG113 block copolymer having ALN anchor groups attached to some of the carboxylic group of the PLE via polymer-analogous modification. The resulting MNCs were loaded with cisplatin using remaining carboxylic and bisphosphonate groups of the PLE. The MNCs were decorated with the LHRH as the targeting groups to enhance delivery of the nanoformulations to ovarian cancer cells overexpressing LHRHr. The LHRH modification enhanced uptake of the MNCs and their drug and MNP payload in the wild-type as well as cisplatin-resistant ovarian cancer cells. Enhanced uptake further translated into superior MRI contrast and significant enhancement in cytotoxicity of the nanoformulated drug. Thus, theranostic nanoformulations were developed here that can be applied for simultaneous MR imaging and targeted drug delivery in cancer cells. The encouraging in vitro results certainly warrant further investigation of the in vivo efficacy of the proposed theranostic nanosystem.

2.5. FUTURE DIRECTIONS

Our *in vitro* studies have demonstrated that MNCs formulated with ALN-modified PLE_{50}-b-PEG_{113} polymer are relatively non-toxic as carriers of potent anti-cancer agents such as cisplatin. The results of in vitro cytotoxicity studies of the LHRHr-targeted formulations in ovarian cancer cells are very encouraging and we have initiated steps in the direction of in vivo evaluation of the formulation. Apart from that, further studies will be aimed at increasing the loading capacity of MNPs and therapeutic payloads in the formulation. We aim to do this by employing a polymer with a longer PLE block such as PLE_{100}. Further refinements in the bisphosphonate conjugation procedure have enabled us to achieve higher D_{conj} on PLE_{100}-*b*-PEG_{113} polymer. For theranostic formulations such as these it is extremely important to strike a correct balance between the contrast agents and the therapeutic agents. Finally, we aim to extend the application of these theranostic MNCs by exploring potential targeting to other malignancies such as glioblastoma and prostate cancer. Our choice of these types of cancers is guided by the fact that till MRI is one of the most efficient contrast systems for imaging of the brain with maximum details. We aim to study, if our biocompatible and biodegradable MNC formulations can address this need, which we perceive as an unmet one.

2.6. REFERENCES.

1. Torchilin, V.; Zhou, F.; Huang, L., pH-sensitive liposomes. *J. Liposome Res.* **1993,** 3, 201-255.

2. Wang, X.-q.; Dai, J.-d.; Chen, Z.; Zhang, T.; Xia, G.-m.; Nagai, T.; Zhang, Q., Bioavailability and pharmacokinetics of cyclosporine A-loaded pH-sensitive nanoparticles for oral administration. *J. Controlled Release* **2004,** 97, 421-429.

3. Du, J.-Z.; Du, X.-J.; Mao, C.-Q.; Wang, J., Tailor-made dual pH-sensitive polymer–doxorubicin nanoparticles for efficient anticancer drug delivery. *J. Am. Chem. Soc.* **2011,** 133, 17560-17563.

4. Sershen, S.; Westcott, S.; Halas, N.; West, J., Temperature-sensitive polymer–nanoshell composites for photothermally modulated drug delivery. *J. Biomed. Mater. Res.* **2000,** 51, 293-298.

5. Na, K.; Lee, K. H.; Lee, D. H.; Bae, Y. H., Biodegradable thermo-sensitive nanoparticles from poly (L-lactic acid)/poly (ethylene glycol) alternating multi-block copolymer for potential anti-cancer drug carrier. *Eur. J. Pharm. Sci.* **2006,** 27, 115-122.

6. Nuopponen, M.; Tenhu, H., Gold nanoparticles protected with pH and temperature-sensitive diblock copolymers. *Langmuir* **2007,** 23, 5352-5357.

7. Cheng, R.; Meng, F.; Deng, C.; Klok, H.-A.; Zhong, Z., Dual and multi-stimuli responsive polymeric nanoparticles for programmed site-specific drug delivery. *Biomaterials* **2013,** 34, 3647-3657.

8. Li, J.; Huo, M.; Wang, J.; Zhou, J.; Mohammad, J. M.; Zhang, Y.; Zhu, Q.; Waddad, A. Y.; Zhang, Q., Redox-sensitive micelles self-assembled from amphiphilic hyaluronic acid-deoxycholic acid conjugates for targeted intracellular delivery of paclitaxel. *Biomaterials* **2012,** 33, 2310-2320.

9. Nguyen, D. H.; Choi, J. H.; Joung, Y. K.; Park, K. D., Disulfide-crosslinked heparin-pluronic nanogels as a redox-sensitive nanocarrier for intracellular protein delivery. *J. Bioact. Compatible Polym.* **2011,** 26, 287-300.

10. Reiss, G.; Hütten, A., Magnetic nanoparticles: applications beyond data storage. *Nat. Mater.* **2005,** 4, 725-726.

11. Terris, B.; Thomson, T., Nanofabricated and self-assembled magnetic structures as data storage media. *J. Phys. D: Appl. Phys.* **2005,** 38, R199.

12. Liu, J.-f.; Zhao, Z.-s.; Jiang, G.-b., Coating Fe3O4 Magnetic Nanoparticles with Humic Acid for High Efficient Removal of Heavy Metals in Water. *Environ. Sci. Technol.* **2008,** 42, 6949-6954.

13. Pankhurst, Q. A.; Connolly, J.; Jones, S.; Dobson, J., Applications of magnetic nanoparticles in biomedicine. *J. Phys. D: Appl. Phys.* **2003,** 36, R167.

14. Perez, J. M.; Simeone, F. J.; Saeki, Y.; Josephson, L.; Weissleder, R., Viral-induced self-assembly of magnetic nanoparticles allows the detection of viral particles in biological media. *J. Am. Chem. Soc.* **2003,** 125, 10192-10193.

15. Gu, H.; Ho, P.-L.; Tsang, K. W.; Wang, L.; Xu, B., Using biofunctional magnetic nanoparticles to capture vancomycin-resistant enterococci and other gram-positive bacteria at ultralow concentration. *J. Am. Chem. Soc.* **2003,** 125, 15702-15703.

16. Wang, L.; Yang, Z.; Gao, J.; Xu, K.; Gu, H.; Zhang, B.; Zhang, X.; Xu, B., A biocompatible method of decorporation: bisphosphonate-modified magnetite nanoparticles to remove uranyl ions from blood. *J. Am. Chem. Soc.* **2006,** 128, 13358-13359.

17. Tombach, B.; Reimer, P.; Bremer, C.; Allkemper, T.; Engelhardt, M.; Mahler, M.; Ebert, W.; Heindel, W., First-pass and equilibrium-MRA of the aortoiliac region with a

superparamagnetic iron oxide blood pool MR contrast agent (SH U 555 C): results of a human pilot study. *NMR Biomed.* **2004,** 17, 500-506.

18. Allkemper, T.; Bremer, C.; Matuszewski, L.; Ebert, W.; Reimer, P., Contrast-enhanced Blood-Pool MR Angiography with Optimized Iron Oxides: Effect of Size and Dose on Vascular Contrast Enhancement in Rabbits. *Radiology* **2002,** 223, 432-438.

19. Taylor, A. M.; Panting, J. R.; Keegan, J.; Gatehouse, P. D.; Amin, D.; Jhooti, P.; Yang, G. Z.; McGill, S.; Burman, E. D.; Francis, J. M.; Firmin, D. N.; Pennell, D. J., Safety and preliminary findings with the intravascular contrast agent NC100150 injection for MR coronary angiography. *Journal of Magnetic Resonance Imaging* **1999,** 9, 220-227.

20. Sosnovik, D. E.; Nahrendorf, M.; Weissleder, R., Molecular Magnetic Resonance Imaging in Cardiovascular Medicine. *Circulation* **2007,** 115, 2076-2086.

21. Jain, T. K.; Foy, S. P.; Erokwu, B.; Dimitrijevic, S.; Flask, C. A.; Labhasetwar, V., Magnetic resonance imaging of multifunctional pluronic stabilized iron-oxide nanoparticles in tumor-bearing mice. *Biomaterials* **2009,** 30, 6748-6756.

22. Gu, H.; Xu, K.; Xu, C.; Xu, B., Biofunctional magnetic nanoparticles for protein separation and pathogen detection. *Chem. Commun.* **2006**, 941-949.

23. Zhang, Q.; Thompson, M. S.; Carmichael-Baranauskas, A. Y.; Caba, B. L.; Zalich, M. A.; Lin, Y.-N.; Mefford, O. T.; Davis, R. M.; Riffle, J. S., Aqueous Dispersions of Magnetite Nanoparticles Complexed with Copolyether Dispersants: Experiments and Theory. *Langmuir* **2007,** 23, 6927-6936.

24. Enochs, W. S.; Harsh, G.; Hochberg, F.; Weissleder, R., Improved delineation of human brain tumors on MR images using a long-circulating, superparamagnetic iron oxide agent. *J. Magn. Reson. Imaging* **1999,** 9, 228-232.

25. Yu, M. K.; Jeong, Y. Y.; Park, J.; Park, S.; Kim, J. W.; Min, J. J.; Kim, K.; Jon, S., Drug-Loaded Superparamagnetic Iron Oxide Nanoparticles for Combined Cancer Imaging and Therapy In Vivo. *Angew. Chem. Int. Ed.* **2008,** 47, 5362-5365.

26. Sanson, C.; Diou, O.; Thevenot, J.; Ibarboure, E.; Soum, A.; Brûlet, A.; Miraux, S.; Thiaudière, E.; Tan, S.; Brisson, A., Doxorubicin loaded magnetic polymersomes: theranostic nanocarriers for MR imaging and magneto-chemotherapy. *ACS nano* **2011,** 5, 1122-1140.

27. Jain, T. K.; Richey, J.; Strand, M.; Leslie-Pelecky, D. L.; Flask, C. A.; Labhasetwar, V., Magnetic nanoparticles with dual functional properties: drug delivery and magnetic resonance imaging. *Biomaterials* **2008,** 29, 4012-4021.

28. Jayson, G. C.; Kohn, E. C.; Kitchener, H. C.; Ledermann, J. A., Ovarian cancer. *The Lancet* 384, 1376-1388.

29. Florea, A.-M.; Büsselberg, D., Cisplatin as an anti-tumor drug: cellular mechanisms of activity, drug resistance and induced side effects. *Cancers (Basel)* **2011,** 3, 1351-1371.

30. Nukolova, N. V.; Oberoi, H. S.; Cohen, S. M.; Kabanov, A. V.; Bronich, T. K., Folate-decorated nanogels for targeted therapy of ovarian cancer. *Biomaterials* **2011,** 32, 5417-5426.

31. Ohno, T.; Imai, A.; Furui, T.; Takahashi, K.; Tamaya, T., Presence of gonadotropin-releasing hormone and its messenger ribonucleic acid in human ovarian epithelial carcinoma. *Am. J. Obstet. Gynecol.* **1993,** 169, 605-610.

32. Emons, G.; Pahwa, G. S.; Brack, C.; Sturm, R.; Oberheuser, F.; Knuppen, R., Gonadotropin releasing hormone binding sites in human epithelial ovarian carcinomata. *Eur. J. Cancer Clin. Oncol.* **1989,** 25, 215-221.

33. Völker, P.; Gründker, C.; Schmidt, O.; Schulz, K.-D.; Emons, G., Expression of receptors for luteinizing hormone-releasing hormone in human ovarian and endometrial cancers: frequency, autoregulation, and correlation with direct antiproliferative activity of luteinizing hormone-releasing hormone analogues. *Am. J. Obstet. Gynecol.* **2002,** 186, 171-179.

34. Dharap, S.; Wang, Y.; Chandna, P.; Khandare, J.; Qiu, B.; Gunaseelan, S.; Sinko, P.; Stein, S.; Farmanfarmaian, A.; Minko, T., Tumor-specific targeting of an anticancer drug delivery system by LHRH peptide. *Proc. Natl. Acad. Sci. U.S.A.* **2005,** 102, 12962-12967.

35. Dharap, S.; Qiu, B.; Williams, G.; Sinko, P.; Stein, S.; Minko, T., Molecular targeting of drug delivery systems to ovarian cancer by BH3 and LHRH peptides. *J. Controlled Release* **2003,** 91, 61-73.

36. Nukolova, N. V.; Oberoi, H. S.; Zhao, Y.; Chekhonin, V. P.; Kabanov, A. V.; Bronich, T. K., LHRH-Targeted Nanogels as a Delivery System for Cisplatin to Ovarian Cancer. *Mol. Pharm.* **2013,** 10, 3913-3921.

37. Kumar, C. S.; Leuschner, C.; Urbina, M.; Ozkaya, T.; Hormes, J., Glutaric acid as a spacer facilitates improved intracellular uptake of LHRH–SPION into human breast cancer cells. *Int. J. Nanomed.* **2007,** 2, 175.

38. van Dam, G. M.; Themelis, G.; Crane, L. M.; Harlaar, N. J.; Pleijhuis, R. G.; Kelder, W.; Sarantopoulos, A.; de Jong, J. S.; Arts, H. J.; van der Zee, A. G., Intraoperative tumor-specific fluorescence imaging in ovarian cancer by folate receptor-[alpha] targeting: first in-human results. *Nat. Med.* **2011,** 17, 1315-1319.

39. Pinna, N.; Grancharov, S.; Beato, P.; Bonville, P.; Antonietti, M.; Niederberger, M., Magnetite Nanocrystals: Nonaqueous Synthesis, Characterization, and Solubility†. *Chem. Mater.* **2005,** 17, 3044-3049.

40. Kovačevič, M.; Gartner, A.; Novič, M., Determination of bisphosphonates by ion chromatography–inductively coupled plasma mass spectrometry. *J. Chromatogr. A* **2004,** 1039, 77-82.

41. Elhabiri, M.; Abada, S.; Sy, M.; Nonat, A.; Choquet, P.; Esteban-Gómez, D.; Cassino, C.; Platas-Iglesias, C.; Botta, M.; Charbonnière, L. J., Importance of Outer-Sphere and Aggregation Phenomena in the Relaxation Properties of Phosphonated Gadolinium Complexes with Potential Applications as MRI Contrast Agents. *Chemistry-A European Journal* **2015,** 21, 6535-6546.

42. Goff, J.; Huffstetler, P.; Miles, W.; Pothayee, N.; Reinholz, C.; Ball, S.; Davis, R.; Riffle, J., Novel phosphonate-functional poly (ethylene oxide)-magnetite nanoparticles form stable colloidal dispersions in phosphate-buffered saline. *Chem. Mater.* **2009,** 21, 4784-4795.

43. Sun, S.; Murray, C.; Weller, D.; Folks, L.; Moser, A., Monodisperse FePt nanoparticles and ferromagnetic FePt nanocrystal superlattices. *Science* **2000,** 287, 1989-1992.

44. Shevchenko, E. V.; Talapin, D. V.; Rogach, A. L.; Kornowski, A.; Haase, M.; Weller, H., Colloidal Synthesis and Self-Assembly of CoPt3 Nanocrystals. *J. Am. Chem. Soc.* **2002,** 124, 13958-13958.

45. Jang, J.-H.; Lee, E.; Park, J.; Kim, G.; Hong, S.; Kwon, Y.-U., Rational syntheses of core-shell Fex@Pt nanoparticles for the study of electrocatalytic oxygen reduction reaction. *Sci. Rep.* **2013,** 3.

46. Kanczler, J. M.; Sura, H. S.; Magnay, J.; Green, D.; Oreffo, R. O.; Dobson, J. P.; El Haj, A. J., Controlled differentiation of human bone marrow stromal cells using magnetic nanoparticle technology. *Tissue Eng Part A* **2010,** 16, 3241-3250.

47. Herzer, G., Grain structure and magnetism of nanocrystalline ferromagnets. *Magnetics, IEEE Transactions on* **1989,** 25, 3327-3329.

48. Yoon, T. J.; Lee, H.; Shao, H.; Weissleder, R., Highly magnetic core–shell nanoparticles with a unique magnetization mechanism. *Angew. Chem. Int. Ed.* **2011,** 50, 4663-4666.

49. Lu, A. H.; Salabas, E. e. L.; Schüth, F., Magnetic nanoparticles: synthesis, protection, functionalization, and application. *Angew. Chem. Int. Ed.* **2007,** 46, 1222-1244.

50. Taqaddas, A., Use of Magnetic Nanoparticles in Cancer Detection with MRI. *International Journal of Medical, Health, Biomedical, Bioengineering and Pharmaceutical Engineering* **2014,** 8, 91-99.

51. Koo, Y.-E. L.; Reddy, G. R.; Bhojani, M.; Schneider, R.; Philbert, M. A.; Rehemtulla, A.; Ross, B. D.; Kopelman, R., Brain cancer diagnosis and therapy with nanoplatforms. *Adv. Drug Del. Rev.* **2006,** 58, 1556-1577.

52. Stephen, Z. R.; Kievit, F. M.; Zhang, M., Magnetite nanoparticles for medical MR imaging. *Mater. Today* **2011,** 14, 330-338.

53. Owens, D. E.; Peppas, N. A., Opsonization, biodistribution, and pharmacokinetics of polymeric nanoparticles. *Int. J. Pharm.* **2006,** 307, 93-102.

54. Otsuka, H.; Nagasaki, Y.; Kataoka, K., PEGylated nanoparticles for biological and pharmaceutical applications. *Adv. Drug Del. Rev.* **2012,** 64, 246-255.

55. Li, C., Poly(l-glutamic acid)–anticancer drug conjugates. *Adv. Drug Del. Rev.* **2002,** 54, 695-713.

56. Kishore, B.; Lambricht, P.; Laurent, G.; Maldague, P.; Wagner, R.; Tulkens, P. M., Mechanism of protection afforded by polyaspartic acid against gentamicin-induced

phospholipidosis. II. Comparative in vitro and in vivo studies with poly-L-aspartic, poly-L-glutamic and poly-D-glutamic acids. *J. Pharmacol. Exp. Ther.* **1990,** 255, 875-885.

57. Sajadi, S., Metal ion-binding properties of L-glutamic acid and L-aspartic acid, a comparative investigation. *Natural Science* **2010,** 2, 85.

58. Xu, C.; Xu, K.; Gu, H.; Zheng, R.; Liu, H.; Zhang, X.; Guo, Z.; Xu, B., Dopamine as a robust anchor to immobilize functional molecules on the iron oxide shell of magnetic nanoparticles. *J. Am. Chem. Soc.* **2004,** 126, 9938-9939.

59. Frey, N. A.; Peng, S.; Cheng, K.; Sun, S., Magnetic nanoparticles: synthesis, functionalization, and applications in bioimaging and magnetic energy storage. *Chem. Soc. Rev.* **2009,** 38, 2532-2542.

60. Xie, J.; Liu, G.; Eden, H. S.; Ai, H.; Chen, X., Surface-engineered magnetic nanoparticle platforms for cancer imaging and therapy. *Acc. Chem. Res.* **2011,** 44, 883-892.

61. Pothayee, N.; Balasubramaniam, S.; Davis, R. M.; Riffle, J. S.; Carroll, M. R. J.; Woodward, R. C.; St. Pierre, T. G., Synthesis of 'ready-to-adsorb' polymeric nanoshells for magnetic iron oxide nanoparticles via atom transfer radical polymerization. *Polymer* **2011,** 52, 1356-1366.

62. Kim, J. O.; Kabanov, A. V.; Bronich, T. K., Polymer micelles with cross-linked polyanion core for delivery of a cationic drug doxorubicin. *J. Controlled Release* **2009,** 138, 197-204.

63. Xue, Z.; Lin, M.; Zhu, J.; Zhang, J.; Li, Y.; Guo, Z., Platinum (II) compounds bearing bone-targeting group: synthesis, crystal structure and antitumor activity. *Chem. Commun.* **2010,** 46, 1212-1214.

64. Markovsky, E.; Koroukhov, N.; Golomb, G., Additive-free albumin nanoparticles of alendronate for attenuating inflammation through monocyte inhibition. *Nanomedicine* **2007,** 2, 545-553.

65. Na, H. B.; Song, I. C.; Hyeon, T., Inorganic nanoparticles for MRI contrast agents. *Adv. Mater.* **2009,** 21, 2133-2148.

66. Strijkers, G. J.; Mulder, M.; Willem, J.; van Tilborg, F.; Geralda, A.; Nicolay, K., MRI contrast agents: current status and future perspectives. *Anticancer Agents Med. Chem.* **2007,** 7, 291-305.

67. Vre, R. M.-D.; Grimee, R.; Parmentier, F.; Binet, J., The use of agar gel as a basic reference material for calibrating relaxation times and imaging parameters. *Magn. Reson. Med.* **1985,** 2, 176-179.

68. Bi, X.; Shi, X.; Baker, J. R., Synthesis, characterization and stability of a luteinizing hormone-releasing hormone (LHRH)-functionalized poly (amidoamine) dendrimer conjugate. *J. Biomater. Sci. Polym. Ed.* **2008,** 19, 131-142.

69. Chauhan, S.; Liang, X.; Su, A.; Pai-Panandiker, A.; Shen, D.; Hanover, J.; Gottesman, M., Reduced endocytosis and altered lysosome function in cisplatin-resistant cell lines. *Br. J. Cancer* **2003,** 88, 1327-1334.

70. Desale, S. S.; Cohen, S. M.; Zhao, Y.; Kabanov, A. V.; Bronich, T. K., Biodegradable hybrid polymer micelles for combination drug therapy in ovarian cancer. *J. Controlled Release* **2013,** 171, 339-348.

71. Oberoi, H. S.; Nukolova, N. V.; Kabanov, A. V.; Bronich, T. K., Nanocarriers for delivery of platinum anticancer drugs. *Adv. Drug Del. Rev.* **2013,** 65, 1667-1685.

72. Maaz, K.; Mumtaz, A.; Hasanain, S.; Ceylan, A., Synthesis and magnetic properties of cobalt ferrite (CoFe 2 O 4) nanoparticles prepared by wet chemical route. *J. Magn. Magn. Mater.* **2007,** 308, 289-295.

73. Tung, L. D.; Kolesnichenko, V.; Caruntu, G.; Caruntu, D.; Remond, Y.; Golub, V.; O'connor, C.; Spinu, L., Annealing effects on the magnetic properties of nanocrystalline zinc ferrite. *Physica B: Condensed Matter* **2002,** 319, 116-121.

74. Sun, S.; Zeng, H., Size-controlled synthesis of magnetite nanoparticles. *J. Am. Chem. Soc.* **2002,** 124, 8204-8205.

75. Miles, W. C.; Huffstetler, P. P.; Goff, J. D.; Chen, A. Y.; Riffle, J.; Davis, R. M., Design of Stable Polyether− Magnetite Complexes in Aqueous Media: Effects of the Anchor Group, Molecular Weight, and Chain Density. *Langmuir* **2011,** 27, 5456-5463.

76. Gyenes, T.; Torma, V.; Gyarmati, B.; Zrínyi, M., Synthesis and swelling properties of novel pH-sensitive poly (aspartic acid) gels. *Acta Biomater.* **2008,** 4, 733-744.

77. Gonzales, D.; Fan, K.; Sevoian, M., Synthesis and swelling characterizations of a poly (gamma-glutamic acid) hydrogel. *J. Polym. Sci., Part A: Polym. Chem.* **1996,** 34, 2019-2027.

78. Markland, P.; Zhang, Y.; Amidon, G. L.; Yang, V. C., A pH-and ionic strength-responsive polypeptide hydrogel: synthesis, characterization, and preliminary protein release studies. *J. Biomed. Mater. Res.* **1999,** 47, 595-602.

79. Desale, S. S.; Soni, K. S.; Romanova, S.; Cohen, S. M.; Bronich, T. K., Targeted delivery of platinum-taxane combination therapy in ovarian cancer. *J. Controlled Release* **2015,** 220, 651-659.

80. Pothayee, N.; Pothayee, N.; Jain, N.; Hu, N.; Balasubramaniam, S.; Johnson, L. M.; Davis, R. M.; Sriranganathan, N.; Riffle, J., Magnetic block ionomer complexes for potential dual imaging and therapeutic agents. *Chem. Mater.* **2012,** 24, 2056-2063.

81. Srkalovic, G.; Schally, A.; Wittliff, J.; Day, T.; Jenison, E., Presence and characteristics of receptors for [D-Trp6] luteinizing hormone releasing hormone and epidermal growth factor in human ovarian cancer. *Int. J. Oncol.* **1998,** 12, 489-587.

82. Meng, J.; Fan, J.; Galiana, G.; Branca, R.; Clasen, P.; Ma, S.; Zhou, J.; Leuschner, C.; Kumar, C.; Hormes, J., LHRH-functionalized superparamagnetic iron oxide nanoparticles for breast cancer targeting and contrast enhancement in MRI. *Mater. Sci. Eng. C Mater. Biol. Appl.* **2009,** 29, 1467-1479.

83. Minko, T.; Patil, M. L.; Zhang, M.; Khandare, J. J.; Saad, M.; Chandna, P.; Taratula, O., LHRH-targeted nanoparticles for cancer therapeutics. In *Cancer Nanotechnol.*, Springer: 2010; pp 281-294.

84. Taheri, A.; Dinarvand, R.; Atyabi, F.; Ahadi, F.; Nouri, F. S.; Ghahremani, M. H.; Ostad, S. N.; Borougeni, A. T.; Mansoori, P., Enhanced anti-tumoral activity of methotrexate-human serum albumin conjugated nanoparticles by targeting with luteinizing hormone-releasing hormone (LHRH) peptide. *Int. J. Mol. Sci.* **2011,** 12, 4591-4608.

85. Pinto, A. L.; Lippard, S. J., Binding of the antitumor drug cis-diamminedichloroplatinum(II) (cisplatin) to DNA. *Biochim. Biophys. Acta* **1985,** 780, 167-180.

86. Jung, Y.; Lippard, S. J., Direct Cellular Responses to Platinum-Induced DNA Damage. *Chem. Rev.* **2007,** 107, 1387-1407.

87. Cole, A. J.; Yang, V. C.; David, A. E., Cancer theranostics: the rise of targeted magnetic nanoparticles. *Trends Biotechnol.* **2011,** 29, 323-332.

88. Singh, A.; Sahoo, S. K., Magnetic nanoparticles: a novel platform for cancer theranostics. *Drug Discovery Today* **2014,** 19, 474-481.

89. Carroll, M. R.; Woodward, R. C.; House, M. J.; Teoh, W. Y.; Amal, R.; Hanley, T. L.; St Pierre, T. G., Experimental validation of proton transverse relaxivity models for superparamagnetic nanoparticle MRI contrast agents. *Nanotechnology* **2010,** 21, 035103.

90. Carroll, M. R.; Huffstetler, P. P.; Miles, W. C.; Goff, J. D.; Davis, R. M.; Riffle, J. S.; House, M. J.; Woodward, R. C.; St Pierre, T. G., The effect of polymer coatings on proton transverse relaxivities of aqueous suspensions of magnetic nanoparticles. *Nanotechnology* **2011,** 22, 325702.

91. Roch, A.; Gossuin, Y.; Muller, R. N.; Gillis, P., Superparamagnetic colloid suspensions: water magnetic relaxation and clustering. *J. Magn. Magn. Mater.* **2005,** 293, 532-539.

92. Matsumoto, Y.; Jasanoff, A., T 2 relaxation induced by clusters of superparamagnetic nanoparticles: Monte Carlo simulations. *Magn. Reson. Imaging* **2008,** 26, 994-998.

93. Ge, J.; Hu, Y.; Biasini, M.; Beyermann, W. P.; Yin, Y., Superparamagnetic Magnetite Colloidal Nanocrystal Clusters. *Angew. Chem. Int. Ed.* **2007,** 46, 4342-4345.

94. Lee, N.; Choi, Y.; Lee, Y.; Park, M.; Moon, W. K.; Choi, S. H.; Hyeon, T., Water-Dispersible Ferrimagnetic Iron Oxide Nanocubes with Extremely High r2 Relaxivity for Highly Sensitive in Vivo MRI of Tumors. *Nano Lett.* **2012,** 12, 3127-3131.

95. Koppolu, B.; Bhavsar, Z.; Wadajkar, A. S.; Nattama, S.; Rahimi, M.; Nwariaku, F.; Nguyen, K. T., Temperature-sensitive polymer-coated magnetic nanoparticles as a potential drug delivery system for targeted therapy of thyroid cancer. *J. Biomed. Nanotechnol.* **2012,** 8, 983-990.

96. Brown, K. A.; Vassiliou, C. C.; Issadore, D.; Berezovsky, J.; Cima, M. J.; Westervelt, R. M., Scaling of transverse nuclear magnetic relaxation due to magnetic nanoparticle aggregation. *J. Magn. Magn. Mater.* **2010,** 322, 3122-3126.

97. Berret, J.-F.; Schonbeck, N.; Gazeau, F.; El Kharrat, D.; Sandre, O.; Vacher, A.; Airiau, M., Controlled clustering of superparamagnetic nanoparticles using block copolymers: design of new contrast agents for magnetic resonance imaging. *J. Am. Chem. Soc.* **2006,** 128, 1755-1761.

98. Neuwelt, E. A.; Hamilton, B. E.; Varallyay, C. G.; Rooney, W. R.; Edelman, R. D.; Jacobs, P. M.; Watnick, S. G., Ultrasmall superparamagnetic iron oxides (USPIOs): a future alternative magnetic resonance (MR) contrast agent for patients at risk for nephrogenic systemic fibrosis (NSF) &quest. *Kidney Int.* **2009,** 75, 465-474.

99. Chen, S.; Wang, L.; Duce, S. L.; Brown, S.; Lee, S.; Melzer, A.; Cuschieri, S. A.; André, P., Engineered biocompatible nanoparticles for in vivo imaging applications. *J. Am. Chem. Soc.* **2010,** 132, 15022-15029.

100. Pronk, B.; Brom, H.; De Jongh, L.; Longoni, G.; Ceriotti, A., Physical properties of metal cluster compounds I: Magnetic measurements on high-nuclearity nickel and platinum carbonyl clusters. *Solid State Commun.* **1986,** 59, 349-354.

CHAPTER 3

CATIONIC MAGNETIC NANOCLUSTERS STABILIZED BY POLY (L-LYSINE)-B- POLY (ETHYLENE GLYCOL) FOR CANCER THERANOSTICS

3.1 INTRODUCTION

Poly-L-lysine (PLK) is a cationic polypeptide that has been used as a modifier for drug-loaded nanoparticles and has been shown to enhance the cellular uptake of drugs[1] by increasing the permeability of various compounds.[2-4] This property of PLK-based polymers has been effectively exploited in designing non-viral vectors for gene and protein delivery. Cationic polymer-based non-viral vectors have been considered as favorable candidates for clinical gene therapy due to their advantages over viral vectors in numerous vital properties including low immunogenicity, easy fabrication, low cost, ease of modification and functionalization such as incorporation of targeting ligands. They were commonly used to package plasmid DNA (pDNA) into nanoscale polyplexes, which can protect pDNA from enzymatic degradation and transport genes into target cells through an endocytic pathway. In addition to PLK, numerous other polymeric gene delivery vectors have been investigated, including poly (ethyleneimine) (PEI)[5-7], chitosan[8-10], poly(amino ester)[11, 12], dendrimeric poly(amidoamine) (PAMAM)[13-15], and their block or graft copolymers with poly(ethylene glycol) (PEG). Among all, PEI and PLK are two of the mostly studied polymers as gene carriers. Both polymers possess high charge density essential for effective pDNA complexation and condensation.

The success of magnetic nanoparticles (MNPs) as theranostic agents relies on their ability to generate superior soft contrasts in the tissue of interest while simultaneously delivering a therapeutic dose to the organ. Both require significant accumulation in the organ. The type of stabilizing agent used to render hydrophilicity and stability to the otherwise hydrophobic and unstable MNPs dictates tissue accumulation of MNPs. In the previous chapter we discussed strategies of enhancing tissue specific uptake of anionic magnetic nanoclusters (MNCs) stabilized by PLE-PEG polymer modified with bisphosphonates. The high charge density of PLK-PEG block ionomers has also been employed to form stable aggregates of magnetic nanoparticles (MNPs), which have been successfully tested for a variety of biological applications. For instance, PLK-labeled MNPs have been extensively used in labeling specific cells such as stem cells[16], dendritic cells[17] and non-phagocytic T cells[18]. Wang et al.[19] observed a specific peroxidase-like activity within PLK-modified MNPs that could greatly reduce intracellular peroxide activity in labeled cancer stem cells derived from glioblastoma. The ability to introduce different functionalities on the side-chain amino groups makes PLK-stabilized MNPs a smart choice for simultaneous drug delivery and MRI.

In this study, we evaluated the efficacy of different PLK-PEG polymers in forming stable magnetic nanoclusters (MNC). Moreover, we modified the available side chain amino groups to conjugate anti-cancer agent doxorubicin onto the stable clusters via a pH sensitive hydrazone linker (DOX-MNC). This end group modification reduced the positive charge density on the clusters, which reduced the uptake-driven toxicity of the PLK-based magnetic nanoparticles. This DOX-MNC formulation exhibited excellent MRI potential with significantly high T_2 relaxivities. The stimuli-responsive drug delivery helped achieve a sustained release exclusively in an acidic environment only, thereby preventing premature leakage of the anti-cancer payload. End group modification did not hinder the intracellular

uptake of the formulations. The formulations were preferentially localized in the acidic lysosomal compartments (~pH 4.5 – 5.5)[20] of A2780 and MDA-MB-231 cancer cells where the pH-driven cleavage of the hydrazone bond resulted in drug release and significant cytotoxicity.

3.2 EXPERIMENTAL SECTION

3.2.1 MATERIALS

Chemicals: Poly (L-lysine$_x$-b-ethylene glycol$_{113}$) polymer (PLK-PEG; x = 10, 50 and 100) was purchased from Alamanda Polymers (Huntsville, AL). N-Succinimidyl 3-[2-pyridyldithio]-propionate (SPDP), iron (III) acetylacetonate (Fe(acac)$_3$), benzyl alcohol (anhydrous), nitric acid (TraceSELECT), hydrochloric acid (TraceSELECT), Fluorescamine and 3-(4,5-dimethyl thiazol-2-yl)-2,5-diphenyl tetrazolium bromide (MTT) were purchased from Sigma-Aldrich (St. Louis, MO). Acetone (histology grade), n,n-dimethylformamide (DMF), 3, 3´-N-[ε-Maleimidocaproic acid] hydrazide (EMCH), trifluoroacetic acid salt, dithiothreitol (DTT), 5,5'-dithiobis-(2-nitrobenzoic acid) (DTNB), DMSO and all other anhydrous HPLC grade organic solvents were purchased from Thermo Fisher Scientific (Waltham, MA). Doxorubicin hydrochloride salt was purchased from LC Laboratories (Woburn, MA). Alexa Fluor®-647, Lysotracker Green and Hoechst 33342 were purchased from Life Technologies (Carlsbad, CA).

Cell lines: Triple negative MDA-MB-231 breast cancer cells and wild-type A2780 ovarian cancer cells were purchased from American Type Culture Collection (ATCC, Manassas, VA). MDA-MB-231 cells were maintained in DMEM (high glucose) supplemented with 10% fetal bovine serum (FBS) and 1% penicillin/streptomycin from Thermo Fisher Scientific (Waltham, MA). A2780 cells were maintained in RPMI 1640 media supplemented with

10% FBS and 1% penicillin/streptomycin. All cell cultures were maintained in 37°C and 5% CO_2 atmosphere.

3.2.2 METHODS

3.2.2.1 Synthesis of Magnetic nanoparticle cores (MNPs).

Magnetic nanoparticles were synthesized by thermal decomposition of iron (III) acetylacetonate (Fe (acac)$_3$) in benzyl alcohol by two methods:

a. Ramp-soak method. This method was similar to Profile B described in section 2.2.2.1 of the Chapter 2, except for a minor change in the initial heating rate from 110°C to 150°C. Briefly, 6.2μmoles of Fe(acac)$_3$ precursor was mixed with 45mL anhydrous benzyl alcohol. The reaction mixture was initially heated at 110°C for 1h to ensure complete removal of moisture. The reaction temperature was gradually increased to 150°C at 2°C/min and maintained constant for 2h. After 2h the mixture was further heated under reflux to 205°C at a rate of 4°C/min and maintained at that temperature for 40h.

b. Hot injection method. This method differed from the previous methods described here and in 2.2.2.1 of the Chapter 2. While in the other methods Fe(acac)$_3$ was dissolved in benzyl alcohol and the entire mixture was heated to reflux at different heating rates, in in this method, only 80% (35mL) of the total solvent without any Fe(acac)$_3$ was heated to reflux. Separately, 6.2μmoles Fe(acac)$_3$ was dissolved in remaining 20% (10mL) benzyl alcohol at RT and rapidly injected into the hot solvent at reflux with the help of a glass syringe. The reaction mixture was allowed to regain the reflux temperature and further heated for 40h under reflux.

The final product was obtained by precipitation and washing in acetone followed by vacuum evaporation. The physico-chemical characteristics were determined by TEM,

TGA and SQUID to determine their particle size distribution, surface benzyl alcohol content and magnetization saturations, respectively.

3.2.2.2 Preparation of cationic magnetic nanoclusters (MNCs).

Cationic MNCs were prepared by the same method as described in **Chapter 2 section 2.2.2.3a** and depicted graphically in **Scheme 2.1**. Briefly, 40mg of PLL-*b*-PEG polymers with different PLL block-lengths were dissolved in de-ionized (DI) water at a concentration of 4 mg/mL. The pH of this solution was adjusted to 10.5 with 1N NaOH. MNP cores were dispersed separately in 10mL of alkaline water (pH 11.9-12.1) at a concentration of 2 mg/mL to obtain a colloidal dispersion. The polymeric solution was added to the magnetic colloidal dispersion under constant stirring. The mixture was further stirred overnight on a magnetic stirrer at approximately 400 - 500 rpm. The excess polymer was then filtered by extensive dialysis in DI water for 72h with six water changes. The dialyzed intermediate was filtered serially through 0.45 μm and 0.22 μm Anotop filters to obtain the final product. The cationic nanoclusters thus obtained were lyophilized and stored under vacuum until further use.

3.2.2.3 Physico-chemical characterization of MNCs.

a. Size and ζ-potential.

The hydrodynamic diameter (z-average) and ζ-potential of the formulations were determined by dynamic light scattering using a Malvern Zetasizer (Malvern Instruments, Malvern, UK). The formulations were diluted to 1mg/mL of total formulation before measurements were performed in clear disposable zeta cells.

b. MNC composition.

The composition of the unloaded nanoclusters was determined by thermogravimetric analysis (TGA) using 5-10mg of the lyophilized unloaded MNC formulation. The

temperature was raised at 5°C/min to 110°C and kept isothermal for 10 minutes in order to remove the moisture followed by steady heating at 5°C/min to 1000°C. The obtained thermogram was analyzed using the Universal Analysis software (TA Instruments, DE) to deduce the total loss of the organic components (LOI) and amount of MNPs per mg of MNCs. The content of benzyl alcohol coating was determined by loss of organic components upon thermal decomposition of MNPs by TGA. The LOI of MNCs was corrected by subtracting the content of benzyl alcohol in the MNPs to obtain the content of polymer in the MNCs.

c. Relaxivity measurements

Longitudinal (T_1) and transverse (T_2) relaxivity measurements of the different formulations were conducted using a Bruker Biospec MRI and Spectroscopy (MS) system (7T/21 cm; Bruker, Karlshure, Germany). The stabilized colloidal dispersions were diluted to 0, 0.018, 0.045, 0.09, 0.18, 0.27 and 0.36 mM Fe with distilled water and 20mM PBS. T_1 and T_2 relaxation times were measured and converted to their corresponding relaxation rates (R_1 and R_2; 1/T; s^{-1}). The sequence used for T_2 mapping was a CPMG phase cycled single slice multiecho sequence. One 1 mm thick coronal image was acquired with an acquisition matrix of 256 x 128, 40 mm field of view, 32 echoes at 10 ms first echo time and 10 ms echo spacing, repetition time of 3000 ms, one average, for a total acquisition time of 6.4 min. The r_1 (longitudinal relaxivity) and r_2 (transverse relaxivity) values ($s^{-1}.mM^{-1}$) were obtained as the slope of the plots of R_1 or R_2 versus the corresponding Fe concentrations.

d. Colloidal stability of MNCs.

The different formulations were dispersed in 20mM PBS (pH 7.4) at a concentration of 1mg.mL^{-1} and their colloidal stability was measured at RT for one month during which period the particle size was measured by DLS at regular intervals.

3.2.2.4 Preparation of pH sensitive doxorubicin-conjugated MNCs

Doxorubicin was conjugated by a pH-labile hydrazone linkage at the ε-amino end group of the PLL block on the MNCs via a hetero-bi-functional linker SPDP. The conjugation procedure is described in brief as follows.

a. Synthesis of activated DOX-hydrazone linker.

The 13-keto position on the doxorubicin (DOX) molecule was targeted by activating DOX with EMCH (3,3′-N-[ε-Maleimidocaproic acid] hydrazide).[21] Then, 0.1 mmol of DOX.HCl was dissolved in 15mL anhydrous methanol in a dry 25mL round bottom flask. EMCH (0.2 mmol) was dissolved in 2mL methanol and added to the DOX.HCl solution. Two drops of trifluoroacetic acid were added to the reaction to catalyze the conjugation of the hydrazide to the 13-keto position of the DOX. The reactants were stirred at room temperature in the dark for 8h. The reaction solution was concentrated by rotary evaporation to 4mL and the DOX-HZN conjugate was obtained by precipitation in ice-cold anhydrous acetonitrile. This purification step was repeated thrice. The product was collected by centrifugation and dried under vacuum. The DOX-HZN was characterized by 1H-NMR and stored at -20°C till further use.

b. Formation of SH-MNC intermediate

First, the available primary amine groups in the formulation were quantified by Fluorescamine assay.[22] Briefly, 2mg of MNC-4 formulation was dispersed in DI water at a concentration of 0.05mg/mL. Fluorescamine reagent was dissolved separately in acetone at a concentration of 3mg/mL. About 0.15mL of the formulation was placed in a flat-bottom black-walled 96-well plate. 50μL of the Fluorescamine reagent was added to each sample and mixed vigorously for a minute. The fluorescence was measured immediately at ex/em wavelengths of 400/460nm on a plate reader. A 6.7 mg/mL (equivalent to 10 μmoles/mL

of –NH$_2$ group) solution of PLK$_{10}$-PEG$_{113}$ polymer was diluted at concentrations equivalent to 0.01, 0.05, 0.1, 0.25, 0.5, 1 and 2 μmoles of –NH$_2$ group, mixed with Fluorescamine and fluorescence intensities were measured to obtain the standard curve.

Of the total available -NH$_2$ groups, 25, 50 and 75 mol% were targeted for conjugation with the heterobifunctional linker SPDP. Briefly, the formulation was dispersed in DDW at 10 mg/mL and divided into three parts of 5mL each. 15mg (48μmoles) SPDP was dissolved in DMF to obtain a 20mM solution and volumes corresponding to 5, 11 and 16 μmoles of SPDP were added to the three vials containing the MNC-4 formulation. The reaction was stirred in dark for 4h followed by centrifugal filtration (3000 MWCO) and three washings to remove the unreacted SPDP and resuspended in PBS. DTT was dissolved in PBS at 10 mg/mL. 0.2mL of this solution was added to each sample and stirred for 8h. Excess DTT was quickly removed by centrifugal filtration. The sample was washed twice and re-suspended in water to obtain the stable SH-MNC intermediates. The success of the conjugation reaction and conversion of the disulfide to free thiol was assessed by DTNB assay for free thiol.[23]

c. Formation of DOX-MNCs

DOX-MNCs were synthesized by conjugation of the activated DOX-HZN to the SH-MNC intermediate. Briefly, DOX-HZN was dissolved in methanol and added to the SH-MNC at a 2:1 molar ratio. The reaction was stirred overnight in dark. The final DOX-MNC formulations namely 4a, 4a and 4c were obtained by centrifugal filtration and extensive washing in PBS to remove the unbound drug. The conjugation efficiency (%CE) was estimated by fluorimetry in pH 4 acetate buffer at ex/em 480/580 nm.

3.2.2.5 Doxorubicin release study

Doxorubicin release from the final formulation was studied in sodium acetate buffer solution pH 5.5 (ABS), sodium phosphate buffered saline pH 7.4 (PBS) and in a combination of PBS (1 day) followed by ABS (4 days). Briefly, the MNC-4B formulation was diluted to concentration equivalent to 10µg/mL DOX in respective buffers. 1mL of each dilution was placed in Float-a-Lyzer dilution membrane tubes and placed in an amber colored vial (30mL) containing 24mL of the corresponding buffer at 37°C as the release medium. The samples (n = 3 per pH group) were stirred at 100rpm. 0.2mL aliquots were collected from the release medium at regular time points and replaced by same volume of fresh buffers. The drug release was quantified by fluorimetry at Ex/ Em of 480/ 580 nm respectively. For the combination group, after 24h in pH 7.4, the release medium in the vial was replaced by same volume pH 5.5 ABS and the study was continued for 4 more days.

3.2.2.6 Determination of Formulation toxicity

The effect of amine-group modification on toxicity of the empty formulations was studied in A2780 human ovarian cancer and MDA-MB-231 triple negative human breast cancer cells by MTT assay. Briefly, 3×10^3 cells per well were seeded in 96 well plates and allowed to adhere for 24h. The cells were then treated with different concentrations of each of the three SH-MNC-4 formulations and incubated for 24h and 72h. At the end of each time point, the supernatant medium was replaced with fresh complete medium and the cells were incubated further for 12h to allow the cells to revive. Finally, the cell viability was measured by standard MTT assay. Briefly, 20µl of a 5mg/mL solution of MTT dye in PBS was added to each well and incubated for 3.5h. The supernatant was then removed and the formed formazan crystals were dissolved in DMSO. Formazan concentration was quantified through measurement of absorbance at 560nm. Cell viability was normalized to

the untreated control to obtain viability percentage values. The cell viability of the modified formulation was compared with that of the unmodified MNC-4 formulation.

3.2.2.7 Cellular uptake of MNCs

A2780-WT ovarian cancer cells and MDA-MB-231 triple negative breast cancer cells (6 million cells/ flask) were treated with a 5mL colloidal dispersion of the different DOX-MNC formulations (equivalent to Fe concentration of 5µg/mL) and incubated for 24h. At various time points during the incubation period the cells were washed once with ice-cold PBS and acid saline (pH 3) and harvested. The viability was determined by trypan blue assay and then the cells were centrifuged to form a pellet. The supernatant was removed completely and 0.5mL of a 100ppb solution of Iridium in 2% HNO_3 was added to the pellets as an internal standard. The cells were then lysed mechanically by probe-sonication. 50µL concentrated nitric acid (TraCERT; Fluka) was added to the cell lysates and the samples were digested overnight at 70°C. The digested samples were then appropriately diluted to 5mL with 2% HNO_3. The cell debris was separated by ultra-centrifugation at 7500 rpm for 10 min. The supernatant was further filtered through 0.2µm syringe filters and analyzed by Nexion 300-D ICP-MS equipped with collision cell and autosampler (Perkin Elmer, location USA). The intensity of the ^{57}Fe isotope was considered for quantification of the uptake. The final Fe content was normalized to the total protein content of the cells (as determined by standard Bicinchoninic acid (BCA) assay) and MNC uptake was expressed as µg of Fe per mg of total cellular protein.

Simultaneously, live-cell confocal microscopy was performed to study the cellular localization pattern of the different fluorescent-labeled DOX-MNC formulation. A2780-WT and A2780-CisR cells were incubated with Alexa Fluor®-647 labeled DOX-MNCs for 1, 3 and 24h followed by visualization under a LSM 710 (Zeiss, CA) confocal microscope equipped with a live-cell imaging stage.

3.2.2.8 *In vitro* Cytotoxicity of DOX-MNCs

The *in vitro* cytotoxic potential of the DOX-MNC formulations was estimated in A2780-WT human ovarian carcinoma and MDA-MB-231 triple negative human mammary adenocarcinoma cell lines. Briefly, the cells were cultured in complete DMEM in conditions mentioned previously. Cells were seeded at a density of 5×10^3 per well in 96-well plates 24h before treatment. The cells were treated with free DOX, blank MNCs or the three DOX-MNC formulations at different concentrations. The cells were incubated for 24h and 72h. At the end of each time point the cells were washed, the culture medium was replaced with fresh complete DMEM and the cells were further incubated for 12h. Finally, the cell viability was estimated by standard MTT assay and described previously in Chapter 2.

***3.2.2.9 In vitro* determination of MR potential**

Approximately 10 million A2780-WT and MDA-MB-231 cells were incubated with DOX-MNC-4c formulation at Fe concentrations of 0.009, 0.018 and 0.09 mM for a period of 24h. After incubation for specified time points, the cells were harvested and cell viability was determined by trypan blue assay. Approximately, 9×10^6 viable cells were re-dispersed in 0.5mL PBS and mixed carefully with equal volume of hot 4% w/v agar solution taking care to prevent entrapment of air bubbles in the solidified gel. The samples were cooled to RT for to allow the formation of a solid matrix. As a control 9×10^6 un-treated cells were used. Phantom gels were scanned in Siemens Magnetom TIM Trio 3T human MR scanner. Images of the phantom gels were obtained by using a multi-gradient echo pulse sequence at a 1.64ms/3000ms TE/ TR and 40° flip angle for T_1 and 112.5ms/ 3000ms TE/ TR for T_2. The cellular phantoms were compared with phantoms of similar concentrations of formulations without any cells.

3.3 RESULTS

3.3.1 SYNTHESIS AND CHARACTERIZATION OF CORE MNPS
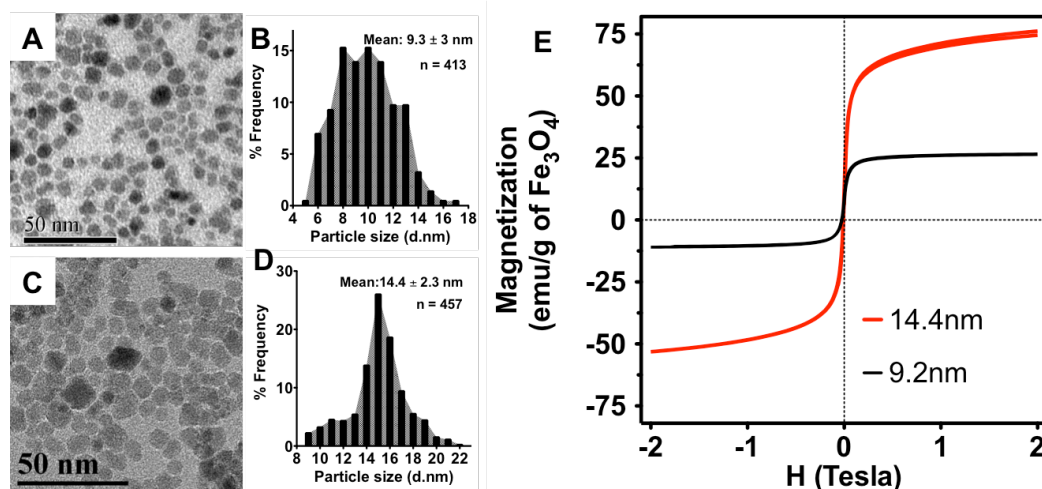
Figure 3.1. Synthesis of core MNP particles from thermal decomposition of Fe(acac)$_3$. TEM images of MNPs synthesized by **A**. ramp-soak and **B.** direct injection method of thermal decomposition and respective size distributions **C** and **D**. Magnetization potential (M) of the two MNPs was determined by SQUID magnetometer (**E**).

Core MNPs with two different mean particle sizes were synthesized by thermal decomposition of Fe (acac)$_3$ in benzyl alcohol using two different techniques. In the first ramp-soak method wherein the reaction mixture was kept isothermal at 150°C for 2hrs, MNP cores of mean size 9.3 nm (**Figure 3.1A**) were obtained with a broad size distribution (**Figure 3.1B**). In comparison, the hot injection method yielded MNPs with a larger core size of 14.4nm (**Figure 3.1C**) with a very narrow size distribution (**Figure 3.1D**) and a significant fraction of the MNP population above 13nm. The magnetization potential of MNP cores was further studied by SQUID magnetometer. MNPs synthesized by hot injection exhibited significantly higher magnetization saturation (M$_s$) of 74.3 emu/g compared to 24.7emu/g for 9.3nm particles (**Figure 3.1E**).

3.3.2 PREPARATION AND CHARACTERIZATION OF CATIONIC MNCS

Poly (l-lysine)$_x$-PEG$_{113}$ polymers of different poly (L-lysine) block lengths (x = 10, 50 or 100) were used to stabilize the MNPs into clusters by a process described previously in Chapter 2. The physico-chemical characteristics of the different formulations are shown in **Table 3.1**. The cluster formation was effected by electrostatic interactions between the MNP surface and the positively charged ε-primary amine end group of the cationic PLK block. As seen in **Figure 3.2**, the cluster size was affected by the poly (L-lysine) block length as well as the size of the core MNPs. 9.3nm MNPs stabilized by PLK$_{10}$-PEG$_{113}$, PLK$_{50}$-PEG$_{113}$ and PLK$_{100}$-PEG$_{113}$ had hydrodynamic diameters (D$_{eff}$) of 36.4, 44.2 and 82.1 nm respectively. MNC-1 formulation showed the maximum MNP content of 29.2 wt%. On the other hand, MNC-4 formulation, comprising of 14.4nm MNP had D$_{eff}$ of 121.3 nm with 28.3 wt% MNP content. The size (r.u.) of the PLK block of the cationic copolymer and the resulting polymer content in the MNCs, together dictated the colloidal stability of the clusters (**Figure 3.3**). While all the formulations maintained colloidal stability over a one-month period in PBS (20mM, pH 7.4), MNC-1, stabilized by PLK$_{10}$-b-PEG$_{113}$ showed a significant increase in D$_{eff}$ from 36.4nm to 68.3nm over this period.

Table 3.1: Physico-chemical characterization of magnetic nanoclusters stabilized by different PLK-PEG block copolymers

Formulation	Abbreviation	Core MNP Size (nm) [a]	Composition [b] (wt%)			DLS Characteristics [d]				
			Organic Components		MNP	DI water			PBS pH 7.4	
			Polymer	BA		D_{eff} (nm)	PDI	ζ-potential (mV)	D_{eff} (nm)	PDI
PLK$_{10}$-PEG$_{113}$-MNP-9	MNC-1	9.2	66.9	3.9	29.2	36.4 ± 6.3	0.211 ± 0.01	+20.5	32.3 ± 3.3	0.202 ± 0.01
PLK$_{50}$-PEG$_{113}$-MNP-9	MNC-2	9.2	74.7	3.1	22.2	44.2 ± 4.1	0.183 ± 0.01	+28.3	43.1 ± 5.2	0.211 ± 0.01
PLK$_{100}$-PEG$_{113}$-MNP-9	MNC-3	9.2	73.3	3.8	22.9	82.1 ± 6	0.209 ± 0.03	+35.4	76.2 ± 5.1	0.219 ± 0.02
PLK$_{50}$-PEG$_{113}$-MNP-14	MNC-4	14.4	68.3	3.8	28.2	121.3 ± 3.4	0.143 ± 0.001	+44.7	114.7 ± 2.4	0.137 ± 0.02

a) The average core size was estimated from TEM images by measuring a minimum of 400 core particle sizes with Image J software.

b) Composition of the MNCs was determined by TGA

c) Benzyl alcohol: Briefly, the content of benzyl alcohol coating on the MNPs was determined by loss of organic components upon thermal decomposition of MNPs. The total loss of the organic components upon thermal decomposition of the MNCs was corrected by subtraction of the content of BA to determine the polymer content of the MNCs

d) DLS characteristics were measured at 25°C at a concentration of 1 mg/mL in DI water and 10mM PBS at pH 7.4 in clear disposable zeta cell with Malvern Nano-ZS Zetasizer. Measurements in PBS were performed in 10 mM PBS at pH 7.4.
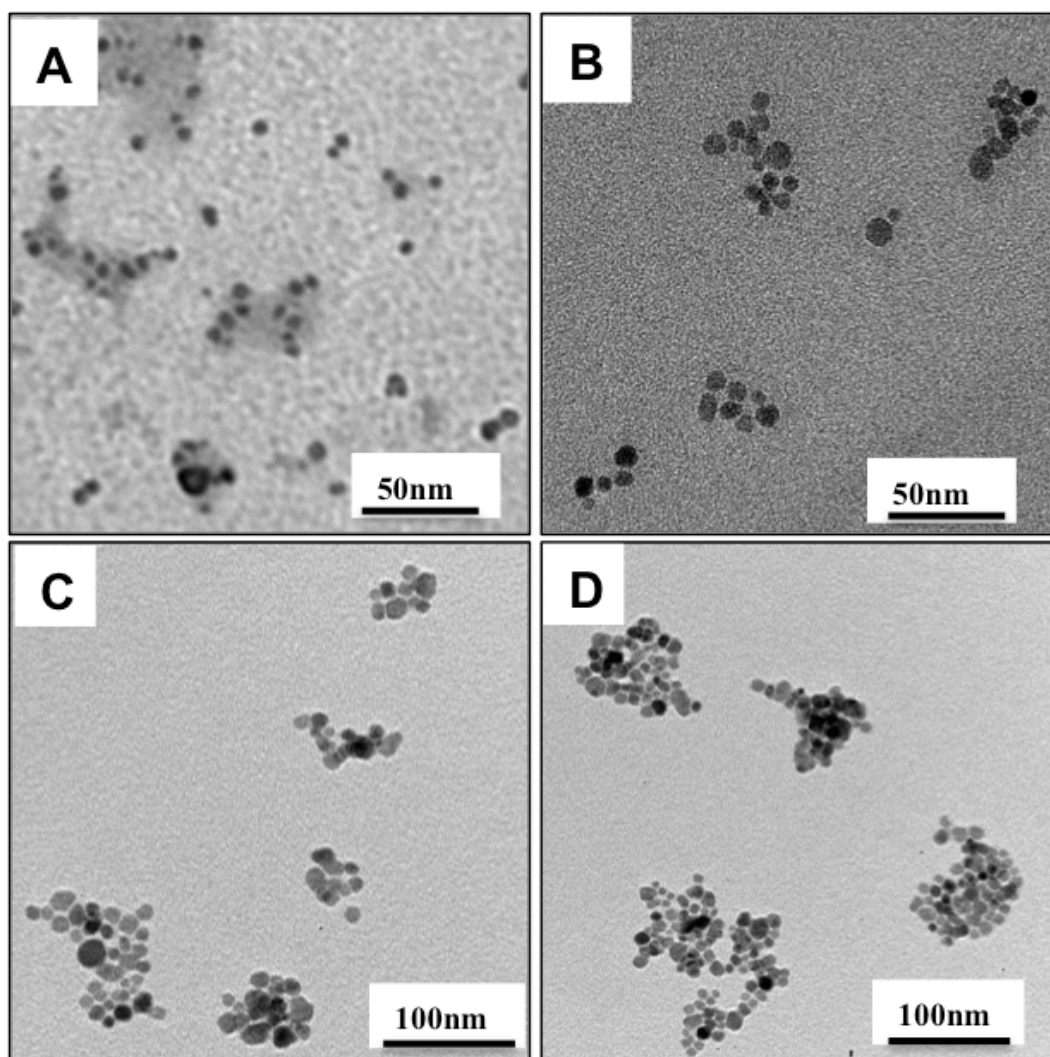
Figure 3.2. TEM images of **A.** MNC-1, **B.** MNC-2, **C**. MNC-3, **D**. MNC-4 clusters synthesized from PLK-b-PEG$_{113}$ polymers with different PLK r.u.
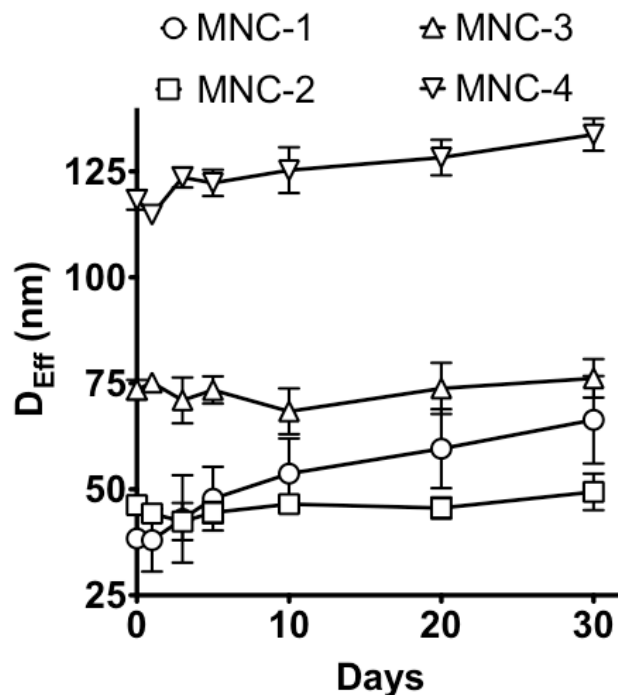
Figure 3.3. Colloidal stability of different MNCs stabilized by PLK-b-PEG with different r.u. of PLK.

Figure 3.1. Relaxivity measurements of different MNC formulations in PBS. R_1 **(A)** and R_2 **(B)** Relaxation rates of were plotted against Fe concentration to obtain r_1 and r_2 relaxivities ($s^{-1}.mM^{-1}$; Table 2) as the slopes of the linear curves so obtained. MNC-4 gel sample dilutions were made in 4% agar gel in PBS

Table 3.2. Longitudinal (r_1) and transverse (r_2) relaxivity values of different MNCs

Formulation	r_1 (s^{-1}.mM^{-1})	r_2 (s^{-1}.mM^{-1})
MNC-1	0.9 ± 0.04	93.2 ± 2.2
MNC-2	0.62 ± 0.02	177.3 ± 6.5
MNC-3	1.28 ± 0.02	294.1 ± 2.1
MNC-4	1.02 ± 0.01	358.5 ± 7.4
MNC-4 in gel	1.01 ± 0.08	313 ± 12.9

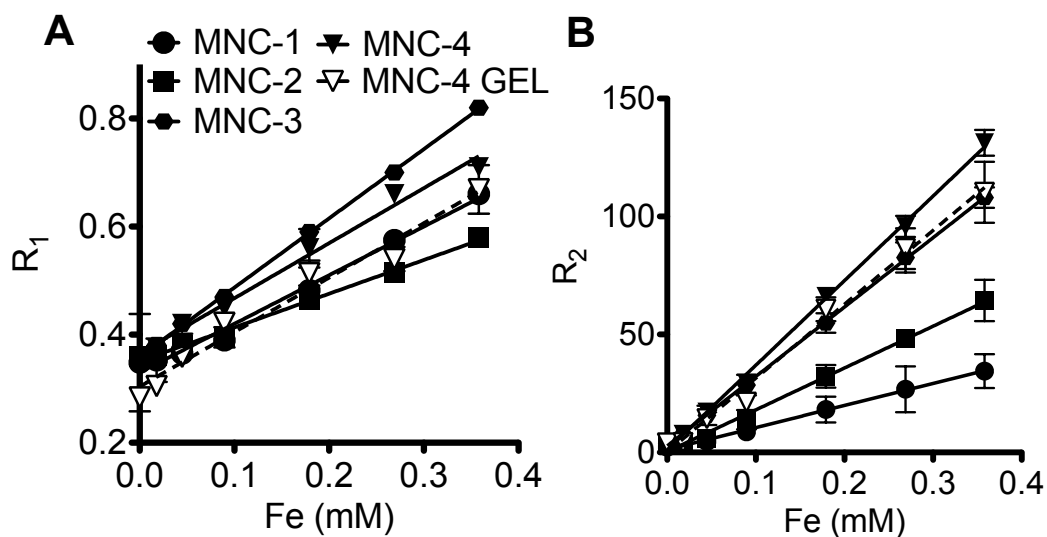Relaxivity measurements of the different MNCs were performed in DI water and PBS on a 7T MRI scanner (**Figure 3.4**). The ability of MNPs to decrease the relaxation time of the surrounding water protons is quantified as relaxivity i.e. the slope of the plots of longitudinal (R_1) or transverse (R_2) relaxation rates vs. Fe concentrations. As tabulated in T**able 3.2**, the transverse relaxivity (r_2) of the different formulations increased with the cluster size and as a function of the total MNP content of the formulations with the exception of MNC-1 formulation, which in spite of having a high MNP content of 29.2 wt%, had the lowest r_2 of 93.2 ± 2.2 s^{-1}.mM^{-1}. This can be attributed to the smaller cluster size of 33nm as well as the lack of compactness of the clusters (Figure 3.2). MNC-2 and MNC-3 clusters had identical MNP content of 23 wt%, but the MNC-3 showed significantly higher relaxivity (358.5 ± 7.4s^{-1}.mM^{-1}) than MNC-2 (294.1 ± 2.1 s^{-1}.mM^{-1}), which had nearly half the D_{eff} as that of MNC-3. MNC-4 formulation, with the core MNP size of 14.4nm, largest cluster size and evidently a higher MNP content of 28 wt% had the maximum r_2 relaxivity of 358.5 ± 2.2 s-^{1}.mM^{-1}. MNC-4 exhibited only a marginal decrease in relaxivity even when embedded in

phantom agar gels. As noted in Chapter 2, agar gel is widely used to mimic soft tissues in *in vitro* assessment of MRI contrast agents. Given the physical characteristics of the MNPs used for MNC preparation, none of the formulations exhibited high longitudinal relaxivity (r_1).

3.3.4 DOXORUBICIN CONJUGATION ON MNCS VIA PH SENSITIVE LINKER

Scheme 3.1. Doxorubicin conjugation to MNC-4 formulation via hetero-bi-functional linker SPDP
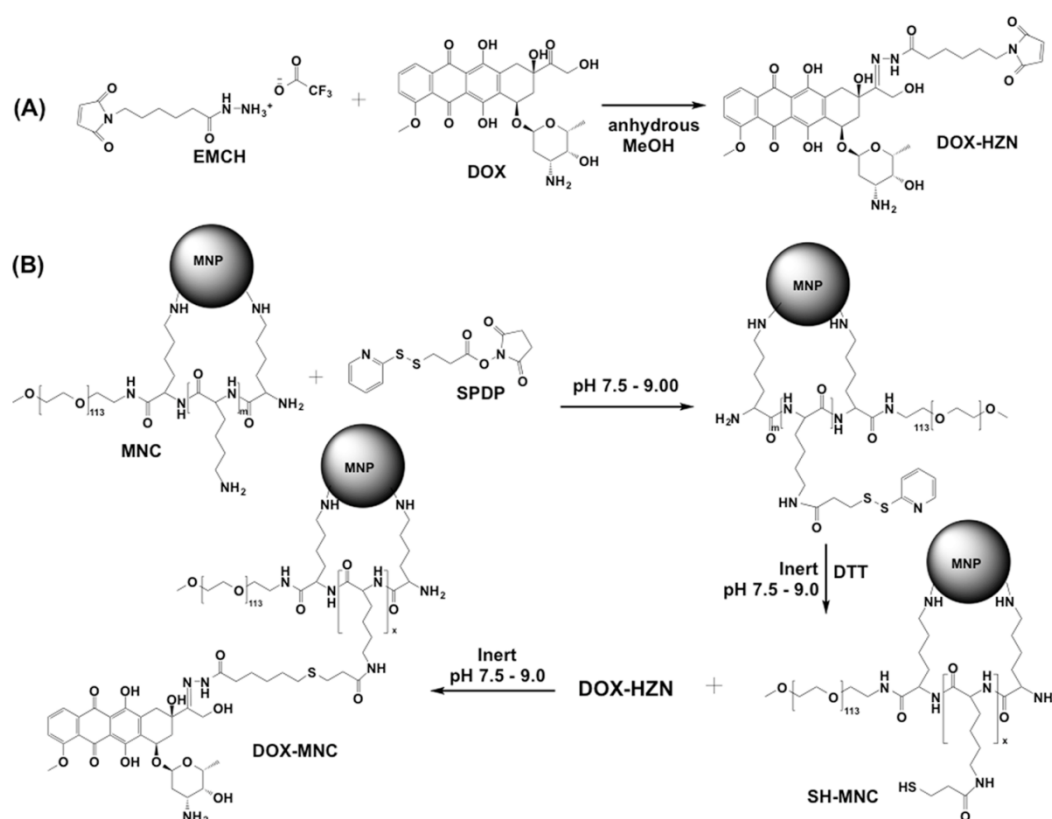
MNC-4 formulation was selected for all further studies due to its excellent colloidal stability and high relaxivity in physiological buffer (PBS). Doxorubicin HCl (DOX) was conjugated onto the formulation via the heterobifunctional pH sensitive linker SPDP in a stepwise manner. Firstly, DOX was activated at its 13-keto position with EMCH, a heterobifunctional hydrazide linker in presence of trifluoroacetic acid as a catalyst as shown in **Scheme 3.1A**. The activated DOX-HZN molecules were characterized by [1]H-

NMR (**Figure 3.5**). In a separate reaction, the side-chain primary amine groups of the poly

(l-lysine) block were conjugated to another heterobifunctional linker SPDP. Following

successful conjugation to the MNCs the disulfide linkage on the other end was reduced

by DTT and DOX-HZN was conjugated to the MNCs via a thioester bond to the SPDP

molecule (**Scheme 3.1B**). Three different target conjugation efficiencies were attempted

as tabulated in **Table 3.2**.
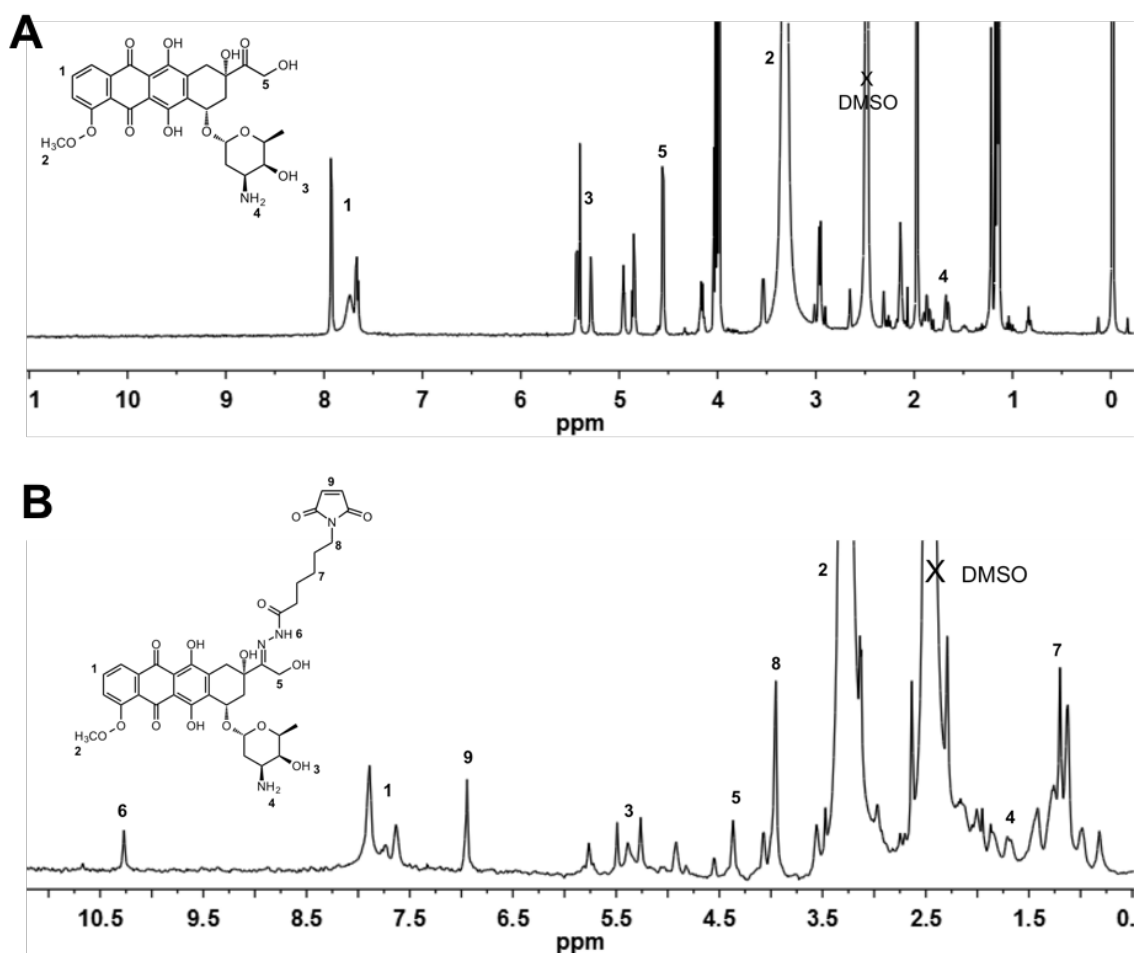
Figure 3.5. ^{1}H-NMR of (**A**) free DOX and (**B**) DOX-HZN. Selected peak assignments common to both (A) and (B) are as follows: δ ppm = 1.7 (2H, m, -NH$_2$, 4), 3.39 (3H, s, -CH$_3$, 2), 4.69 (2H, d, -CH$_2$, 5), 5.37 (1H, s, -OH, 3), 7.65 (1H, s, -CH, 1). Additional peak assignments of the modified DOX-HXN are as follows: 1.32 (2H, s, -CH$_2$, 7), 4.0 (2H, s, -CH$_2$, 8), 7.86 (H-H, CH-CH, 9), 10.57 (1H, s, -NH, 6).

Depending on the number of primary amino groups targeted for DOX-HZN, all three formulations showed a %CE of approximately ~5 wt%. Formulation DOX-MNC-4c exhibiting the maximum %LC of 2.48 wt%. DOX conjugation had no effect on the cluster size as well as PDI of the formulations. However, this modification significantly reduced the zeta potential of the final formulations. MNC-4 formulation had a zeta potential of +44 mV before DOX conjugation, which reduced to less than +25 mV (**Table 3.3**) following DOX-HZN conjugation, which we anticipated would help reduce the charge-induced formulation toxicity of the MNCs.

Table 3.3: Physico-chemical characteristics of DOX-MNC conjugates

Formulation	Target Conjugation (Eq. mol % of available primary amino groups [a]	DLS Characteristics in DDW[b]			%CE [c]	%LC [d]
		Deff	PDI	ζ-potential (mV)		
DOX-MNC-4a	15	129.7 ± 4.2	0.163 ± 0.005	21.5	5.3	0.93
DOX-MNC-4b	30	121.7 ± 5.3	0.161 ± 0.004	17.7	4.2	1.51
DOX-MNC-4c	50	125.7 ± 2.7	0.153 ± 0.002	13.8	4.6	2.48

a) The total primary amino groups (µmoles) available for DOX conjugation per mL of the MNC formulation was determined by Fluorescamine assay.
b) Physical characteristics of the final DOX-MNC formulations was determined by DLS
c) Conjugation efficiency: Defined as the %fraction of the targeted µmoles of primary amino groups that was conjugated by DOX. DOX content per mL of the formulation was quantified by fluorimetry at Excitation/ Emission wavelengths of 480nm/ 580nm
d) Loading Capacity was determined as the weight percent of DOX.HCl per the dispersed phase. Briefly, the drug-loaded MNCs were lyophilized and the amount of DOX.HCl per mg of the formulation was determined by fluorimetry. Briefly 0.2mL of the final DOX-loaded formulations was lyophilized. The lyophilized formulation was weighed and dispersed in pH 4.5 acetate buffer for 48h followed by sonication for 1h and ultra- centrifugation at 10,000 rpm for 15 minutes. The fluorescence of the supernatant was measured by fluorimetry as mentioned in (c)

3.3.5. PH RESPONSIVE RELEASE OF DOX FROM MNCS

The efficacy of the acid-labile hydrazone linkage in achieving a physiological stimuli-responsive drug release was studied on DOX-MNC-4b formulation, which had the intermediate %LC of the three formulations. We evaluated DOX release separately for a period of five days in pH 7.4 PBS, pH 5.5 ABS. In addition, we also studied the effect of sequential exposure to both pH conditions. For this study the formulation was placed in PBS for 24h after which the release medium was changed to pH 5.5 ABS and the release was further monitored for the remaining four days. The last approach was adopted specifically to evaluate the potential effect of pre-exposure to physiological buffer may have on the release rate of the drug in acidic pH.

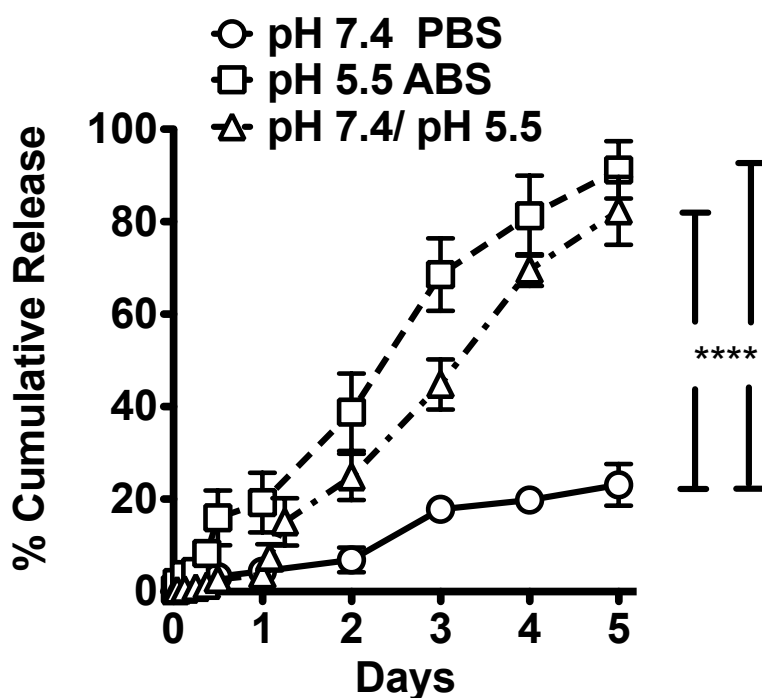**Figure 3.6.** Release of DOX from MNC-4b formulation at different pH conditions. DOX release was measured in either 50mM pH 5.5 sodium acetate buffer (ABS), 10mM pH 7.4 PBS or sequentially in pH 5.5 ABS buffer for 24h followed by pH 7.4 PBS for a total of 5 days Drug release was quantified at regular time points by fluorimetry at Ex/Em wavelengths of 480/580 nm. (n = 3 per group). Data are mean ± SD. ****: p < 0.0001

As expected, the acid-labile hydrazone bond efficiently prevented the release of DOX from the clusters (**Figure 3.6**). Only 4.3% drug was release in PBS in the first day and overall only 23.3% DOX was released in PBS over a five-day period. On the other hand, formulation in pH 5.5 ABS responded favorably to the acidic environment and 22% of the conjugated DOX in the first 24h. Over a five-day period 92% release was achieved in ABS. Formulation exposed sequentially in PBS for 1day followed by ABS for four days did not show any aberration in the release profile following changeover to ABS medium from PBS after 24h.

Thus, DOX conjugation on the MNCs via acyl hydrazone linkage allows for controlled release in response to pH stimuli inside the cell. However, it is noteworthy that hydrazone hydrolysis occurs rather slowly even at pH 5.5, a condition similar to that found in subcellular compartments. In summary, the rate of drug release appears to be determined primarily by the intrinsic rates of hydrazone hydrolysis and is governed by pH changes only.

3.3.6 FORMULATION TOXICITY STUDIES

Cationic polymers such a poly (L-lysine) and nanocarriers thereof present with one major challenge; that of charge induced toxicity of the polymer itself. It is now known that molecular weights as well as the cationic charge density of the polycations are the key parameters for the interaction with the cell membranes and consequently cell damage. [24] Studies on poly(ethyleneimine) (PEI) polymer revealed that the polymer does not cause apoptosis but rather a necrotic cell reaction. Nonetheless, cationic polymers are exclusively used in gene delivery wherein condensation of the negatively charged DNA neutralizes the net charge of the polyplexes.
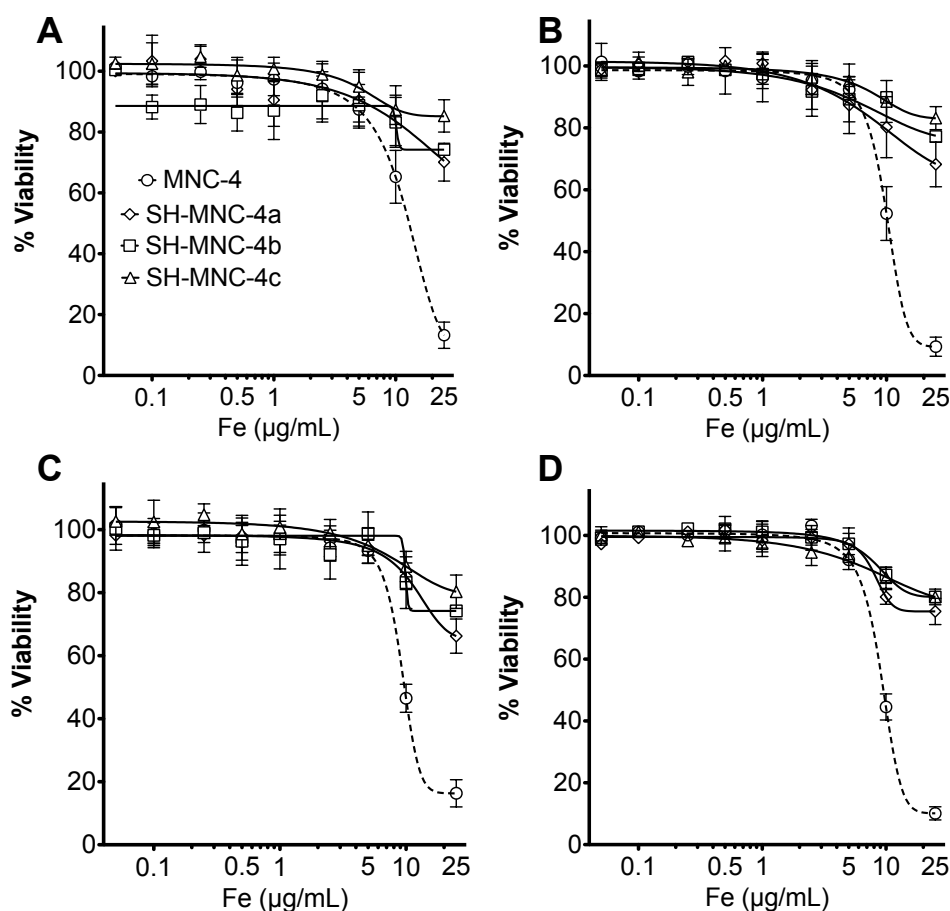
Figure 3.7. Toxicity of SH-MNC formulations prior to DOX-HZN conjugation in MDA-MB-231 **(A,B)** and A2780-WT cells at 24h **(A,C)** and 72h **(B, D)**

In order to determine the toxicity of our formulation before DOX conjugation we conducted toxicity studies on the unloaded MNC-4 formulations (SH-MNC-4a-c) in the two cancer cells lines, namely MDA-MB-231 triple negative breast cancer cells and A2780 wild type ovarian cancer cells. Cells were exposed to different concentrations of SH-MNC formulations for 24h and 72h. At the end of each time point, the treatment was removed, the cells were washed with heparinized PBS (0.2 mg/mL Heparin sulfate) and allowed to grow for additional 12h in fresh media. The cell viability was measured by MTT assay as described in **Section 2.2.2.9** of Chapter 2. SPDP conjugation and subsequent reduction of the disulfide bond significantly reduces the toxicity of the cationic MNC-4 formulations

(**Figure 3.7**). Depending on the extent of SPDP conjugation on the side-chain primary amine, the formulation toxicity decreased as SH-MNC-4a > SH-MNC-4b > SH-MNC-4c. The formulations exhibited marginally higher toxicity in A2780 cells at 24h compared to MDA-MB-231 cells. However, at the end of 72h both the cell lines showed similar toxicity profiles. Overall, all the modified formulations were well-tolerated up to concentration equivalent to 10 µg/mL of Fe with cell viabilities being above 80% in all cases. Formulation SH-MNC-4a showed relatively higher toxicity at 25 µg/mL of Fe. Nonetheless, compared to the unmodified MNC-4 formulation, all the SH-MNC-4 formulations showed marked reduction in charge-induced toxicity.

3.3.7 CELLULAR UPTAKE STUDIES
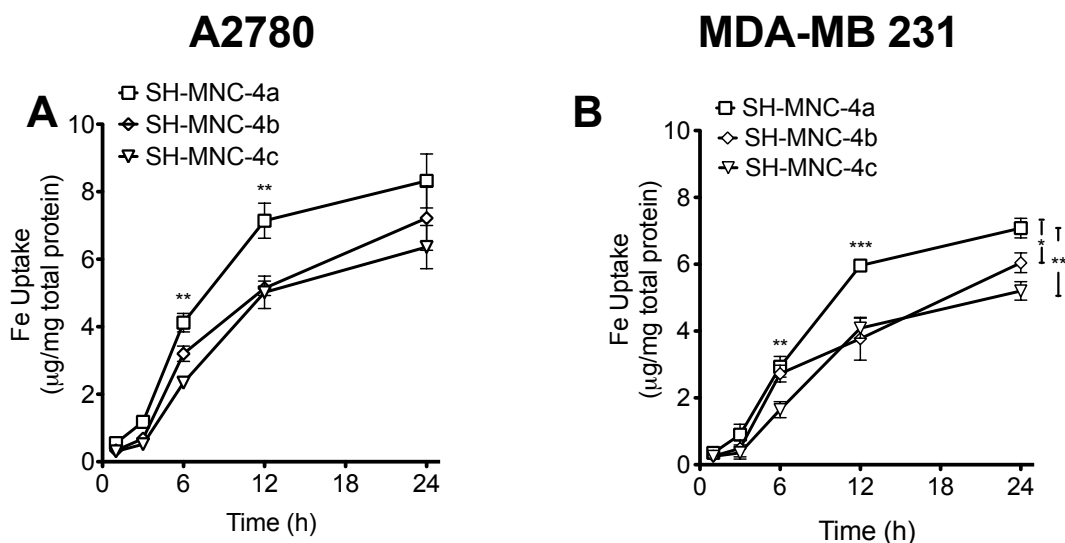
A2780

MDA-MB 231

Figure 3.8. Cellular uptake of SH-MNC formulations in **A**. 2780 (wild type) and **B.** MDA-MB-231 cells over a period of 24h quantified by ICPMS Data represented as Mean ± SD. Statistical significance denoted as **: $p < 0.01$, ***: $p < 0.001$

Intracellular uptake of the cationic formulations was studied by ICPMS and confocal microscopy in A2780-WT ovarian cancer and MDA-MB-231 triple negative breast cancer cells. We first evaluated the effect of SPDP conjugation on the cellular uptake of the three SH-MNC formulations by ICPMS. It was observed that the degree of modification inversely

affected the cellular uptake. Thus, SH-MNC-4a formulation, which had the least SPDP

modification and a higher positive zeta potential showed maximum uptake in both the cell
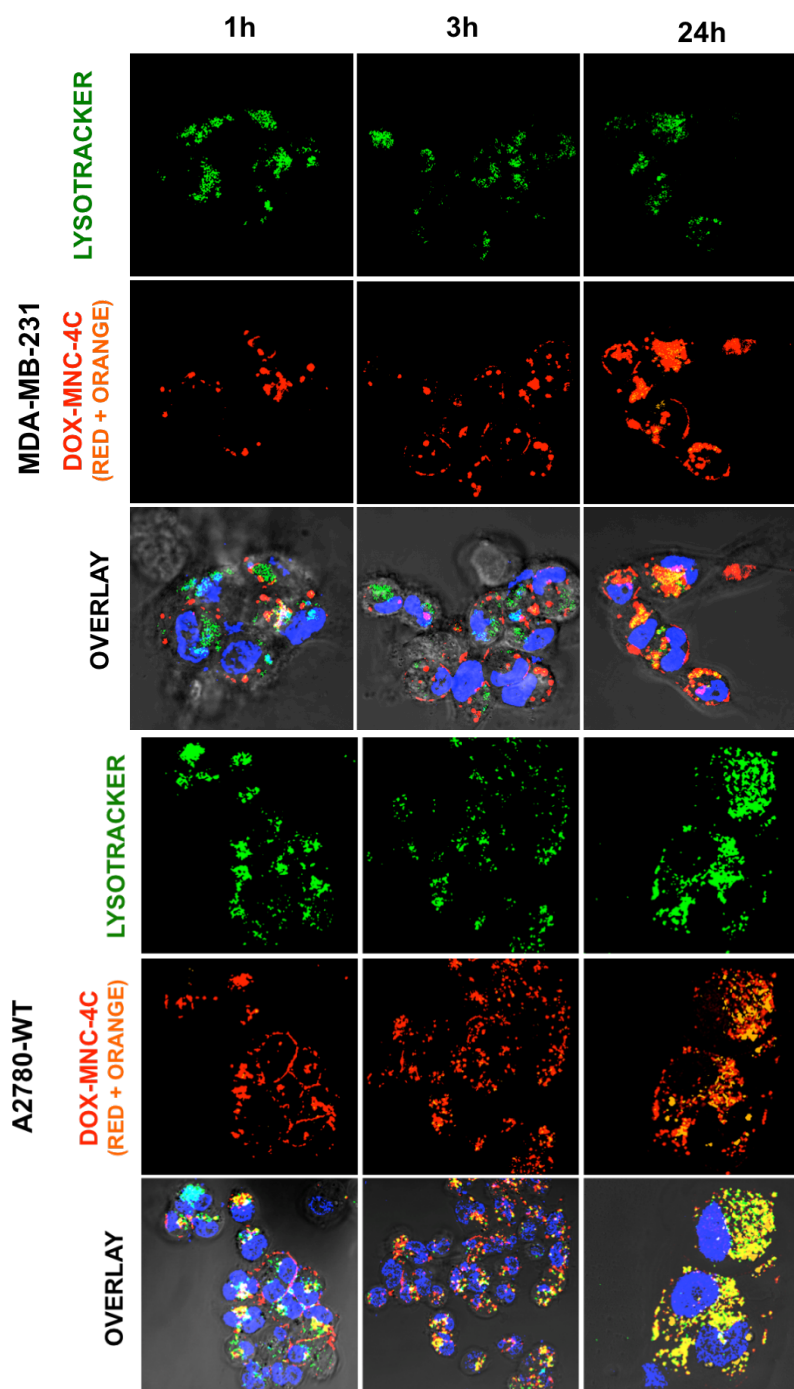
Figure 3.9: Qualitative estimation of cellular uptake of DOX-MNC-4c formulation over a period of 24h in A2780-WT ovarian cancer and MDA-MB-231 cancer cells by confocal microscopy. Cells were incubated with DOX-MNC-4c formulation (Orange) conjugated with Alexa-Fluor 647 (Red) for different time intervals followed by incubation with Lysotracker (Green) and Hoechst nuclear stain (Blue). Colocalization of the MNCs in lysosomes is seen in overlay (yellow punctate regions).

 lines. The other two formulations did not show a significant difference in cellular uptake. Between the two cell lines, uptake rate was faster in the ovarian cancer cell line. At the end of 24h ovarian cancer cells showed an uptake equivalent to 8.4 µg/mg of total protein while the breast cancer cells showed an uptake of 6.6 µg/mg of total protein (**Figure 3.8**).

Of the three DOX-loaded formulations, DOX-MNC-4c was further selected for confocal microscopy studies to qualitatively evaluate the uptake of the formulation and also to study the cellular localization pattern of the formulation. For this study the cells were seeded in 8-Chamber confocal slides and allowed to grow for 24h. The cells were then incubated with Alexa-Fluor 647-labelled DOX-MNC-4c formulation for 1h, 3h and 24h. At end of each time period the cells were washed thoroughly and further incubated with lysosomal marker lysotracker green and Hoechst nuclear stain for 1h and 30min respectively. As seen in **figure 3.9** cationic formulations (red/ red + orange) were associated with the cell membrane immediately (1h) post incubation. As time progressed, the membrane-associated MNCs were internalized and localized within the lysosomes as seen from the yellow overlay images. DOX, either bound with the formulation or as a free drug (orange punctate either by itself or embedded in red MNC fluorescence) was also seen localized within the lysosomes. Confocal microscopy confirmed the results of ICPMS wherein A2780-WT cells showed rapid cellular uptake than MDA-MB-231 cells.

3.3.8 *IN VITRO* ANTI-CANCER EFFICACY STUDIES OF DOX-MNC FORMULATION
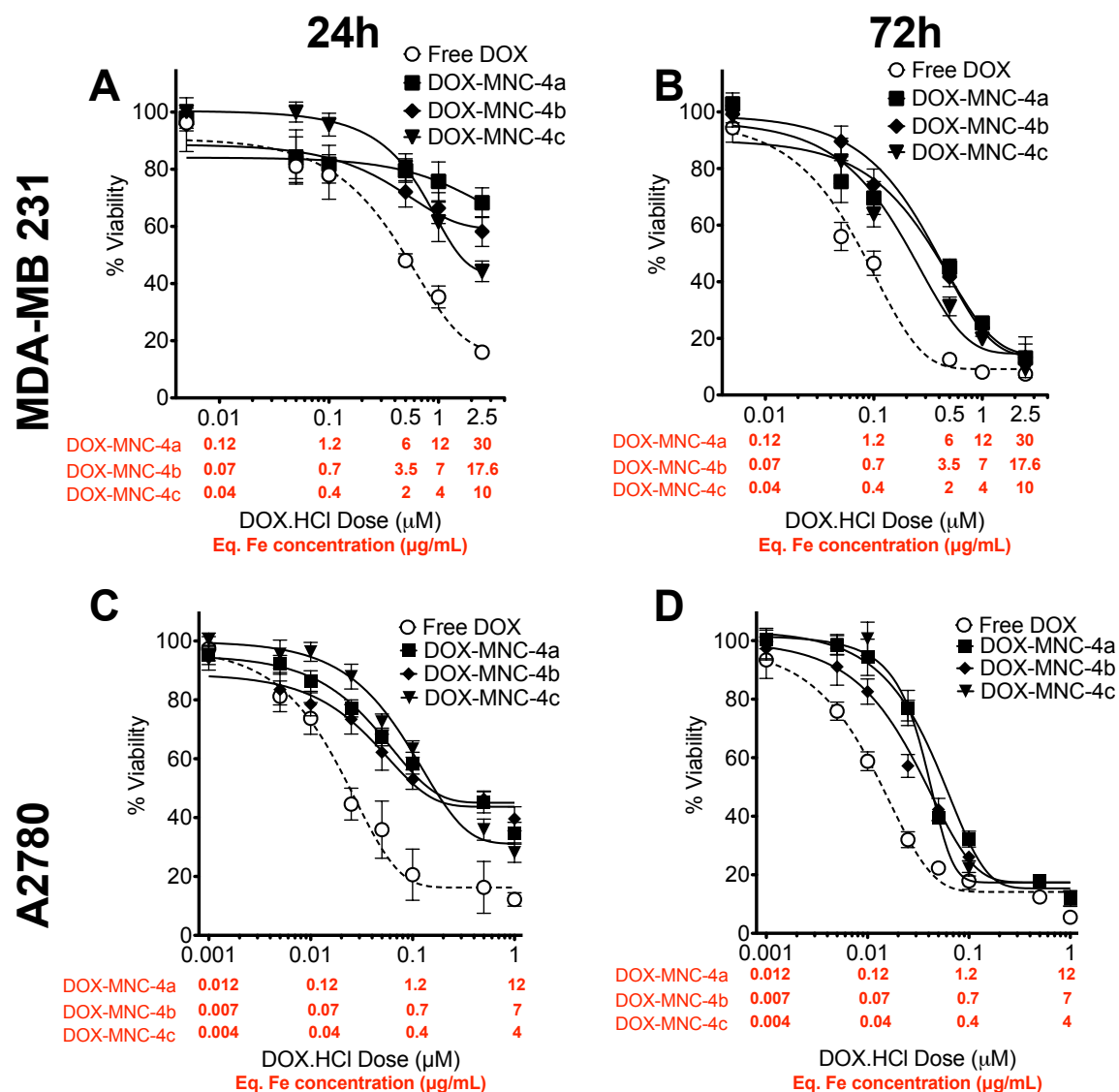
Figure 3.10: Cytotoxic efficacy of different DOX-MNC-4 formulations in MDA-MB-231 **(A, B)** A2780-WT **(C, D)** cells at 24 and 72h. Data represented as Mean ± SD (n = 6)

Table 3.4: IC$_{50}$ values (μM) of the different DOX-MNC-4 formulations in A2780-WT ovarian cancer and MDA-MB-231 breast cancer cells

Group	A2780-WT		MDA-MB-231	
	24h	72h	24h	72h
DOX.HCl	0.024 ± 0.013	0.014 ± 0.003	0.496 ± 0.028	0.08 ± 0.009
DOX-MNC-4a	0.145 ± 0.01	0.059 ± 0.006	--	0.371 ± 0.021
DOX-MNC-4b	0.103 ± 0.006	0.038 ± 0.01	--	0.382 ± 0.019
DOX-MNC-4c	0.162 ± 0.002	**0.042 ± 0.008**	1.55 ± 0.024	**0.223 ± 0.016**

The *in vitro* therapeutic efficacy of the three cationic DOX-MNC-4 formulations with different %LC of DOX was determined in A2780-WT and MDA-MB-231 cells by MTT assay. As anticipated, all formulations showed higher IC_{50} values than free DOX. The cytotoxicity was dependent on the rate of uptake of the formulations. Also, DOX release was guided by a pH-dependent mechanism wherein the drug could be released and available for activity only in the lysosomal pH. Likewise, all formulations showed lower cytotoxicity at the end of 24h, particularly in MDA-MB-231 cells wherein only DOX-MNC-4a formulation exhibited at least 50% toxicity (**Figure 3.10** and **Table 3.4**). At 72h, however, the formulations exhibit toxicity proportional to %LC of DOX in each. Thus, DOX-MNC-4b and 4c formulations had similar IC_{50} of 0.038 and 0.042 µM respectively in A2780-WT cells. Triple negative MDA-MB-231 cells, due to a slower uptake rate showed a nearly 4-fold higher IC_{50} than A2780 cells across all treatment groups, with DOX-MNC-4c formulation showing the highest cytotoxicity of all the nanoformulations tested. The IC_{50} of DOX-MNC-4c in MDA-MB231 at 72h was 0.223 µM.

3.3.9 IN VITRO DETERMINATION OF MRI POTENTIAL OF CATIONIC MNCS
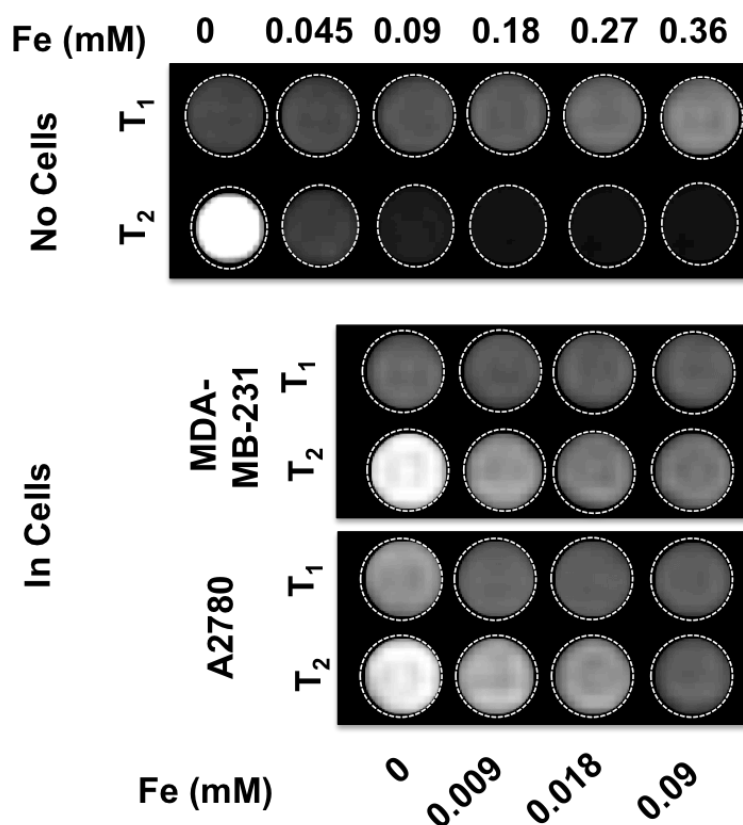
Figure 3.11: In vitro evaluation of MRI potential of DOX-MNC-4c formulation. T_1 and T_2 images of phantom gels of A2780-WT and MDA-MB-231 cells incubated with different concentrations of DOX-MNC-4c formulation. The contrasts of the cellular phantom gels were compared with those obtained from serial dilutions of the formulation in absence of cells

In the next step, we evaluated the MRI potential of DOX-MNC-4c formulation was evaluated in both the cell lines mentioned in the previous section. Following 24h incubation with the said formulation at concentrations equivalent to 0.009, 0.018 and 0.09 mM Fe, the cell viability was determined by trypan blue assay and 9 million live cells per group were mixed uniformly with molten agar and cooled to mimic soft tumor mass. These gels were then scanned in Siemens 3T human scanner to obtain T_1 and T_2-weighted contrasts (**Figure 3.11**). The phantom contrasts without cells echoed the trend seen in relaxivity

measurements. The formulation did not show any change in positive (T_1) contrast. The negative (T_2) contrast, on the other hand showed a dose dependent increase. The cellular phantom gels also showed significant dose-dependent increase in contrast. A2780 cells showed a greater contrast compared to MDA-MB-231 cells due to comparatively higher uptake in A2780 cells. It is noteworthy that the contrast obtained for the cationic MNC is significantly higher in comparison to that obtained with the anionic MNCs discussed in the previous chapter.

3.4. DISCUSSION

In spite of significant advances made in the field of nanomedicine for cancer therapy, numerous problems continue to plague the successful entry of these promising drug delivery systems into clinical use. A major cause of this impediment is insufficient characterization and lack of understanding of the interactions of various nanoformulations *in vivo*. Although the enhanced permeability and retention (EPR) effect is viewed as a key motivation for the use of nano-scale drugs to treat solid tumors, physiological barriers posed by the tumor microenvironment hamper uniform delivery of nanoparticles in amounts sufficient to eradicate cancer. Nanoparticle size, shape and surface charge (zeta potential) have been seen as key factors interacting with physiological tissues and thus affecting the uptake of the particles. Predominantly, zeta potential or surface charge density of the nanoparticles significantly affects their intracellular uptake. Even relatively small positive zeta potential has been shown to cause more than two folds increase in intracellular uptake as well as transvascular flux of the nanoparticles.[25] PLK-based nanocarriers, by virtue of their high cationic nature, have shown significant increase in cellular uptake of such nanocarriers *in vitro* as well as *in vivo*. Cationic nanoparticles made from these polymers have shown significant anti-angiogenic properties in animal models[26] due to the enhanced uptake and accumulation of these intravenously administered cationic systems in the tumor tissue. Poly (L-lysine) serves as a good polymer for development of nanocarriers capable of interacting favorably with the cell membranes to achieve enhanced drug delivery.

Development of MNPs for cancer theranostics requires development of nanoparticle cores with superior magnetic properties, which are governed by their core size. A precise control over the nucleation and growth phases during the synthesis of core MNPs is a prerequisite to synthesizing monodisperse magnetic nanoparticles. Thermal

decomposition method provides this control over particle size, thereby enabling synthesis of larger MNPs, which are known to show higher T_2 relaxivity. The prolonged *in situ* tempering of the formed MNPs at high temperatures further enhances the magnetization saturation of the resulting MNPs. Size distribution of the cores so formed is also a critical parameter. In the ramp and soak technique, which was similar to the techniques described in the precious chapter, this separation was achieved by heating the reactants at 150°C (nucleation temperature deduced in chapter 2) for 2hrs during which time maximum amount of $Fe(acac)_3$ was reduced by the solvent to form nuclei. The subsequent ramp in temperature to reflux initiated the growth phase, which utilized the remaining precursor for increasing the core particle size. This method resulted in a broad size distribution. Hot injection method offered significant advantages over this conventional method. The fast injection of the precursor in a solvent, which was already at reflux, induced a high degree of super-saturation, resulting in a transient burst of nucleation as the temperature dropped to about 165°. As the temperature rose rapidly once again to reflux it prevented any further nucleation and promoted uniform growth of the formed nuclei. This entire step was very short and lasted for about 10 minutes only and led to large-sized nanoparticles above 13nm and with a very narrow size distribution.

The prolonged high temperature annealing of the formed MNPs imparts superior magnetic properties to the MNPs formed by both methods. However, several factors affect the magnetic properties, most predominant being the core diameter and size distribution. In the nanometer regime, the MNPs comprise of single domains and hence exhibit properties different than those of the bulk material. In such clusters of single-domain MNPs, the magnetic moment of each particle interacts with its neighbors and the field to align in the direction of the magnetic field. The magnetization at which all the moments are aligned is referred to as the saturation magnetization (M_s).[27] Particles obtained by hot

injection method exhibited nearly 3-fold higher M_s compared to those obtained from the ramp soak method. Even in comparison to the once commercially available Feridex[®28], the MNPs obtained by hot injection method had higher M_s. This is predominantly due to the particle size and narrow size distribution of the core particles. The complete absence of hysteresis indicated absence of any remnant magnetization upon removal of the magnetic field, thereby confirming their superparamagnetic nature.

MNCs were prepared by formation of coordination complexes between the MNP surface and the pendant primary amino groups of the PLK-*b*-PEG copolymers. Due to the absence of strong hydrophobic surfactants such as oleic acid and oleylamine coating the MNP surface, this synthesis could be carried out by a completely hydrophilic process similar to the process described in Chapter 2. The resulting cluster size was dictated by the r.u. of l-lysine in the PLK block. The block length also affected the colloidal stability of the MNCs. In a sharp contrast with the MNCs stabilized by anionic block copolymers in the previous chapter, the cationic MNCs showed significant stability thus suggesting that the coordination complex between the primary amino group and MNP surface is significantly stronger than that between the carboxylate group and MNPs. Hence, none of the clusters showed complete loss of stability. MNC-1 clusters however, showed an increase in D_{eff} over the period of one month. This increase can be attributed to the lack of compactness in the MNCs (**Figure 2**) formed by the shortest copolymer (PLK r.u. 10). .Compared to the other MNCs, MNC-1 also had significantly less polymer content, which also indicates incomplete surface coverage and hence a high propensity to lose colloidal stability. In comparison, MNC-4 clusters, which were synthesized from PLK_{50}-*b*-PEG_{113} and MNPs with core size 14.4nm, showed only marginally higher polymer content than MNC-1 and yet this formulation showed significantly higher colloidal stability. This highlights the important role played by the PLK block length in stabilization of the clusters.

Copolymers with a larger PLK block imparted significantly greater interactions with the MNP surface, thus covering a greater MNP surface area, thus preventing agglomeration and loss of colloidal properties.

As mentioned in Chapter 2, relaxivity is an important property of MNPs. It is a measure of the MRI potential of the contrast agent. Numerous factors such as method of MNP synthesis, MNP core size, the type of stabilizing agent and the MNP content in the cluster, all cumulatively affect relaxivity of MNP-based MR contrast agents. This reflects in the T_2 relaxivity (r_2) of the MNCs as mentioned in Table 3.2. In spite of having the highest MNP content amongst the four different types of clusters synthesized, MNC-1 showed the lowest r_2 values. The lack of compactness of the MNC-1 clusters is a prime cause of this result. MNPs are known to exhibit higher r_2 when held together closely in clusters. The use of hydrophilic polymers further enhances r_2 by increasing not only the diffusion but also the retention time of water molecules in close proximity with the MNP surfaces.[29-31] As a result, in clusters with same core MNP sizes, the composition of the cluster, cluster size and the resulting compactness governed the diffusion and retention of water molecules in the interior of the clusters and hence also the relaxivity. MNC-4 clusters exhibited the maximum r_2 relaxivity due to a large core size, largest cluster size and effectively maximum water retention in the core.

DOX loading onto the MNCs was achieved by conjugation of the modified DOX-HZN molecule to the pendant $-NH_2$ groups on the MNC clusters. DOX molecule can be activated at two sites, the 3'-amino and the 13-keto position. However, DOX ligated at 3'-amino group has reduced anti-cancer activity due to energetically unfavorable intercalation of DOX in the minor groove of DNA.[32] Conjugates obtained by modification at 13-keto position do not cause any change in the activity of the molecule. Hence we selectively targeted the hydrazine-containing EMCH molecule to this site to obtain a pH

sensitive DOX-HZN molecule Further, the DOX-HZN was conjugated to the SPDP-modified MNCs via thioether ester over the traditional disulfide linkage due to the previously reported reduced stability of the disulfide bond under physiological conditions.[33] The disulfide bond is susceptible to reductive mechanisms such as those of molecules such as glutathione and other thiol containing molecules in the liver and plasma, which can lead to premature release of the molecule and undesired toxicity. We intended to achieve drug release selectively in the acidic environments of the lysosomal-late endosomal compartments. Stimuli-responsive systems are specifically designed in order to achieve rapid release only under specific conditions such as pH. The acid labile linkers such as cis-aconityl[26, 32] or hydrazone linkers[34, 35] exhibit sufficient extracellular stability and prevent the encapsulated payload from leaching during circulation. Such strategies are also advantageous from the point of reducing the drug dose, as the likelihood of maximum dose reaching the target tissue is very high in comparison to the passive slow diffusion of the drug from the nanocarriers, which is governed primarily by hydrolysis. Drug conjugation also imparts considerable control over the amount of drug loaded in the nanocarriers. This control is absolutely essential in case of nanocarriers carrying multiple modalities such as diagnostic and therapeutic payloads. An optimum drug: MNP ratio needs to be achieved in the development of co-encapsulating theranostic nanosystems in order to achieve a good contrast in the target tissue while ensuring that the DOX levels are also sufficient to achieve a therapeutic effect.

Shielding of the ε-amino groups by thiol end groups marginally reduced the positive zeta potential of the formulations. However, it did not affect the charge-induced intracellular uptake of the MNCs in human ovarian and triple negative breast cancer cells. The MNCs were internalized as early as 1h-post incubation. The shielding of the ε-amino groups also reduced the toxicity of the unloaded

clusters significantly. The higher uptake of the formulations translated into significant intracellular toxicity of the formulations.

DOX is an anthracycline antibiotic used in the treatment of a wide variety of malignancies such as breast, ovarian, sarcomas, lymphomas, and acute luekemias. Intracellular free DOX accumulation varies from one cell line to another. However, most cells achieve intracellular steady-state levels within 2–8 hr.[36] In addition to intracellular accumulation, doxorubicin's mechanism of action is also variable for different cell types. For instance, Fulda et al.[37, 38] concluded that DOX induces the apoptotic death signal in different ways depending upon the cell line. Also, in comparison to the free drug (DOX.HCl), DOX encapsulated within or bound to nanovehicles is expected to show a slower onset of action, which is governed by the release profile of the drug from the nanocarriers. Although in this case, the cationic MNCs show significantly faster uptake within the first three hours, the pH-triggered release of DOX is a relatively slow mechanism as seen in the in vitro drug release studies (**Section 3.3.5 and Figure 3.6**). All these factors contribute to the slower onset of cytotoxicity and hence a higher IC_{50} compared to the free drug. The different formulations exhibit different cytotoxic potential depending on the %LC of DOX. This trend was seen in both cell lines, though was more prominent in MDA-MB-231 cells wherein DOX IC_{50} values decreased with increase in DOX loading. We attribute this difference to the DOX: MNP ratio in the three formulations. A lower DOX %LC or more MNP content can sterically hinder the exposure of the hydrazone linkage to acidic pH and thus can retard DOX release. Nonetheless, the systems successfully function as a pH controlled drug release nanoformulation, which by virtue of a sustained release can prolong the therapeutic effect.

While MNPs larger than 7nm are predominantly negative contrast agents, the cluster size and compactness of the cluster plays an important role in the enhancement of T_2-

weighted MR capability. DOX loading did not affect the MR potential of the MNCs. The core MNPs used in MNC-4 clusters were above 13nm in diameter. The resulting high Ms and significantly high r_2 relaxivity values translated into superior negative contrasts of the clusters embedded in agar phantom gels. The significantly higher cellular uptake of the MNCs further enhanced the contrast of the MNCs.

3.5 CONCLUSION

In summary, we successfully synthesized MNP cores devoid of any hydrophobic surfactants and in the 14-20nm-size range by a one-step direct injection method. Compared to the conventional ramp-soak method, the cores were highly monodisperse. The larger 14nm MNPs showed stronger magnetic susceptibility and had a higher M_s compared to the 9.3nm cores, which had a broader size distribution. PLK-PEG polymers form a stable complex with MNP surfaces depending on the lysine block-length. The cluster size also governed the relaxivity of the formulations. In comparison to the relaxivity of Feridex (269.4 $s^{-1}.mM^{-1}$), MNC-4 formulation stabilized by PLK_{50}-b-PEG_{113} showed significantly higher relaxivity values. The cellular uptake of these formulations was facilitated by their interaction with the negatively charged cell surface and subsequent endosmolytic uptake. Compared to anionic formulations discussed in the previous chapter, cationic MNCs showed a significantly higher cellular uptake. This can induce significant toxicity in the cells. Modification of the free cationic side-chain primary amino groups by heterobifunctional linker SPDP and subsequent reduction by DTT to introduce thioester functionality significantly reduced the toxicity of the cationic formulation. DOX modified by hydrazone linker was conjugated onto these thiol end groups to form a stable thioester conjugate which would cleave only at the hydrazone linkage at an acidic pH with no effect of redox conditions. Introduction of the pH sensitive linker resulted in a sustained release of DOX exclusively in the acidic pH. End group modification also reduced the zeta potential of the formulations, which in turn also altered the uptake of the formulations depending on the degree of modification.

The formulations showed differential uptake in A2780 ovarian cancer and MDA-MB-231 triple negative breast cancer cells. This difference in uptake also influenced the cytotoxic efficacy of the DOX-MNC-4 formulations. Interestingly, formulation DOX-MNC-

4a, which had the least %LC also showed significantly higher IC_{50} values in both the cell lines. This difference can be attributed to the higher MNP content in the 4a formulation, which can shield the cleavage of the hydrazone bond and further prolong the release of DOX from the clusters. Finally, the higher cellular uptake also resulted in significantly higher MRI potential of the cationic formulations. The formulations resulted in higher negative contrasts at lower Fe concentrations compared to the anionic formulations. Thus we can conclude that cationic polymers are capable of forming very stable stimuli-responsive theranostic MNCs without any modification of the polymer to introduce favorable functional groups.

3.6 FUTURE DIRECTIONS

This work holds tremendous potential in development of protein theranostics. PLK-PEG, by virtue of this positive charge can efficiently condense proteins and nucleic acids onto itself. We have initiated initial studies to load anti-oxidant enzymes such a superoxide dismutase (SOD) and catalase, which show tremendous potential in neurodegenerative disorders.

Previous work in our group has already demonstrated the ability of MNCs to alter enzyme kinetics in response to an alternating (AC) magnetic field.[39] We intend to study the effect of such AC fields on the structural integrity of these clusters. Our initial work has shown promising results. However, additional confirmatory studies are required before the phenomena can be revealed.

Finally, *in vivo* pharmacokinetics of the DOX-conjugated MNC will be evaluated in xenografts models and therapeutic efficacy studies will be conducted in near future.

3.6 REFERENCES

1. Tahara, K.; Furukawa, S.; Yamamoto, H.; Kawashima, Y., Hybrid-modified poly(d,l-lactide-co-glycolide) nanospheres for a novel cellular drug delivery system. *Int. J. Pharm.* **2010,** 392, 311-313.

2. Yu, X. Y.; Schofield, B. H.; Croxton, T.; Takahashi, N.; Gabrielson, E. W.; Spannhake, E. W., Physiologic modulation of bronchial epithelial cell barrier function by polycationic exposure. *Am. J. Respir. Cell Mol. Biol.* **1994,** 11, 188-198.

3. Yin, P.; Wang, Y.; Qiu, Y.; Hou, L.; Liu, X.; Qin, J.; Duan, Y.; Liu, P.; Qiu, M.; Li, Q., Bufalin-loaded mPEG-PLGA-PLL-cRGD nanoparticles: preparation, cellular uptake, tissue distribution, and anticancer activity. *Int. J. Nanomed.* **2012,** 7, 3961.

4. Niidome, T.; Yamauchi, H.; Takahashi, K.; Naoyama, K.; Watanabe, K.; Mori, T.; Katayama, Y., Hydrophobic cavity formed by oligopeptide for doxorubicin delivery based on dendritic poly (L-lysine). *J. Biomater. Sci. Polym. Ed.* **2014,** 25, 1362-1373.

5. Dai, J.; Zou, S.; Pei, Y.; Cheng, D.; Ai, H.; Shuai, X., Polyethylenimine-grafted copolymer of poly (l-lysine) and poly (ethylene glycol) for gene delivery. *Biomaterials* **2011,** 32, 1694-1705.

6. Pfeifer, C.; Hasenpusch, G.; Uezguen, S.; Aneja, M. K.; Reinhardt, D.; Kirch, J.; Schneider, M.; Claus, S.; Frieß, W.; Rudolph, C., Dry powder aerosols of polyethylenimine (PEI)-based gene vectors mediate efficient gene delivery to the lung. *J. Controlled Release* **2011,** 154, 69-76.

7. Shim, M. S.; Kwon, Y. J., Stimuli-responsive polymers and nanomaterials for gene delivery and imaging applications. *Adv. Drug Del. Rev.* **2012,** 64, 1046-1059.

8. Kievit, F. M.; Veiseh, O.; Bhattarai, N.; Fang, C.; Gunn, J. W.; Lee, D.; Ellenbogen, R. G.; Olson, J. M.; Zhang, M., PEI–PEG–chitosan-copolymer-coated iron oxide nanoparticles for safe gene delivery: synthesis, complexation, and transfection. *Adv. Funct. Mater.* **2009,** 19, 2244-2251.

9. Bowman, K.; Leong, K. W., Chitosan nanoparticles for oral drug and gene delivery. *Int. J. Nanomed.* **2006,** 1, 117.

10. Roy, K.; Mao, H.-Q.; Huang, S.-K.; Leong, K. W., Oral gene delivery with chitosan–DNA nanoparticles generates immunologic protection in a murine model of peanut allergy. *Nat. Med.* **1999,** 5, 387-391.

11. Lim, Y.-b.; Kim, S.-M.; Lee, Y.; Lee, W.-k.; Yang, T.-g.; Lee, M.-j.; Suh, H.; Park, J.-s., Cationic hyperbranched poly (amino ester): a novel class of DNA condensing molecule with cationic surface, biodegradable three-dimensional structure, and tertiary amine groups in the interior. *J. Am. Chem. Soc.* **2001,** 123, 2460-2461.

12. Akinc, A.; Anderson, D. G.; Lynn, D. M.; Langer, R., Synthesis of poly (β-amino ester) s optimized for highly effective gene delivery. *Bioconj. Chem.* **2003,** 14, 979-988.

13. Huang, R.-Q.; Qu, Y.-H.; Ke, W.-L.; Zhu, J.-H.; Pei, Y.-Y.; Jiang, C., Efficient gene delivery targeted to the brain using a transferrin-conjugated polyethyleneglycol-modified polyamidoamine dendrimer. *The FASEB Journal* **2007,** 21, 1117-1125.

14. Dufès, C.; Uchegbu, I. F.; Schätzlein, A. G., Dendrimers in gene delivery. *Adv. Drug Del. Rev.* **2005,** 57, 2177-2202.

15. Kim, T.-i.; Seo, H. J.; Choi, J. S.; Jang, H.-S.; Baek, J.-u.; Kim, K.; Park, J.-S., PAMAM-PEG-PAMAM: novel triblock copolymer as a biocompatible and efficient gene delivery carrier. *Biomacromolecules* **2004,** 5, 2487-2492.

16. Babic, M.; Horák, D.; Trchová, M.; Jendelová, P.; Glogarová, K.; Lesný, P.; Herynek, V.; Hájek, M.; Syková, E., Poly (L-lysine)-modified iron oxide nanoparticles for stem cell labeling. *Bioconj. Chem.* **2008,** 19, 740-750.

17. Martin, A. L.; Bernas, L. M.; Rutt, B. K.; Foster, P. J.; Gillies, E. R., Enhanced cell uptake of superparamagnetic iron oxide nanoparticles functionalized with dendritic guanidines. *Bioconj. Chem.* **2008,** 19, 2375-2384.

18. Thorek, D. L. J.; Tsourkas, A., Size, charge and concentration dependent uptake of iron oxide particles by non-phagocytic cells. *Biomaterials* **2008,** 29, 3583-3590.

19. Wang, X.; Tu, Q.; Zhao, B.; An, Y.; Wang, J.-C.; Liu, W.; Yuan, M.-S.; Ahmed, S. M.; Xu, J.; Liu, R., Effects of poly (l-lysine)-modified Fe 3 O 4 nanoparticles on endogenous reactive oxygen species in cancer stem cells. *Biomaterials* **2013,** 34, 1155-1169.

20. Oh, Y.-K.; Straubinger, R. M., Intracellular fate of Mycobacterium avium: use of dual-label spectrofluorometry to investigate the influence of bacterial viability and opsonization on phagosomal pH and phagosome-lysosome interaction. *Infect. Immun.* **1996,** 64, 319-325.

21. Furgeson, D. Y.; Dreher, M. R.; Chilkoti, A., Structural optimization of a "smart" doxorubicin–polypeptide conjugate for thermally targeted delivery to solid tumors. *J. Controlled Release* **2006,** 110, 362-369.

22. Read, M. L.; Etrych, T.; Ulbrich, K.; Seymour, L. W., Characterisation of the binding interaction between poly (L-lysine) and DNA using the fluorescamine assay in the preparation of non-viral gene delivery vectors. *FEBS Lett.* **1999,** 461, 96-100.

23. Oberg, B. P.; Mcmenamin, E.; Lucas, F. L.; McMonagle, E.; Morrow, J.; T ALP, I.; Himmelfarb, J., Increased prevalence of oxidant stress and inflammation in patients with moderate to severe chronic kidney disease. *Kidney Int.* **2004,** 65, 1009-1016.

24. Fischer, D.; Li, Y.; Ahlemeyer, B.; Krieglstein, J.; Kissel, T., In vitro cytotoxicity testing of polycations: influence of polymer structure on cell viability and hemolysis. *Biomaterials* **2003,** 24, 1121-1131.

25. Stylianopoulos, T.; Soteriou, K.; Fukumura, D.; Jain, R. K., Cationic nanoparticles have superior transvascular flux into solid tumors: insights from a mathematical model. *Ann. Biomed. Eng.* **2013,** 41, 68-77.

26. Al-Jamal, K. T.; Al-Jamal, W. T.; Wang, J. T. W.; Rubio, N.; Buddle, J.; Gathercole, D.; Zloh, M.; Kostarelos, K., Cationic Poly-l-lysine Dendrimer Complexes Doxorubicin and Delays Tumor Growth in Vitro and in Vivo. *ACS Nano* **2013,** 7, 1905-1917.

27. Frey, N. A.; Peng, S.; Cheng, K.; Sun, S., Magnetic nanoparticles: synthesis, functionalization, and applications in bioimaging and magnetic energy storage. *Chemical Society reviews* **2009,** 38, 2532-2542.

28. Li, W.; Tutton, S.; Vu, A. T.; Pierchala, L.; Li, B. S. Y.; Lewis, J. M.; Prasad, P. V.; Edelman, R. R., First-pass contrast-enhanced magnetic resonance angiography in humans using ferumoxytol, a novel ultrasmall superparamagnetic iron oxide (USPIO)-based blood pool agent. *J. Magn. Reson. Imaging* **2005,** 21, 46-52.

29. Paquet, C.; de Haan, H. W.; Leek, D. M.; Lin, H.-Y.; Xiang, B.; Tian, G.; Kell, A.; Simard, B., Clusters of superparamagnetic iron oxide nanoparticles encapsulated in a hydrogel: a particle architecture generating a synergistic enhancement of the T2 relaxation. *ACS Nano* **2011,** 5, 3104-3112.

30. de Haan, H. W., Mechanisms of proton spin dephasing in a system of magnetic particles. *Magn. Reson. Med.* **2011,** 66, 1748-1758.

31. de Haan, H. W.; Paquet, C., Enhancement and degradation of the R 2* relaxation rate resulting from the encapsulation of magnetic particles with hydrophilic coatings. *Magn. Reson. Med.* **2011,** 66, 1759-1766.

32. Di Marco, A.; Gaetani, M.; Scarpinato, B., Adriamycin (NSC-123,127): a new antibiotic with antitumor activity. *Cancer Chemother. Rep.* **1969,** 53, 33.

33. Trail, P. A.; Willner, D.; Knipe, J.; Henderson, A. J.; Lasch, S. J.; Zoeckler, M. E.; TrailSmith, M. D.; Doyle, T. W.; King, H. D.; Casazza, A. M., Effect of linker variation on the stability, potency, and efficacy of carcinoma-reactive BR64-doxorubicin immunoconjugates. *Cancer Res.* **1997,** 57, 100-105.

34. Casi, G.; Neri, D., Antibody–drug conjugates: basic concepts, examples and future perspectives. *J. Controlled Release* **2012,** 161, 422-428.

35. Kaminskas, L. M.; Kelly, B. D.; McLeod, V. M.; Sberna, G.; Owen, D. J.; Boyd, B. J.; Porter, C. J., Characterisation and tumour targeting of PEGylated polylysine dendrimers bearing doxorubicin via a pH labile linker. *J. Controlled Release* **2011,** 152, 241-248.

36. Jackson, T. L., Intracellular accumulation and mechanism of action of doxorubicin in a spatio-temporal tumor model. *J. Theor. Biol.* **2003,** 220, 201-213.

37. Fulda, S.; Sieverts, H.; Friesen, C.; Herr, I.; Debatin, K.-M., The CD95 (APO-1/Fas) system mediates drug-induced apoptosis in neuroblastoma cells. *Cancer Res.* **1997,** 57, 3823-3829.

38. Fulda, S.; Strauss, G.; Meyer, E.; Debatin, K.-M., Functional CD95 ligand and CD95 death-inducing signaling complex in activation-induced cell death and doxorubicin-induced apoptosis in leukemic T cells. *Blood* **2000,** 95, 301-308.

39. Klyachko, N. L.; Sokolsky-Papkov, M.; Pothayee, N.; Efremova, M. V.; Gulin, D. A.; Pothayee, N.; Kuznetsov, A. A.; Majouga, A. G.; Riffle, J. S.; Golovin, Y. I., Changing the

Enzyme Reaction Rate in Magnetic Nanosuspensions by a Non-Heating Magnetic Field.

Angew. Chem. **2012,** 124, 12182-12185.

CHAPTER 4

NON-IONIC MAGNETIC NANOCLUSTERS FOR DUAL-PURPOSE MRI IMAGING

4.1 INTRODUCTION

Superparamagnetic iron oxide nanoparticles (MNPs) are well known for being able to shorten the transverse relaxation time of water protons and have been used as a negative contrast agents in MRI.[1] Recently, aggregated or assembled MNPs are drawing greater attention in MRI applications because they can provide even higher contrast than individually dispersed MNPs.[2-6] For biomedical applications such as diagnostics and drug delivery, several characteristics of MNPs such as core particle size, cluster size, surface charge, colloidal stability and biocompatibility of stabilizing compounds are of critical importance since these control the various pharmacokinetic parameters of the MNPs in vivo.

Different methods have been used to automate and precisely control the process of formation of uniform magnetic nanoclusters (MNCs) such as spray drying[7], mixing with a conventional high speed homogenizer[8], Confined Impinging Jet (CIJ) mixer[9, 10] and Multi-Inlet Vortex Mixer (MIVM)[11]. In comparison to thermodynamically controlled processes such as dialysis and emulsification-evaporation[12], which are slow and result in drug/matrix separation and low drug loading, kinetically controlled techniques such as flash nanoprecipitation with the MIVM and jet impingement have been shown to result in high drug loading and formation of the stable complexes.[13-16] The CIJ mixer and MIVM show numerous advantages over uncontrolled self-assembly method such as narrow particle

size distributions, ability to control the particle size and particle composition and enhance drug loading capacity.[14] These kinetically controlled methods of self-assembly were chosen for their ability to induce mixing and resultant precipitation in significantly lesser time than the characteristic precipitation times of organic/inorganic materials.[17] These kinetically controlled processes have two requisites. First is the creation of a region of highly turbulent energy dissipation. High-energy dissipation occurs for impinging jets because the kinetic energy of each jet stream is converted into a turbulent-like motion through collision and redirection of the flow in a very small volume. Second requisite is to ensure that the process streams for mixing pass through the high intensity region. The first step ensures the proper scale for mixing and the second ensures that the desired molar flow ratios are preserved during the rapid mixing process.[11]

Rapid precipitation of organic and inorganic components of nanoparticles at high supersaturation requires controlled homogenous mixing to control the particle size distribution, which is possible to achieve in a Multi-Inlet Vortex Mixer (MIVM). The four-stream MIVM allows control of both, the supersaturation and the final solvent quality by precisely varying stream velocities with the help of precisely defined Reynolds numbers (R_e). The Reynolds number is defined as the ratio of momentum forces to viscous forces and consequently quantifies the relative importance of these two types of forces for given flow conditions.[18] Reynolds numbers frequently arise in fluid dynamics and are used to characterize different flow regimes within a similar fluid, such as

- Laminar flow: Occurs at low Reynolds numbers, where fluid viscosity is dominant, and is characterized by smooth, constant fluid motion;

- Turbulent flow: Occurs at high Reynolds numbers where inertial forces are dominant tend to produce chaotic eddies and other flow instabilities

The MIVM design enables mixing of streams of unequal volumetric flows, which is not possible with alternate confined impinging jet (CIJ) mixing geometries, thus making it a more versatile method with a potential for complete automation, high degree of reproducibility and control of critical parameters such as particle size and distribution.

We first employed the MIVM to control the cluster formation process of MNPs with the help of Pluronic amphiphilic tri-block copolymers. As mentioned earlier, the magnetic properties and MRI potential of MNPs such as T_2 relaxivity is enhanced when they are packed into compact and stable clusters.[19] We studied the effect of numerous factors such as MNP and polymer content at different mixing speeds which were controlled by adjusting the R_e. Subsequently, we also attempted to co-encapsulate a hydrophobic anti-cancer agent paclitaxel (PTX) with these MNCs formed by kinetically controlled flash nanoprecipitation in a MIVM. The results showed that MIVM served as an ideal method for rapid and formation of large volumes of MNCs with precise control over the cluster size. Pluronic F127 by itself or in combination with Pluronic P123 efficiently encapsulated the oleic acid coated MNPs (OMPs) alone to form very well defined MNCs. However, the tri-block Pluronic polymers showed a potential limitation. Negligible to no paclitaxel loading was achieved when using F127 alone. Inclusion of P123 as a stabilizing polymer increased the encapsulation efficiency, but the % loading of PTX albeit, was still very low. Nonetheless, the excellent control over cluster formation is very encouraging and warrants further work as mentioned in the future directions of this chapter.

4.2 MATERIALS AND METHODS

4.2.1 Materials

Iron (III) acetylacetonate (Fe(acac)$_3$), Benzyl ether, nitric acid (TraceSELECT), ICP grade standards for Fe (Fluka) were purchased from were purchased from Sigma-Aldrich (St. Louis, MO), Ethanol (200 proof), tetrahydrofuran (anhydrous), n-hexane, acetone (histology grade), chloroform (anhydrous), acetonitrile (HPLC grade), methanol (HPLC grade) and other HPLC grade solvents were purchased from Thermo Fisher Scientific (Waltham, MA). Pluronic F127 (M. wt 12,600, PEO$_{100}$PPO$_{65}$PEO$_{100}$) and Pluronic P123 (M.wt. 5750, PEO$_{20}$PPO$_{70}$PEO$_{20}$) were kindly provided by BASF (Florham Park, New Jersey). Paclitaxel (PTX) was purchased from LC Labs (Woburn, MA).

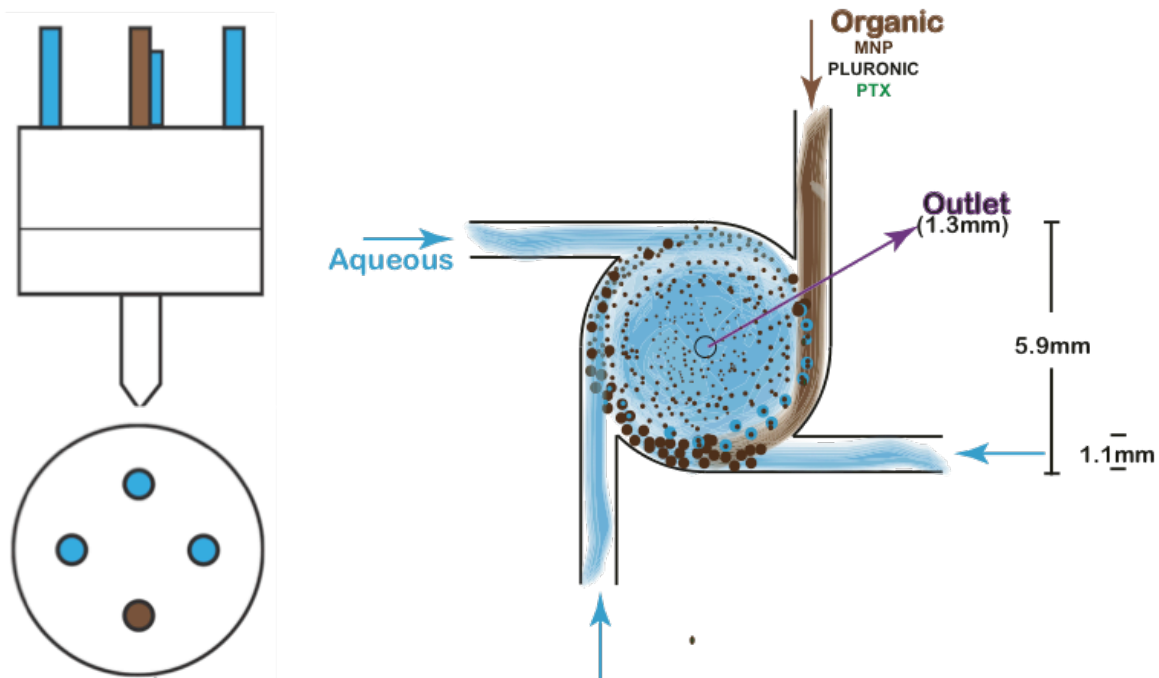### 4.2.2. Design of a Multi Inlet Vortex Mixer (MIVM)

Figure 4.1. Design of a multi-inlet vortex mixer used for fabrication of MNCs

The MIVM is made from a fiberglass composite material, which is resistant to organic solvents typically used in the chemical industry. Four external inlets lead vertically downwards to the four inlet streams (1.1mm diameter) that open tangentially in the boundary of the central mixing chamber (5.9mm). The final product exits the mixing chamber at the center as shown in **Figure 4.1**.

The theory behind the functioning of the MIVM is that the different flow rates and hence the different energies from each stream contribute separately to drive fast micromixing into the chamber. In MIVM different volumetric flow rates in each stream, defined by the Re, can be run and still obtain good mixing. One of the advantages of using the MIVM is that the final fluid phase is mostly aqueous. Therefore, the stability of the nanoparticles increases in solution by depressing the rate of Ostwald ripening, when the solubility of the precipitating species is high enough to permit this process. The importance of the vortex mixer is that a turbulent region can be created to form and precipitate homogeneous nanoparticles. The momentum of the four inlet streams through the mixing chamber creates the turbulent region. Once in the confines of the mixing chamber, the four fluid streams mix by convection energy (macro scale). Turbulent eddies formed in the mixing chamber (meso scale) result in formation of daughter vortices by turbulent diffusion. Eventually, molecular diffusion occurs in the turbulent eddies and eliminates region of segregations, resulting in efficient encapsulation of the organic components within the polymeric nanostructures.[20]

The inlet velocities are selected by choosing an appropriate R_e, inlet velocities, and physical properties of the inlet streams. The inlet velocities depend on the desired Reynolds numbers and volume fractions in the mixing chamber. The four inlet flow rates can be controlled using mechanical pumps. R_e depends upon the inlet stream velocities (u_i) and kinematic viscosities (v_i) of the inlet streams and is defined as[11] :

$$R_e = D_{mixer} [u_1/v_1 + u_2/v_2 + u_3/v_3 + u_4/v_4] \qquad \text{Eqn 4.1}$$

where D_{mixer} is the diameter of the mixer

4.2.3 METHODS

4.2.3.1 Synthesis of oleic acid coated MNPs

Oleic acid-coated MNPs (OMPs) were synthesized by thermal decomposition of $Fe(acac)_3$ by at method previously described by Sun et al.[21] Briefly, 2mmoles of $Fe(acac)_3$, 6mmoles of oleic acid, 6mmoles of oleylamine, 10mmoles of 1,2 hexadecandiol were dissolved in 20mL benzyl ether in a 3-necked round bottom flask. The mixture was heated at 110°C for 30 minutes in order to remove any traces of water in the reaction mixture. The temperature was then raised to 200°C at 3°C/min. The reaction was kept isothermal at 200°C for 2h following which the temperature was further increased to reflux (~295°C) and maintained isothermal for 2.5h. At the end of the reaction, the mixture was cooled and precipitated with twice the amount of reagent alcohol. The precipitate was separated by centrifugation at 4000 rpm for 45 minutes and washed with reagent alcohol.   The final product was dried by rotary evaporation and stored under vacuum for further use.

4.2.3.2 Preparation of MNCs by flash nanoprecipitation

a. Determination of critical aggregation concentration (cac) of F127

We determined the concentration at which Pluronic F127 (CMC 2.8µM)[22] started aggregating in a mixture of 9.1%v/v aqueous mixture of tetrahydrofuran (THF) by DLS. Briefly, F127 was dissolved at different concentration in 9.1% v/v THF and allowed to rest for 15 minutes prior to measurements. The kilo counts per second function of DLS measurements was recorded for each dilution and plotted as a function of the concentration of F127. The point of inflection was determined as the cac of F127 for the

given solvent system. For all further mixing procedures, the polymer concentration was maintained above the cac value.

b. Determination of supersaturation (S) of paclitaxel

Prior to determination of S, the solubility of paclitaxel (PTX) in 9.1% v/v THF was determined. Briefly, 10mg of PTX was dispersed in 5mL of 9.1% THF and stirred continuously at RT for 72h. The dispersion was centrifuged at 10000 rpm followed by filtration of the supernatant through 0.2µm nylon syringe filter. The amount of PTX dissolved in the supernatant was determined by HPLC and denoted as C_{inf}. Supersaturation (S) of PTX in the chamber was determined as a ratio of the total drug exiting the mixer (mg) and C_{inf}. S is a critical parameter to ensure efficient precipitation of the drug in the given solvent system along with the other organic components. It is recommended to maintain S at values above 40. Similar study was performed for MNPs and for all further experiments, the S_{MNP} was maintained above 3×10^{10}.

c. Cluster-formation

All organic components, namely Pluronic, MNPs, and PTX (wherever included), were dissolved in THF. The MIVM was connected to two high-speed syringe pumps in order to obtain two different flow rates for the organic and aqueous phases. One inlet of the MIVM was connected to the glass syringe filled with organic solution and placed on one of the two pumps. The other three inlets were connected to 140mL syringes filled with DI water. The pump flow rates could by controlled separately by computer software to which the pumps were connected. We performed different trials by changing the R_e, the theoretical loading capacity ($\%TLC_{MNP}$) of the MNPs and PTX ($\%TLC_{PTX}$) loading as tabulated in **table 4.1**. In all experiments THF: water ratio was maintained at 0.091 (9.1%v/v). The crude product exiting the mixer was immediately placed in centrifugal filters (30,000 MWCO) and centrifuged at 1500 rpm. The concentrated product was further washed thrice with water

and passed serially through 0.45 and 0.2µm nylon syringe filter. The dead micelles, i.e. Pluronic micelles without any MNPs encapsulated in them were removed by magnetic separation to obtain the final product.

Table 4.1: MIVM and formulation parameters for the different trials

Formulation	Polymer	Theoretical Loading		R_e
		%LC$_{MNP}$	%LC$_{PTX}$	
A1		44	11	6300
A2		9	4	8400
A3		9	4	12000
A4	F127	15	8	12000
A5		8	10	12000
A6		4	15	12000
A7		8	7	12000
B1	20% P123+	10	5	12000
B2	80% F127	5	5	12000

4.2.3.3 Characterization of MNCs

a. DLS: The particle size and zeta potential of the MNCs so formed was determined by DLS, as described in chapters 2 and 3. The total solid content of the aqueous formulation was determined by TGA and the formulations were diluted to 1mg/mL in DI water for DLS analysis.

b. Composition: The composition of blank formulations (without PTX) was determined by TGA by a method described in the previous chapters. The total polymer content was obtained by subtracting the oleic acid content on the MNPs from the total loss on ignition

(LOI). In case of PTX loaded MNCs, PTX %LC was determined by HPLC connected to a reverse phase C18 column (Phenomenex, Torrance, CA) column and a diode array detector. Briefly, the 0.1mg of the lyophilized formulation was dispersed in acetonitrile and sonicated for 45 minutes following which the sample was centrifuged at 10000 rpm. The supernatant was diluted with mobile phase (Acetonitrile: water 55:45) and injected to obtain a peak at 8 minutes with a method run time of 10 minutes.

c. Colloidal stability of MNCs

Colloidal stability of the MNC formulation was determined on 1mg/mL solutions of MNCs in DI water and phosphate buffered saline (PBS; 10mM; 0.14mM NaCl) at room temperature (RT) and 37°C. The particle size and PDI of the formulations was measured over the period of one month.

4.2.3.4 Evaluation of MRI contrast capacity in phantom gels

MRI contrast capacity of formulations B1 and B2 was determined by embedding the formulations in 2% agar gels in 10mM PBS and taking scans in a 3T human MRI scanner using the protocol mentioned in Chapter 2.

4.3 RESULTS AND DISCUSSION

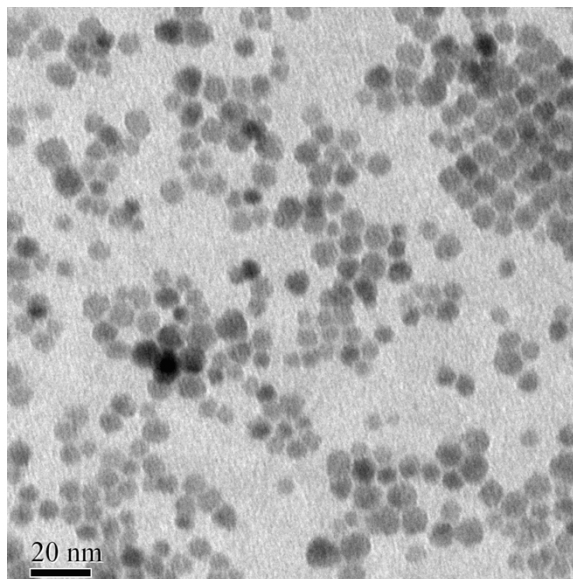### 4.3.1 SYNTHESIS OF OLEIC ACID COATED MNPS

Figure 4.2. TEM image of magnetic nanoparticles coated with hydrophobic fatty acid surfactants oleic acid and oleylamine

Particle size of MNPs obtained by thermal decomposition of Fe (acac)$_3$ in presence of oleic acid and oleylamine surfactants were analyzed by TEM. MNPs so formed had a core size of 6.3 ± 2nm. We further determined the amount of hydrophobic coating on the core particles by TGA. The MNPs had a surfactant coating of 22.6% w/w.

A surfactant-mediated synthetic approach was adopted for this project since we aimed to form the clusters by flash nanoprecipitation by using amphiphilic Pluronic block copolymers. In this synthesis, 1,2 hexadecandiol was added as a reducing agent for the thermal decomposition of Fe(acac)$_3$. The oleic acid and oleylamine acts as a surfactant during the synthesis for the formation of the iron oleate nuclei at 200°C, which act as the seeds growth of the crystals. These hydrophobic coatings also act as ligands for anchoring of the central PPO block of the Pluronic moieties. Benzyl ether was chosen for its high

boiling point (~295°C). This allowed for the rapid annealing of the MNPs once the growth is complete. It has been extensively reported that amphiphilic block copolymers such as Pluronic stabilize MNPs by a ligand exchange mechanism wherein the polymer exchanges with the hydrophobic surfactant on the crystal surface.[23, 24] Surfactant-mediated synthesis enables precise control over the size of the cluster in a two-step process wherein the initial cores in the 3-6 nm range are further used as seeds to grow particles as large as 50nm.[21]
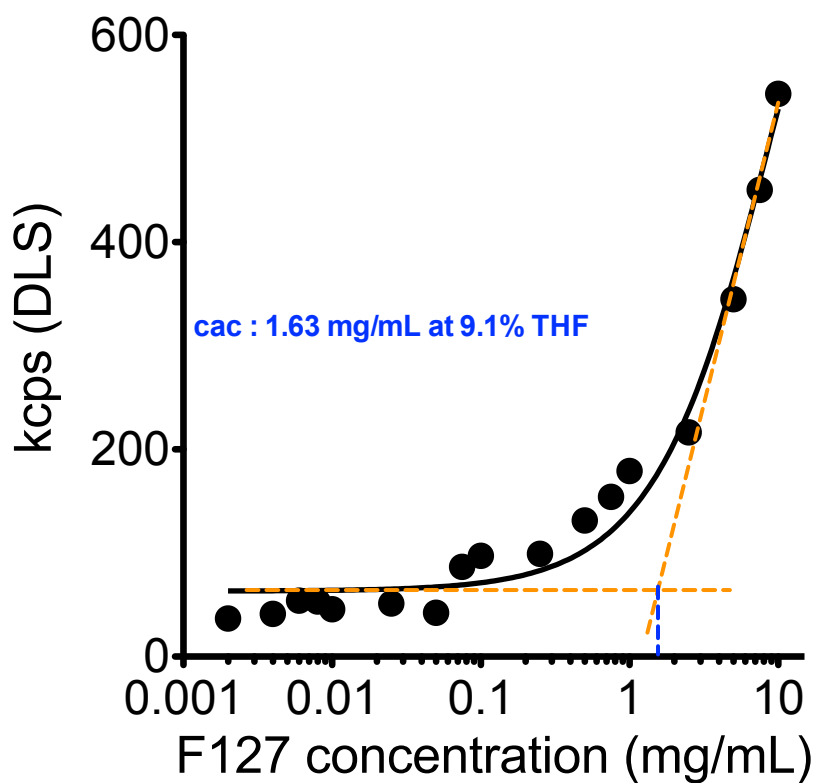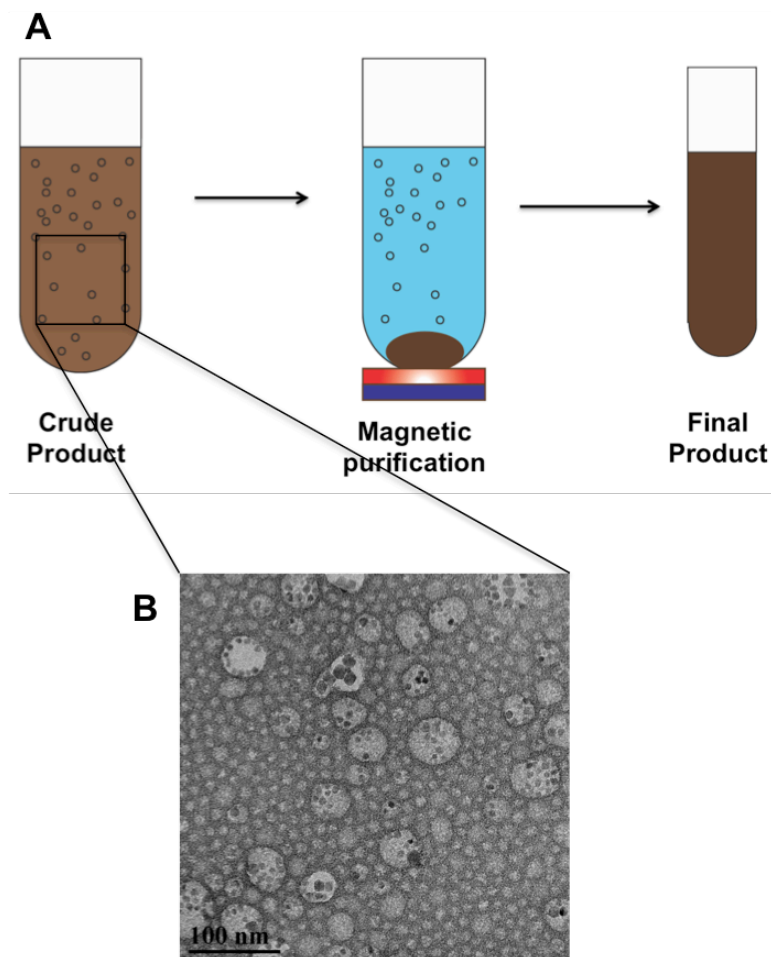

Figure 4.3. CAC determination of Pluronic F127 in 9.1%v/v aqueous THF solution

4.3.2 PREPARATION AND CHARACTERIZATION OF MNCS BY MIVM

Scheme 4.1. MNC purification process post MIVM. **A** Scheme showing magnetic separation of final product from a crude mixture. **B** Different components of the crude product obtained after MIVM removal of organic solvent.

Prior to MNCs preparation the critical aggregation concentration (cac) of Pluronic F127 was determined by DLS. Pluronic had a cac value of 1.63 mg/mL in the selected solvent systems comprising of 9.1% v/v THF in water. Hence, for all trials, care was taken to maintain the polymer concentration in the mixing chamber above the cac value.

Different trials, as mentioned in table 4.1, were conducted for formation of MNCs by MIVM. As shown in **figure 4.3,** the crude formulation consists of a mixture of desired MNCs, un-encapsulated MNPs, dead micelles i.e. micelles with only drug and no MNPs encapsulated (shown by empty black circles) and un-encapsulated crystalline drug (PTX).
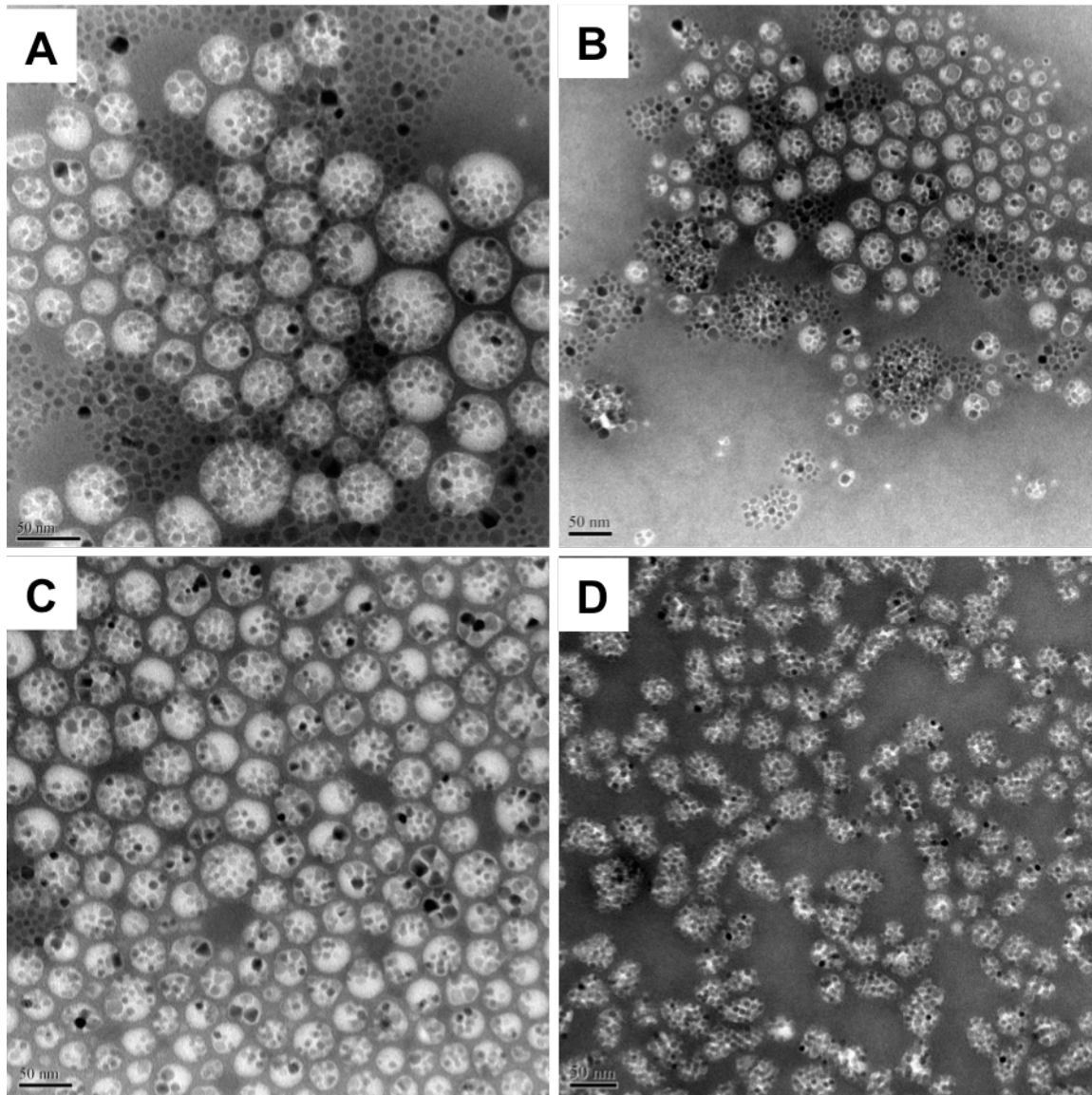
Figure 4.4. TEM images of the different purified MNCs formulations obtained from different trials in Table 4.1 **A**. Formulation A1 obtained at R_e 6300 **B**. Formulation A2 obtained at R_e 8400, and formulations A3 (**C**.) and A6 (**D**) obtained at R_e 12000.

The TEM images of the final products obtained after magnetic separation are shown in Figure 4.3. It can be seen that at lower R_e values, the mixing was inefficient. As a result, there was a significant population of MNPs, which were either individually or at least very loosely held together by the polymer (**figures 4.5A and B**). In contrast, R_e values above 10,000, resulted in distinct, well-defined MNCs (**figures 4.5C and D**). As observed from the DLS data (**Figure 4.6**), all formulations showed particle sizes in the 50-150nm ranges

and good PDI. Formulations A1 and A2 in particular, showed lower D_{eff} due to the presence of a large population of individual and loose MNPs stabilized by Pluronic F127.
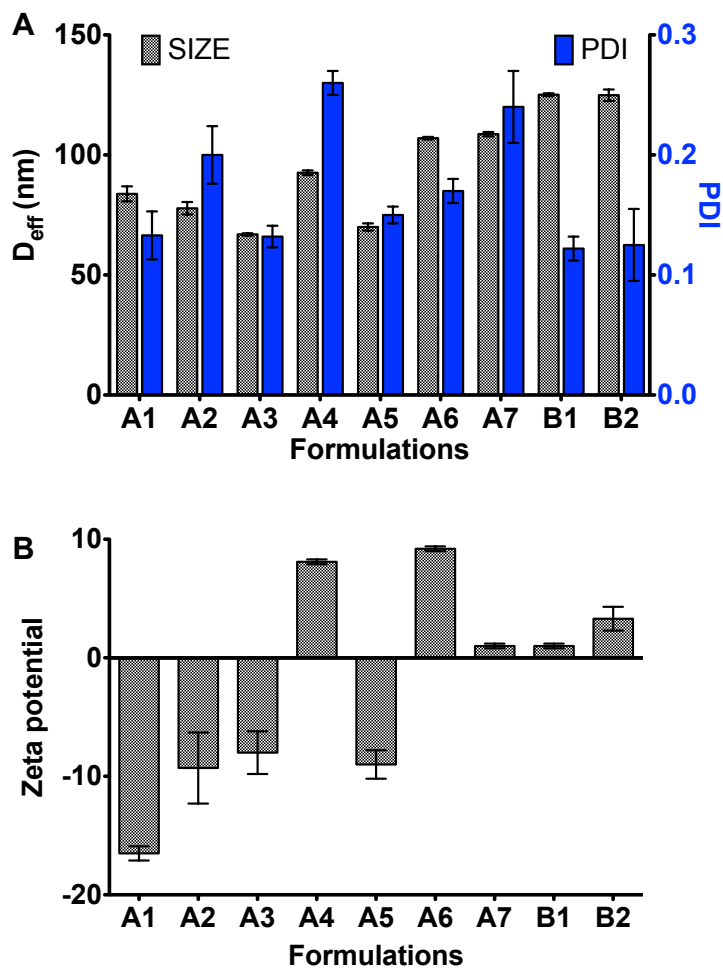
Figure 4.5. Particles size (**A**) and Zeta potential(**B**) of different formulations prepared by MIVM

The cluster size was governed by the targeted %LC$_{MNP}$ in the formulations prepared at R$_e$ 12000. Also, introduction of a more hydrophobic P123 polymer resulted in an increase in cluster size while the PDI was reduced significantly. Zeta potentials of the formulations were in the -15mV to +10mV range hinting at a mild surface charge. We further determined the composition of selected formulations prepared at R$_e$ 12000 by TGA. For this study, PTX loading was determined separately by HPLC and that along with the

surfactant content were deducted from the total loss of ignition (LOI) to obtain the polymer content in the clusters. As seen in **Figure 4.7,** the targeted loading capacities of MNPs (%TLC_{MNP}) dictated the composition of the formulations. Polymer type did not affect MNP encapsulation. However, incorporation of P123 polymer resulted in an increased in drug loading (%LC). However, the MNC formulations did not have high PTX loading.

Inclusion of P123 has been shown to significantly increase the %LC of PTX and other hydrophobic drugs in Pluronic-based micellar systems.[25-28] Hence we had anticipated a similar effect with MNC formulations as well. However, the effect was only marginal. We speculate that the hydrophobic block of Pluronic is insufficient to encapsulate both MNCs as well as PTX and hence MNC encapsulation predominates over PTX.
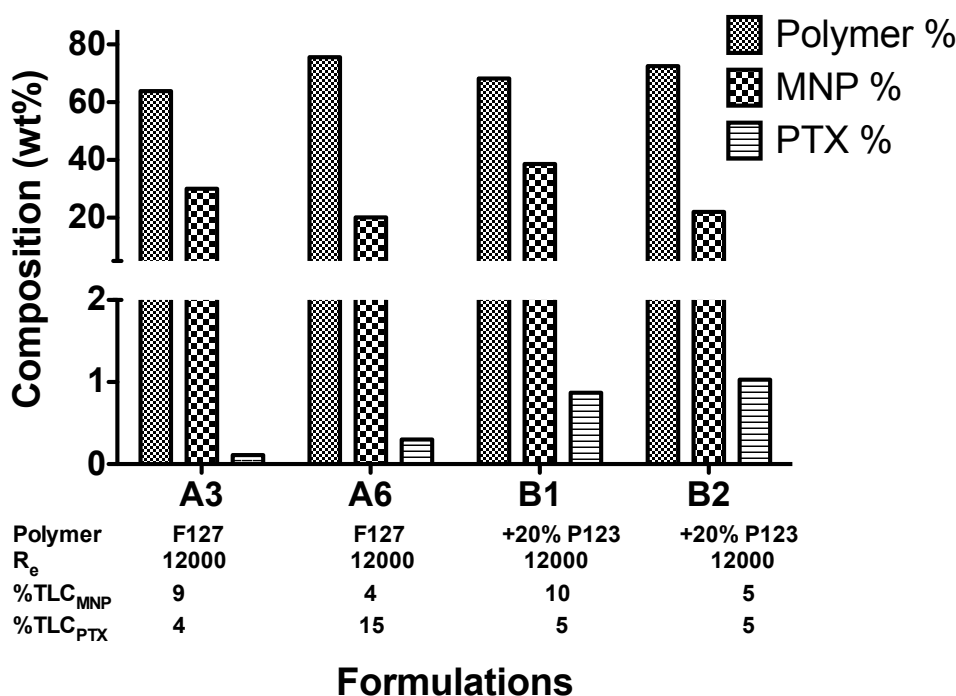
.**Figure 4.6.** % composition of MNCs prepared by MIVM at R_e 12000

Further, we conducted extensive colloidal stability studies of formulation A4 in PBS (pH 7.4;10 mM) and DI water at room temperature (RT) and physiological temperature. The formulation was stable over the entire period of the study with minimal increase in both size as well as PDI (**Figure 4.8**).
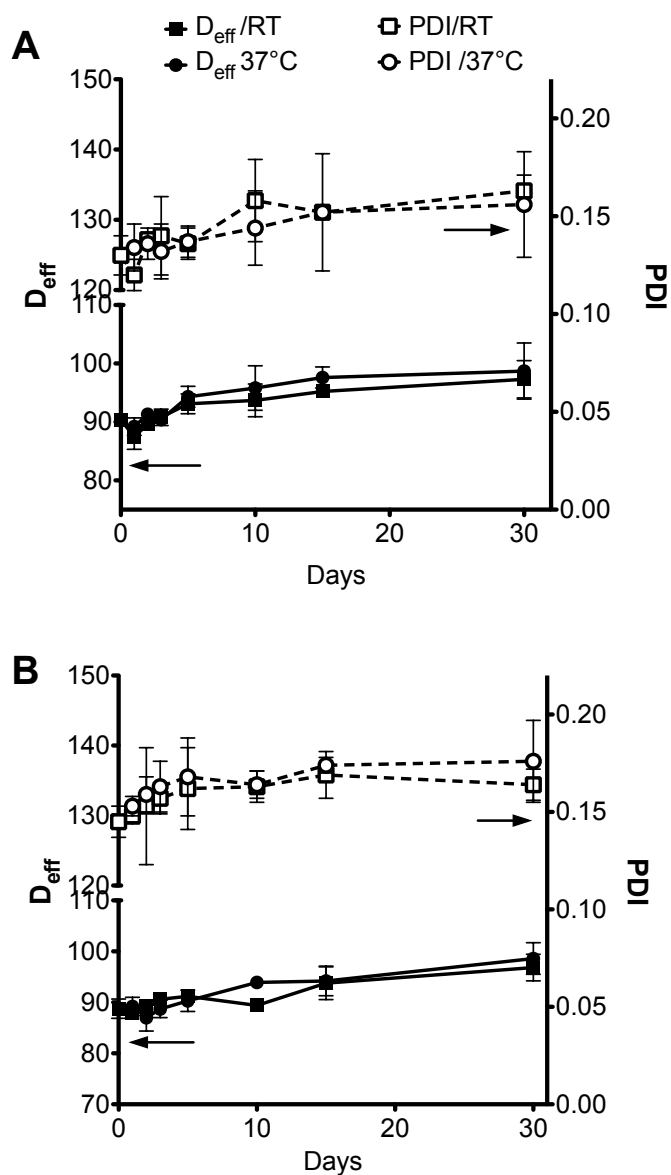

Figure 4.7. Colloidal stability of formulation A6 in **A.** Water and **B.** PBS (pH 7.4)

4.3.3 MRI CAPACITY OF MNCS PREPARED BY MIVM
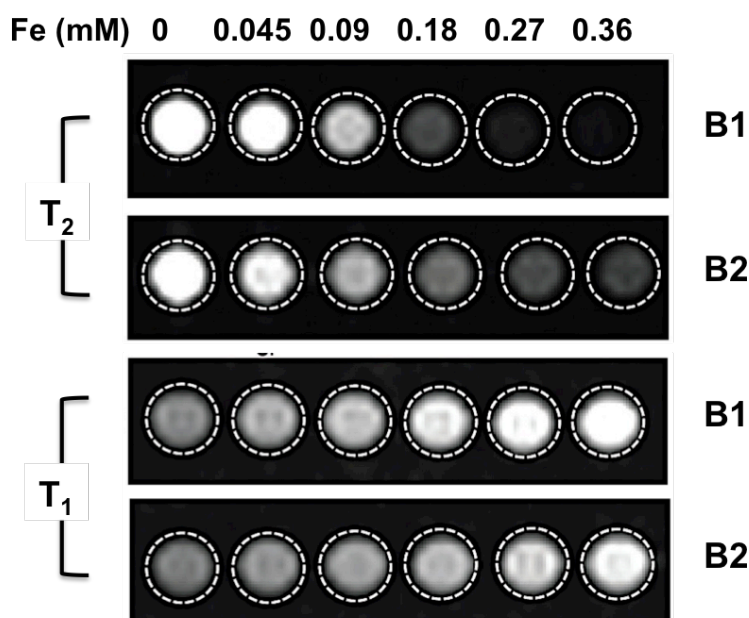
Figure 4.8. MRI potential of MNCS prepared by MIVM

Finally, we studied the MRI potential of two MNC formulations prepared from a blend of P123 and F127 (1:4 wt%) with 10% (Formulation B1) and 5% (Formulation B2) %TLC$_{OMP}$ respectively. MNCs were prepared at R$_e$ 12000. We prepared serial dilutions of the MNCs in 2% w/v molten agar gel. After the gels solidified at RT, MRI scans were taken in a 3T Siemens human MRI scanner. The protocol for T$_1$ and T$_2$-weighted images was similar to that followed in the previous chapters. As seen in **figure 4.9**, the contrast intensities were governed by %LC$_{MNP}$. Formulation B1, with 10% TLC showed stronger negative contrast at lower concentrations than formulation B2 which had a 5% TLC. Interestingly, the formulations also exhibited superior T$_1$ (positive) contrasts as well at higher concentration. It should be noted at MNPs less than 7nm core sizes (USPIOs) have been successfully used as T$_1$ contrast agents. The MNPs used in this case were 6.3nm

and hence showed an enhanced positive contrast as well. Further, the compact cluster formation also added to the phenomenon.

3.5 DISCUSSION

The advent of nanotechnology in the field of medicine and healthcare has initiated a radical change in the treatment of various diseases, especially those which, till now were perceived as fatal and untreatable. Several research studies have provided significant proofs of the concept by demonstrating unprecedented therapeutics efficacy of these nanoparticles loaded with the same therapeutic agents currently used in clinical practice, albeit with limited efficacy and severe side effects. However, large-scale production of uniform-sized nanoparticles of organic and inorganic hydrophobic compounds by an economical, scalable process is a considerable challenge. Flash nanoprecipitation is an advanced technique that relies on fast mixing of two or more streams to create supersaturation. In this technique dissolved solute/ solutes and stabilizing amphiphilic polymer are rapidly mixed with an anti-solvent to create supersaturation over a time period shorter than the typical nucleation and growth time scales for the hydrophobic components. The rapid nucleation and uniform growth of the nanoparticles is curbed by the uniform adsorption of the amphiphilic block copolymers on the particle surface. The process results in very narrow particle size distributions.

An understanding of rapid precipitation of the dissolved components requires an understanding of the role of macro-, meso- and micromixing on the development of supersaturation. Different types mixing devices have been developed and characterized, such as stirred-tank precipitators[29] and impinging-jet precipitators[17]. Johnson and Prud'homme have studied the dependence of mixing time on a critical process parameter called the Reynolds number (R_e) and geometry in a Confined Impinging Jet mixer (CIJ).[20] The MIVM overcomes a prime shortfall of the CIJ such as the requirement of equal flow rate of the solvent and anti-solvent streams entering the device. The ability to modulate the momentum of each stream contributes independently to drive micromixing in the cell.

The choice of R_e dictates the performance of the MIVM and is independent of the configuration of the inlet streams. Above a certain threshold R_e value, usually about 2000, very uniform mixing can be obtained for simple reaction mixtures. This threshold changes with the type of application. For nanoparticle formation R_e value above 5000 usually provides highly uniform mixing and results in nanoparticles with significantly low PDI values. In case of MNCs formed by MIVM, this threshold R_e value in the range of 5000-6000. [30] The physicochemical properties of the solute encapsulated in the clusters plays a significant role in the efficiency of cluster formation. The solubility of the various components of the organic anti-solvent stream such as the drug, the MNPs and the polymers are significantly different and thus it is essential to select an appropriate R_e such that all the components precipitate simultaneously upon super saturation in the mixing chamber. In addition, the concentration of the organic solutes in comparison with that of the stabilizing amphiphilic polymer was also a critical parameter. Thus, MNCs prepared in trial A1, showed a significant population of loosely held MNPs, which were individually stabilized by Pluronic following mixing at a R_e 6,300. The PDI of this formulation was low most likely due to the presence of a significant proportion of individual highly monodisperse 7nm MNPs. This population of individually stabilized MNPs or 'loose MNCs' decreased significantly upon reducing the MNP concentration in the THF stream to 20 wt% of that in Trial A1 and increasing R_e to 8400. Further increase in R_e to 12,000 and beyond resulted in complete absence of 'loose MNCs' with significant improvement in PDI. As the momentum of the mixing streams increased, it increased the mixing speed thereby prompting simultaneous precipitation of the MNPs and polymer and causing the polymer to stabilize the cluster promptly and efficiently. Any further increase in R_e up to a maximum of 16,250 did not cause any improvement in the MNC characteristics or PDI (data not shown).

The negligible $\%LC_{PTX}$ in all trials conducted with F127 only can be due to two factors. First is the type of polymer being used and second is the precipitation rate of the drug in the mixing chamber. Encapsulation of hydrophobic payloads within micellar systems or related core-shell structures comprising of a hydrophobic core and hydrophilic shell is governed by the properties of the amphiphilic polymers used for formation of the nanostructures. Pluronic F127 is a triblock copolymer with a relatively small central hydrophobic poly (propylene oxide (PPO) block having a molecular weight of 3775 Da (65 PO r.u.). MNPs with fatty acid ligands on the surface are known to be stabilized by a process known as ligand exchange.[31-33] As known from the previous two chapters and as discussed in the literature,[33] there exists a hierarchy of binding of different functional groups with catechol showing the maximum ligand exchange with oleic acid from MNP surfaces followed by phosphates, amines and lastly carboxylates. Given the structure of the central PPO block of Pluronic and absence of any of these functional groups, we believe that the efficient micromixing in the mixer further accentuates the strong hydrophobic interactions between the PPO block and the oleic acid brushes on the MNP surface and it is these interactions that result in the formation of stable and well-defined spherical MNCs. However, in doing so, the PPO blocks get completely utilized by the MNPs leaving absolutely no hydrophobic polymeric region available for entrapment of PTX. Attempts were made to reduce MNP feed and increase PTX feed (trial A6). However, these attempts resulted in a high proportion of dead micelles and unentrapped free PTX with only a marginal increase in $\%LC_{PTX}$. Given the high HLB of Pluronic F127 (HLB 22), it is also very likely that upon reaching supersaturation in the mixing chamber, PTX precipitates rapidly leading to separation stabilization by the polymer and thus minimal co-entrapment in the MNCs. In order to decrease the HLB of the polymeric system, 20 wt% Pluronic P123 (M.wt. 5750, HLB 8, PPO block M.wt. 3775) was mixed with 80 wt% of F127 (Trials B1 and B2). Such a mixture has been shown to significantly enhance loading

capacity of hydrophobic drug in resulting mixed micellar systems due to a decrease in the overall.[26-28] This approach resulted in a significant increase in PTX loading. However, from the point of therapeutic efficacy and balance between the two functional components, this %LC was not sufficient and highlighted the limitations of Pluronic polymers for synthesis of co-encapsulated nanosystems such as the MNCs prepared here. An amphiphilic di-block copolymer with a larger hydrophobic block of at least 6 KDa may be required to co-encapsulate both the hydrophobic components in appreciable amounts in order to achieve the desired theranostic goals.

It should be noted here that $\%LC_{MNP}$ could be controlled easily by changing MNP concentration in the THF stream. This was evident when the MRI potential of the MNCs obtained from Trials B1 and B2 was studied in phantom gels. MNCs synthesized in Trial B1 with 10 wt% concentration of MNPs in THF stream resulted in 39 wt% MNP content in comparison with Trial B2 wherein the MNP content in the THF stream was 5 wt% and resulted in 22 wt% MNP content (Figure 4.7). Interestingly, these MNCs showed significantly higher r_1 signals as well. MNPs, specifically, USPIOs in the core size range of 4-7nm are known to undergo both R_1 and R_2 relaxation resulting a dual-modal contrast capability.[34-36] This finding further expands the scope of biomedical applications of these MNCs beyond tumor contrast and drug delivery agents. Such MRI contrast agents can also function effectively as blood pool agents in cardiovascular and cerebrovascular disorders.

3.6 CONCLUSIONS

. Flash precipitation or MIVM involves rapid nucleation at rates less that 50ms, growth and kinetically induced polymeric stabilization of the nanoparticles. We attempted to design theranostic magnetic nanoclusters by co-encapsulating anticancer agents PTX along with oleic acid coated MNPs (OMPs) stabilized by Pluronic block copolymers during the rapid micro-mixing of the organic solvent stream containing dissolved polymer, MNPs and PTX into miscible anti-solvent streams at time scales in the order of 1-2ms. MNCs fabricated by MIVM displayed uniform spherical structure and had a narrow size distribution and relatively low polydispersity. By changing the Reynolds number (R_e), the cluster size and size distribution could be controlled easily. Given the higher HLB of Pluronic F127, inclusion of a relatively hydrophobic Pluronic P123 enabled successful encapsulation of Paclitaxel along with the MNPs. Although, considerably less than conventional micellar systems, the obtained PTX loading was in line with our anticipation given the relatively smaller hydrophobic blocks of Pluronic F127 as well P123. These resulting compact MNC formulations produced a higher negative T_2-weighted contrast under a 3T MRI scanner indicating at significantly higher relaxivity (r_2) values. Thus, we report the successful fabrication of a biocompatible theranostic system with potential applications in cancer therapy wherein the site-specific chemotherapeutic efficacy and visualization of tumor regression can be achieved simultaneous over an extended period of time.

3.5 FUTURE DIRECTIONS

The ability of MNCs prepared by MIVM to function as both T_1 and T_2 contrast agents, as shown in the phantom gel results is a highly desirable feature and hence we propose that the same core size be used. While Pluronic block copolymers resulted in stable MNCs by MIVM, the polymer structure was the main factor limiting the co-encapsulation of PTX and MNPs. Hence future studies will be directed towards studying the effect of polymers with longer hydrophobic blocks. Given the advantages of polypeptide-based polymers, we propose to design MNCs stabilized by poly (phenyl alanine)-PEG polymer. Given the highly hydrophobic nature of poly (phenyl alanine), synthesis of the diblock copolymers may require a longer PEG block, such as that with M. wt 10,000 in order to balance a poly (phenyl alanine) block of more than 50 r.u. Subject to successful loading of both MNPs and significant amounts of PTX or any other anti-cancer agents, we also propose extensive *in vitro* and *in vivo* studies to establish the theranostic potential of these MNCs prepared by MIVM.

3.6. REFERENCES

1. Sun, C.; Lee, J. S.; Zhang, M., Magnetic nanoparticles in MR imaging and drug delivery. *Adv. Drug Del. Rev.* **2008,** 60, 1252-1265.

2. Ely, T. O.; Amiens, C.; Chaudret, B.; Snoeck, E.; Verelst, M.; Respaud, M.; Broto, J.-M., Synthesis of nickel nanoparticles. Influence of aggregation induced by modification of poly (vinylpyrrolidone) chain length on their magnetic properties. *Chem. Mater.* **1999,** 11, 526-529.

3. Luo, B.; Song, X.-J.; Zhang, F.; Xia, A.; Yang, W.-L.; Hu, J.-H.; Wang, C.-C., Multi-functional thermosensitive composite microspheres with high magnetic susceptibility based on magnetite colloidal nanoparticle clusters. *Langmuir* **2009,** 26, 1674-1679.

4. Yan, B.; Thubagere, A.; Premasiri, W. R.; Ziegler, L. D.; Dal Negro, L.; Reinhard, B. M., Engineered SERS substrates with multiscale signal enhancement: nanoparticle cluster arrays. *ACS Nano* **2009,** 3, 1190-1202.

5. Kim, J.; Kim, H. S.; Lee, N.; Kim, T.; Kim, H.; Yu, T.; Song, I. C.; Moon, W. K.; Hyeon, T., Multifunctional uniform nanoparticles composed of a magnetite nanocrystal core and a mesoporous silica shell for magnetic resonance and fluorescence imaging and for drug delivery. *Angew. Chem. Int. Ed.* **2008,** 47, 8438-8441.

6. Lee, J. E.; Lee, N.; Kim, H.; Kim, J.; Choi, S. H.; Kim, J. H.; Kim, T.; Song, I. C.; Park, S. P.; Moon, W. K., Uniform mesoporous dye-doped silica nanoparticles decorated with multiple magnetite nanocrystals for simultaneous enhanced magnetic resonance imaging, fluorescence imaging, and drug delivery. *J. Am. Chem. Soc.* **2009,** 132, 552-557.

7. Huang, H.-Y.; Shieh, Y.-T.; Shih, C.-M.; Twu, Y.-K., Magnetic chitosan/iron (II, III) oxide nanoparticles prepared by spray-drying. *Carbohydr. Polym.* **2010,** 81, 906-910.

8. Lee, S.-J.; Jeong, J.-R.; Shin, S.-C.; Kim, J.-C.; Chang, Y.-H.; Chang, Y.-M.; Kim, J.-D., Nanoparticles of magnetic ferric oxides encapsulated with poly (D, L latide-co-glycolide) and their applications to magnetic resonance imaging contrast agent. *J. Magn. Magn. Mater.* **2004,** 272, 2432-2433.

9. Siddiqui, S. W.; Zhao, Y.; Kukukova, A.; Kresta, S. M., Characteristics of a confined impinging jet reactor: energy dissipation, homogeneous and heterogeneous reaction products, and effect of unequal flow. *Ind. Eng. Chem. Res.* **2009,** 48, 7945-7958.

10. Siddiqui, S. W.; Unwin, P. J.; Xu, Z.; Kresta, S. M., The effect of stabilizer addition and sonication on nanoparticle agglomeration in a confined impinging jet reactor. *Colloids Surf. Physicochem. Eng. Aspects* **2009,** 350, 38-50.

11. Liu, Y.; Cheng, C.; Prud'homme, R. K.; Fox, R. O., Mixing in a multi-inlet vortex mixer (MIVM) for flash nano-precipitation. *Chem. Eng. Sci.* **2008,** 63, 2829-2842.

12. Kumar, V.; Prud'Homme, R. K., Thermodynamic limits on drug loading in nanoparticle cores. *J. Pharm. Sci.* **2008,** 97, 4904-4914.

13. Han, J.; Zhu, Z.; Qian, H.; Wohl, A. R.; Beaman, C. J.; Hoye, T. R.; Macosko, C. W., A simple confined impingement jets mixer for flash nanoprecipitation. *J. Pharm. Sci.* **2012,** 101, 4018-4023.

14. D'Addio, S. M.; Prud'homme, R. K., Controlling drug nanoparticle formation by rapid precipitation. *Adv. Drug Del. Rev.* **2011,** 63, 417-426.

15. Chiou, H.; Chan, H.-K.; Heng, D.; Prud'homme, R. K.; Raper, J. A., A novel production method for inhalable cyclosporine A powders by confined liquid impinging jet precipitation. *J. Aerosol Sci* **2008,** 39, 500-509.

16. Johnson, B. K.; Prud'homme, R. K., Flash nanoprecipitation of organic actives and block copolymers using a confined impinging jets mixer. *Aust. J. Chem.* **2003,** 56, 1021-1024.

17. Mahajan, A. J.; Kirwan, D. J., Micromixing effects in a two-impinging-jets precipitator. *AICHE J.* **1996,** 42, 1801-1814.

18. Jung, C.; de Roo, T.; Mecking, S., Conjugated Polymer Composite Nanoparticles by Rapid Mixing. *Macromol. Rapid Commun.* **2014,** 35, 2038-2042.

19. Qiu, P.; Jensen, C.; Charity, N.; Towner, R.; Mao, C., Oil Phase Evaporation-Induced Self-Assembly of Hydrophobic Nanoparticles into Spherical Clusters with Controlled Surface Chemistry in an Oil-in-Water Dispersion and Comparison of Behaviors of Individual and Clustered Iron Oxide Nanoparticles. *J. Am. Chem. Soc.* **2010,** 132, 17724-17732.

20. Johnson, B. K.; Prud'homme, R. K., Chemical processing and micromixing in confined impinging jets. *AICHE J.* **2003,** 49, 2264-2282.

21. Sun, S.; Zeng, H., Size-controlled synthesis of magnetite nanoparticles. *J. Am. Chem. Soc.* **2002,** 124, 8204-8205.

22. Kozlov, M. Y.; Melik-Nubarov, N. S.; Batrakova, E. V.; Kabanov, A. V., Relationship between pluronic block copolymer structure, critical micellization concentration and partitioning coefficients of low molecular mass solutes. *Macromolecules* **2000,** 33, 3305-3313.

23. Majewski, P.; Thierry, B., Functionalized magnetite nanoparticles—synthesis, properties, and bio-applications. *Crit. Rev. Solid State Mater. Sci.* **2007,** 32, 203-215.

24. Frimpong, R. A.; Hilt, J. Z., Poly (n-isopropylacrylamide)-based hydrogel coatings on magnetite nanoparticles via atom transfer radical polymerization. *Nanotechnology* **2008,** 19, 175101.

25. Zhao, L.; Du, J.; Duan, Y.; Zhang, H.; Yang, C.; Cao, F.; Zhai, G., Curcumin loaded mixed micelles composed of Pluronic P123 and F68: preparation, optimization and in vitro characterization. *Colloids Surf. B. Biointerfaces* **2012,** 97, 101-108.

26. Zhang, W.; Shi, Y.; Chen, Y.; Ye, J.; Sha, X.; Fang, X., Multifunctional Pluronic P123/F127 mixed polymeric micelles loaded with paclitaxel for the treatment of multidrug resistant tumors. *Biomaterials* **2011,** 32, 2894-2906.

27. Zhang, W.; Shi, Y.; Chen, Y.; Yu, S.; Hao, J.; Luo, J.; Sha, X.; Fang, X., Enhanced antitumor efficacy by paclitaxel-loaded pluronic P123/F127 mixed micelles against non-small cell lung cancer based on passive tumor targeting and modulation of drug resistance. *Eur. J. Pharm. Biopharm.* **2010,** 75, 341-353.

28. Wei, Z.; Hao, J.; Yuan, S.; Li, Y.; Juan, W.; Sha, X.; Fang, X., Paclitaxel-loaded Pluronic P123/F127 mixed polymeric micelles: formulation, optimization and in vitro characterization. *Int. J. Pharm.* **2009,** 376, 176-185.

29. Garside, J.; Tavare, N. S., Mixing, reaction and precipitation: Limits of micromixing in an MSMPR crystallizer. *Chem. Eng. Sci.* **1985,** 40, 1485-1493.

30. Balasubramaniam, S.; Kayandan, S.; Lin, Y.-N.; Kelly, D. F.; House, M. J.; Woodward, R. C.; St. Pierre, T. G.; Riffle, J. S.; Davis, R. M., Toward Design of Magnetic Nanoparticle Clusters Stabilized by Biocompatible Diblock Copolymers for T2-Weighted MRI Contrast. *Langmuir* **2014,** 30, 1580-1587.

31. Jain, T. K.; Richey, J.; Strand, M.; Leslie-Pelecky, D. L.; Flask, C. A.; Labhasetwar, V., Magnetic nanoparticles with dual functional properties: drug delivery and magnetic resonance imaging. *Biomaterials* **2008,** 29, 4012-4021.

32. Zhang, T.; Ge, J.; Hu, Y.; Yin, Y., A general approach for transferring hydrophobic nanocrystals into water. *Nano Lett.* **2007,** 7, 3203-3207.

33. Davis, K.; Qi, B.; Witmer, M.; Kitchens, C. L.; Powell, B. A.; Mefford, O. T., Quantitative Measurement of Ligand Exchange on Iron Oxides via Radiolabeled Oleic Acid. *Langmuir* **2014,** 30, 10918-10925.

34. Trivedi, R. A.; Mallawarachi, C.; Jean-Marie, U.; Graves, M. J.; Horsley, J.; Goddard, M. J.; Brown, A.; Wang, L.; Kirkpatrick, P. J.; Brown, J., Identifying inflamed carotid plaques using in vivo USPIO-enhanced MR imaging to label plaque macrophages. *Atertio. Thromb. Vasc. Biol.* **2006,** 26, 1601-1606.

35. Frascione, D.; Diwoky, C.; Almer, G.; Opriessnig, P.; Vonach, C.; Gradauer, K.; Leitinger, G.; Mangge, H.; Stollberger, R.; Prassl, R., Ultrasmall superparamagnetic iron oxide (USPIO)-based liposomes as magnetic resonance imaging probes. *Int. J. Nanomed.* **2012,** 7, 2349.

36. Skouras, A.; Mourtas, S.; Markoutsa, E.; De Goltstein, M.-C.; Wallon, C.; Catoen, S.; Antimisiaris, S. G., Magnetoliposomes with high USPIO entrapping efficiency, stability and magnetic properties. *Nanomed. Nanotechnol. Biol. Med.* **2011,** 7, 572-579.

CHAPTER 5

SUMMARY

The superparamagnetic properties of magnetic nanoparticles (MNPs) have continued to attract the attention of scientists from various field for more than three decades. These concerted efforts have resulted in numerous applications of magnetic iron oxide nanoparticles as noted in the previous chapters. Of particular interest are the biomedical applications of MNPs. The ability to precisely control the sizes of MNPs from a few nanometers to a few tens of nanometers further expands the scope of these biomedical applications. These MNPs can be manipulated by an external magnetic field gradient. The magnitude of such a manipulation depends largely on the size of the magnetic cores. This 'remote control', combined with the fundamental penetrability of magnetic fields into human tissue can be exploited in numerous applications such as those involving the transport and/or immobilization of magnetic nanoparticles, or of magnetically tagged biological entities. MNPs or polymer-stabilized formulations thereof can be developed to deliver a wide variety of therapeutic payloads such as an anticancer drug, or a regiment of radionuclide atoms to a targeted region of the body, such as a tumor. The magnetic nanoparticles can be made to transfer of energy in the form of heat from the exciting field to the nanoparticle. This has led to their use as hyperthermia agents, producing toxic amounts of thermal energy in targeted bodies such as tumors; or as adjunct therapy in combination with chemotherapy and radiotherapy.

These and many other possibilities are available in nanomedicine as a result of the special physical properties of MNPs. Of all these application, the ability of MNPs to serve as MRI contrast agents has attracted tremendous attention from the theranostic view point. However, the successful design of MNPs into theranostic agents requires a formulation

that shows minimal toxicity, sufficient drug loading capacity and most importantly a precise balance between the two components i.e. MNPs (diagnostic) and chemotherapeutic agents. Achieving this balance is critical to the success of MNPs as co-encapsulated theranostic agents, and certainly poses significant challenges in the development of MNPs for cancer theranostics.

This dissertation was aimed at designing a biodegradable theranostic nanosystem capable of simultaneous drug delivery of anti-cancer agents and MRI contrast agents i.e. MNPs which serve as excellent T_2- contrast agents. Based on the published literature on development of MNPs as theranostic agents, it can be concurred that there are critical factors for the successful development of a MNP-based theranostic system. They are:-

a. The physicochemical characteristics of the core MNPs

b. The selection of the stabilizing polymer

Accordingly, our efforts were focused on synthesizing MNP cores with enhanced magnetic properties followed by a comprehensive evaluation of different block copolymers as potential stabilizing and cluster forming components of the resulting MNCs. Given the continued emphasis of your group on development of biocompatible drug delivery technologies, we employed biocompatible and biodegradable polymers in these projects. In Chapter 1 we first modified a simple on-pot procedure for synthesis of MNPs by thermal decomposition of the organometallic precursor Fe(acac)$_3$. The magnetic properties of MNPs, which are essential for their MRI contrast function, are governed by the chemical nature and oxidation state of the MNP crystal along with the size of the MNPs. We successfully demonstrated that we can control the crystal size by precisely controlling the rate of heating of the reaction mixture. The rate at which the reaction mixture was heated controlled the two critical staged of crystallization i.e. nucleation and growth. Thus the largest particles (14nm) were achieved by increasing the reaction rate to 4°C/min.

The stabilization of these MNPs were carried out by coating with completely hydrophilic anionic poly (glutamic acid)-*b*-poly (ethylene glycol) polymers with different poly (glutamic acid) block (PLE) lengths. However, the clusters so formed were unstable in physiological media resulting in aggregation and loss of colloidal properties. This was attributed to the PLE block length and the weak coordination complex formed between the carboxylate endgroups of the polymer and the MNP surface, which was easily displaced by the physiological electrolytes that have a higher affinity for MNP surface. This necessitated the structural modification of the polymer to incorporate bisphosphonate containing end groups, which are known to form very strong coordination complexes with MNP surfaces. Inclusion of bisphosphonate containing end groups on the PLE block significantly enhanced the colloidal stability of the MNCs in physiological conditions. The degree of conjugation (D_{conj}) of the bisphosphonate-containing ALN molecule on the PLE block dictated the stability of the clusters with maximum stability obtained at a Dconj of 19 and a cluster size of approximately 70nm.

Cisplatin was successfully conjugated on the MNCs via electrostatic interactions with the available carboxylate groups at pH 9.5. The release rate was also controlled by Dconj. MNCs with highest Dconj also exhibited the slowest release profile. Overall, the MNCs exhibited a sustained pH dependent release profile which was significantly faster at the acidic pH. The D_{conj} and the resulting cluster size, along with the size of the core MNP particles controlled the magnetic properties of the MNCs. In addition, inclusion of cisplatin also positively affected the T_2 relaxivity of the resulting MNC formulations. The incorporation of the Pt metal resulted in close proximity with the MNPs resulted in a metal cluster effect which is speculated as a reason for the increase in relaxivity of the MNCs following cisplatin incorporation.

These anionic MNCs had very low nonspecific cellular uptake in ovarian cancer cells. This is a highly desired feature in nanoformulations as it enables site specific targeting of the nanoformulations thereby significantly reducing the undesired side effects due to uptake in the healthy tissue as well. We targeted this formulation exclusively to ovarian cancer tissue overexpressing LHRH receptor. The MNCs were decorated with synthetic LHRH peptide. LHRH conjugation enhanced the cellular uptake significantly. The effect was more pronounced in cisplatin resistance ovarian cancer (A2780-CisR) cells than the wild type cells (A2780-WT). This active targeting strategy successfully translated into enhanced anticancer efficacy wherein the targeted formulations reduced the IC50 by almost half in comparison to the non-targeted MNCs. LHRHr targeting and the resulting increase in target-specific uptake of the MNPs significantly enhanced the in vitro MRI contrast of the formulation when measured in ovarian cancer cells embedded in agar phantom gels.

Following the successful evaluation of the anionic biocompatible polymer PLE_X-b-PEG_{113} as a surface stabilizer for theranostic MNCs, we studied the potential of a cationic block copolymer in development of stable of MNCs for cancer theranostics (Chapter 3). For this purpose, we employed classical poly (l-lysine)-b-poly (ethylene glycol) block copolymers of different l-lysine repeating units (X = 10, 50 or 100). The MNPs synthesis was modified to further enhance the magnetic properties without compromising on the larger core size and greater saturation magnetization. (M_s). MNCs stabilized by PLK_X-b-PEG_{113} polymers. The cationic block copolymers stabilized the MNPs more efficiently than the anionic PLE-based polymers discussed in Chapter 1. However, similar to the anionic block copolymers, the stability of the resulting clusters was dictated by the PLK block length. Nonetheless, the resulting cationic MNCs did not exhibit any instability in physiological buffers.

The MNCs so developed exhibited significantly higher T_2-relaxivities which increased depending on the MNP size as well as the D_{eff} of the clusters. MNC-3 and MNC-4 had r_2 values significantly higher when compared to the once commercially available T_2-contrast agent Feridex®. The therapeutic functionality was introduced onto the most stable MNC-4 clusters in the form of anti-cancer agent doxorubicin (DOX). DOX was conjugated onto the MNCs at the pendant side chain primary amino group via a pH sensitive hydrazine bond using hetero-bi-functional linker SPDP. The utilization of this end terminal significantly reduced the charge induced toxicity of the formulations. A maximum of 2.5 wt% DOX conjugation was achieved on the MNCs. The pH sensitive hydrazine bond successfully prevented premature release of the chemotherapeutic agent in the physiological medium. As desired, the drug was released rapidly in a sustained manner in acidic pH. The cationic MNCs had significantly higher cellular uptake; almost 20-folds higher when compared that of the targeted anionic MNCs discussed in the previous chapter. Of the two cell lines tested, triple negative breast cancer MDA-MB-231 cells exhibited a relatively slower rate of uptake than the A2780-WT ovarian cancer cells. Confocal microscopy of the ovarian cancer and triple negative breast cancer cells revealed that post-internalization, the clusters were lodged in the lysosomal vesicles, thus supporting the strategy adopted for triggering the drug release from the clusters. Finally, the DOX-loaded pH sensitive MNCs exhibited cytotoxicity efficacy consistent with that expected from a stimuli-responsive sustained release nanoformulation. The IC_{50} values of the formulations was dependent on the drug loading. DOX-MNC-4c formulation was further tested for its MRI contrast potential in vitro by incubating it with the above mentioned cell lines for a 24h period. Cationic MNCs, by virtue of a higher cellular uptake exhibited significantly stronger T_2-weighted contrast in agar phantom gels. Thus, the cationic polymers are more efficient in stabilizing bare uncoated (without oleic acid) MNPs into larger and more compact clusters when compared to anionic polymers. MNPs

synthesized by thermal decomposition have seldom been stabilized via hydrophilic routes and hydrophilic. We showed that in comparison with the co-precipitation technique for synthesis of MNPs, the MNCs formed here were significantly superior from the point of stability, cluster integrity and magnetic properties. Based on the observations in Chapters 2 and 3, it can also be concluded that the strength of the coordination complexes between the MNP surface and the polymers is dictated by the available functional groups and that the strength of these complexes increases as follows $-COOH < -NH_2 \leq (PO(OH)_2)_2$.

In Chapter 4, we studied the effect of multi-inlet vortex mixing (MIVM) or flash precipitation on cluster formation and co-encapsulation of MNPs and hydrophobic anti-cancer agent paclitaxel (PTX). MIVM technique is based on the principal of kinetically controlled supersaturation and the resulting kinetically controlled precipitation of MNPs into highly monodisperse MNCs stabilized by amphiphilic block copolymers. In sharp contrast to the MNPs and polymers used in the previous chapters, here we employed the widely used thermal decomposition technique to coat the MNPs with hydrophobic surfactants oleic acid and oleylamine *in situ* while the polymers were triblock amphiphilic Pluronic block copolymers.

The clustering formation is governed by four critical factors namely

a. The flow rate of the opposing streams during the mixing process (Reynolds number R_e)

b. The final ratio of organic and inorganic solvents in the mixing chamber, which leads to supersaturation and precipitation

c. The concentration of the organic components in the miscible organic fraction and the critical aggregation concentration (cac) of all the organic components in the final mixed solvent system in the chamber

d. The HLB of the polymer and the length of the hydrophilic block

The cluster formation process showed maximum efficiency at Re between 9000 and 12,500. Beyond 12,500 the cluster formation showed no significant improvement. Re controls the supersaturation of the system and hence the onset and rate of precipitation of the organic components. The R_e was optimized to 12000. Any further increase in Re did not cause any changes in the efficiency. Polymer characteristics play a significant role in MNC formation. Since the cluster formation is caused by interaction of the hydrophobic block of the polymer and the hydrophobic surfactants coating the MNPs, the hydrophobic block length and thus the overall HLB of the polymer played a critical role in MNC formation as well as co-encapsulation of PTX along with the MNPs. With Pluronic F127 and P123, the hydrophobic blocks do provide ample hydrophobic environment for co-encapsulating significant amounts of PTX, most likely due to the presence of MNPs, which utilize most of the hydrophobic blocks for stabilization into clusters. Nonetheless, in comparison to single polymer F127, a 4:1 blend of F127 and P123 resulted in an increase in co-encapsulation of PTX. Thus, MIVM provides a highly efficient technique for formation of MNCs with low polydispersity. Due to technical difficulties, the drug loading could not be maximized. Nonetheless, the results have provided a good understanding into the variables that are critical to the enhancement of drug loading.

Thus, to summarize, we successfully studied the physicochemical factors affecting formation of MNP-based theranostic. In doing so, we successfully developed highly stable theranostic MNCs from three different types of block copolymers namely, anionic, cationic and non-ionic block copolymers. This success and the insights gained into the development of MNPs as MRI contrast agents warrant further research into the in vivo characterization of these different theranostic nanosystems.